Interface Engineering for Organic Electronics

Manufacturing of Hybrid Inorganic–Organic Molecular Crystal Devices

Peter de Veen

INTERFACE ENGINEERING FOR ORGANIC ELECTRONICS

MANUFACTURING OF HYBRID INORGANIC–ORGANIC MOLECULAR CRYSTAL DEVICES

PETER DE VEEN

PhD committee

Chairman and secretary:

Prof. dr. G. van der Steenhoven	University of Twente

Supervisors:

Prof. dr. ing. D.H.A. Blank	University of Twente
Prof. dr. ing. A.J.H.M. Rijnders	University of Twente

Members:

Prof. dr. J.J.L.M. Cornelissen	University of Twente
Dr. ir. G. Koster	University of Twente
Prof. dr. T.T.M. Palstra	University of Groningen
Prof. dr. W.G. van der Wiel	University of Twente

Cover: *On the background, an optical microscopy image of a pentacene single-crystal.*

The work described in this thesis was carried out at the Inorganic Materials Science group at the Faculty of Science and Technology & the MESA$^+$ Institute for Nanotechnology, University of Twente, P.O. Box 217, 7500 AE Enschede, The Netherlands.

This research is supported by NanoNed, a national nanotechnology program coordinated by the Dutch Ministry of Economic Affairs.

P.J. de Veen

Interface Engineering for Organic Electronics:
Manufacturing of Hybrid Inorganic–Organic Molecular Crystal Devices

PhD Thesis, University of Twente; Enschede, The Netherlands

ISBN: 978-90-365-3236-5
DOI: 10.3990/1.9789036532365
Printed by GildePrint; Enschede, The Netherlands

INTERFACE ENGINEERING FOR ORGANIC ELECTRONICS

MANUFACTURING OF HYBRID INORGANIC–ORGANIC MOLECULAR CRYSTAL DEVICES

PROEFSCHRIFT

ter verkrijging van
de graad van doctor aan de Universiteit Twente,
op gezag van de rector magnificus,
prof. dr. H. Brinksma,
volgens besluit van het College voor Promoties
in het openbaar te verdedigen
op vrijdag 30 september 2011 om 16:45 uur

door

Peter Jan de Veen

geboren op 7 april 1980
te Hardenberg

Dit proefschrift is goedgekeurd door:

Prof. dr. ing. D.H.A. Blank	Promotor
Prof. dr. ing. A.J.H.M. Rijnders	Promotor

Contents

Chapter 1

Introduction to Organic Electronics

Chapter 1: Introduction to Organic Electronics

Abstract

The field of Organic Electronics has grown rapidly in recent years, mainly due to the perspective of fabricating electronic devices on large, flexible substrates at low cost. In this chapter, a comprehensive introduction is given to this field of research and to the organic semiconducting materials that are at its basis. Important technological aspects, as well as various scientific characteristics, will be discussed, highlighting the interesting position of the field. Finally, the motivation for this work and the outline of this thesis will be presented.

1.1 Introduction

Organic semiconductors are at the basis of the new and broad field of *Organic Electronics* (or *Plastic Electronics*). Simply said, organic semiconductors are materials formed by organic molecules that have semiconducting properties. In the field of organic chemistry, a molecule is defined as a group of atoms in a relatively fixed arrangement, which are bonded by strong covalent bonds. Organic molecules are primarily constructed of carbon (C) and hydrogen (H) atoms, but often contain also nitrogen (N), oxygen (O), sulfur (S) or selenium (Se) atoms. The unique properties of these organic semiconducting materials lead to a number of advantages, which is expected to result in a large variety of new commercial applications. In fact, the field of organic electronics is entering its commercial phase at the moment and the first organic electronic products can be found in the stores nowadays.

In this chapter, an introduction to the field of organic electronics is given. The advantages and disadvantages of organic semiconductors with respect to the mainstream silicon semiconductor technology will be discussed first in paragraph 1.2. In the next paragraph, 1.3, the industrial relevance of organic electronics will be discussed and illustrated by some present and future applications. Paragraph 1.4 offers a quite extensive historic overview on the development and major scientific breakthroughs of the organic electronic research domain. Paragraph 1.5 introduces the organic semiconducting materials. Distinction is made between the two main categories of organic semiconductors: polymers and small molecules; and between the various deposition techniques typically applied to the two material groups. The mechanism of electrical conductivity in organic semiconductors will be discussed in section 1.6. The influence of this mechanism on the charge carrier transport properties will be pointed out, and the main charge carrier models will be introduced. Finally, in paragraph 1.7, the motivation for this work and the outline of this thesis will be presented.

1.2 Why Organic Electronics?

The starting point of the developing field of organic electronics is the use of organic semiconductors as the basis for electronic devices. In organic electronics, one or more of the inorganic components in an electronic device are replaced by organic materials, eventually leading to all-organic devices. First of all, electronics based on organic semiconductors is by no means expected to replace the inorganic semiconductor technology that is widely used today. Nowadays, it is quite clear that organic semiconductors cannot challenge the high performance of the mainstream inorganic (silicon) semiconductors. This is illustrated in figure 1.1, where the charge carrier mobility is presented for both state-of-the-art inorganic and organic field effect transistors (*e.g.* the mobility μ is a measure of how easily charge carriers can move in a particular material). The field of organic electronics is therefore not considered as a competitor to the mainstream inorganic semiconductor technology.

Instead, organic electronics is aiming at complementary applications where it can benefit from its own key properties. The three key properties of organic semiconductors are:

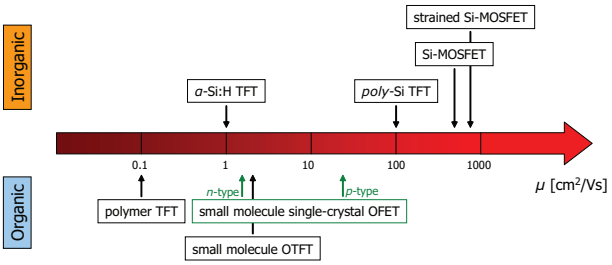

Figure 1.1 *Charge carrier mobility in field-effect transistors based on inorganic (top) and organic (bottom) semiconductors.*

- *Organic semiconductors can be processed at low temperatures*. Bonding between the organic molecules is generally weak. Because no strong bonds need to be broken or reformed, organic semiconductors can be manipulated using a small energetic input.
- *Organic molecules have no dangling bonds and posses semiconducting properties on the molecular level.*
- *A large variety of organic semiconductors can be synthesized, and their physical properties can be 'chemically tailored'.*

These three points are the key enablers to the appealing properties of organic electronics:

- Due to the lack of dangling bonds in the molecules, thin films of organic semiconductors can be deposited on a *large variety of substrates*. The inherent properties of the molecules are hereby preserved, and no epitaxial templating is required to achieve at least some semiconducting properties.
- Thanks to the low thermal budget required, organic semiconductors can be deposited at room temperature (or only slightly above) on substrates that cannot withstand high temperatures, like *flexible substrates* such as paper and (polymer) foils, and on other active organic electronic devices. Besides that, mismatches due to thermal expansion differences are relatively unimportant at low-temperature processing.
- The possibility to process on flexible substrates enables manufacturing on *large-area* substrates, in a reel-to-reel manner with a *high-volume throughput*. Vacuum deposition techniques traditionally used in inorganic semiconductor processing can be replaced by printing-based techniques (*e.g.* screen printing, microcontact printing, inkjet printing), stamping or low-vacuum deposition methods, such as organic vapor phase deposition (OVPD). The ease of fabrication by the absence of high temperatures and vacuum, combined with a high-volume throughput, makes this a potentially *low-cost technology*.
- A wide range of the properties of organic materials, such as solubility in different solvents or the color of light-emission, can be fine-tuned via chemical synthesis to meet the requirements of specific applications. Organic semiconductors promise far superior possibilities for *chemical tailoring* of the physical properties (*e.g.* crystal structure, bandgap, molecular overlap) than is presently possible with inorganic semiconductors.

Due to a combination of these unique properties, organic electronic devices will be used in various applications coexisting with inorganic electronics.

Obviously, organic electronics also have some shortcomings and drawbacks. The weak bonding and ease of manipulation of organic semiconductors often comes at a price of a lower total performance. It also means that the structure and properties of organic semiconductor thin films can be easily disrupted.

More general, there is still a mismatch between the performance of *p*-type and *n*-type organic transistors, which limits the fabrication of complementary devices and circuits. Especially, but not limited to, *n*-type organic semiconductors suffer from a lack of stability in ambient conditions. Another important aspect is the possibility of device downscaling, which is for organic semiconductors not yet as reliable as it is for inorganic devices.

As can be seen in figure 1.1, organic electronics can compete nowadays with the hydrogenated amorphous silicon (*a*-Si:H) technology. However, these amorphous silicon thin film transistors, functioning as pixel drivers, already dominate the display market, which makes it difficult for a new technology to penetrate this market. So far, industrial acceptance of organic electronics has been limited, with organic light-emitting diodes (OLEDs) being the exception to the rule (see paragraph 1.3.2). One of the primary goals of the research community is therefore the development of applications that uniquely exploit the key properties of organic semiconductors.

1.3 Technological Applications

As introduced in the previous paragraph, the research effort in the field of organic electronics is almost completely based on the perspective of processing on large, flexible substrates at a low cost. This point of view is reflected by the fact that most applications mentioned in literature are explicitly based on at least one of the key properties of organic semiconductors. Many organic materials are currently being investigated and used in applications such as organic field-effect transistors [1,2], organic light-emitting devices [3,4], organic photovoltaic cells [5,6] and organic non-volatile memories [7]. This section gives a comprehensive overview of the three organic electronic devices mostly investigated (see figure 1.2), and of the corresponding end products closest to commercialization.

1.3.1 Organic thin film transistors: display circuits and RFIDs

Organic field-effect transistors (OFETs) are now routinely made using organic semiconductors [8,9]. Organic thin film transistors (OTFTs) generated a high level of interest the last decade and are ready to enter the commercial phase [10]. Two main applications that are often quoted with respect to OTFTs are the passive radio frequency identification (RFID) tags and the backplane driving circuitry for active matrix displays [11]. Besides these two applications, use of organic transistors for sensing applications is also receiving a lot of interest [12].

In short, a transistor is a three-terminal device that effectively acts as a switch (see figure 1.2A), and transistors are basic building blocks for integrated circuitry. When a bias is applied to the gate electrode, charges accumulate capacitively at the organic semiconductor – dielectric interface. This, in turn, creates a channel in which holes or electrons (depending on the nature of the organic semiconductor and contacts, and the bias applied) transport

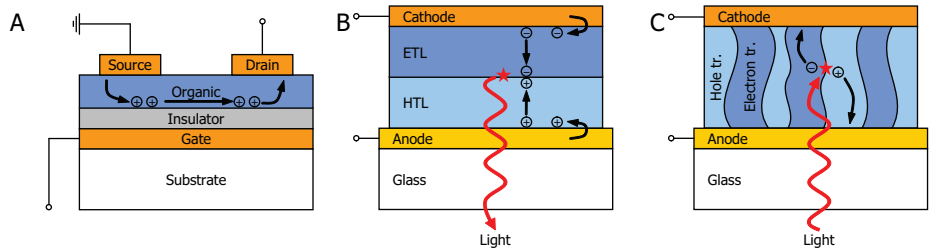

Figure 1.2 *Different types and working principles of organic semiconductor devices are shown. A) Organic field-effect transistor (OFET). B) Organic light-emitting diode (OLED). C) Organic photovoltaic cell (OPV).*

between the source and drain electrodes. It is thus the gate electrode that controls the switching of the device between its *on* and *off* states.

Currently, organic transistors are most promising in display applications, as the performance of OTFTs is now acceptable for many display driving circuitry. Using an organic transistor to drive an organic light-emitting diode display is very attractive in reducing production costs, but mostly in the quest to fabricate the ultimate goal of organic electronics: a complete organic flexible and rollable display.

RFID tags are widely used nowadays, especially in the retail sector. RFID technology uses wireless radio communication to uniquely identify objects or people. Although state-of-the-art RFID tags are fabricated in a cheap inorganic technology, they are still far too expensive for item-level tagging (*e.g.* attaching a tag to every single item in a warehouse). Utilization of organic transistor circuitry in RFID technology is expected to reduce the production costs dramatically (*e.g.* by using inexpensive printing methods), so efficient item-level tagging can be introduced (see figure 1.3A). However, compared to OTFTs, RFID tags and logic applications are staying behind, as adoption of standards, integration and high-frequency operation are current hurdles to commercialization [10].

1.3.2 Organic light emitting diodes: displays and lighting

Many organic semiconductors offer appealing optoelectronic properties, which can be applied by organic light-emitting diodes (OLEDs) in displays and ambient solid-state lighting [13]. OLED technology is at the moment the most advanced organic electronic device platform and the technology has shifted from the research and development phase to the scale-up phase [10].

Organic LEDs operate through injection of charge carriers from opposite contacts (*i.e.* hole injection from the anode and electron injection from the cathode), electron-hole capture within the bulk of the organic semiconductor film to form bound excitons, and subsequent radiative emission from those excitons (see figure 1.2B). The charge injection requires low energy barriers at the metal–organic interfaces for both contacts to inject equal amounts of electrons and holes, which is required for a balanced charge carrier flow. Although many simple diode structures function as OLEDs, one typical approach to achieve a balanced charge carrier flow is using a hetero-layered structure: a combination of hole transport layers (HTL), electron transport layers (ETL) and emission layers (EML).

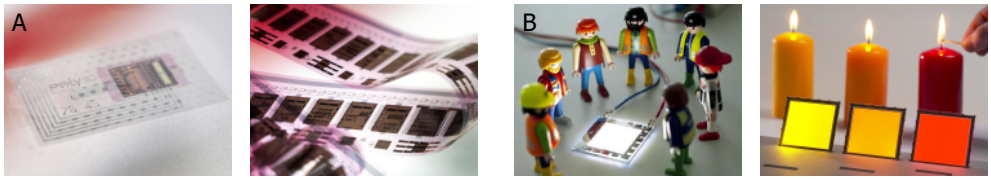

Figure 1.3 *A) Sample of the first printed polymer RFID tag (13.56 MHz) and mile-long printed logic circuits for RFID tags, and B) OLEDs for solid-state lighting. Copyright pictures: PolyIC, Philips.*

In the display field, OLED technology can compete with liquid-crystal and plasma displays. The technology offers unique attributes, such as ultra-brilliant colors and low-power consumption, in addition to a wide viewing angle and a thin display.

More recently, solid-state lighting has been gaining interest (see figure 1.3B), mostly due to the improved efficiency of white OLEDs. OLED light sources are fully dimmable, diffuse and many colors can be realized on a large area. Thanks to the ability of processing OLEDs on flexible foils, the light source can be thin, flat and lightweight, while leaving the freedom to design panels in any shape; especially the architectural and display sectors represent potentially huge opportunities for new product designs. Device lifetimes, color shifts, and deep blue electroluminescence, however, remain challenges to be solved before these devices become common in the market [10].

1.3.3 Organic photovoltaics: solar cells

Another device application of organic semiconductors is in organic photovoltaics (OPV) [14]. These devices, also called organic solar cells, now emerge as a major area of interest [10].

OPVs operate on the reverse principle to OLEDs (see figure 1.2C). These devices are diode structures, typically comprising both an electron donor light-absorbing semiconductor and an electron acceptor semiconductor. Working principle is making the energy difference between the valence and conduction band levels across the interfacial heterojunction sufficiently large, so that the energy advantage of separating electrons and holes outweighs the binding energy of electron and hole in an exciton. Systems constructed as abrupt bilayer hetero-junctions are relatively inefficient, because photogenerated excitons must reach the junction interface to ionize (*e.g.* the exciton diffusion length is ~10 nm). Efficient OPV systems use the distributed or bulk heterojunction concept of blending donor and acceptor in one layer.

Typical reported OPV efficiency is about 3 - 5%, well below efficiencies routinely obtained with inorganic solar cells (14 - 17%). However, expected benefits like cheap production and the use of flexible substrates drive the research on OPVs. Many of the organic materials investigated today are sensitive to air and moisture, and some even tend to degrade under illumination, which is quite undesirable for a solar cell. Current technical challenges, besides increasing the efficiency, are therefore increasing the device stability and lifetime [10].

1.4 Historical Overview

The field of organic electronics is rather new: the main scientific breakthroughs in the field were achieved only at the end of the eighties. Academic and industrial interest slowly increased during the nineties; however, the major boost in research took place at the beginning of the new millennium, as can be seen in figure 1.4.

The beginning of the field is mostly marked by the discovery of electrical conductivity in doped polyacetylene in 1977 by Heeger, Shirakawa, MacDiarmid and co-workers [15], for which they were given the Nobel Prize in Chemistry in 2000 *"for the discovery and development of conductive polymers"* [16]. They found that oxidation with chlorine, bromine or iodine vapor made polyacetylene films up to 10^9 times more conductive than without doping the polymer film [17]. This Nobel Prize is surrounded with some controversy, as early work by McGinness, Corry and Proctor on conducting melamine from 1974 [18], and much earlier work on electrical conduction in polypyrrole by Bolto, McNeill and Weiss in 1963 [19], were in principle similar discoveries.

If we broaden the spectrum and, besides the polymer systems mentioned so far, also include studies on electrical conductivity in small organic molecular systems, even more early work should be given credit. Already in 1948, Eley studied the conductivity of metal-free and copper phthalocyanine crystals [20]. Heilmeier and Zanoni performed field-effect measurements on copper phthalocyanine (CuPc) thin films in 1964 [21]. In 1970, Barbe and Westgate showed the influence of the atmosphere (*e.g.* vacuum, hydrogen and oxygen ambient) on the field-effect properties of metal-free phthalocyanine single-crystals [22]. Research on the electrical conductivity in acene systems started the same year, when Williams and Schadt investigated the current-voltage characteristics of doped and undoped anthracene crystals [33], followed by the discovery of field-effect properties in anthracene crystals a year later by Bauser und

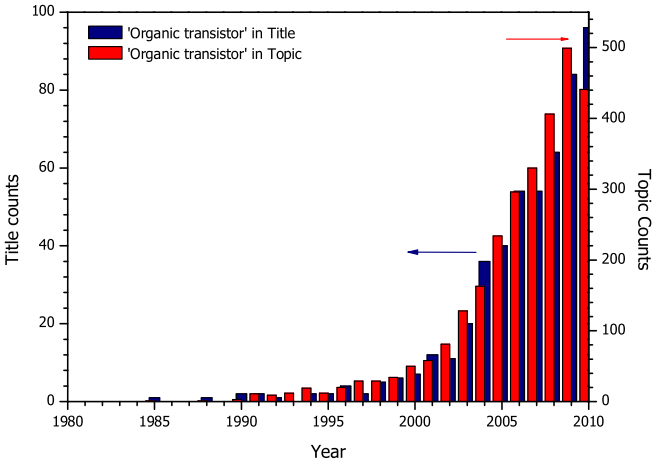

Figure 1.4 *Number of publications in which 'organic transistor' is mentioned in the title (blue, left) or topic (red, right) in the ISI web of knowledge.*

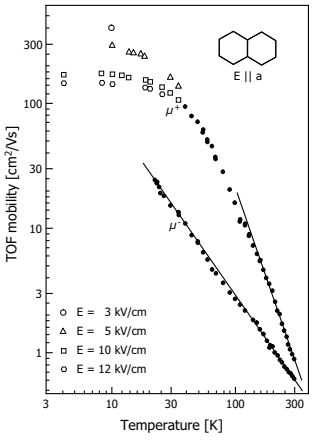

Figure 1.5 *Electron and hole time-of-flight mobilities μ in naphthalene crystals [29].*

Pernisz [24]. Electroluminescence of these anthracene crystals had already been demonstrated in 1963, by Pope *et al.* [25].

Research in the field continued slowly in the beginning of the eighties. In 1983, metal–insulator–semiconductor diodes with undoped poly-acetylene as organic semiconductor were fabricated by Ebisawa, Kurokawa and Nara [26], and Partridge showed electroluminescence from polyvinylcarbazole films [27]. Kudo *et al.* performed field-effect measurements on organic dye films (merocyanine) in 1984 [28]. Benchmark studies by Karl and co-workers in 1985 reported very high electron and hole mobilities in ultrapure naphthalene single-crystals, measured by time-of-flight spectroscopy (see figure 1.5 and paragraph 2.6.1) [29,30].

Major breakthroughs were achieved in 1986 and 1987, giving an enormous boost to research on electrical devices based on an active organic semiconducting layer. First, Tang reported an organic heterojunction solar cell, fabricated with two thin layers of phthalocyanine and a perylene tetracarboxylic derivative [31]. Second, Tsumura, Koezuka and Ando reported the first organic field-effect transistor (based on polythiophene) with a significant current gain [32,33]. And third, Tang and VanSlyke [34] reported the appearance of organic light-emitting materials (Alq_3 and diamine). These three studies demonstrated the possibility of fabricating organic field-effect transistors, organic light-emitting devices and organic solar cells, based on cheap materials and inexpensive production methods. New technological applications became feasible, as flexibility, transparency and large-area production could also be easily incorporated.

Increasing research efforts led in 1989 to the fabrication of the first metal–insulator–semiconductor field-effect transistor with an active conjugated oligomer (*α*-sexithienyl) as semiconductor by Horowitz *et al.* [35], to the first appearance of light-emitting diodes based on conjugated polymers by Burroughes *et al.* in 1990 [36] and to the first *n*-type organic thin film transistor with tetracyanoquinodimethane (TCNQ) as active material by Brown *et al.* in 1994 [37]. In 1992, pentacene entered the field, being applied in organic thin film transistors by Horowitz *et al.* [38]. The highest values of the field-effect mobility in this period were in the range of 10^{-4} - 10^{-3} cm^2/Vs. Large steps were made the next years, as the first organic integrated circuits were reported by Brown and co-workers in 1995 [39], and in 1997 the 1 cm^2/Vs charge carrier mobility barrier was broken by Lin *et al.* [40]. Their pentacene-based thin film transistors, with the SiO_2 dielectric pre-treated with a self-assembled monolayer (SAM), showed that organic thin film transistors can compete with the inorganic amorphous silicon thin film transistor technology. This report boosted research on organic transistors; the mobility has been gradually increasing after this improvement and many organic transistors with high mobilities (>1 cm^2/Vs) have been demonstrated since.

In 2000-2002, attention to organic electronics and acene chemistry was at an all-time high, due to claims of superconductivity in anthracene, tetracene and pentacene single-crystals [41] and polythiophene thin films [42], and lasing in tetracene single-crystals [43]. Also several 'record-breaking' results on ambipolar pentacene single-crystal field-effect transistors with extremely high mobility for both holes (up to 1200 cm^2/Vs) and electrons (up to 320 cm^2/Vs) were presented [44]. In 2002, the reputation of the organic electronics field suffered much

Figure 1.6 *Examples of organic electronics applications available on the consumer market; A) the Philishave Sensotec 8894 B) the Polymer Vision Readius; C) the Samsung Google Nexus S; and D) the LG EL9500 OLED television. Pictures copyright: Philips, Polymer Vision, Google and LG Display.*

damage, as a large scientific fraud by Schön was made public [45]. Most of his Science, Nature and Physical Review papers were retracted (see [46] for an extended list), as a result of an independent investigation conducted at Bell Laboratories [47]. The co-authors of these articles were all rehabilitated, however, and are still among the major scientific players in the field.

The first commercial application of organic electronics was brought to the consumer market by Philips in 2002, as the Philishave Sensotec 8894 (the 'James Bond shaver', due to its sponsored appearance in 'Die another day') contained a polymer light-emitting diode display (see figure 1.6A) [48]. Meanwhile, the performance of pentacene transistors was improved by Klauk and co-workers using a polymer dielectric material as gate [49]. Most importantly, besides the high mobility of 3 cm^2/Vs, they achieved a low threshold voltage (<10 V) and a large current on/off ratio of 10^5.

The last years, more organic electronic applications show up in the stores. At the end of 2007, Sony launched in Japan the 11 inch XEL-1, the first commercially available television with an OLED display, which is 3 mm thick and has a 178° viewing angle [10,50]. In 2008, Polymer Vision started marketing the Readius, the first commercially available *e*Book pocket reader, with a 5 inch rollable display based on a 16-grayscale E-Ink electrophoretic imaging film (see figure 1.6B) [51]. Active-matrix OLED (AMOLED) displays are at the moment frequently applied in mobile smartphones (see figure 1.6C). In may 2010, LG Display introduced the 15 inch EL9500 OLED television to the European consumer market (see figure 1.6D) and is expected to start producing 30 inch OLED-TV panels in 2012.

To conclude this historic overview, the current record charge carrier mobilities will be given, showing the present benchmarks. In 2004, Sundar *et al.* laminated an elastomeric transistor stamp against the surface of a rubrene single-crystal and measured mobilities up to 15 cm^2/Vs [52]. The same year, Jurchescu *et al.* reported a hole mobility of 35 cm^2/Vs at room temperature for pentacene single-crystals grown from double-purified powder [53]. In 2006, Lee *et al.* reported a hole mobility of 5 cm^2/Vs in pentacene thin film transistors [54]. Finally, Takeya *et al.* [55] reported a hole mobility of 40 cm^2/Vs at room temperature for purified rubrene single-crystal transistors laminated on a SAM-modified SiO_2 gate insulator.

1.5 Organic Semiconductors

To organize the broad amount of organic compounds that have semiconducting properties, one can divide them in separate classes depending on specific properties. The first main distinction normally made is between polymers and small molecules. Another option is to discern between *p*-type and *n*-type semiconducting materials.

1.5.1 Polymers vs. small molecules

Two main classes of organic semiconducting materials can be discerned. On one side, there are the polymer semiconductors; on the other hand, there are the low-molecular weight organic materials or small molecules. An important difference between the two classes of materials is the way they can be processed to form thin films. The choice for either one of the two material classes has major implications on the deposition techniques available for the fabrication of devices and applications.

One category of organic semiconductors are the polymer semiconductors. Polymers consist of long organic molecules, of which the chain length (and thus the molecular weight) is not uniquely defined. The semiconducting polymers are typically based on a small group of functional conjugated monomer units [56]. Examples of polymer semiconductors are poly-thiophenes and polyvinylenes, both with many variations and different functional side groups (see [57] for a review). Polymers generally cannot be deposited from the gas phase. By adding functional side chains to the backbone, the solubility of polymers is enhanced and they can be deposited from the liquid phase. Examples of processing techniques for polymers from solution are spin-coating and printing techniques, like inkjet and roll-to-roll.

Small organic semiconducting molecules, that have a well-defined molecular structure and a low molecular weight, comprise the other main category of organic semiconductors. This class of materials is often classified as oligomers. Examples of small organic semiconducting molecules are the acenes, thiophenes, phthalocyanines, porphyrins, triphenylamines, fullerenes, naphthalene and perylene diimides, all with many derivatives (see [57] for a review). In fact, the variety of available small molecules is infinite. Small molecules are generally not easily soluble in common solvents. Without addition of functional side groups, they cannot be deposited from the liquid phase. Instead, small molecules are usually deposited from the gas phase, for example by sublimation or thermal evaporation in a (ultra)high vacuum chamber, or by organic vapor phase deposition (OVPD) in a moderate vacuum. Additionally, a number of low-molecular materials can be grown as single-crystals, which allows the study of (intrinsic) electronic properties on single-crystalline model systems.

1.5.2 p-type vs. n-type

Organic semiconductors are either *p*-type or *n*-type semiconductors. It should be noted that these terms do not have the same meaning for organic semiconductors as they have for (simple) inorganic semiconductors. In the (simple) inorganic case, *p*-type and *n*-type refers to the type of dopant, and therefore majority carrier, in a semiconductor (*i.e.* doping with electron acceptors or donors, respectively). In these materials, both holes and electrons can

usually be transported reasonably well. In the organic case, conversely, the materials are not intentionally doped. Often, they only support or strongly favor one type of charge carrier and are properly referred to as hole or electron transporting. Nevertheless, it is common to refer to hole transporting materials as *p*-type and electron transporting materials as *n*-type, as this describes their majority carriers and semiconducting behavior [56,58]. Accordingly, transistors are classified as *p*-type transistors or *n*-type transistors.

In organic semiconductors, *p*-type conduction is much more common than *n*-type conduction (*i.e.* hole transport is favored in most materials). So far, the electron mobility is in general considerably lower than the hole mobility. Several factors are the cause of this asymmetry; one of them is that electrons are much more easily trapped by defects at the organic – dielectric interface than holes [59]. The main reason for the disproportionate development of *n*-type transistors versus *p*-type is the inherent instability of organic anions; the negatively charged organic molecules react with oxygen and water under operating conditions, thus resulting in unstable devices [60]. There are, however, quite some reports on stable *n*-type organic semiconductors [61-63], and also *ambipolar* organic materials have been identified (*i.e.* materials showing both *p*-type and *n*-type behavior, dependent on the gate voltage) [59,64,65]. Ambipolar transport is expected to be an intrinsic characteristic of organic semiconductors, meaning that pure undoped organic materials should allow both hole and electron transport. However, the study of ambipolar transport behavior in these materials is rather complex in devices due to the easy trapping of electrons by the gate dielectric [59].

1.6 Charge Transport in Organic Semiconductors

Many organic solids and polymers are perfect insulators and are applied extensively as such (*e.g.* plastic insulation of electrical cables). There is, however, also a large number of organic materials that has semiconductor properties. Charge transport in these organic semiconductors differs on several key points from classical inorganic semiconductor charge transport. This paragraph covers the basics of organic semiconductors and illustrates what mechanisms allow the transport of charge carriers through the material. Although this paragraph introduces the charge carrier transport behavior through organic semiconductors in general, the main focus will be on charge transport through ordered crystalline systems.

1.6.1 Charge transport in organic molecules

The charge transport in organic semiconductors contains two separate processes: intramolecular transport and intermolecular transport. The intramolecular transport is feasible as all organic semi-conductors share a common structural feature: the bonding in the molecule or along the polymer backbone consists of alternating single and double carbon-carbon bonds. This alternation is termed conjugation, and it is this conjugated nature that leads to the semi-conducting properties of these organic materials.

Since the electronic properties of organic semiconductors are directly linked to the electronic structure of an individual molecule, the electronic states of single molecules will be discussed in some detail first. In each carbon atom, the electrons are divided over states that

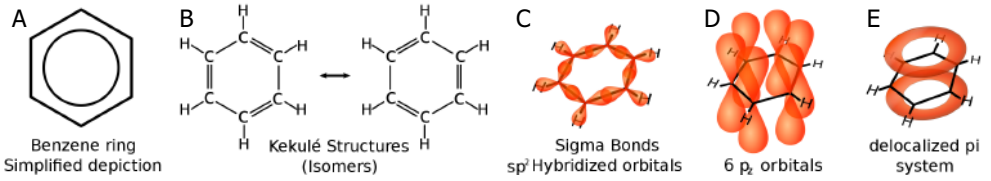

Figure 1.7 *Various representations for benzene. Copyright picture: WikiCommons.*

are characterized by a wavefunction, described as an orbital, and a discrete energy. For an isolated carbon atom, the electronic configuration consists of two electrons occupying the 1*s* orbital, two the 2*s* orbital and two the 2*p* orbitals. The core electrons in the 1s orbital are strongly bound to the atom and are therefore not participating in the formation of chemical bonds. The outermost electrons, situated in the 2*s* and 2*p* orbital, are only loosely bound to the atom. When carbon atoms bond together in a molecule, a mixing of their 2*s* and 2*p* orbitals occurs, leading to *sp*-hybridization. For conjugated molecules, the sp^2-hybridization is particularly important. In the sp^2-hybridization, three identical in-plane sp^2 orbitals are constructed out of the 2*s*, $2p_x$ and $2p_y$ orbitals; whereas the fourth out-of-plane orbital, $2p_z$, remains unhybridized. Covalent *σ*-bonds between the atoms are formed by overlapping sp^2 orbitals. The $2p_z$ orbitals of neighboring carbon atoms overlap and can form *π*-bonds. The combination of a *σ*-bond and a *π*-bond is referred to as a double bond [66].

As is illustrated in figure 1.7A-B for the simple heterocyclic conjugated molecule benzene, different, but equivalent configurations (*i.e.* different Kekulé resonance structures) exist for the alternating single and double bonds. Interchanging the position of the single and double bonds does not affect the electronic structure. Benzene is a relatively simple example: there are two clearly defined isomer resonance forms that are equivalent in energy. Larger molecules have many more resonance forms which lack the symmetry of benzene and some will be more energetically favorable than others [56]. The electronic structure of an actual benzene molecule is determined by a linear combination of all the possible resonance structure [67]. This means that in a conjugated system, the *π*-orbitals are substantially delocalized over the molecule or along segments of the polymer chain. As a consequence, the electrons are delocalized as well and form a *π*-cloud that is shared by all atoms of the conjugated system (see figure 1.7C-E). This delocalization of electrons in a conjugated system lowers the overall energy of the molecule and thereby increases its stability. Within the conjugated part, the electrons can freely move and the mobility along one molecule can be large [68]. The sideways overlap of the $2p_z$ orbitals results in a *π*-system that is most dense above and below the plane of the molecule, with a node in the molecular plane. Shortly summarized, planar conjugated molecules possess clouds of delocalized *π*-electrons situated above and below the molecular plane.

As compared to the *σ*-bonds that form the backbone of the molecule, the *π*-bonding is significantly weaker. Therefore, the *π*-electrons involved in the *π*-bonds are responsible for many chemical and physical properties of the conjugated molecules. The lowest energy reactions and electronic excitations of conjugated molecules are the

π-*π** transitions between the highest occupied molecular bonding *π*-orbital (HOMO) and lowest unoccupied molecular anti-bonding *π**-orbital (LUMO) [69].

1.6.2 Intermolecular charge transport

In molecular semiconductors, transport of charge between molecules requires adequate overlap of the *π*-orbitals between adjacent molecules. If two conjugated molecules are brought together, the *π*-orbitals of both will overlap. The strength of the intermolecular (van der Waals and quadrupole) interactions determines how close the molecules can approach each other and this influences the extend of *π*-orbital overlap between neighboring molecules. If molecules are brought together in the solid state, the *π*-overlap is greatly affected by the orientation and packing of the molecules.

When the conjugated molecules are put together in a crystal, the overlapping *π*-orbitals hybridize together, resulting in broadening of each discrete molecular energy level into an energy band. The filled HOMO orbitals transform into the HOMO band and the empty LUMO orbitals into the LUMO band, corresponding to the valence band and conduction band in inorganic semiconductors, respectively. The energy difference between these bands corresponds to the bandgap. The energy gap between the HOMO and LUMO band of organic semiconductors is typically in the range of 1 - 4 eV, leading to light absorption or emission in the visible spectral range [67,69].

In an organic molecular crystal, the intermolecular interactions are weak and produce only small changes in the electronic structure of the individual molecules; the molecules maintain their 'identity' [70]. The weak intermolecular interactions directly affect the bandwidth of the valence and conduction band, which is typically small compared to that of inorganics (*e.g.* in the order of 0.3 - 0.6 eV for acene crystals compared to 10 - 12 eV for inorganics [67,71,72]). The bandwidths for a given crystal, caused by splitting of the energy levels through the intermolecular interactions, can be quantified from molecular orbital calculations through the *transfer integral t*. Theoretically, the narrow bands limit the intermolecular charge transport and result in a low mobility (*e.g.* in the order of 10^{-5} - 10^{1} cm^2/Vs for organic semiconductors *vs.* 50 - 500 cm^2/Vs in silicon at room temperature) [67]. Due to the asymmetric nature of the organic crystal structure, transfer integrals vary strongly with the crystallographic directions and often show a large anisotropy [73].

The weak bonding of the molecules makes the organic crystal sensitive to phonons (molecular motions like molecular and lattice vibrational modes, rotational modes and translational modes), photons and impurities [74]. The weak interaction between constituent molecules in an organic molecular crystal is also responsible for the characteristic mechanical and elastic properties, such as flexibility, low melting and sublimation temperatures, and low mechanical strength.

1.6.3 Polaron formation

The intermolecular forces in organic semiconductors are much weaker compared to the covalent and ionic bonds in simple inorganic semiconductors [67]. Due to the narrow bandwidth in organic crystals, the charge carriers are not completely delocalized as happens in simple

inorganic solids. If a charge carrier is localized, it induces almost spontaneously polarization effects to the local crystal environment, which relaxes into a new equilibrium state. A propagating charge carrier carries a polarization cloud and is therefore able to locally distort its host material. This results in a deformation of the lattice and induces new vibrational modes in the closest atoms. The charge carrier combined with the accompanying deformed section of the lattice can be treated as a quasi-particle, called a *polaron* [75,76]. Polaron formation generally reduces the carrier mobility, as the lattice polarization hinders the movement of the charge [70]. The energy involved in polaron self-exchange (*i.e.* an electron delocalized from one polaron and being captured again to form a new polaron) is known as the *reorganization energy λ*. Single-crystals with a low reorganization energy are expected to have a high mobility, as is for example calculated for pentacene crystals [77,78].

Generally, polarons formed by the localized charge and the accompanying deformation of the lattice are called Holstein polarons [79,80], which have a short-range interaction (*i.e.* in the order of the lattice parameter). Recently, interplay by charge carriers with the adjacent dielectric material in field-effect devices is shown to determine the electronic transport properties in organic molecular crystal transistors (see paragraph 2.6.4) [81-84]. These quasi-particles are called Fröhlich polarons [85,86] and consist of a charge carrier bound to an ionic polarization cloud in the surrounding medium (*i.e.* the gate dielectric). Fröhlich polarons have a longer range of interaction compared to the Holstein polarons.

1.6.4 Localization by defect states

The discussion so far on charge transport in organic semiconductors is based on perfect defect-free organic crystal lattices. The intrinsic properties of the organic molecular crystals can be disguised by the influence of defects in the crystal, like lattice imperfections or chemical impurities. Every defect will act as a scattering site for charge carriers, because it causes a distortion in the ideal periodic lattice potential. However, the effect of a defect on charge transport is much stronger if it additionally acts as a trapping centre [68].

Imperfections in the lattice distort the intrinsic charge transport in several ways [67]. Point defect-like vacancies may decrease the polarization energy of the surrounding molecules and act as carrier scattering centers. Line dislocations lead to the presence of accessible energy levels in the bandgap of the organic semiconductor, and enable the trapping of carriers. In addition, line dislocations enhance the chemical reactivity in their vicinity, which may cause the accumulation of impurities. Planar defects like grain boundaries and amorphous regions strongly distort the electronic structure and can be considered as a series of carrier trapping sites. Impurity point defects have a more complicated effect on the charge transport.

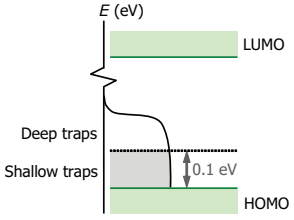

Figure 1.8 *Schematic diagram of the distribution of localized electronic states near the HOMO level in the energy gap between the HOMO and LUMO bands in p-type organic single-crystal OFETs.*

Impurities do not commonly act as substitutional dopants (like boron and phosphorous dopants in silicon), but form interstitial defects and distort the original lattice geometry. In most devices, impurities are considered as deep traps for charge transport.

Overall, most defects act as traps for electrons, holes or both [67]. Each defect introduces a distribution of traps of varying trap depth energy, E_t. Traps close to the HOMO and LUMO bands of organic semiconductors (*viz.* traps with E_t within several hundreds of meVs of the bands) are of special interest, as carriers captured there have the potential to be released into the bands by external energy. Especially defects that induce one or more energy levels in the bandgap are relevant, as a passing charge carrier prefers to occupy this lower energy state, and the trap localizes the charge carrier at its site [87]. These traps generally have depths less than 100 meV (a few k_BT) from the band edge and are recognized as *shallow traps*. Correspondingly, traps with an activation energy larger than 100 meV from the band edge are tagged as *deep traps* (see figure 1.8). The common concept for deep and shallow traps is that they limit charge transport by localization of charge carriers [67]. The influence of defects can be neutralized by increasing the charge carrier density; when a trap is filled with a charge carrier, it cannot trap another carrier and has thus become ineffective.

1.6.5 Charge transport models: band-like vs. hopping transport

Along with the increased understanding of the interaction between molecules, polarons in organic semiconductors, and the influence caused by defects, several charge transport models have been proposed. In general, one can distinguish between two main charge transport mechanism models: *band-like* transport and *hopping* transport.

The simplest model is the band-like transport model, which is directly duplicated from inorganic semiconductor models. In this model, free charge carriers are treated as completely delocalized wavefunctions in the bands of a perfect crystal (see figure 1.9A). As the temperature increases, the lattice vibrations (phonons) are more pronounced and will introduce extra potential barriers in the band that cause scattering of the charge carriers, and thus limit the mobility. As a result, the charge carrier mobility μ for band-like transport decreases with increasing temperature T as $\mu \propto T^{-n}$ [74]. Band-like transport in organic materials is only expected for highly ordered systems like single-crystals, when the mean free path of the carrier exceeds the intermolecular distance [74]. In literature, various models that describe band transport in organic molecular crystals can be found [89-91].

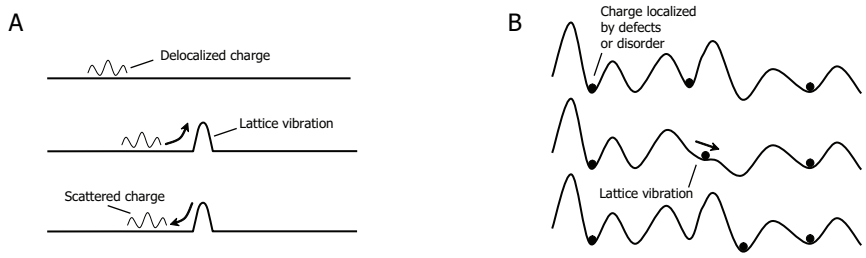

Figure 1.9 *Charge transport models: A) band-like transport model and charge carrier scattering by a phonon, and B) hopping transport model with the influence of phonon and crystal defects.*

Compared to the band-like transport model, the hopping transport model places emphasis on the localization of charge carriers, which is typical for disordered materials such as organic thin films (both polymer and small molecular). In this model, the charge carriers are no longer considered as wavefunctions; instead, they are considered as particles localized on individual molecules or defects (see figure 1.9B). Transport occurs via hopping of charges between localized molecular states and strongly depends on parameters like temperature, electric field, grain boundaries, traps present in the material and the carrier concentration [92]. An external energy (*e.g.* thermal, optical, and electrical energy) is required to assist the charge carriers to overcome the potential barrier for hopping to another site. Thus, hopping transport can be thermally activated and the mobility μ increases with increasing temperature as $\mu \propto \exp(E_{Act} / k_B T)$, with E_{Act} the activation energy and k_B the Boltzmann constant. Various models that describe hopping transport in disordered organic semi-conducting materials can be found in literature [93-96].

The mobility in band-like transport models is considerably larger than 1 cm^2/Vs at room temperature, while hopping transport commonly yields lower mobility values. In practice, the transport regime of carriers in organic molecular crystals is in the crossover regime between band-like transport and hopping transport, as they have mobilities around 1 cm^2/Vs, and is controlled by a combination of both transport mechanisms. The charge transport in organic crystals can be explained by the *multiple trap-and-release* (MTR) model [97,98] , in which the influence of crystal defects are treated as trap states located in the band gap. In the MTR model, each charge carrier spends a limited amount of time inside a trap before it can be activated. Once the carrier is released, it moves freely in the band until being captured by another trap. Again, the mobility has an exponential relationship with temperature, since the time of trapping is directly affected by the thermal activation energy. A comparable approach is not focusing on the motion of individual carriers, but assumes that a large portion of the total carriers is permanently trapped while the rest are moving along the band [99].

For polymers and other amorphous organic semiconductors, that generally have a mobility several orders of magnitude lower than 1 cm^2/Vs, charge transport is governed by the hopping process. Here, a carrier can either hop over a short distance trap site with a high activation energy, or hop over a long distance trap site with a low activation energy; a process that can be described by the *variable-range hopping* (VRH) model [93]. Again, an Arrhenius-like temperature dependent mobility is obtained in the VRH charge transport model.

1.7 Outline of this Thesis

The objective of the work described in this thesis is *"to fabricate high-quality organic molecular single-crystal devices"*. To achieve this objective, the fabrication of complete field-effect transistor devices, by direct deposition of metal contacts and an oxide dielectric on the surface of organic single-crystals, without destroying the interfaces, is selected as main approach. In this paragraph, the outline of this thesis is presented and the research described in the following chapters to achieve the objective is introduced and placed in perspective.

In the first chapter, a general introduction to the field of Organic Electronics and the organic semiconducting materials that are at its basis is given. This field of research has grown rapidly in the recent years, mainly due to the perspective of fabricating electronic devices on large, flexible substrates at a low cost. For the manufacturing of organic electronic devices, working with thin films is the most attractive. However, the imperfections in the thin film structure and the polycrystalline orientation limit the study of the intrinsic properties of these materials. The best approach to investigate the intrinsic electronic properties and explore the physical limitations of organic semiconductors is therefore the study of single-crystalline systems, which is best illustrated by the improved performance of the organic single-crystal field-effect transistors developed the last couple of years. For that reason, chapter 2 will carry on with a more in-depth analysis on the fundamentals of organic molecular crystal devices. The basic aspects and the growth of organic single-crystals, and the methods currently used to fabricate high-quality devices will be discussed. The chapter continues with a review on the typical single-crystal device characteristics found in literature.

Fabrication of high-quality organic single-crystal devices demands a high control on the applied manufacturing techniques. In this thesis, the main used fabrication technique is pulsed laser deposition (PLD) at room temperature, in combination with (quasi-dynamic) patterning through stencils that function as shadow mask. The basic concepts of PLD that are of interest when combined with stencil patterning are described in chapter 3. The analytical tools to obtain information on the electrical properties, structure, composition and morphology of the substrate, the deposited films and patterns, and fabricated devices are introduced as well. Special focus is on the electrical characterization of the organic molecular crystal devices in a nano probing system.

Pentacene, the benchmark material studied in this work, is by far the most popular organic semiconductor used in the fabrication of organic field-effect transistors for organic electronic applications. In chapter 4, the crystal structure, growth mechanism, geometry and surface morphology of vapor-grown pentacene single-crystals will be explored, as these organic crystals function as substrate in the fabrication of devices in the upcoming chapters.

Chapter 5 will emphasize on the stability of pentacene single-crystals towards oxidation, as oxidation degradation is believed to be one of the major reasons for a reduced performance and early device failure. The most common impurity and oxidation product of pentacene is 6,13-pentacenequinone. The presence and arrangement of the quinone impurities in the crystal bulk and on the surface will be examined in this chapter. After that, the possibilities of obtaining a pentacene crystal surface that is free from oxidation products (by performing a heating treatment or cleaving the crystal) are investigated, as the quinone molecules at the conducting interface in a field-effect geometry will form scattering sites, reduce the mobility and, in a worst case, suppress the field-effect completely.

In order to fabricate complete organic molecular single-crystal field-effect transistors, the direct deposition of various metals and oxide patterns through a stencil on the surface of pentacene single-crystals with PLD is investigated in chapter 6. The fabrication of organic molecular crystal devices by direct deposition is not straightforward and poses a

technological challenge, as the surface of the fragile organic crystals can be damaged very easily. Nevertheless, well-controlled interfaces between the organic crystal and the deposited patterns (that have a well-defined geometry) can be obtained with the direct deposition approach. By taking several precautions in the PLD process, which basically all reduce the kinetic energy of the impinging species or reduce build-up of stress during deposition, low-kinetic energy deposition or *'soft-landing'* of a variety of different materials can be realized on the surface of the pentacene single-crystals, without mechanical failure of the deposited patterns or obvious destruction to the fragile organic substrate. To investigate the diffusion of pulsed-laser deposited species into the pentacene single-crystal lattice, the patterning of an alkylphosphate self-assembled monolayer is investigated as well, as for this model system the penetration of ablated species into the organic molecular material can be easily quantified by performing electrochemical deposition experiments.

In chapter 6, it is also observed that the surface morphology of the underlying pentacene substrate (*i.e.* the 1.4 nm high *d*(001) pentacene terrace steps) is often still noticeable on top of the deposited patterns (with a thickness up to several tens of nanometers). To explore this observation further, the research in chapter 7 will focus on the morphology, growth evolution and dynamic scaling of the surface roughness for pulsed-laser stencil deposited gold patterns on pentacene single-crystal and silicon oxide substrates.

In chapter 8, the influences of the manufacturing procedure and the heating treatment on the electrical properties of the pentacene single-crystals will be investigated. For this, fabricated space-charge-limited current (SCLC) and field-effect transistor (FET) devices are electrically characterized with a nano probing system. The focus of this chapter is on the influence of the different deposition parameters (*i.e.* the *'hard-landing'* settings versus the *'soft-landing'* settings) on the final electrical properties, and on the influence of performing a heating treatment on a pentacene crystal before applying the metal contacts.

1.8 Concluding Remarks

In this chapter, an extensive introduction to the field of organic electronics has been given. The current status of the field, its industrial relevancy and huge potential for commercialization have been highlighted. Besides that, many aspects that are important for the upcoming chapters of this thesis have been introduced.

1.9 References

[1] Crone, B.; Dodabalapur, A.; Lin, Y.Y.; Filas, R.W.; Bao, Z.; LaDuca, A.; Sarpeshkar, R.; Katz, H.E.; Li, W.; "Large-scale complementary integrated circuits based on organic transistors"; *Nature*; 403; **2000**; 521-523

[2] Dimitrakopoulos, C.D.; Purushothaman, S.; Kymissis, J.; Callegari, A.; Shaw, J.M.; "Low-voltage organic transistors on plastic comprising high-dielectric constant gate insulators"; *Science*; 283; **1999**; 822-825

[3] Friend, R.H.; Gymer, R.W.; Holmes, A.B.; Burroughes, J.H.; Marks, R.N.; Taliani, C.; Bradley, D.D.C.; Dos Santos, D.A.; Brédas, J.L.; Lögdlund, M.; Salaneck, W.R.; "Electroluminescence in conjugated polymers"; *Nature*; 397; **1999**; 121-128

[4] Baldo, M.A.; O'Brien, D.F.; You, Y.; Shoustikov, A.; Sibley, S.; Thompson, M.E.; Forrest, S.R.; "Highly efficient phosphorescent emission from electroluminescent devices"; *Nature*; 395; **1998**; 151-154

[5] Halls, J.J.M.; Walsh, C.A.; Greenham, N.C.; Marseglia, E.A.; Friend, R.H.; Moratti, S.C.; Holmes, A.B.; "Efficient photodiodes from interpenetrating polymer networks"; *Nature*; 376; **1995**; 498-500

[6] Yu, G.; Gao, J.; Hummelen, J.C.; Wudl, F.; Heeger, A.J.; "Polymer photovoltaic cells enhanced efficiencies via a network of internal donor-acceptor heterojunctions"; *Science*; 270; **1995**; 1789-1791

[7] Asadi, K.; Leeuw, D.M. de; Boer, B. de; Blom, P.W.M.; "Organic non-volatile memories from ferroelectric phase-separated blends"; *Nat. Mater.*; 7; **2008**; 547-550

[8] Sirringhaus, H.; Ando, M.; "Materials challenges and applications of solution-processed organic field-effect transistors"; *MRS Bulletin*; 33; **2008**; 676-682

[9] Chabinyc, M.L.; Jimison, L.H.; Rivnay, J.; Salleo, A.; "Connecting electrical and molecular properties of semi-conducting polymers for thin-film transistors"; *MRS Bulletin*; 33; **2008**; 683-689

[10] Loo, Y.L.; McCulloch, I.; "Progress and challenges in commercialization of organic electronics"; *MRS Bulletin*; 33; **2008**; 653-658

[11] Forrest, S.R.; "The path to ubiquitous and low cost organic electronic appliances on plastic"; *Nature*; 428; **2004**; 911-918

[12] Someya, T.; Pal, B.; Huang, J.; Katz, H.E.; "Organic semiconductor devices with enhanced field and environmental responses for novel applications"; *MRS Bulletin*; 33; **2008**; 690-696

[13] So, F.; Kido, J.; Burrows, P.; "Organic light-emitting devices for solid-state lighting"; *MRS Bulletin*; 33; **2008**; 663-669

[14] Brabec, C.J.; Durrant, J.R.; "Solution-processed organic solar cells"; *MRS Bulletin*; 33; **2008**; 670-675

[15] Chiang, C.K.; Fincher, C.R.; Park, Y.W.; Heeger, A.J.; Shirakawa, H.; Louis, E.J.; Gau, S.C.; MacDiarmid, A.G.; "Electrical conductivity in doped polyacetylene"; *Phys. Rev. Lett.*; 39; **1977**; 1098-1101

[16] Official website of the Nobel Foundation; The Nobel Prize in Chemistry 2000; http://nobelprize.org/nobel_prizes/chemistry/laureates/2000/; last visited on 11-10-2009

[17] Vusser, S. de; Organic thin film transistors – Process technology and circuit design; PhD Thesis; **2006**; University of Leuven; Leuven, Belgium

[18] McGinness, J.; Corry, P.; Proctor, P.; "Amorphous semiconductor switching in melanins"; *Science*; 183; **1974**; 853-855

[19] Bolto, B.A.; McNeill, R.; Weiss, D.E.; "Electronic conduction in polymers III. Electronic properties of polypyrrole"; *Aust. J. Chem.*; 16; **1963**; 1090-1103

[20] Eley, D.D.; "Phthalocyanines as semiconductors"; *Nature*; 162; **1948**; 819

[21] Heilmeier, G.H.; Zanoni, L.A.; "Surface studies of alpha-copper phthalocyanine films"; *J. Phys. Chem. Solids*; 25; **1964**; 603-61

[22] Barbe, D.F.; Westgate, C.R.; "Surface state parameters of metal-free phthalocyanine single crystals"; *J. Phys. Chem. Solids*; 31; **1970**; 2679-2687

[23] Williams, D.F.; Schadt, M.; "DC and pulsed electroluminescence in anthracene and doped anthracene crystals"; *J. Chem. Phys.*; 53; **1970**; 3480-348

[24] Bauser, H.; Pernisz, U.; "Field effect in anthracene crystal"; *Chem. Phys. Lett.*; 11; **1971**; 213-215

[25] Pope, M.; Kallmann, H.P.; Magnante, P.; "Electroluminescence in organic crystals"; *J. Chem. Phys.*; 38; **1963**; 2042

[26] Ebisawa, F.; Kurokawa, T.; Nara, S.; "Electrical properties of polyacetylene/polysiloxane interface"; *J. Appl. Phys.*; 54; **1983**; 3255-3259

[27] Partridge, R.H.; "Electroluminescence from polyvinylcarbazole films: 1. Carbazole cations"; *Polymer*; 24; **1983**; 733-738

[28] Kudo, K.; Yamashina, M.; "Field effect measurements of organic dye films"; *Jpn. J. Appl. Phys., Part 1*; 23; **1984**; 130

[29] Warta, W.; Stehle, R.; Karl, N.; "Ultrapure, high mobility organic photoconductors"; *Appl. Phys. A*; 36; **1985**; 163-171

[30] Warta, W.; Karl, N.; "Hot holes in naphthalene: high, electric-field-dependent mobilities"; *Phys. Rev. B*; 32; **1985**; 1172-1182

[31] Tang, C.W.; "Two-layer organic photovoltaic cell"; *Appl. Phys. Lett.*; 48; **1986**; 183-185

[32] Tsumura, A.; Koezuka, H.; Ando, T.; " Macromolecular electronic device: field-effect transistor with a polythiophene thin film"; *Appl. Phys. Lett.*; 49; **1986**; 1210-1212

[33] Koezuka, H.; Tsumura, A.; Ando, T.; "Field-effect transistor with polythiophene thin film"; *Synth. Met.*; 18; **1987**; 699-704

[34] Tang, C.W.; VanSlyke, S.A.; "Organic electroluminescent diodes"; *Appl. Phys. Lett.*; 51; **1987**; 913-915

[35] Horowitz, G.; Peng, X.Z.; Fichou, D.; Garnier, F.; "A field-effect transistor based on conjugated alpha-sexithienyl"; *Solid State Commun.*; 72; **1989**; 381-384

[36] Burroughes. J.H.; Bradley, D.D.C.; Brown, A.R.; Marks, R.N.; Mackay, K.; Friend, R.H.; Burns, P.L.; Holmes, A.B.; "Light-emitting diodes based on conjugated polymers"; *Nature*; 347; **1990**; 539-541

[37] Brown, A.R.; Leeuw, D.M. de; Lous, E.J.; Havinga, E.E.; "Organic *n*-type field-effect transistors"; *Synth. Met.*; 66; **1994**; 419-424

[38] Horowitz, G.; Peng, X.Z.; Fichou, D.; Garnier, F.; "Role of the semiconductor/insulator interface in the characteristics of pi-conjugated oligomer-based thin-film transistors"; *Synth. Met.*; 51; **1992**; 419-424

[39] Brown, A.R.; Pomp, A.; Hart, C.M.; Leeuw, D.M. de; "Logic gates made from polymer transistors and their use in ring oscillators"; *Science*; 270; **1995**; 972-974

[40] Lin, Y.Y.; Gundlach, D.J.; Nelson, S.F.; Jackson, T.N.; "Stacked pentacene layer organic thin-film transistors with improved characteristics"; *IEEE Electron. Device Lett.*; 18; **1997**; 606-608

[41] Schön, J.H.; Kloc, Ch.; Batlogg, B.; "Superconductivity in molecular crystals induced by charge injection"; *Nature*; 406; **2000**; 702-704

[42] Schön, J.H.; Dodabalapur, A.; Bao, Z.; Kloc, Ch.; Schenker, O.; Batlogg, B.; "Gate-induced superconductivity in a solution-processed organic polymer film"; *Nature*; 410; **2001**; 189-192

[43] Schön, J.H.; Kloc, Ch.; Dodabalapur, A.; Batlogg, B.; "An organic solid state injection laser"; *Science*; 289; **2000**; 599-601

[44] Schön, J.H.; Berg, S.; Kloc, Ch.; Batlogg, B.; "Ambipolar pentacene field-effect transistors and inverters"; *Science*; 287; **2000**; 1022-1023

[45] Reich, E.S.; Plastic fantastic – How the biggest fraud in physics shook the scientific world; **2009**; Palgrave Macmillan; New York, NY, U.S.A.

[46] Wikipedia, the free encyclopedia; Jan Hendrik Schön; http://en.wikipedia.org/wiki/ Jan_Hendrik_Sch%C3%B6n; last visited on 11-10-2009

[47] Beasley, M.R.; Datta, S.; Kogelnik, H.; Kroemer, H.; Monroe, D.; Report of the investigation committee on the possibility of scientific misconduct in the work of Hendrik Schön and coauthors; **2002**; Bell Labs; Murray Hill, NJ, U.S.A.

[48] Shirakawa, H.; McDiarmid, A.; Heeger, A.; " Twenty-five years of conducting polymers";*Chem. Commun.*; 1; **2003**; 1-4

[49] Klauk, H.; Halik, M.; Zschieschang, U.; Schmid G.; Radlik, W.; "High-mobility polymer gate dielectric pentacene thin film transistors"; *J. Appl. Phys.*; 92; **2002**; 5259-5263

[50] Sony corporation; Sony launches world's first OLED TV; http://www.sony.net/SonyInfo/News/Press/200710/07-1001E/index.html; last visited on 11-10-2009

[51] Polymer Vision; Readius, the first pocket eReader; http://www.readius.com/; last visited on 11-10-2009

[52] Sundar, V.C.; Zaumseil, J.; Podzorov, V.; Menard, E.; Willett, R.L.; Someya, T.; Gershenson, M.E.; Rogers, J.A.; "Elastomeric transistor stamps: reversible probing of charge transport in organic crystals"; *Science*; 303; **2004**; 1644-1646

[53] Jurchescu, O.D.; Baas, J.; Palstra, T.T.M.; "Effect of impurities on the mobility of single crystal pentacene"; *Appl. Phys. Lett.*; 84; **2004**; 3061-3063

[54] Lee, S.; Koo, B.; Shin, J.; Lee, E.; Park, H.; Kim, H.; "Effects of hydroxyl groups in polymeric dielectrics on organic transistor performance"; *Appl. Phys. Lett.*; 88; **2006**; 162109

[55] Takeya, J.; Yamagishi, M.; Tominari, Y.; Hirahara, R.; Nakazawa, Y.; Nishikawa, T.; Kawase, T.; Shimoda, T.; Ogawa, S.; "Very high-mobility organic single-crystal transistor with in-crystal conduction channels"; *Appl. Phys. Lett.*; 90; **2007**; 102120

[56] Kymissis, I.; Organic field effect transistors – Theory, fabrication and characterization; **2009**; Springer; New York, NY, U.S.A.

[57] Mallik, A.B.; Locklin, J.; Mannsfeld, S.C.B.; Reese, C.; Roberts, M.E.; Senatore, M.L.; Zi, H.; Bao, Z.; "Design, synthesis, and transistor performance of organic semiconductors"; Ch. 3.1 in Organic field-effect transistors; Ed. Bao, Z.; Locklin, J.; **2007**; CRC Press; Taylor & Francis Group; New York, NY, U.S.A.

[58] Klauk, H.; Organic electronics – Materials, manufacturing and applications; **2006**; Wiley-VCH; Weinheim, Germany

[59] Chua, L.L.; Zaumseil, J.; Chang, J.F.; Ou, E.C.W.; Ho, P.K.H.; Sirringhaus, H.; Friend, R.H.; "General observation of *n*-type field-effect behaviour in organic semiconductors"; *Nature*; 434; **2005**; 194-199

[60] Dimitrakopoulos, C.D.; Malenfant, P.R.L.; "Organic thin film transistors for large area electronics"; *Adv. Mater.*; 14; **2002**; 99-117

[61] Facchetti, A.; "Semiconductors for organic transistors"; *Mater. Today*; 10; **2007**; 28-37

[62] Katz, H.E.; Lovinger, A.J.; Johnson, J.; Kloc, C.; Siegrist, T.; Li, W.; Lin, Y.Y.; Dodabalapur, A.; "A soluble and air-stable organic semiconductor with high electron mobility"; *Nature*; 404; **2000**; 478-481

[63] Yamashita, Y.; "Development of high-performance *n*-type organic field-effect transistors based on nitrogen heterocycles"; *Chem. Lett.*; 38; **2009**; 870-875

[64] Meijer, E.J.; Leeuw, D.M. de; Setayesh, S.; Veenendaal, E. van; Huisman, B.H.; Blom, P.W.M.; Hummelen, J.C.; Scherf, U.; Klapwijk, T.M.; "Solution-processed ambipolar organic field effect transistors and inverters"; *Nature Mater.*; 2; **2003**; 678-682

[65] Boer, R.W.I. de; Stassen, A.F.; Craciun, M.F.; Mulder, C.L.; Molinari, A.; Rogge, S.; Morpurgo, A.F.; "Ambipolar Cu- and Fe-phthalocyanine single-crystal field-effect transistors"; *Appl. Phys. Lett.*; 86; **2005**; 262109

[66] Solomons, T.W.G.; Organic chemistry; **1996**; 6th ed.; John Wiley & Sons, Inc.; New York, NY, U.S.A.

[67] Pope, M.; Swenberg, C.E.; Electronic processes in organic crystals and polymers; **1999**; 2nd ed.; Oxford university press; New York, NY, U.S.A.

[68] Boer, R.W.I. de; Organic single-crystal field-effect transistors; PhD Thesis; **2005**; University of Delft; Delft, The Netherlands

[69] Brütting, W.; Physics of organic semiconductors; **2005**; Wiley-VCH; Weinheim, Germany

[70] Silinsh, E.A.; Organic molecular crystals - Their electronic states; **1980**; Springer-Verlag; Berlin, Germany

[71] Cheng, Y.C.; Silbey, R.J.; Silva Filho, D.A. da; Calbert, J.P.; Cornil, J.; Brédas, J.L.; "Three-dimensional band structure and bandlike mobility in oligoacene single crystals: a theoretical investigation"; *J. Chem. Phys.*; 118; **2003**; 3764-3774

[72] Brocks, G.; Brink, J. van den; Morpurgo, A.F.; "Electronic correlations in oligo-acene and -thiophene organic molecular crystals"; *Phys. Rev. Lett.*; 93; **2004**; 146405

[73] Coropceanu, V.; Cornil, J.; Silva Filho, D.A. da; Olivier, Y.; Silby, R.; Brédas, J.L.; "Charge transport in organic semiconductors"; *Chem. Rev.*; 107; **2007**; 926-952

[74] Schwoerer, M.; Wolf, H.C.; Organic Molecular Solids; **2005**; Wiley-VCH; Weinheim, Germany

[75] Landau, L.D.; "Ueber die Bewegung der Elektronen in Kristalgitter"; *Phys. Z. Sowjetunion*; 3; **1933**; 644-645

[76] Brazovskii, S.A.; Kirova, N.N.; "Excitons, polarons, and bipolarons in conducting polymers";*Sov. Phys. JETP*; 33; **1981**; 4-8

[77] Gruhn, N.E.; Silva Filho, D.A. da; Bill, T.G.; Malagoli, M.; Coropceanu, V.; Kahn, A.; Brédas, J.L.; "The vibrational reorganization energy in pentacene: molecular influences on charge transport"; *J. Am. Chem. Soc.*; 124; **2002**; 7918-7919

[78] Mas-Torrent, M.; Hadley, P.; Bromley, S.T.; Ribas, X.; Tarrés, J.; Mas, M.; Molins, E.; Veciana, J.; Rovira, C.; "Correlation between crystal structure and mobility in organic field-effect transistors based on single crystals of tetrathiafulvane derivatives"; *J. Am. Chem. Soc.*; 126; **2004**; 8546-8553

[79] Holstein, T.; "Studies of polaron motion. Part I. The molecular-crystal model"; *Ann. Phys.*; 8; **1959**; 325-342

[80] Holstein, T.; "Studies of polaron motion. Part II. The 'small' polaron"; *Ann. Phys.*; 8; **1959**; 343-389

[81] Veres, J.; Ogier, S.D.; Leeming, S.; Cupertino, D.C.; Khaffaf, S.M.; "Low-*k* insulators as the choice of dielectrics in organic field-effect transistors"; *Adv. Funct. Mater.*; 13; **2003**; 199-204

[82] Stassen, A.F.; Boer, R.W.I. de; Iosad, N.N.; Morpurgo, A.F.; "Influence of the gate dielectric on the mobility of rubrene single-crystal field-effect transistors"; *Appl. Phys. Lett.*; 85; **2004**; 3899-3901

[83] Hulea, I.N.; Fratini, S.; Xie, H.; Mulder, C.L.; Iossad, N.N.; Rastelli, G.; Ciuchi, S.; Morpurgo, A.F.; "Tunable Fröhlich polarons in organic single-crystal transistors"; *Nat. Mater.*; 5; **2006**; 982-986

[84] Fratini, S.; Morpurgo, A.F.; Ciuchi, S.; "Electron-phonon coupling and electron-electron interactions in organic field effect transistors"; *J. Phys. Chem. Sol.*; 69; **2008**; 2195-2198

[85] Fröhlich, H.; Pelzer, H.; Zienau, S.; "Properties of slow electrons in polar materials"; *Phil. Mag.*; 41; **1950**; 221-242

[86] Fröhlich, H.; "Electrons in lattice fields"; *Adv. Phys.*; 3; **1954**; 325-361

[87] Goldmann, C.; Krellner, C.; Pernstich, K.P.; Haas, S.; Gundlach, D.J.; Batlogg, B.; "Determination of the interface trap density of rubrene single-crystal field-effect transistors and comparison to the bulk trap density"; *J. Appl. Phys.*; 99; **2006**; 034507

[88] Xia, Y.; Fabrication and characterization of organic single crystal and printed polymer transistors; PhD Thesis; **2009**; University of Minesota; Minesota, MN, U.S.A.

[89] Hannewald, K.; Stojanovic, V.M.; Schellekens, J.M.T.; Bobbert, P.A.; Krese, G.; Hafner, J.; "Theory of polaron bandwidth narrowing in organic molecular crystals"; *Phys. Rev. B*; 69; **2004**; 075211

[90] Cheng, Y.C.; Silbey, R.J.; "A unified theory for charge-carrier transport in organic crystals"; *J. Chem. Phys.*; 128; **2008**; 114713

[91] Ortman, F.; Bechstedt, F.; Hannewald, K.; "Theory of charge transport in organic crystals: beyond Holstein's small-polaron model"; *Phys. Rev. B*; 79; **2009**; 235206

[92] Zuppiroli, L.; Bussac, M.N.; Paschen, S.; Chauvet, O.; Forro, O.; "Hopping in disordered conducting polymers"; *Phys. Rev. B*; 50; **1994**; 5196-5203

[93] Vissenberg, M.C.J.M.; Matters, M.; "Theory of the field-effect mobility in amorphous organic transistors"; *Phys. Rev. B*; 57; **1998**; 12964-12967

[94] Bässler, H.; "Charge transport in disordered organic photoconductors: a Monte Carlo simulation study"; *Phys. Stat. Sol. B*; 175; **1993**; 15-56

[95] Nelson, S.F.; Lin, Y.Y.; Gundlach, D.J.; Jackson, T.N.; "Temperature-independent transport in high-mobility pentacene transistors"; *Appl. Phys. Lett.*; 72; **1998**; 1854-1856

[96] Pasveer, W.F.; Cottaar, J.; Tanase, C.; Coehoorn, R.; Bobbert, P.A.; Blom, P.W.M.; Leeuw, D.M. de; Michels, M.A.J.; "Unified description of charge-carrier mobilities in disordered semiconducting polymers"; *Phys. Rev. Lett.*; 94; **2005**; 206601

[97] Horowitz, G.; "Organic thin film transistors: from theory to real devices"; *J. Mater. Res.*; 19; **2004**; 1946-1962

[98] Podzorov, V.; "Charge carrier transport in single-crystal organic field-effect transistors"; Ch. 2 in Organic field-effect transistors; Ed. Bao, Z.; Locklin, J.; **2007**; CRC Press; Taylor & Francis Group; New York, NY, U.S.A.

[99] Butko, V.Y.; Chi, X.; Lang, D.V.; Ramirez, A.P.; "Field-effect transistor on pentacene single crystal"; *Appl. Phys. Lett.*; 83; **2003**; 4773-4775

Chapter 2

Fundamentals of Organic Molecular Crystal Devices

Chapter 2: Fundamentals of Organic Molecular Crystal Devices

Abstract

The fundamentals of organic molecular crystal devices are being reviewed in this chapter. Growth of ultrapure organic single-crystals, fabrication of high-quality single-crystal devices and their typical device characteristics are all subject of inspection.

2.1 Introduction

In chapter 1, a general introduction to the field of organic electronics has been given. Chapter 2 will continue reviewing the literature, but its focus is on the fundamentals of a specific area in the field, namely the organic molecular crystal devices.

This chapter starts with a short introduction on organic solid materials in paragraph 2.2, followed by a description of a special class of the organic solids, namely the organic molecular single-crystals, in paragraph 2.3. In this paragraph, it will be discussed that fabrication of (field-effect transistor) devices based on these organic molecular single-crystals is the best approach for the study of the intrinsic electronic properties and the physical limitations of organic semi-conducting materials. The various crystal growth techniques available to obtain ultrapure and high-quality organic single-crystals are listed in paragraph 2.4. Although the manufacturing of organic single-crystal devices poses some technological challenges, several approaches have been employed successfully the last couple of years. An overview of these fabrication methods is presented in paragraph 2.5. Finally, several properties specifically observed in experiments with organic molecular single-crystal devices are highlighted in paragraph 2.6.

2.2 Organic Solids

In the field of solid-state physics, focus has traditionally been on metals. The last decades, inorganic semiconductors, oxide materials, ceramics and superconductors took over the forefront of interest in basic research and applications of materials science. The last years, research to another group of materials has greatly increased: the organic solids. Examples of organic solids are organic molecular crystals (OMCs) of aliphatic or aromatic hydrocarbons, weak donor-acceptor complex crystals that are non-polar in the ground state, strong donor-acceptor complex crystals that are polar in the ground state (or charge-transfer crystals), radical-ion salts, polymer single-crystals and inorganic-organic hybrid crystals.

The fundamental difference between inorganic solids and organic molecular solids is illustrated in figure 2.1 [1]. This figure shows an electronic energy diagram of an individual atom, a single molecule, a molecular solid and an inorganic solid. As can be seen, an inorganic solid is constructed directly from a group of atoms. On the other hand, a molecular solid is an assembly of individual molecules. Every molecule itself is made of constituent atoms and possesses its own properties. In most molecular solids, the molecules as such remain intact and have a direct influence on the charge transport through the material, and thus directly determine the physical properties of the material (see paragraph 1.6.2).

Most interest is on organic solids which contain conjugated π-systems in their skeletal structure, as the π-electrons determine the interactions that hold together the molecules in the solid state and mainly characterize the physical properties of the organic solid. For an organic solid, when the periodic arrangement of molecules is perfect and extents throughout the specimen without interruption, the result is an organic molecular single-crystal.

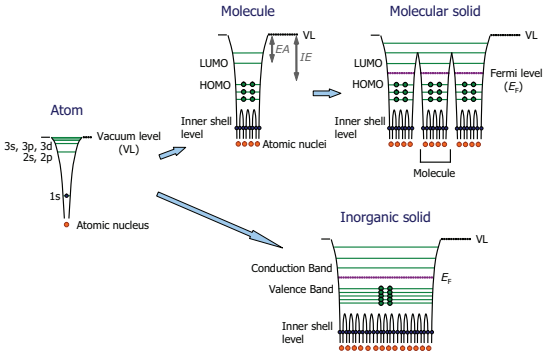

Figure 2.1 *Electronic energy diagram of an individual atom, a single molecule, a molecular solid and an inorganic solid. Figure with permission from [1].*

EA: electron affinity.

IE: ionization energy.

LUMO: lowest unoccupied molecular orbital.

HOMO: highest occupied molecular orbital.

2.3 Why Organic Molecular Single-Crystal Devices?

In chapter 1, the great interest in organic materials for electronic applications has been highlighted, as they possess many fundamental advantages over their inorganic counterparts. Over the past two decades, a large effort in the development of organic thin film transistors (OTFTs) has resulted in an impressive improvement of the characteristics of these devices, so that, currently, the best OTFTs have surpassed the widely used amorphous hydrogenated silicon transistors in performance [2]. However, there are several reasons why even the best OTFTs *"may not be appropriate vehicles for illuminating basic mechanisms in organic materials"* [3] and thus cannot be reliably used to investigate the intrinsic electronic properties and physical limitations of organic semiconductors.

In thin film devices, organic semiconductors are commonly either thermally evaporated or applied from solution to form an active layer on a pre-patterned substrate. Such thin films are typically polycrystalline because the crystal growth starts from various nucleation sites on the substrate surface. Besides that, the performance of the thin film devices is greatly affected by many aspects of the fabrication procedure, such as surface treatment, temperature, material purity, device structure, and testing and deposition vacuum conditions [4-6]. These fabrication conditions have a large influence on the film growth and morphology, as can be noticed by a varying crystallinity, different microstructure, and an altered molecular packing and alignment. Although thin films are more attractive for organic electronic devices, the imperfections in the film structure and the polycrystalline orientation limit the study of the intrinsic properties of the material (*viz.* the properties not limited by static disorder), as charge transport is hampered by these structural defects and chemical impurities [7-9]. As a result, reproducibility between labs is low due to the dependence on fabrication processes and handling environment. Comparison of literature results is difficult, as results may vary over an order of magnitude, even for devices with the same organic active layer and fabricated similarly [3]. As a consequence, properties intrinsic to molecular arrangement, such as electrical anisotropy, can be easily masked by these imperfections.

To study the intrinsic electronic properties and physical limitations of organic semiconductors, it is crucial to achieve the highest degree of order and minimize or eliminate inconsistencies in molecular order and device quality. Such systems would offer the best

overall performance, and offer an upper limit for the performance of less-ordered films (making them ideal for screening of novel materials). Only when single-crystalline systems are used, a correct insight on the interplay between the effects of chemical structure and molecular orientation on the charge transport process can be accomplished. The study of devices based on single-crystals of organic semiconductors is therefore needed, similar to the single-crystal structures of inorganic electronics. Examples of various organic crystals are presented in figure 2.2. Organic single-crystals typically possess a low defect concentration and have a high purity. Variation in molecular order is minimized by a significantly reduced (static) disorder and a near-perfect order over the crystal's entirety (up to cm's in size). Single-crystals are –at the moment– not meant to be incorporated in applications, but serve as model systems, for which structure-property correlations can be explored.

The best examples illustrating the improved performance of single-crystalline devices are the organic single-crystal field-effect transistors developed the last couple of years [10-18]. Their significantly reduced disorder enabled to explore the fundamental processes that determine the operation and reliability of organic electronic devices. These systems provided, for the first time, the observation of intrinsic transport of field-effect induced charges at organic surfaces [16,19,20]. The charge carrier mobility in these devices is an order of magnitude larger than that in the best performing organic thin film transistors [13]. Another example illustrating the benefits of single-crystalline systems is the rise of rubrene into the field that, since the discovery of an excellent hole-transport in its single-crystalline form [10], received much attention and is deposited as a thin film as well [21].

Although the device quality still varies in literature, the reproducibility is high: devices fabricated in different laboratories exhibit similar characteristics. And despite the fact that the material performance is ultimately still limited by impurity- and disorder-induced defects [19,22-24], the superior and relatively consistent performance of organic single-crystal devices reflects their advantages above thin film devices.

2.4 Growth of Organic Single-Crystals

The first step in the fabrication of high-quality organic single-crystal devices is the growth of ultrapure organic crystals [13,29-31]. The crystals can be grown either from the solution-phase or from the vapor-phase, depending on specific material properties.

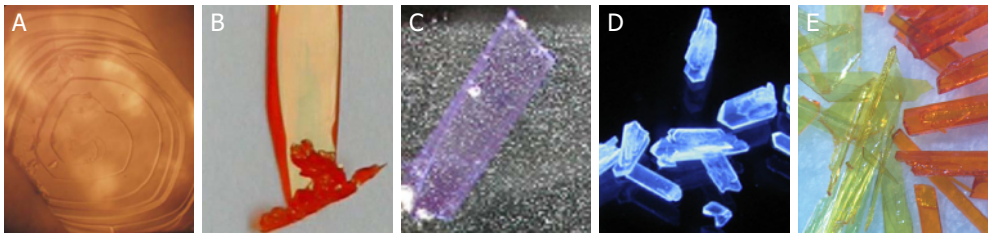

Figure 2.2 *Examples of various organic molecular crystals under an optical microscope: A) anthracene (using phase contrast microscopy), B) tetracene, C) anthracene, D) cis-TSDTB (under ultraviolet light), and E) TCNQ (yellow) and TTF (orange) crystals. Figures with permission from [25-28].*

2.4.1 Solution-phase crystal growth

The simplest method to grow organic crystals is from the solution-phase. In this method, crystals are obtained by drop-casting a highly concentrated or supersaturated solution of a soluble organic semiconductor onto a substrate and allowing the solvent to evaporate slowly, or by dip-coating the substrate into the solution and allowing the crystals to precipitate from the solution [29]. This approach can be applied for both small molecules [32] and polymers [33], as long as a solvent with appropriate volatility can be found to dissolve the source material. The solvent can affect the shape and surface smoothness of the grown crystals, and can sacrifice the crystal quality as some solvent may remain on or inside the crystal acting as an impurity. Several groups have been successful in rendering insoluble organic semiconductors soluble, by addition of functional side groups to the aromatic core of these molecules, although this may compromise the original crystal properties [34-36]. Also not irrelevant, many solution-grown crystals are relatively small in size and difficult to handle. Overall, crystallization from solution usually results in substantially lower field-effect mobilities compared to crystals grown from the vapor-phase [37].

2.4.2 Physical vapor transport crystal growth

Another method to grow organic crystals is from the vapor-phase. To date, the best results in field-effect studies have been obtained with the organic single-crystals (*e.g.* rubrene, pentacene) grown by the *physical vapor transport* (PVT) technique. Karl succeeded to grow centimeter-sized anthracene single-crystals using the PVT method for the first time, in a vertical set-up [38]. After that, Laudise, Kloc and co-workers designed a more convenient horizontal set-up, in which high-quality single-crystals of oligothiophene, anthracene, pentacene and copper phthalocyanine were grown [39-41]. Up to now, most of the high-quality single-crystals have been grown in PVT set-ups similar to the design of Laudise *et al.* [40].

In the physical vapor transport method, the starting material is loaded into the high-temperature zone of a furnace where sublimation takes place; crystal growth occurs further along the furnace at a lower temperature, the vaporized material carried there by an inert transport gas (see figure 2.3) [40]. A PVT furnace typically consists of a quartz tube with a stabilized temperature profile created along the tube by external heaters (*e.g.* by resistive heating of heater coils). Large, high-purity organic crystals can be obtained by the PVT growth method. The crystals can grow either self-standing (for subsequent manual manufacturing after harvesting), or directly onto pre-fabricated transistor templates. The growth process may last anywhere from tens of minutes to several days, depending on the type of material and the size and shape of crystals desired.

Several factors affect the size, morphology and quality of the PVT-grown organic single-crystals. Most crystals are shaped as thin platelets or needles, and typically vary in size from tens of nanometers to several micrometers in thickness, with the longest dimensions reaching centimeters in platelet-like crystals. Crystal dimensions depend explicitly on the chemical structure and packing of the organic material; *i.e.*, more specifically on the strength and symmetry of the intermolecular interactions. Due to the complicated nature of the organic molecules as well as the weak van der Waals interaction, a common feature for the

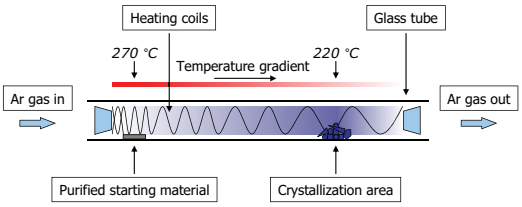

Figure 2.3 *Set-up for the growth of organic crystals via physical vapor transport. The temperature settings correspond to pentacene crystal growth.*

organic crystals is their low degree of symmetry. This asymmetry plays an important role in determining the macroscopic shape of the grown single-crystal. Generally, crystals always tend to grow faster along directions that have the lowest interaction energy, so that the total energy can be minimized. The 'easy-grow' direction depends on the packing and symmetry of the organic crystals: a needle-shaped crystal is obtained if the molecules are more easily attached along one direction than the others, whereas platelet-shaped crystals are formed when two or more directions in the same plane are equally feasible for growth. In practice, the crystal shape can already be affected by a small difference in growth conditions (*e.g.* temperature, pressure, distribution of impurities) and both platelet-like and needle-shaped crystals have for example been observed in the same growth batch [42-44].

Two important parameters that co-determine the speed of crystal growth and affect the size and quality of PVT-grown crystals are the gas flow and the temperature of the sublimation zone [42]. Increasing the gas flow enhances both the sublimation of the source material and the transport of the sublimed molecules down the growth tube. This results in an increased availability of sublimed molecules for a growing crystal, and thus in an accelerated crystal growth. A few reports suggest that an increased gas flow during crystal growth leads to two-dimensional, rather than three-dimensional growth, and hence thinner crystals [16,22,45]. Increasing the temperature of the sublimation zone accelerates the sublimation process and crystal growth as well, and is considerably more effective in reducing the growth time than increasing the gas flow at some given temperature. Increasing both temperature and/or gas flow too much leads to a lower yield of high-quality crystals, as the crystal growth zone is pushed further downstream (into the steep temperature gradient at the end of the furnace tube), where crystal growth occurs very quickly and with little or no impurity separation [42].

Ultrahigh-purity argon, nitrogen, helium and hydrogen gasses have been used as a carrier agent. The inert carrier gas should be as pure as possible, as residual water or oxygen impurities can react with the sublimed molecules [46]. The growth process is generally performed in the dark, as oxygen impurities in the carrier gas will cause photo-oxidation of most organic molecules [47]. Moreover, some organic crystals need to be grown under reduced pressure to decrease the operating temperature and prevent the source material from thermally degrading [48]. How the transport gas exactly affects the crystal quality is still unclear, yet an influence on the crystal size is clearly present. For example, tetracene and rubrene crystals grown in helium were very thin, yet growth in hydrogen or argon yielded rather thick crystals [31]. Then again, others observed no significant change in the growth of tetracene crystals when switching between argon or a nitrogen-hydrogen gas [49].

It is worth noting that not all organic semiconducting materials are suitable for PVT crystal growth. Crystals with a preferred growth along one of the crystalline directions may result in the formation of entangled wires or ribbons. For materials with a low vapor pressure (*e.g.* copper phthalocyanine, some thiophenes), a too high source temperature is generally required for the crystal growth, and the grown crystals are often too small to handle [40,50].

2.4.3 Other vapor-phase crystal growth techniques

In addition to the PVT crystal growth technique, several other vapor growth methods have been developed the last years. Most interesting is the vapor-Bridgman growth technique, which was reported to grow large tetracene crystals for TOF studies [51,52]. The conventional Bridgman technique utilizes growth from the melt; *i.e.* melting the source material in a closed glass ampoule and then allowing it to re-crystallize under reduced temperature. This technique is only suitable for materials that are stable upon melting (*e.g.* anthracene) and is inapplicable for most organic semiconductors studied today, due to decomposition upon melting. In the modified vapor-Bridgman method, the crystal is grown in a sealed ampoule from saturated vapor instead of the melt state. The starting material is first sublimed inside the hot zone of the ampoule, and then re-crystallizes at the cold region. The growth front is controlled by slowly moving the hot zone position, and eventually a bulk crystal can be obtained in the ampoule. Finally, the crystal is released, and can even be sawed and polished along desired crystallographic planes. In general, vapor-Bridgman grown crystals are more brittle and measured TOF mobilities were lower compared to vapor-phase grown crystals, probably due to a higher content of chemical impurities [51].

Other vapor-phase growth techniques focus on controlling the growth conditions of traditional physical vapor deposition (PVD) techniques that are originally applied to deposit organic thin films. These methods include mask-shadowing vapor deposition [53], hot wall deposition [54], and hot wall epitaxy [53]. So far, only small single-crystals (~10 μm) were obtained with these methods.

2.4.4 Purification of the starting material

Another important parameter affecting the size, morphology and quality of the PVT-grown crystals is the purity of the starting material. First of all, the density of impurities can be reduced by performing several re-growth cycles, in which previously grown crystals are used as starting material for the next growth [31]. This *in situ* purification of the material is intrinsically provided by the PVT set-up, as sublimed organic impurities will crystallize at a slightly different temperature based on their composition (*e.g.* in the first growth cycle, differently colored crystals are typically observed closer or further along the tube). For a good separation between the desired crystals and the solidified impurities, the temperature gradient along the tube should be sufficiently small. Besides that, a residue of unsublimed impurities left in the crucible after the first growth cycle can be observed; this residue is typically not present after subsequent growth cycles. Generally, the beneficial effect of the *in situ* purification is limited to two or three growth cycles, after which no further increase in mobility is observed [31].

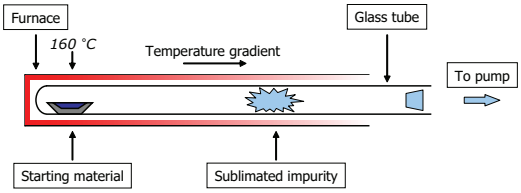

Figure 2.4 *Set-up for pre-purification of starting powder via vacuum sublimation under a temperature gradient. The temperature settings correspond to pentacene purification.*

Obviously, the higher the purity of the starting material, the fewer re-growth cycles are required and the higher the final mobility will be [13]. Prepurification of the starting material is therefore of great importance, especially as even the *sublimed grade* of commercial available materials only have a 99.0 to 99.9% purity [55]. Several methods have been used to purify the as-received materials; however, they can often be applied to specific organic materials only, as the examples below demonstrate. Performing multiple recrystallizations from solution is limited to organic materials that are well soluble in a common solvent [31]. Zone-refinement techniques require the existence of a coherent liquid phase (*i.e.* the melting temperature has to be lower than the temperature of decomposition) [31]. Vacuum sublimation methods are limited to organic materials with the sublimation temperature below the melting point [56]. Purification by chromatography can also be an option [29].

In the *vacuum sublimation under a temperature gradient* technique, the starting powder is placed inside a glass tube in the hot zone of a furnace, at a temperature below its sublimation temperature (see figure 2.4) [56]. A vacuum and a controlled temperature gradient is then applied along the furnace tube. The impurity molecules having a sufficiently low vapor pressure will sublime and condense in the cold zone of the tube, thus increasing the purity of the material that remains in the crucible.

2.5 Fabrication of Organic Single-Crystal Devices

Fabrication of organic molecular crystal devices (*i.e.* field-effect transistors, FETs) to study their intrinsic behavior poses a technological challenge, as the surface of organic single-crystals can be damaged much more easily than that of their inorganic counterparts. Many conventional (silicon) microelectronic processing techniques irreversibly destroy the molecular order at the surface, creating interfacial trap sites and barriers to charge injection, which makes the device performance very sensitive to the manufacturing conditions. Organic crystals are therefore largely incompatible with conventional processing techniques, such as photolithography, sputtering, etc. [13,29]. In addition, electron-beam and focused ion-beam deposition techniques are known to contaminate and damage the organic crystals [57].

Instead, several alternative approaches for the fabrication of organic single-crystal devices have been investigated. So far, four approaches have been employed successfully:

1. The 'flip-crystal' method, in which an organic crystal is manually placed on a pre-fabricated transistor template, after which electrostatic 'bonding' of the crystal to this template takes place [12,14,17,45,58].
2. Growth of an organic crystal directly on a pre-fabricated transistor template [59,60].

3. An organic crystal is brought in contact with a pre-fabricated gate dielectric substrate with back gate; the source and drain contacts are applied next onto the crystal surface [61,62].
4. Fabrication of a complete free-standing crystal device by direct deposition of the contacts and gate insulator onto the crystal surface [10,11,37].

The architecture of the resulting field-effect transistors is diverse for the four fabrication methods: a bottom-contact, bottom-gate configuration is created with the first two approaches; a top-contact, bottom-gate configuration in approach three; and, finally, a top-contact, top-gate configuration in the fourth approach.

In the next paragraphs, these various manufacturing methods will be discussed in more detail. The third approach, which has been mainly applied to fabricate organic single-crystal nanowire transistors [33,53,63-65], will not be treated here separately as this fabrication method can be considered a combination of the other approaches.

2.5.1 'Flip-crystal' method on transistor template

In the first technique of single-crystal OFET fabrication, the 'flip-crystal' method, an organic single-crystal is laminated by electrostatic bonds (*i.e.* attractive van der Waals forces) on a pre-fabricated transistor template (or 'stamp'), see figure 2.5. This method involves flipping a single-crystal onto the substrate (with transistor circuitry on it) with tweezers or similar tools. To laminate the crystal, a gently pressure is applied to one edge of the crystal positioned on the substrate, after which the van der Waals forces then spontaneously cause a 'wetting' front that proceeds across the crystal surface. Lamination works best for perfectly flat crystals or very thin (<1 μm thick) and bendable crystals that stick spontaneously to the substrate. However, it can also be applied (with a lower success yield) to thicker crystals by gently pressing on the crystal to assist the adhesion process [13]. With this method, crystals can be aligned on the transistor circuitry with the most homogeneous surface and along the desired orientation, which improves the device performance and enables the anisotropy research.

Conventional microelectronic (photolithography) processing techniques can be used to fabricate the transistor circuitry. The template contains source and drain electrodes and a gate dielectric patterned on either a highly-doped wafer or a substrate containing a gate electrode. As the entire device fabrication is performed separately, the need for deposition of metals and dielectrics directly onto organic crystals is eliminated; therefore, the possibility of crystal destruction is largely avoided. Two kinds of transistor templates have been used: rigid silicon wafers (with either thermally grown SiO_2 or sputtered high-κ dielectrics) [12,13,14,53] and flexible polymer (Kapton or poly-dimethylsiloxane, PDMS) substrates [66].

Figure 2.5 *Electrostatic bonding of a rubrene single-crystal to a pre-fabricated transistor template with an Al_2O_3 dielectric layer and Au source and drain electrodes. Figure with permission from [68].*

Rigid transistor templates

In the first case, the source and drain circuitry is patterned on the surface of a heavily doped Si wafer (serving as bottom-gate electrode), covered with a dielectric layer of thermally grown SiO_2 [12,14,17,67] or sputtered high-κ dielectric (*e.g.* Al_2O_3 [68], Ta_2O_5 [67,68] or ZrO_2 [67]). As a final step, a thin organic crystal is electrostatically bonded to the transistor template.

Good experimental results have been obtained with this method; yet leakage, hysteresis, and other non-ideal transistor behavior were observed when bare oxide dielectrics are used. Attempts to passivate the oxide surface included reactive ion etching [12], oxygen plasma [69], and treatment with self-assembled monolayers (SAMs) [14,70-72], and each of these techniques achieved an improved performance. Replacement of the oxide dielectric with inert, non-polar dielectrics such as spin-coated polymers [73-76] or elastomers [16,45] resulted also in high field-effect mobilities with consistent transistor characteristics.

Flexible transistor templates

In the second case, the transistor circuitry is fabricated on top of a flexible polymer or elastomer substrate (*e.g.* PDMS), to which an organic crystal is then laminated [66]. The flexibility of the PDMS stamp enables to establish a good contact, even with crystals that are not perfectly flat (*i.e.* the flexible PDMS surface and the ductile Au contacts adjust easily to the crystal shape). Moreover, the technique is reversible and non-destructive for some thick robust crystals: the contact can be re-established many times without breaking the crystal and without noticeable degradation to the crystal's surface [16,19]. For this reason, the anisotropy of the field-effect mobility within the *ab*-plane of rubrene single-crystals could be observed for the first time [16,19]. However, some organic single-crystals, like pentacene, are too fragile to be manipulated in this manner; the crystals would break during separation from the PDMS stamp after the first measurement [77]. Besides the PDMS stamp, also high-performance transistors on flexible Kapton substrates have been demonstrated [58].

To preserve the pristine crystal surface, a modification of the PDMS stamping techniques was introduced that eliminates the direct contact between the crystal and the gate dielectric. In the so-called 'free-space' or 'gap-type' configuration, the conventional dielectric is replaced by a micrometer-sized gap between the gate electrode and the surface of the semi-conducting crystal [20]. The gap can be vacuum [78], filled with a gas (*e.g.* air, nitrogen) [19,79] or polymer gel or ionic liquid electrolyte [80-82] that plays the role of gate dielectric. The free-space configuration enables studies on the effect of different gases and other environmental agents on the conduction channel in single-crystal OFETs [79,83]. An important feature for the gap-type single-crystal OFETs filled with air or another gas is their low capacitance, due to the small dielectric constant and relative large thickness of the dielectric gas layer; hence the injected carrier density is considerably lower compared to the conventional SiO_2 based organic transistors [84]. In the gap-type transistor devices filled with an ionic liquid electrolyte, high-speed switching and a high mobility and transconductance was achieved, due to the high capacitance of the electric double layer [85,86].

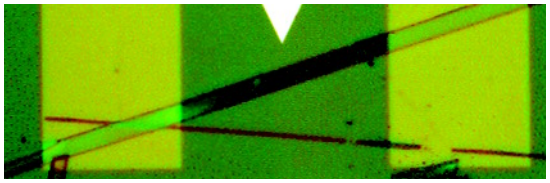

Figure 2.6 *DT-TTF single-crystal grown in solution on a pre-fabricated transistor template. Figure with permission from [59].*

2.5.2 Crystal growth on transistor template

Instead of laminating an organic crystal to a pre-fabricated transistor template manually, growing the crystal directly on this template can be an interesting option. In this situation, the crystal is no longer handpicked and placed onto the transistor template (the handpicking can introduce contamination and crystal damage, resulting in a lower device performance [65]). Fabrication of bottom-contact single-crystal OFETs from solution has primarily been performed by dip-coating or drop-cast formation of crystals on substrates with a large array of pre-formed transistor templates, whereby a random number of crystals formed in solution will bridge the source and drain electrodes and form functioning devices (see figure 2.6) [29]. This technique has been employed to examine the mobility in several materials systems (*e.g.* DT-TTF derivatives and substituted CH_4T crystals) [32,59,60,87], however, the total device yield is low as there is no control over where on the substrate the crystals nucleate and grow. Only a limited amount of crystals can be found with good connection to both source and drain electrodes. Even for these crystals, the alignment is random and the crystal orientation along the transistor channel is uncontrollable. For vapor-grown crystals like tetracene, a non-dissolving, volatile liquid such as hexane can be used to transfer the crystals to the substrate; however, the final location of the crystals is again highly unpredictable [88].

Selective nucleation of many anthracene crystals grown from solution on SAM-modified Au substrates has been reported by Bao and co-workers in 2005 (see figure 2.7A-B) [89]. Follow-up studies resulted in arrays of functioning transistors (see figure 2.7C), this time by growing various organic single-crystals from the vapor phase selectively onto octadecyl-triethoxysilane-treated source-drain electrodes of pre-fabricated transistor templates [90] or onto carbon nanotubes [91]. The rough SAM domains on a further smooth surface were found to act as preferential nucleation sites for the growth of single-crystals measuring up to a few hundred micrometers in size [92]. Using a similar approach based on solvent de-wetting to selectively pattern the semiconductor solution, functioning transistors with crystals grown from solution have also been demonstrated by the same group [35,93].

After these initial reports, much research has started the last years on the controlled deposition and growth of organic crystals from vapor [94] or solution [95,96] and of polycrystalline films [97,98] on chemically modified transistor templates; and has recently been reviewed [61].

2.5.3 Direct deposition

Direct deposition of contacts and gate dielectric on a free-standing organic molecular crystal acting as substrate is not straightforward. The organic single-crystals are incompatible with most conventional thin film processing techniques, like photolithography, sputtering and thermal evaporation [13,29]. Solvents, photoresist and elevated temperature are known to

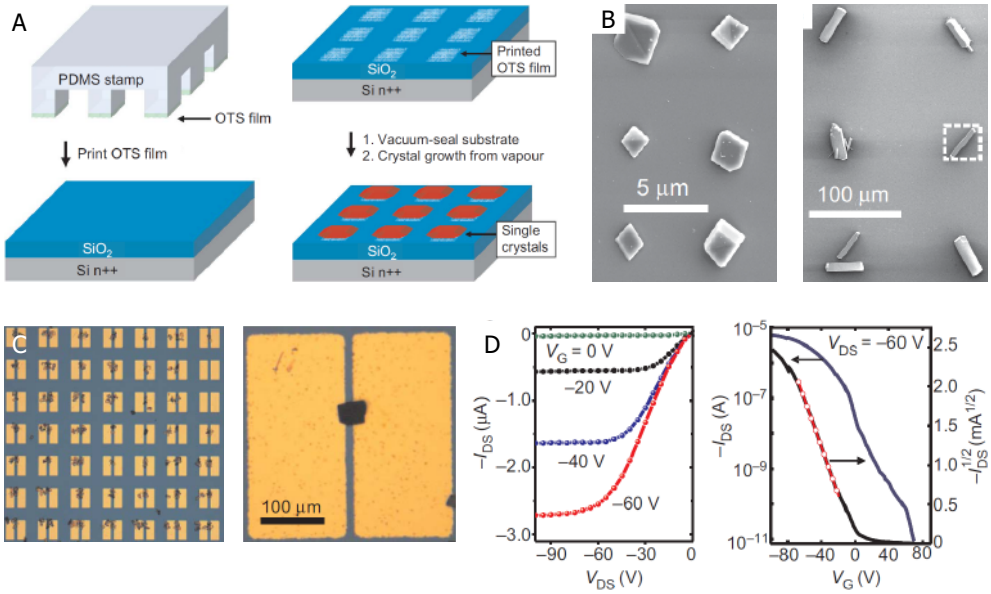

Figure 2.7 *A) Procedure to grow organic single-crystals on SAM-patterned substrates. B) Patterned pentacene and rubrene single-crystals. C) Arrays of patterned pentacene single-crystal transistors. D) Characterization of a pentacene single-crystal transistor. Figure with permission from [90].*

destroy the crystal structure and molecular order at the surface, making photolithography not an option [13]. Sputtering of Al_2O_3 and other dielectrics eroded the crystal surface, and high-energy particles penetrating the crystal created such a high density of defects that the field-effect in the device channel was completely suppressed [13]. Positioning the organic crystals in the shadow region of the sputter chamber, where the deposition rate was zero, and attempts to shield the surface from high-energy charged particles by electrostatic deflection did not improve the situation. Finally, thermal evaporation of SiO_2 was also unsuccessful, probably due to a too high temperature of the deposition source [13]. Nevertheless, direct fabrication has been successful in a few cases, in which thick free-standing crystals (>10 µm thick) were typically used, after manual handpicking and positioning them on a supporting substrate [82].

Direct deposition of the source and drain contacts

Two routes have been followed for the successful deposition of source and drain contacts on the surface of organic crystals. The simplest route is applying metallic contacts on the crystal surface by manually 'painting' of a conducting silver paste [15,99], a water-based colloidal carbon or graphite dispersion [22,31,100,101] or a solvent-free silver epoxy dispersion [102]. This route has been successfully applied to pentacene [15,102] and rubrene single-crystals [62]. The manual paint-on electrode technique is relatively straightforward and results in a low contact resistance [31]. Preparing small, nicely-shaped and well-defined contacts is rather difficult; large crystal sizes are needed and the number of devices per crystal is limited. In addition, it often resulted in formation of traps at the metal–organic interface, as space-charge-limited transport experiments on tetracene crystals did show [52].

The second route reported is via thermal evaporation of metals through a shadow mask on the crystal surface [10]. As a general rule, the thermal load on the crystal surface in the deposition process has to be minimized, as it can damage the ordering of the molecules on the crystal surface and create traps at the metal – organic interface causing irreproducible characteristics. This phenomenon has regularly been observed in space-charge-limited current and field-effect devices with the metal contacts evaporated on top of the organic films [103-105]. Most thermal load originates from infrared radiation of the evaporation boat, limiting the choice of metals to that with a relatively low evaporation temperature. Despite the technological difficulties, successful deposition of high-quality silver electrodes by thermal evaporation could be achieved, with minimal damage to the crystal substrate, after optimizing to very mild deposition parameters (*i.e.* low deposition rate, large source to sample distance, cooling the sample and shielding infrared irradiation from the evaporation source) [11]. In an optimized deposition chamber, high-quality OFETs with evaporated metal contacts have been fabricated on the surface of several organic crystals (rubrene, pentacene, TCNQ) [11]. Vacuum deposition of CuI electrodes on perylene single-crystals has also been reported [106]. Contamination of the channel area between the contacts is reported by oblique incidence and diffusion of silver atoms under the shadow mask (presumably from scattering by residual gas molecules); however this could be minimized by depositing through a long narrow tube (called collimator) positioned just above the crystal surface.

In several reports on organic single-crystal nanowire transistors, top-contacts were fabricated by thermal evaporation of gold using a copper grid [33,107,108], a thin Au wire (~20 μm in diameter) [64,65] or a thin polyethylene wire [109,110] as shadow mask on the tiny organic crystals. Long and thin, micrometer-sized organic ribbons (*e.g.* copper phthalocyanine, CuPc, or anthracene-derivative single-crystalline wires) laminated on the crystal surface have been used as mask as well; the so-called *'two-dimensional organic ribbon mask'* technique [57,111,112].

Recently, another approach to make gold source and drain electrodes on organic single-crystals without thermal evaporation has been developed by Zhu and co-workers; the *'gold-layer sticking'* technique [113,114]. In this method, a small piece of a pre-deposited thin Au layer is peeled off from a silicon wafer with a probe tip and mechanically transferred onto the organic crystal, to which it is laminated by van der Waals forces.

Direct deposition of the gate dielectric

The deposition of a dielectric layer on top of the organic crystals (with or without metal contacts already deposited) has proven even more problematic than the deposition of the contacts. Attempts with sputtering oxides onto the crystal irreversible damaged them [13]. So far, successful deposition of inorganic dielectric oxides onto the surface of organic crystals by sputtering or other techniques has not been reported.

The first successful deposition of a gate dielectric on a free-standing crystal has been achieved by coating the crystal with a thin insulating polymeric film of parylene. This method, introduced by Podzorov *et al.* [10], can be considered as the breakthrough in the direct

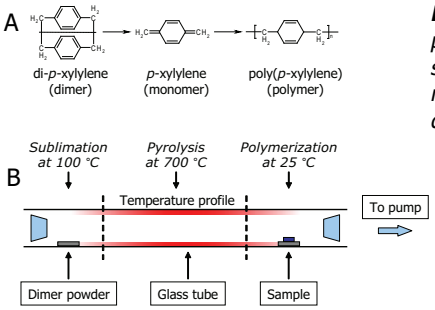

Figure 2.8 *Parylene deposition. A) Reactions involved in parylene deposition: sublimation of dimers at 100 °C, splitting into monomers at 700 °C, and polymerization at room temperature. B) set-up for parylene dielectric layer deposition on organic single-crystals.*

fabrication of free-standing single-crystal OFETs. Parylene, first discovered in 1948 [115], is chemically inert and can be deposited from the vapor phase as a transparent pinhole-free film at room temperature. It can be deposited on a free-standing crystal without apparently destroying its surface or introducing many traps at the dielectric – crystal interface. The transparency of the parylene film opens the possibility to perform optical studies by illuminating the conducting channel through a transparent gate electrode [116].

In ref. [10], parylene was deposited in a reactor with three temperature zones under a reduced nitrogen gas pressure (see figure 2.8). The metastable parylene dimers [117], sublimed at 100 °C, split into monomers at 700 °C and polymerize as they enter the room temperature section of the tube, producing an insulating coating on the sample's surface. After the deposition, gate electrodes are painted on the parylene gate dielectric to cover the region between source and drain electrodes.

Using this method, record-high mobilities have been reported for a variety of organic crystals [11,22,37,99-101,106]. Organic single-crystal FETs with a parylene gate dielectric are very stable: a 2-year storage of rubrene transistors at room temperature in air and in the dark did not affect their characteristics [31,116]. The Hall effect in rubrene crystals [78] and a controlled threshold voltage shift by the introduction of deep traps in tetracene crystals [116] have been demonstrated using this method too. However, a limitation of this method is that damage to the parylene layer by the evaporation of top metal contacts has been reported [118].

Another successful direct deposition of an organic dielectric on a free-standing crystal was shown by Jurchescu *et al.* [119]. Their investigations on pentacene single-crystals showed that the largest impurity fraction, 6,13-pentacenequinone, is located preferentially on the crystal surface. By evaporating ordered 6,13-pentacenequinone films as gate dielectric, the traps are considerably minimized as they are incorporated into the gate dielectric. A high-quality interface could be obtained, yielding record-high FET mobilities ($\mu = 15 - 40$ cm^2/Vs).

2.6 Organic Single-Crystal Device Characteristics

In this paragraph, literature results from time-of-flight measurements (section 2.6.1), space-charge-limited current spectroscopy (2.6.2), and field-effect experiments (2.6.3 and further) on organic single-crystalline systems will be discussed. Several properties specifically observed in experiments with organic single-crystal devices will be highlighted.

2.6.1 Time-of-flight measurements on organic single-crystals

The time-of-flight (TOF) experiments by Karl *et al.* in 1985 [120,121] (see figure 1.7) with very pure acene crystals were benchmark studies that initiated further research on charge transport in organic semiconductors. Two characteristics in these experiments demonstrate that intrinsic polaronic band-like conduction can be realized in the bulk of these organic crystals [122-124]. First, the charge transport regime is characterized by a rapid increase of the carrier mobility with decreasing temperature; *i.e.* the intrinsic mobility μ typically varies as an inverse power of temperature via $\mu \propto T^{-n}$, with $n \approx 2 - 3$ (depending on the specific organic molecules) [122]. Second, a pronounced anisotropy of the mobility is observed, which reflects the anisotropy of the intermolecular transfer integrals [125,126].

Successful TOF measurements have been performed on various organic single-crystals. In various papers, Karl and co-workers reported high mobilities at low temperature in ultrapure naphthalene (300 cm^2/Vs) [120,121], anthracene (50 cm^2/Vs) [124], perylene (100 cm^2/Vs) [120,123], biphenyl (30 cm^2/Vs) [123] and phenanthrene (8 cm^2/Vs) [123] single-crystals. At room temperature, all these crystals showed a mobility of about 1 cm^2/Vs. De Boer *et al.* [52] measured a room-temperature mobility $\mu = 0.5 - 0.8$ cm^2/Vs for vapor-grown tetracene crystals. Niemax *et al.* [51] measured a room-temperature mobility μ of about 1 cm^2/Vs for vapor-grown tetracene crystals. To conclude with, rubrene single-crystals were found to be unsuitable for TOF measurements, for form and shape reasons [13]. As no literature is found, the same explanation probably holds for the even more fragile pentacene single-crystals.

2.6.2 Space-charge-limited current spectroscopy on organic single-crystals

Prior to the achievement of high charge carrier mobilities in organic single-crystal field-effect transistor devices, high mobility values were demonstrated in space-charge-limited current (SCLC) measurements on ultrapure organic single-crystals. In this paragraph, the results from these measurements on pentacene and other organic single-crystals will be discussed.

Charge transport in organic single-crystals has been described by various space-charge-limited current models using various electrode geometries (see paragraph 8.2.3). In 1962, Mark and Hefrich [127] were the first to detect the space-charge-limited currents in organic molecular crystals; *i.e.*, in *p*-terphenyl, *p*-quarterphenyl and anthracene crystals. More recently, tetracene [52,128] and rubrene [129] single-crystals with sandwich-structured electrodes were analyzed by the Mott-Gurney model, which was also applied on TCNQ-coronene co-crystals [130] with a gap-type geometry. Perylene crystals have been investigated at different temperatures with both gap-type contacts and in the sandwich geometry [131].

Mattheus *et al.* [46,132] investigated the space-charge transport in pentacene single-crystals, with evaporated metal contacts in the gap-structure geometry. The trap filling limit was reached in none of the measurements in air. In high vacuum and darkness, however, the current-voltage curves showed an ohmic and space-charge-limited regime, and the trap filling limit was reached at 10^5 V/cm. Large differences were observed in one crystal and reproducibility of the measurements was rather low (*e.g.* twelve hours waiting time in-between measurements was necessary to observe the trap filing limit again).

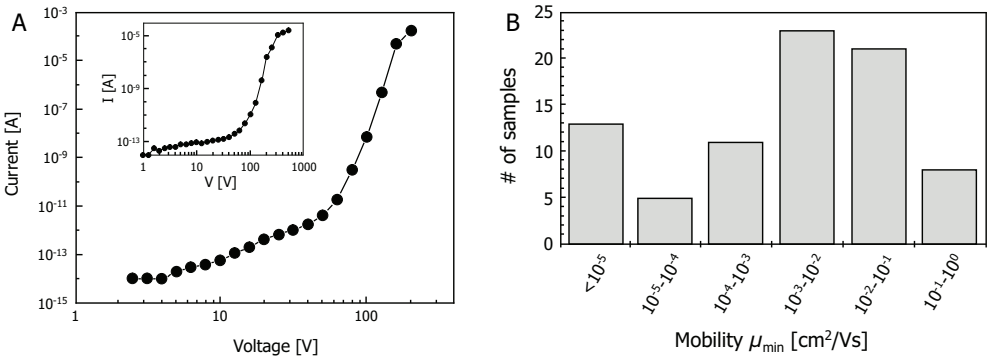

Figure 2.9 *A) Typical I-V measurements on a tetracene single-crystal (μ_{min} = 0.59 cm²/Vs; inset μ_{min} = 0.014 cm²/Vs). B) Histogram of values for μ_{min} calculated from I-V measurements performed on about 100 tetracene single-crystals. Figures with permission from [52].*

In the follow-up project by Jurchescu [133], a mobility μ of 35 cm2/Vs was reported for pre-purified and double-grown pentacene single-crystals at room temperature, increasing to μ = 58 cm²/Vs at 225 K [134]. They also reported a gradual cross-over from the 1D to 2D space-charge-limited models (depending on the crystal thickness *h* and the distance *L* between the contacts), for pentacene single-crystals with parallel silver-epoxy contacts painted on the crystal surface [135]. For rubrene single-crystals, the 1D to 2D model transition in SCLC-behavior has also been observed [136]. Jurchescu *et al.* [102] also investigated the electronic transport properties of pentacene single-crystals upon exposure to (dry and ambient) air. In the ohmic regime at low voltages, no marked changes in the conductivity were induced by the presence of air; the SCLC regime, however, is influenced by exposure to air.

De Boer *et al.* [52,118] observed that the precise shape of the current-voltage characteristics measured for more than 100 tetracene single-crystal samples exhibited large deviations and yielded a broad distribution of different apparent mobilities, ranging from 10^{-6} to 10^{0} cm²/Vs (see figure 2.9B). They noticed an approximately quadratic current increase with voltage in the lower voltage range, up to 10-100 V, depending on the sample. Around or just above 100 V, the current started to increase steeply (typically six to eight decades, for a one-decade increase in voltage), which is attributed to the filling of deep traps. Only in a few cases, the rapid current increase terminated by crossing over into an approximately quadratic dependence on voltage: the trap-free regime (see figure 2.9A). In most cases the samples failed before reaching this point. The wide range of apparent mobilities was attributed to strongly different contact qualities and the presence of surface traps at the interface.

2.6.3 Field-effect measurements on organic single-crystals

The organic semiconductors used in OFETs are in general intentionally undoped, and mobile charge carriers in these devices must be injected from the metallic contacts. In most single-crystal OFET devices fabricated up to the year 2005, the injection barrier at the contact or the field-effect threshold for either *n*-type or *p*-type conductivity was so large that the OFETs exhibited only *unipolar* operation. Most commonly observed is the *p*-type conductivity, for

instance in tetracene, pentacene and rubrene crystals, whereas *n*-type conductivity has been observed in TCNQ crystals. However, single-crystal OFETs can potentially operate in both the electron- and hole-accumulation modes, depending on the polarity of the gate voltage, and *ambipolar* operation has indeed been observed in recent years.

Charge injection

As OFET devices are intentionally undoped, they belong to the class of injection- or Schottky-limited FETs. This situation is significantly different compared to silicon-based semiconductor devices, in which doping is conventionally utilized to enhance the tunneling efficiency and carrier injection from the contacts, as well as to control *p*- and *n*-type carrier injections. The charge carriers in OFETs are injected into the conduction channel through the interfacial Schottky-barrier at the metal−organic semiconductor interface of height Φ_B. As will be discussed in more detail in paragraph 8.2, the charge carrier injection is a complex process that depends on the metal work function Φ_M, the ionization energy of the semi-conductor *IE*, and the interfacial dipole moment Δ possibly formed due to charge transfer at the interface. The maximum height of the barrier Φ_B remains fixed due to pinning of the energy levels at the interface, yet its width can be modified by an external electric field. When a negative gate voltage V_G is applied, the effective width of the barrier for hole injection decreases. This results in a decrease of the contact resistance R_C, which depends on the barrier height Φ_B, its effective thickness, and temperature. Carrier injection is allowed via thermally activated excitation above the barrier and via tunneling under the barrier, and the resultant injection mechanism, called *thermionic emission* [137]. This injection mechanism is typified by an exponential increase of the contact resistance R_C with decreasing temperature and a dependence of the contact resistance on the gate voltage V_G.

Contact resistance

The Schottky contact resistance in single-crystal OFETs is typically high; in many cases the contact resistance R_C is comparable or even greater than the channel resistance R_{Ch} (especially at low temperatures and in short-channel transistors). However, if the channel is long enough, the devices are not contact-limited at room temperature. Examples of reported devices not limited by the contact-resistance at room temperature are rubrene and tetracene single-crystal OFETs with either graphite or laminated gold contacts [31]. Devices with evaporated silver or gold contacts typically have a higher contact resistance [31].

Generally, the contact resistance R_C is strongly dependent on the temperature and on the biasing regime. Typically, R_C increases with decreasing temperature T and, for a *p*-type device, R_C decreases with an increasing positive bias V_D applied to the hole-injecting contact and with a negative V_G applied to the gate. However, in the limit of a large enough V_G and V_D, the contact resistance becomes small, and even the devices with evaporated metal contacts are not dominated by the contact resistance [11].

The total source-drain resistance R_{SD} can be represented by three resistors connected in series (so that $R_{SD} = 2R_C + R_{Ch}$). To measure the contact and channel resistance in single-crystal OFETs, two-probe measurements [138], four-point measurements (with two additional

small voltage probes in the channel)[10,11,16], and the channel length scaling analysis developed for amorphous silicon transistors[139,140] have been performed. Of these methods, only the four-probe measurements provide the characteristics of the channel resistance independent of the contact resistances. However, for a large enough V_G and V_D, the results of two- and four-probe measurements converge at room temperature, as R_C becomes negligible[11].

The relatively large contact resistance found for gold contacts on rubrene single-crystals at room temperature ($R_C > 100$ kΩ cm)[16] could be reduced to 1 - 2 kΩ cm by modifying the gold contacts with a self-assembled monolayer before the crystal lamination[14,17]. Using the channel length scaling analysis, Morpurgo *et al.* found that using nickel instead of gold also resulted in a remarkable low contact resistance (0.1 - 0.4 kΩ cm)[140]. In two follow-up papers, the same authors also showed that (partly oxidized) Ni, Cu and Co electrodes have a much better reproducibility than Au and Pt contacts (*e.g.* the spread in contact resistance values ranges from two for Ni to more than three orders of magnitude for Au)[141] and modeled these results with the thermionic emission model for Schottky diodes[142].

Single-crystal OFET operation

In this section, the operation of single-crystal OFET devices will be further introduced. Generally, the two-point OTFT theory can be used for single-crystalline devices, assuming the contact resistance R_C is negligible compared to the channel resistance R_{Ch}. In practice, this is valid for most single-crystal OFETs with long channels at room temperature.

There are two pronounced differences that clearly indicate that the theoretical models developed for organic thin film transistors are not one-to-one applicable to single-crystal OFETs. First, a gate voltage V_G-independent mobility μ has been observed in devices based on single-crystals of rubrene[11,16,17], pentacene[14,15], tetracene[12], and TCNQ[20]. This observation contrasts sharply with the strong V_G-dependent mobility commonly observed in OTFTs, due to the presence of structural defects[7,143,144]. The V_G-independent mobility in single-crystal OFETs suggests that the charge transport in these devices does not require thermal activation to the mobility edge and the mobile field-induced carriers occupy energy states within the HOMO-band[31]. This is consistent with the second difference observed between single-crystal OFETs and OTFTs, namely the dependence of the mobility on temperature. An increase in mobility upon cooling is observed in high-quality single-crystal OFETS, in contrast to a decrease in mobility upon cooling in OTFTs (see section 2.6.5).

n-type operation

Single-crystal OFETs operating in the *p*-type mode are most commonly observed, whereas examples of *n*-type operation with high mobility are rare. Several factors are the cause of this asymmetry: the HOMO bandwidth is typically larger than the LUMO bandwith[145], a stronger trapping of *n*-type polarons[122] and a larger Schottky barrier for electron injection into organic semiconductors from the most commonly used high work function metals.

An example of a single-crystal OFET with *n*-type operation and a high electron mobility of 1.6 cm^2/Vs is based on TCNQ crystals[20], but also crystalline ribbons of fluorinated copper phthalocyanines ($F_{16}CuPc$) have shown an electron mobility of 0.2 cm^2/Vs[146].

Ambipolar operation

It has been shown in TOF experiments with high-quality perylene crystals, that both electrons and holes are mobile in the crystal bulk at room temperature [123,124]. Nevertheless, realization of high-mobility ambipolar operation in OFETs is quite a challenge, as two difficult problems must be solved simultaneously: both *p*- and *n*-type carriers must be effectively injected from the contacts into the organic semiconductor, and the density of traps for both carriers in the channel and at the organic–dielectric interface must be minimized. Therefore, organic single-crystals with a low density of traps offer a unique opportunity to realize the ambipolar operation with a relatively high mobility of both types of carriers.

Ambipolar operation has been observed recently in single-crystal OFETs based on metal phthalocyanines (*i.e.* FePc and CuPc) [147], pentacene [148], tetracene [149], rubrene [62,149,150], and other single-crystals [151-153]. In the metal phthalocyanines, both electrons and holes could be injected from contacts made with the same high work function (Au), due to the relatively small band gap of the organic crystal (~1.5 eV) [147]. In tetracene and rubrene crystals, holes were injected from a high work function metal (Au) electrode and electrons from a low work function metal (Ca) contact [149].

The realization of high-mobility ambipolar operation in single-crystal OFETs enabled the further development of a novel class of multi-functional organic devices, namely the organic light-emitting field-effect transistor, and a further study on the intrinsic electroluminescence process in absence of grain boundaries (see paragraph 2.6.5).

2.6.4 Charge carrier mobility in single-crystal OFETs

The charge carrier mobility μ is one of the most important parameters in the characterization of field-effect transistors. In this paragraph, the dependence of the mobility on various factors observed in single-crystal OFETs is reviewed.

Anisotropy of the mobility

Due to the low symmetry in the molecular packing of organic crystals (*e.g.* the acenes typically form crystals with a herringbone packing of the molecules, see paragraph 4.2.3), one can expect anisotropy in their transport properties (*i.e.* charge carrier transport though different directions of the crystal proceeds at different speeds). Indeed, the transfer integrals between the adjacent molecules in these crystals vary significantly depending on the crystallographic direction (*e.g.* generally, the orientation with the best π-orbital overlap between neighboring molecules is the most feasible direction for carrier transport) [145,154-156].

A strong anisotropy of transport properties has been well documented in the time-of-flight experiments by Karl on the acene crystals [123,124]. However, prior to the development of single-crystal OFETs, the anisotropy had not been observed in the measurements on organic thin film transistors. By eliminating grain boundaries and other types of defects, the correlation between the molecular packing and the intrinsic anisotropic transport properties could be observed in single-crystal OFETs for the first time. Currently, mobility anisotropy has been demonstrated on the *ab*-surface of rubrene [16,19,20,23,157], (functionalized-)pentacene [77,158], tetrathia-fulvalene-based [32] and thiophene-based [159] single-crystals.

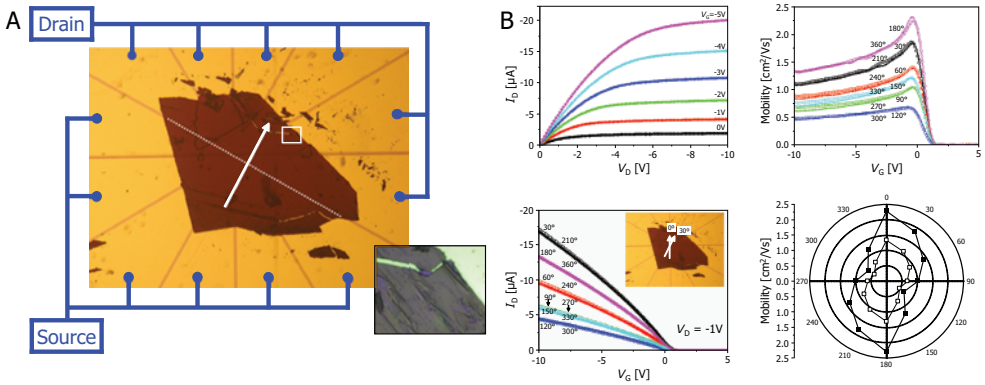

Figure 2.10 *Anisotropic mobility in pentacene single-crystals. A) Optical microscopy image of a pentacene single-crystal placed on fan-shaped electrodes. B) Output and transfer transistor characteristics and a polar plot of the measured mobility. Figures with permission from [77].*

In experiments based on the repeated lamination of the same thick rubrene single-crystal with different orientations onto a metal-coated air-gap PDMS substrate (see paragraph 2.5.1), the mobility along the crystallographic *b*-axis is found to be a factor of three to four larger than along the *a*-axis [16]. A similar ratio has been observed for a rubrene transistor with deposited parylene insulator and colloidal graphite contacts painted on the crystal surface [23].

To measure the anisotropic field-effect mobility in pentacene, Lee *et al.* laminated a pentacene single-crystal to a pre-patterned fan-shape transistor electrode structure on a back-gate SiO_2 substrate [77]. Again, a pronounced anisotropic mobility was observed in the *ab*-plane (see figure 2.10); however, the different transport angles were not coupled to the precise crystallographic directions. The ratio between the highest mobility value (2.3 cm^2/Vs) and the lowest mobility value (0.66 cm^2/Vs) is again about three to four. These measurements also showed that the threshold voltage V_T and subthreshold swing S did not depend on the charge transport direction.

Temperature-dependent mobility

Podzorov *et al.* [19] reported on the temperature-dependent mobility for rubrene single-crystal OFETs. Two transport regimes can be clearly distinguished in their data: an *intrinsic band-like regime* observed at high temperatures, where the mobility increased with cooling, and a *shallow-trap-dominated regime* at low temperatures, where the mobility decreased rapidly with cooling. The crossover between these two regimes occured around 150 - 175 K for this device. Similar behavior of temperature-dependent mobility has been observed in OFETs based on tetracene [12,52] (see figure 2.11) and anthracene [18] single-crystals, although the observed crossover in the tetracene device is attributed to a structural phase transition.

This mobility behavior can be explained by the multiple trap-and-release (MTR) model, see paragraph 1.6.5. In the high temperature regime, the time a polaron spends in a shallow trap is negligible compared to the time a polaron is propagating between traps (due to a large k_BT). Therefore, the mobility in this regime should be independent with temperature and

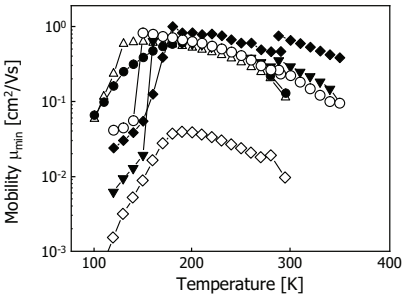

Figure 2.11 *Temperature dependence of the lower limit to the SCLC mobility μ_{min} measured for several tetracene single-crystals. Figure with permission from [52]*

approximately the same to the intrinsic mobility of the material. In reality, a slight increase of mobility upon cooling was observed due to a decrease of polaron-phonon interactions. In the low temperature regime, the time a polaron spends in a shallow trap dominates the carrier transport, thus the mobility is thermally activated. Consistent with the MTR model is the observation that in the trap-dominated regime the mobility anisotropy in rubrene single-crystal devices also vanished at low temperatures [19].

A similar temperature dependent mobility has been observed in the past by Karl *et al.* [123,124] in the TOF experiments on ultrapure naphthalene and perylene crystals, and Jurchescu *et al.* [134] showed in SCLC experiments on pentacene single-crystals as well that the mobility increased with decreasing temperature (from room temperature to 225 K).

Dielectric-dependent mobility

Experiments with rubrene single-crystal OFETs by Morpurgo *et al.* [68,160] revealed a strong dependence of the charge carrier mobility on the dielectric constant ε of the gate insulator. Figure 2.12A shows that the room temperature mobility in these devices decreased with increasing dielectric constant (approximately as ε^{-1}), for a wide variety of gate dielectrics (Ta_2O_5, $\varepsilon = 25$; Al_2O_3, $\varepsilon = 9.4$; Si_3N_4, $\varepsilon = 7.5$; SiO_2, $\varepsilon = 3.9$; Parylene C, $\varepsilon = 3.15$; Parylene N, $\varepsilon = 2.65$; air-gap PDMS, $\varepsilon = 1$). Earlier, a similar trend was observed for OTFTs based on soluble polymers by Veres *et al.* [161]. The observed dependence indicates that there are differences between polaronic conduction in the bulk and at the surface of organic crystals, and that the mobility of charges at the interface between an organic semiconductor and an insulator is a property of the interface, rather than of the organic semiconductor alone.

Moreover, the temperature dependent mobility results (see figure 2.12B) showed that the charge transport changes from band-like to thermally activated hopping with increasing ε. This behavior was attributed to the formation of Fröhlich polarons (see section 1.6.3) when the gate dielectric was sufficiently polar [162]. Earlier, it was already predicted that the intrinsic mobility of polarons at an interface with a highly polarizable dielectric may decrease due to an increase of the effective polaronic mass [163,164].

Pressure-dependent mobility

By applying a hydrostatic pressure to single-crystal rubrene transistors, a linear increase in drain current and field-effect hole mobility was measured with increasing pressure [165]. The results were reversible and threshold voltages shifts with pressure were small. These

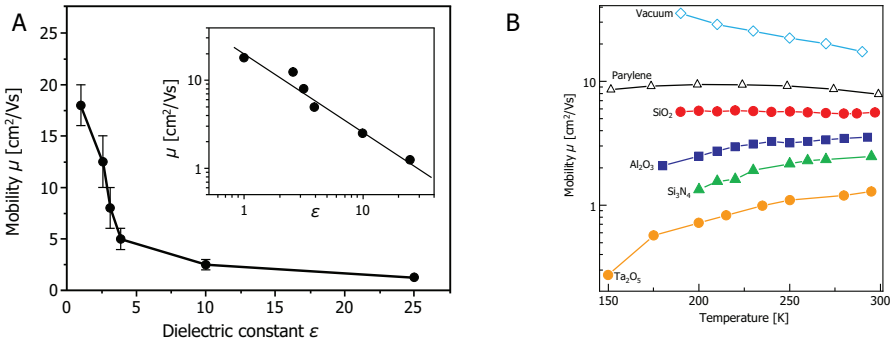

Figure 2.12 *Influence of gate dielectric on the mobility of rubrene single-crystal OFETs. A) Decrease of mobility μ with increasing dielectric constant ε, the inset shows a linear relationship between log(μ) and log(ε), with slope equal to -1. B) Temperature dependence of the mobility μ for various gate dielectric materials. Figures with permission from [68,160].*

experiments provided the opportunity to investigate the dependence of the polaronic mobility on the intermolecular distance of the crystal lattice *d*, as the latter can be directly tuned by the hydrostatic pressure P applied ($\Delta d \sim 1.5\%$ at $\Delta P = 0.5$ GPa). These observations are in line with expectations based on polaronic models and first principle calculations on naphthalene single-crystals: the mobility should depend linearly on pressure for small variations of the intermolecular distance [166]. This dependence could only be observed in the intrinsic single-crystal model systems, where trapping is not dominant.

Results of similar experiments on tetracene single-crystal transistors did not show the clear linear trend, and the increase in mobility as a function of applied stress was attributed to a better contact between the crystal and substrate [167].

2.6.5 Other single-crystal OFET characteristics

In this paragraph, the most important other features specifically observed in single-crystal OFETs for the first time as well will be highlighted.

Hall conductivity

One of the successful achievements of developing high-mobility single-crystal OFET devices is the demonstration of the Hall effect in rubrene single-crystal transistors, independently reported in 2005 by Podzorov *et al.* [78] and Takeya *et al.* [168]. In the Hall effect, a voltage across the conducting channel is induced by applying a magnetic field perpendicular to the channel [169]. The origin of this effect is the Lorentz force, which is proportional to the microscopic velocity of the charge carrier propagating along the channel in a transverse magnetic field; *i.e.* from the velocity of charge carriers that are transported 'freely' along the band. A charge carrier hopping between trap sites, on the other hand, does not have a classic velocity, and thus will not sense the Lorentz force (apart from quantum interference mechanisms [170]). For trapped carriers, the Lorentz force is zero as well, and therefore trapped carriers also do not contribute to the Hall signal. Thus, the Hall mobility μ_H is the intrinsic, trap-free mobility μ_0, even if considerable trapping occurs.

As a result, it is strongly evidenced that intrinsic band-like transport is indeed realized for the charge carriers generated in organic single-crystals with highly overlapping π-orbitals between the molecules [31,48,82]. The Hall mobility μ_H continues to increase with decreasing temperature, even at low temperature, in contrast to the mobility μ from field-effect measurements [78]. At high temperatures, μ_H and μ are approximately the same and both increase upon cooling. Therefore, charge transport can be considered intrinsic within this temperature range. At low temperatures, μ decreases, indicating the crossover from band-like transport to thermally activated transport. As proof of its intrinsic nature, the Hall mobility μ_H, on the other hand, keeps increasing with decreasing temperature down to ~150 K; at even lower temperatures, the measurements were hindered by too much noise.

Photo-induced processes

Surprisingly, not so much is known about photo-induced effects in OFETs [171,172], although organic transistors are intended to be operated in the backplane driving circuitry in OLED displays [173]. Again, single-crystals with a low density of defects are the ideal model systems to investigate the intrinsic photoinduced processes at organic surfaces and interfaces [31].

Several light-induced effects have been observed using rubrene single-crystal transistors. Podzorov *et al.* [174] observed switching from an off-state into a persistent on-state by a short pulse of light in back-gated rubrene single-crystal devices, caused by additional carriers photogenerated in the bulk. In semitransparent front-gated rubrene devices, they observed a shift of the threshold voltage, due to a photoinduced charge transfer across the interface of the ordered crystal and the disordered gate insulator [116]. Later studies using time-resolved photoluminescence and measuring conductivity induced by short light pulses provided more information on charge-carrier excitation mechanisms, their mobility, and lifetimes [165,175-176].

Electroluminescence

Electroluminescence in organic thin film transistors has been demonstrated for conjugated small-molecules [177] in 2003, and later also for polymers [73,178]. In these devices, the light emission is due to recombination radiation in the channel and can be controlled with the gate bias. Since the discovery of this novel class of multi-functional organic devices, namely the *organic light-emitting field-effect transistor* (OLET, see figure 2.13), the integration of a light source (LED) and a switching function (FET) in one device gained considerable attention [179]. OLET devices require an ambipolar operation with a high electron and hole mobility, and a balanced injection of both carriers. Therefore, organic single-crystals with a low density of traps offer a unique opportunity to realize the ambipolar operation with a relatively high mobility of both types of carriers, and enable the investigation of the electroluminescence process in absence of grain boundaries.

The first reported single-crystal OLET was based on a phenylthiophene derivative [180]. However, because hole and electron currents were not balanced in these devices yet, only unipolar *p*-type behavior was observed, even when the device was emitting light. In the first ambi-polar single-crystal OLET, based on rubrene, equally mobile electrons and holes were injected from separate Au and Mg contacts, respectively, and recombined radiatively within

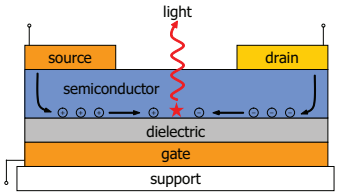

Figure 2.13 *Schematic diagram showing ambipolar light-emitting operation in an OLET, in which holes and electrones are independently injected from opposing electrodes; subsequently, they recombine within the conduction channel, thereby emitting light.*

the channel [150]. By varying the applied voltages, the position of the emission zone could be moved to any position along the channel. Later, electroluminescence in ambipolar tetracene [149], phenylpyrene derivative [151], phenylthiophene derivative [152] and other [153] single-crystal OLETs was demonstrated as well. These experiments demonstrate the theoretical viewpoint, that pure organic semiconductors support electron and hole conduction equally [181].

Organic spintronics

The field of *organic spintronics* is a relatively new research area, in which organic materials are applied to control a spin-polarized signal [182-184]. In spin electronics, the application of the spin (*i.e.* the intrinsic angular moment) of electrons in solid-state devices, instead of or in addition to its charge, is being studied for a new class of electronic devices (*e.g.* the spin-valve). Organic materials attracted attention, as they have a potentially very long spin relaxation time (*e.g.* in the order of microseconds for organic materials *vs.* nanoseconds for metals and low-doped silicon at room temperature), due to their small spin-orbit coupling and weak hyperfine interactions [185-187].

Organic single-crystals are ideal model systems to study the intrinsic spin injection and transport properties in organic materials, due to their high mobility and low impurity density. Recently, Naber *et al.* [188,189] fabricated spin-valve FETs of rubrene single-crystals with ferro-magnetic Co electrodes and Al_2O_3 tunnel barriers for the first time; however, the spin-valve effect could not be realized in combination with the observed FET functionality yet.

Surface and bulk defects

The major factor that determines the record performance of high-quality single-crystal OFETs is their low density of surface defects (*e.g.* the surface density of electronic defects can be less than 10^{10} cm^{-2}, corresponding to distances of ~0.1 µm between defects [19]). Nevertheless, there are many phenomena that can occur at the semiconductor – dielectric interface and thereby affect the electrical characteristics. As the polaronic transport is very sensitive to these phenomena, a few of them will be highlighted in this section.

First of all, the density of defects in the bulk of organic crystals depends on the crystal growth method (see section 2.4). After growing high-quality single-crystals, traps might originate from the tendency of the organic material to react with oxygen and water from the environment, in the presence of light. These defects related to photo-oxidation and other processes will be reviewed and further discussed in chapter 5 of this thesis.

The defects in organic crystals can also be the result of handling the crystals in a high-vacuum environment, in which the crystals are typically stored and handled to prevent

oxidation related processes. In experiments with rubrene and tetracene single-crystal OFETs, it was observed that deep and shallow traps are generated at the crystal surface in vacuum [79]. The trap generation is assigned to the *gauge effect*: interaction of the crystal surface with chemically active species produced by carbon hydrocracking at vacuum gauges or hot surfaces such as heating filaments. As a result, a decrease of the source-drain current was observed in an operating device when the vacuum gauge was turned on.

Defects in the organic semiconductor that act as traps can also be generated during operation of the device. The creation of such defects has been observed in tetracene, perylene, and rubrene single-crystal OFETs with Ta_2O_5 gate dielectric at large gate fields [67]. The defects originated from a leakage current through the gate insulator, and resulted in an irreversible decrease of the current I_D and a substantial increase of the threshold voltage V_T. Most likely, the leakage current at high V_G induced degradation of the molecular material by creating a large density of deep traps.

A controlled X-ray treatment on rubrene single-crystal OFETs showed an increase of the threshold voltage V_T during exposure, and thus an increase in the density of deep traps [19]. By breaking the molecules, X-rays can create defects in organic semiconductors. As the mobility, and its temperature dependence, were not affected by the X-ray irradiation, it was suggested that the created deep traps did not scatter the mobile polarons.

2.7 Concluding Remarks

In this chapter, the fundamentals of organic molecular crystal devices were extensively reviewed. The various techniques to grow ultrapure single-crystals and the possible techniques to fabricate high-quality devices were highlighted. Besides that, the typical characteristics of these organic single-crystal devices were discussed as well, showing this is the best approach to study the intrinsic electronic properties and explore the physical limitations of organic semiconducting materials.

2.8 References

[1] Inokuchi, H.; "The discovery of organic semiconductors: Its light and shadow"; *Org. Electr.*; 7; **2006**; 62-76

[2] Horowitz, G.; "Organic thin film transistors: From theory to real devices"; *J. Mater. Res.*; 19; **2004**; 1946-1962

[3] Nelson, S.F.; Lin, Y.Y.; Gundlach, D.J.; Jackson, T.N.; "Temperature-independent transport in high-mobility pentacene transistors"; *Appl. Phys. Lett.*; 72; **1998**; 1854-1856

[4] Zhu, Z.T.; Mason, J.T.; Dieckmann, R.; Malliaras, G.; "Humidity sensors based on pentacene thin-film transistors"; *Appl. Phys. Lett.*; 81; **2002**; 4643-4645

[5] Ling, M.M.; Bao, Z.; "Thin film deposition, patterning, and printing in organic thin film transistors"; *Chem. Mater.*; 16; **2004**; 4824-4840

[6] Li, D.; Borkent, E.J.; Nortrup, R.; Moon, H.; Katz, H.; Bao, Z.; "Humidity effect on electrical performance of organic thin-film transistors"; *Appl. Phys. Lett.*; 86; **2005**; 042105

[7] Dimitrakopoulos, C.D.; Malenfant, P.R.L.; "Organic thin film transistors for large area electronics"; *Adv. Mater.*; 14; **2002**; 99-117

[8] Horowitz, G.; "Tunneling current in polycrystalline organic thin-film transistors"; *Adv. Funct. Mater.*; 13; **2003**; 53-60

[9] Campbell, I.H.; Smith, D.L.; "Physics of organic electronic devices"; Ch. 1 in Solid state physics"; 55; Ed. Ehrenreich, H.; Spaepen, F.; **2001**; Academic Press; New York, NY, U.S.A.

[10] Podzorov, V.; Pudalov, V.M.; Gershenson, M.E.; "Field-effect transistors on rubrene single crystals with parylene gate insulator"; *Appl. Phys. Lett.*; 82; **2003**; 1739-1741

[11] Podzorov, V.; Sysoev, S.E.; Loginova, E.; Pudalov, V.M.; Gershenson, M.E.; "Single-crystal organic field effect transistors with the hole mobility ~8 cm^2/Vs"; *Appl. Phys. Lett.*; 83; **2003**; 3504-3506

[12] Boer, R.W.I. de; Klapwijk, T.M.; Morpurgo, A.F.; "Field-effect transistors on tetracene single crystals"; *Appl. Phys. Lett.*; 83; **2003**; 4345-4347

[13] Boer, R.W.I. de; Gershenson, M.E.; Morpurgo, A.F.; Podzorov, V.; "Organic single-crystal field-effect transistors"; *Phys. Stat. Sol. A*; 201; **2004**; 1302-1331

[14] Takeya, J.; Goldmann, C.; Haas, S.; Pernstich, K.P.; Ketterer, B.; Batlogg, B.; "Field-induced charge transport at the surface of pentacene single crystals: a method to study charge dynamics of two-dimensional electron systems in organic crystals"; *J. Appl. Phys.*; 94; **2003**; 5800-5804

[15] Butko, V.Y.; Chi, X.; Lang, D.V.; Ramirez, A.P.; "Field-effect transistor on pentacene single crystal"; *Appl. Phys. Lett.*; 83; **2003**; 4773-4775

[16] Sundar, V.; Zaumseil, J.; Podzorov, V.; Menard, E.; Willett, R.L.; Someya, T.; Gershenson, M.E.; Rogers, J.A.; "Elastomeric transistor stamps: reversible probing of charge transport in organic crystals"; *Science*; 303; **2004**; 1644-1646

[17] Goldmann, C.; Haas, S.; Krellner, C.; Pernstich, K.P.; Grundlach, D.J., Batlogg, B.; "Hole mobility in organic single crystals measured by a 'flip-crystal' field-effect technique"; *J. Appl. Phys.*; 96; **2004;** 2080-2086

[18] Aleshin, A.N.; Lee, J.Y.; Chu, S.W.; Kim, J.S.; Park, Y.W.; "Mobility studies of field-effect transistor structures based on anthracene single crystals"; *Appl. Phys. Lett.*; 84; **2004**; 5383-5385

[19] Podzorov, V.; Menard, E.; Borissov, A.; Kiryukhin, V.; Rogers, J.A.; Gershenson, M.E.; "Intrinsic charge transport on the surface of organic semiconductors"; *Phys. Rev. Lett.*; 93; **2004**; 086602

[20] Menard, E.; Podzorov, V.; Hur, S.H.; Gaur, A.; Gershenson, M.E.; Rogers, J.A.; "High-performance *n*- and *p*-type single-crystal organic transistors with free-space gate dielectric"; *Adv. Mater.*; 16; **2005**; 2097-2101

[21] Stingelin-Stutzmann, N.; Smits, E.; Wondergem, H.; Tanase, C.; Blom, P.; Smith, P.; Leeuw, D. de; "Organic thin-film electronics from vitreous solution-processed rubrene hypereutectics"; *Nat. Mater.*; 4; **2005**; 601-606

[22] Roberson, L.B.; Kowalik, J.; Tolbert, L.M.; Kloc, Ch.; Zeis, R.; Chi, X.; Fleming, R.; Wilkins, C.; "Pentacene disproportionation during sublimation for field-effect transistors"; *J. Am. Chem. Soc.*; 127; **2005**; 3069-3075

[23] Zeis, R.; Besnard, C.; Siegrist, T.; Schlockermann, C.; Chi, X.; Kloc. Ch.; "Field effect studies on rubrene and impurities of rubrene"; *Chem. Mater.*; 18; **2006**; 244-248

[24] Lang, D.V.; Chi, X.; Siegrist, T.; Sergent, A.M.; Ramirez, A.P.; "Amorphouslike density of gap states in single-crystal pentacene"; *Phys. Rev. Lett.*; 93; **2004**; 086802

[25] Pflaum, J.; Niemax, J.; Tripathi, A.K.; "Chemical and structural effects on the electronic transport in organic single crystals"; *Chem. Phys.*; 325; **2006**; 152-159

[26] Jo, S.; Yo, H.; Fujii, A.; Takenaga, M.; "Surface morphologies of anthracene single crystals grown from vapor phase"; *Appl. Surf. Sci.*; 252; **2006**; 3514-3519

[27] Liu, Y.; Tao, X.; Wang, F.; Dang, X.; Zou, D.; Ren, Y.; Jiang, M.; "Efficient non-doped pure blue organic light-emitting diodes based on an asymmetric phenylenevinylene with *cis* double bond"; *Org. Electr.*; 9; **2008**; 609-616

[28] Kirtley, J.R.; Mannhart, J.; "When TTF met TCNQ"; *Nat. Mater.*; 7; **2008**; 520-521

[29] Reese, C.; Bao, Z.; "Organic single-crystal field-effect transistors"; *Mater. Today*; 10; **2007**; 20-27

[30] Gershenson, M.E.; Podzorov, V.; Morpurgo, A.F.; "Colloquium: electronic transport in single-crystal organic transistors"; *Rev. Mod. Phys.*; 78; **2006**; 973-989

[31] Podzorov, V.; "Charge carrier transport in single-crystal organic field-effect transistors"; Ch. 2.1 in "Organic field-effect transistors"; Ed. Bao, Z.; Locklin, J.; **2007**; CRC Press; Taylor & Francis Group; New York, NY, U.S.A.

[32] Mas-Torrent, M.; Hadley, P.; Bromley, S.T.; Ribas, X.; Tarrés, J.; Mas, M.; Molins, E.; Veciana, J.; Rovira, C.; "Correlation between crystal structure and mobility in organic field-effect transistors based on single crystals of tetrathiafulvalene derivatives"; *J. Am. Chem. Soc.*; 126; **2004**; 8546-8553

[33] Kim, D.H.; Han, J.T.; Park, Y.D.; Jang, Y.; Cho, J.H.; Hwang, M.; Cho, K.; "Single-crystal polythiophene microwires grown by self-assembly"; *Adv. Mater.*; 18; **2006**; 719-723

[34] Anthony, J.E.; Eaton, D.L.; Parkin, S.R.; "A road map to stable, soluble, easily crystallized pentacene derivatives"; *Org. Lett.*; 4; **2002**; 15-18

[35] Mannsfeld, S.C.B.; Sharei, A.; Liu, S.; Roberts, M.E.; McCulloch, I.; Heeney, M.; Bao, Z.; "Highly efficient patterning of organic single-crystal transistors from the solution phase"; *Adv. Mater.*; 20; **2008**; 4044-4048

[36] Payne, M.M.; Parkin, S.R.; Anthhony, J.E.; Kuo, C.C.; Jackson, T.N.; "Organic field-effect transistors from solution-deposited functionalized acenes with mobilities as high as 1 cm^2/Vs"; *J. Am. Chem. Soc.*; 127; **2005**; 4986-4987

[37] Moon, H.; Zeis, R.; Borkent, E.J.; Besnard, C.; Lovinger, A.J.; Siegrist, T.; Kloc, Ch.; Bao, Z.; "Synthesis, crystal structure, and transistor performance of tetracene derivatives"; *J. Am. Chem. Soc.*; 126; **2004**; 15322-15323

[38] Karl, N.; "Growth and electrical properties of high purity organic molecular crystals"; *J. Cryst. Growth*; 99; **1990**; 1009-1016

[39] Kloc, Ch.; Simpkins, P.G.; Siegrist, T.; Laudise, R.A.; "Physical vapor growth of centimeter-sized crystals of α-hexathiophene"; *J. Cryst. Growth*; 182; **1997**; 416-427

[40] Laudise, R.A.; Kloc, Ch.; Simpkins, P.G.; Siegrist, T.; "Physical vapour growth of organic semiconductors"; *J. Cryst. Growth*; 187; **1998**; 449-454

[41] Kloc, Ch.; "Single crystal growth of organic semiconductors for field effect applications"; *Proc. SPIE*; 6336; **2006**; 633606

[42] Ullah, A.R.; Micolich, A.P.; Cochrane, J.W.; Hamilton, A.R.; "The effect of temperature and gas flow on the physical vapour growth of mm-scale rubrene crystals for organic FETs"; *Proc. SPIE*; 6800; **2007**; 680005

[43] Horowitz, G.; Bachet, B.; Yassar, A.; Lang, P.; Demanze, F.; Fave, J.L.; Garnier, F.; "Growth and characterization of sexithiophene single crystals"; *Chem. Mater.*; 7; **1995**; 1337-1341

[44] Sondermann, U.; Kutoglu, A.; Bässler, H.; "X-ray diffraction study of the phase transition in crystalline tetracene"; *J. Phys. Chem.*; 89; **1985**; 1735-1741

[45] Reese, C.; Chung, W.J.; Ling, M.M.; Roberts, M.; Bao, Z.; "High-performance microscale single-crystal transistors by lithography on an elastomer dielectric"; *Appl. Phys. Lett.*; 89; **2006**; 202108

[46] Mattheus, C.C.; Polymorphism and electronic properties of pentacene; PhD Thesis; **2002**; University of Groningen; Groningen, The Netherlands

[47] Dabestani, R.; Nelson, R.; Sigman, M.E.; "Photochemistry of tetracene adsorbed on dry silica: products and mechanism"; *Photochem. Photobio.*; 64; **1996**; 80-86

[48] Xia, Y.; Fabrication and characterization of organic single crystal and printed polymer transistors; PhD Thesis; **2009**; University of Minesota; Minesota, MN, U.S.A.

[49] Miyamoto, S.; Shimada, T.; Ohtomo, M.; Chikamatsu, A.; Hasegawa, T.; "Direct observation of gas phase nucleation during physical vapor transport growth of organic single crystals using a transparent furnace"; *Jap. J. Appl. Phys.*; 48; **2009**; 118003

[50] Zeis, R.; Siegrist, T.; Kloc, Ch.; " Single-crystal field-effect transistors based on copper phthalocyanine"; *Appl. Phys. Lett.*; 86; **2005**; 022103

[51] Niemax, J.; Tripathi, A.K.; Pflaum, J.; "Comparison of the electronic properties of sublimation- and vapor-Bridgman-grown crystals of tetracene"; *Appl. Phys. Lett.*; 86; **2005**; 122105

[52] Boer, R.W.I. de; Jochemsen, M.; Klapwijk, T.M.; Morpurgo, A.F.; Niemax, J.; Tripathi, A.K.; Pflaum, J.; "Space charge limited transport and time of flight measurements in tetracene single crystals: a comparative study"; *J. Appl. Phys.*; 95; **2004**; 1196-1202

[53] Ichikawa, M.; Yanagi, H.; Shimizu, Y.; Hotta, S.; Suganuma, N.; Koyama, T.; Taniguchi, Y.; "Organic field-effect transistors made of epitaxially grown crystals of a thiophene/phenylene co-oligomer"; *Adv. Mater.*; 14; **2002**; 1272-1275

[54] Käfer, D.; Witte, G.; "Growth of crystalline rubrene films with enhanced stability"; *Phys. Chem. Chem. Phys.*; 7; **2005**; 2850-2853

[55] Sigma-Aldrich; 684848 pentacene, sublimed grade, ≥99.9% trace metals basis; www.sigmaaldrich.com; last visited on 24-10-2009

[56] McGhie, A.R.; Garito, A.F.; Heeger, A.J.; "A gradient sublime for purification and crystal growth of organic donor and acceptor molecules"; *J. Cryst. Growth*; 22; **1974**; 295-297

[57] Tang, Q.; Jiang, L.; Tong, Y.; Li, H.; Liu, Y.; Wang, Z.; Hu, W.; Liu, Y.; Zhu, D.; "Micrometer- and nanometer-sized organic single-crystalline transistors"; *Adv. Mater.*; 20; **2008**; 2947-2951

[58] Briseno, A.L.; Tseng, R.J.; Ling, M.M.; Falcao, E.H.L.; Yang, Y.; Wudl, F.; Bao, Z.; "High-performance organic single-crystal transistors on flexible substrates"; *Adv. Mater.*; 18; **2006**; 2320-2324

[59] Mas-Torrent, M.; Durkut, M.; Hadley, P.; Ribas, X.; Rovira, C.; "High mobility of dithiophene-tetrathiafulvalene single-crystal field effect transistors"; *J. Am. Chem. Soc.*; 126; **2004**; 984-985

[60] Mannsfeld, S.C.B.; Locklin, J.; Reese, C.; Roberts, M.E.; Lovinger, A.J.; Bao, Z.; "Probing the anisotropic field-effect mobility of solution-deposited dicyclohexyl-α-quarterthiophene single crystals"; *Adv. Funct. Mater.*; 17; **2007**; 1617-1622

[61] Liu, S.; Wang, W.M.; Briseno, A.L.; Mannsfeld, S.C.B.; Bao, Z.; "Controlled deposition of crystalline organic semi conductors for field-effect-transistor applications"; *Adv. Mater.*; 21; **2009**; 1217-1232

[62] Takahashi, T.; Takenobu, T.; Takeya, J.; Iwasa, Y.; "Ambipolar organic field-effect transistors based on rubrene single crystals"; *Appl. Phys. Lett.*; 88; **2006**; 033505

[63] Briseno, A.L.; Mannsfeld, S.C.B.; Jenekhe, S.A.; Bao, Z.; Xia, Y.; "Introducing organic nanowires transistors"; *Mater. Today*; 11; **2008**; 38-39

[64] Tang, Q.; Li, H. He, W.; Hu, C.; Liu, C.; Chen, K.; Wang, C.; Liu, Y.; Zhu, D.; "Low threshold voltage transistors based on individual single-crystalline submicrometer-sized ribbons of copper phthalocyanine"; *Adv. Mater.*; 18; **2006**; 65-68

[65] Tang, Q.; Li, H.; Song, Y.; Xu, W.; Hu, W.; Jiang, L.; Liu, Y.; Wang, X.; Zhu, D.; "In situ patterning of organic single-crystalline nanoribbons on a SiO_2 surface for the fabrication of various architectures and high-quality transistors"; *Adv. Mater.*; 18; **2006**; 3010-3014

[66] Zaumseil, J.; Someya, T.; Bao, Z.; Loo, Y.L.; Cirelli, R.; Rogers, J.A.; "Nanoscale organic transistors that use source/drain electrodes supported by high resolution rubber stamps"; *Appl. Phys. Lett.*; 85; **2003**; 793-795

[67] Boer, R.W.I. de; Iosad, N.N.; Stassen, A.F.; Klapwijk, T.M.; Morpurgo, A.F.; "Influence of the gate leakage current on the stability of organic single-crystal field-effect transistors"; *Appl. Phys. Lett.*; 86; **2005**; 032103

[68] Stassen, A.F.; Boer, R.W.I. de; Iosad, N.N.; Morpurgo, A.F.; "Influence of the gate dielectric on the mobility of rubrene single-crystals field-effect transistors"; *Appl. Phys. Lett.*; 85; **2004**; 3899-3901

[69] Newman, C.R.; Chesterfield, R.J.; Merlo, J.A.; Frisbie, C.D.; "Transport properties of single-crystal tetracene field-effect transistors with silicon dioxide gate dielectric"; *Appl. Phys. Lett.*; 85; **2004**; 422-424

[70] Pernstich, K.P.; Haas, D.; Oberhoff, D.; Goldmann, C.; Gundlach, D.J.; Batlogg, B.; Rashid, A.N.; Schitter, G.; "Threshold voltage shift in organic field effect transistors by dipole monolayers on the gate insulator"; *J. Appl. Phys.*; 96; **2004**; 6431-6438

[71] Takeya, J.; Nishikawa, T.; Takenobu, T.; Kobayashi, S.; Iwasa, Y.; Mitani, T.; Goldmann, C.; Krellner, C.; Batlogg, B.; "Effects of polarized organosilane self-assembled monolayers on organic single-crystal field-effect transistors"; *Appl. Phys. Lett.*; 85; **2004**; 5078-5080

[72] Takeya, J.; Yamagishi, M.; Tominari, Y.; Hirahara, R.; Nakazawa, Y.; Nishikawa, T.; Kawase, T.; Shimoda, T.; Ogawa, S.; "Very high-mobility organic single-crystal transistors with in-crystal conduction channels"; *Appl. Phys. Lett.*; 90; **2007**; 102120

[73] Chua, L.L.; Zaumseil, J.; Chang, J.F.; Ou, E.C.W.; Ho, P.K.H.; Sirringhaus, H.; Friend, R.H.; "General observation in *n*-type field-effect behaviour in organic semiconductors"; *Nature*; 434; **2005**; 194-199

[74] Takeya, J.; Kato, J.; Hara, K.; Yamagishi, M.; Hirahara, R.; Yamada, K.; Nakazawa, Y.; Ikehata, S.; Tsukagoshi, K.; Aoyahi, Y.; Takenobu, T.; Iwasa, Y.; "In-crystal and surface charge transport of electric-field-induced carriers in organic single-crystal semiconductors"; *Phys. Rev. Lett.*; 98; **2007**; 196804

[75] Kalb, W.L.; Mathis, T.; Haas, S.; Stassen, A.F.; Batlogg, B.; "Organic small molecule field-effect transistors with Cytop^{TM} gate dielectric: eliminating gate bias stress effects"; *Appl. Phys. Lett.*; 90; **2007**; 092104

[76] Uno, M.; Tominari, Y.; Takeya, J.; "Fabrication of high-mobility organic single-crystal field-effect transistors with amorphous fluoropolymer gate insulator"; *Org. Electr.*; 9; **2008**; 753-756

[77] Lee, J.Y.; Roth, S.; Park, Y.W.; "Anisotropic field effect mobility in single crystal pentacene"; *Appl. Phys. Lett.*; 88; **2006**; 252106

[78] Podzorov, V.; Menard, E.; Rogers, J.A.; Gershenson, M.E.; "Hall effect in the accumulation layers on the surface of organic semiconductors"; *Phys. Rev. Lett.*; 95; **2005**; 226601

[79] Podzorov, V.; Menard, E.; Pereversev, S.; Yakshinsky, B.; Madey, T.; Rogers, J.A.; Gershenson, M.E.; "Interaction of organic surfaces with active species in the high-vacuum environment"; *Appl. Phys. Lett.*; 87; **2005**; 093505

[80] Takeya, J.; Yamada, K.; Hara, K.; Shigeto, K.; Tsukagoshi, K.; Ikehata, S.; Aoyagi, Y.; "High-density electrostatic carrier doping in organic single-crystal transistors with polymer gel electrolyte"; *Appl. Phys. Lett.*; 88; **2006**; 112102

[81] Ono, S.; Seki, S.; Hirahara, R.; Tominari, Y.; Takeya, J.; "High-mobility, low-power, and fast-switching organic field-effect transistors with ionic liquids"; *Appl. Phys. Lett.*; 92; **2008**; 103313

[82] Hasegawa, T.; Takeya, J.; "Organic field-effect transistors using single crystals"; *Sci. Technol. Adv. Mater.*; 10; **2009**; 024314

[83] Someya, T.; Pal, B.; Huang, J.; Katz, H.E.; "Organic semiconductor devices with enhanced field and environmental responses for novel applications"; *MRS Bulletin*; 33; **2008**; 690-696

[84] Xia, Y.; Kalihari, V.; Frisbie, C.D.; Oh, N.K.; Rogers, J.A.; "Tetracene air-gap single-crystal field-effect transistors"; *Appl. Phys. Lett.*; 90; **2007**; 162106

[85] Uemura, T.; Hirahara, R.; Tominari, Y.; Ono, S.; Seki, S.; Takeya, J.; "Electronic functionalization of solid-to-liquid interfaces between organic semiconductors and ionic liquids: realization of very high performance organic single-crystal transistors"; *Appl. Phys. Lett.*; 93; **2008**; 263305

[86] Ono, S.; Miwa, K.; Seki, S.; Takeya, J.; "A comparative study of organic single-crystal transistors gated with various ionic-liquid electrolytes"; *Appl. Phys. Lett.*; 94; **2009**; 063301

[87] Mas-Torrent, M.; Hadley, P.; Bromley, S.T.; Crivillers, N.; Veciana, J.; Rovira, C.; "Single-crystal organic field-effect transistors based on dibenzo-tetrathiafulvalene"; *Appl. Phys. Lett.*; 86; **2005**; 012110

[88] Katz, H.E.; Kloc, Ch.; Sundar, V.; Zaumseil, J.; Briseno, A.L.; Bao, Z.; "Field-effect transistors made from macroscopic single crystals of tetracene and related semiconductors on polymer dielectrics"; *J. Mater. Res.*; 19; **2004**; 1995-1998

[89] Briseno, A.L.; Aizenberg, J.; Han, Y.J.; Penkala, R.A.; Moon, H.; Lovinger, A.J.; Kloc, Ch.; Bao, Z.; "Patterned growth of large oriented organic semiconductors single crystals on self-assembled monolayer templates"; *J. Am. Chem. Soc.*; 127; **2005**; 12164-12165

[90] Briseno, A.L.; Mannsfeld, S.C.B.; Ling, M.M.; Liu, S.; Tseng, R.J.; Reese, J.; Roberts, M.E.; Yang, Y.; Wudl, F.; Bao, Z.; "Patterning organic single-crystal transistor arrays"; *Nature*; 444; **2006**; 913-917

[91] Liu, S.; Briseno, A.L.; Mannsfeld, S.C.B.; You, W.; Locklin, J.; Lee, H.W.; Xia, Y.; Bao, Z.; "Selective crystallization of organic semiconductors on patterned templates of carbon nanotubes"; *Adv. Funct. Mater.*; 17; **2007**; 2891-2896

[92] Mannsfeld, S.C.B.; Briseno, A.L.; Liu, S.; Reese, C.; Roberts, M.E.; Bao, Z.; "Selective nucleation of organic single crystals from vapor phase on nanoscopically rough surfaces": *Adv. Funct. Mater.*; 17; **2007**; 3545-3553

[93] Liu, S.; Wang, W.M.; Mannsfeld, C.B.; Locklin, J.; Erk, P.; Gomez, M.; Richter, F.; Bao, Z.; "Solution-assisted assembly of organic semiconducting single crystals on surfaces with patterned wettability"; *Langmuir*; 23; **2007**; 7428-7432

[94] Liu, S.; Mannsfeld, S.C.B.; Wang, W.M.; Sun, Y.S.; Stoltenberg, R.M.; Bao, Z.; "Patterning of α-sexithiophene single crystals with precisely controlled sizes and shapes"; *Chem. Mater.*; 21; **2009**; 15-17

[95] Minari, T.; Kano, M.; Miyadera, T.; Wang, S.D.; Aoyagi, Y.; Tsukagoshi, K.; "Surface selective deposition of molecular semiconductors for solution-based integration of organic field-effect transistors"; *Appl. Phys. Lett.*; 94; **2009**; 093307

[96] Tong, Y.; Tang, Q.; Lemke, H.T.; Moth-Poulsen, K.; Westerlund, F.; Hammershøj, P.; Bechgaard, K.; Hu. W.; Bjørnholm, T.; "Solution-based fabrication of single-crystalline arrays of organic nanowires"; *Langmuir*; 26; **2010**; 1130-1136

[97] Di, C.; Yu, G.; Liu, Y.; Guo, Y.; Sun, X.; Zheng, J.; Wen, Y.; Wu, W.; Zhu, D.; "Selective crystallization of organic semiconductors for high performance organic field-effect transistors"; *Chem. Mater.*; 21; **2009**; 4873-4879

[98] Luo, L.; Liu, G.; Hwang, L.; Cao, X.; Liu, M.; Fu, H.; Yao, J.; "Solution-based patterned growth of rubrene nanocrystals for organic field effect transistors"; *Appl. Phys. Lett.*; 95; **2009**; 263312

[99] Yamada, K.; Takeya, J.; Shigeto, K.; Tsukagoshi, K.; Aoyagi, Y.; Iwasa, Y.; "Charge transport of copper phthalocyanine single-crystal field-effect transistors stable above 100 °C"; *Appl. Phys. Lett.*; 88; **2006**; 122110

[100] Butko, V.Y.; Lashley, J.C.; Ramirez, A.P.; "Low-temperature field-effect in a crystalline organic material"; *Phys. Rev. B*; 72; **2005**; 081312(R)

[101] Zeis, R.; Kloc, Ch.; Takimiya, K.; Kunugi, Y.; Konda, Y.; Niihara, N.; Otsubo, T.; "Single-crystal field-effect transistors based on organic selenium-containing semiconductor"; *Jpn. J. Appl. Phys.*; 44; **2005**; 3712-3714

[102] Jurchescu, O.D.; Baas, J.; Palstra, T.T.M.; "Electronic transport properties of pentacene single crystals upon exposure to air"; *Appl. Phys. Lett.*; 87; **2005**; 052102

[103] Shen, C.; Kahn, A.; "Electronic structure, diffusion, and p-doping at the Au/F_{16}CuPc interface"; *J. Appl. Phys.*; 90; **2001**; 4549-4554

[104] Liu, J.; Guo, T.; Yang, Y.; "Solvation induced morphological effects on the polymer/metal contacts"; *J. Appl. Phys.*; 89; **2001**; 3668-3673

[105] Rep, D.B.A.; Morpurgo, A.F.; Klapwijk, T.M.; "Doping-dependent charge injection into regioregular poly-(3-hexylthiophene)"; *Org. Electr.*; 4; **2003**; 201-207

[106] Kotani, M.; Kakinuma, K.; Yoshimura, M.; Ishii, K.; Yamazaki, S.; Kobori, T.; Okuyama, H.; Kobayashi, H.; Tada, H.; "Charge carrier transport in high purity perylene single crystal studied by time-of-flight measurements and through field effect transistor characteristics"; *Chem. Phys.*; 325; **2006**; 160-169

[107] Xiao, S.; Tang, J.; Beetz, T.; Guo, X.; Tremblay, N.; Siegrist, T.; Zhu, Y.; Steigerwald, M.; Nuckolls, C.; "Transferring self-assembled, nanoscale cables into electrical devices"; *J. Am. Chem. Soc.*; 128; **2006**; 10700-10701

[108] Kim, D.H.; Lee, D.Y.; Lee, H.S.; Lee, W.H.; Kim, Y.H.; Han, J.I.; Cho, K.; "High-mobility organic transistors based on single-crystalline microribbons of triisopropylsilylethynyl pentacene via solution-phase self-assembly"; *Adv. Mater.*; 19; **2007**; 678-682

[109] Zhou, Y.; Liu, W.J.; Ma, Y.; Wang, H.; Qi, L.; Cao, Y.; Wang, J.; Pei, J.; "Single microwire transistors of oligoarenes by direct solution process"; *J. Am. Chem. Soc.*; 129; **2007**; 12386-12387

[110] Sun, Y.; Tan, L.; Jiang, S.; Qian, H.; Wang, Z.; Yan, D.; Di, C.; Wang, Y.; Wu, W.; Yu, G.; Yan, S.; Wang, C.; Hu, W.; Liu, Y.; Zhu, D.; "High-performance transistor based on individual single-crystalline micrometer wire of perylo[1,12-b,c,d]thiophene"; *J. Am. Chem. Soc.*; 129; **2007**; 1882-1883

[111] Jaing, L.; Gao, J.; Wang, E.; Li, H.; Wang, Z.; Hu, W.; Jiang, L.; "Organic single-crystalline ribbons of a rigid "H"-type anthracene derivative and high-performance, short-channel field-effect transistors of individual micro/nanometer-sized ribbons fabricated by an "organic ribbon mask" technique"; *Adv. Mater.*; 20; **2008**; 2735-2740

[112] Li, R.; Jiang, L.; Meng, Q.; Gao, J.; Li, H.; Tang, Q.; He, M.; Hu, W.; Liu, Y.; Zhu, D.; "Micrometer-sized organic single crystals, anisotropic transport, and field-effect transistors of a fused-ring thienoacene"; *Adv. Mater.*; 21; **2009**; 4492-4495

[113] Tang, Q.; Tong, Y.; Li, H.; Ji, Z.; Li, L.; Hu, W.; Liu, Y.; Zhu, D.; "High-performance air-stable bipolar field-effect transistors of organic single-crystalline ribbons with an air-gap dielectric"; *Adv. Mater.*; 20; **2008**; 1511-1515

[114] Tang, Q.; Tong, Y.; Li, H.; Hu, W.; "Air/vacuum dielectic organic single crystalline transistors of copper-hexadecafluorophthalocyanine ribbons"; *Appl. Phys. Lett.*; 92; **2008**; 083309

[115] Szwarc, M.; "The C-H bond energy in toluene and xylenes"; *J. Chem. Phys.*; 16; **1948**; 128-136

[116] Podzorov, V.; Gershenson, M.E.; "Photoinduced charge transfer across the interface between organic molecular crystals and polymers": *Phys. Rev. Lett.*; 95; **2005**; 016602

[117] Gorham, W.F.; "A new, general synthetic method for the preparation of linear poly-p-xylylenes"; *J. Pol. Sci. A. Pol. Chem.*; 4; **1966**; 3027-3039

[118] Boer, R.W.I. de; Morpurgo, A.F.; "Influence of surface traps on space-charge limited current"; *Phys. Rev. B*; 72; **2005**; 073207

[119] Jurchescu, O.D.; Popinciuc, M.; Wees, B.J. van; Palstra, T.T.M.; "Interface-controlled, high-mobility organic transistors"; *Adv. Mater.*; 19; **2007**; 688-692

[120] Warta, W.; Stehle, R.; Karl, N.; "Ultrapure, high mobility organic photoconductors"; *Appl. Phys. A*; 36; **1985**; 163-171

[121] Warta, W.; Karl, N.; "Hot holes in naphthalene: high, electric-field-dependent mobilities"; *Phys. Rev. B*; 32; **1985**; 1172-1182

[122] Karl, N.; "Charge-carrier mobility in organic crystals"; Ch. 8 in Organic electronic materials; Ed. Farchioni, R.; Grosso, G.; **2001**; 283-326; Springer-Verlag; Berlin, Germany

[123] Karl, N.; Kraft, K.H.; Marktanner, J.; Münch, M.; Schatz, F.; Stehle, R.; Uhde, H.M.; "Fast electronic transport in organic molecular solids?"; *J. Vac. Sci. Technol. A*; 17; **1999**; 2318-2328

[124] Karl, N.; Marktanner, J.; "Electron and hole mobilities in high purity anthracene single crystals"; *Mol. Cryst. Liq. Cryst.*; 355; **2001**; 149-173

[125] Hannewald, K.; Bobbert, P.A.; "Ab initio theory of charge-carrier conduction in ultrapure organic crystals"; *Appl. Phys. Lett.*; 85; **2004**; 1535-1537

[126] Coropceanu, V.; Cornil, J.; Silva Filho, D.A. da; Olivier, Y.; Silby, R.; Brédas, J.L.; "Charge transport in organic semiconductors"; *Chem. Rev.*; 107; **2007**; 926-952

[127] Mark, P.; Helfrich, W.; "Space-charge-limited currents in organic crystals"; *J. Appl. Phys.*; 33; **1962**; 205-215

[128] Reynaert, J.; Arkhipov, V.I.; Borghs, G.; Heremans, P.; "Current–voltage characteristics of a tetracene crystal: space charge or injection limited conductivity?"; *Appl. Phys. Lett.*; 85; **2004**; 603-605

[129] Podzorov, V.; Sysoev, S.E.; Loginova, E.; Pudalov, V.M.; Gershenson, M.E.; "Single-crystal organic field effect transistors with the hole mobility ~8 cm^2/Vs"; *Appl. Phys. Lett.*; 83; **2003**; 3504-3506

[130] Chi, X.; Besnard, C.; Thorsmolle, V.K.; Butko, V.Y.; Taylor, A.J.; Siegrist, T.; Ramirez, A.P.; "Structure and transport properties of the charge-transfer salt coronene-TCNQ"; *Chem. Mater.*; 16; **2005**; 5751-5755

[131] Reynaert, J.; Poot, K.; Arkhipov, V.; Borghs, G.; Heremans, P.; "Effect of surface localized states on conductivity in an organic crystal"; *J. Appl. Phys.*; 97; **2005**; 063711

[132] Mattheus, C.C.; Dros, A.B.; Baas, J.; Oostergetel, G.T.; Meetsma, A.; Boer, J.L. de; Palstra, T.T.M.; "Identification of polymorphs of pentacene"; *Synt. Met.*; 138; **2003**; 475-481

[133] Jurchescu, O.D.; Molecular organic semiconductors for electronic devices; PhD Thesis; **2006**; University of Groningen; Groningen, The Netherlands

[134] Jurchescu, O.D.; Baas, J.; Palstra, T.T.M.; "Effect of impurities on the mobility of single crystal pentacene"; *Appl. Phys. Lett.*; 84; **2004**; 3061-3063

[135] Jurchescu, O.D.; Palstra, T.T.M.; "Crossover from one- to two-dimensional space-charge-limited conduction in pentacene single crystals"; *Appl. Phys. Lett.*; 88; **2006**; 122101

[136] Braga, D.; Battaglini, N.; Yassar, A.; Horowitz, G.; Campione, M.; Sassella, A.; Borghesi, A.; "Bulk electrical properties of rubrene single-crystals: measurements and analysis"; *Phys. Rev. B*; 77; **2008**; 115205

[137] Sze, S.M.; Physics of semiconductor devices; **1981**; Wiley-Interscience; New York, NY, U.S.A.

[138] Chwang, A.B.; Frisbie, C.D.; "Field effect transport measurements on single grains of sexithiophene: role of contacts"; *J. Phys. Chem. B*; 104; **2000**; 12202-12209

[139] Zaumseil, J.; Baldwin, K.W.; Rogers, J.A.; "Contact resistance in organic transistors that use source and drain electrodes formed by soft contact lamination"; *J. Appl. Phys.*; 93; **2003**; 6117-6124

[140] Hulea, I.N.; Russo, S.; Molinari, A.; Morpurgo, A.F.; "Reproducible low contact resistance in rubrene single-crystal field-effect transistors with nickel electrodes"; *Appl. Phys. Lett.*; 88; **2006**; 113512

[141] Molinari, A.; Gutiérrez, I.; Hulea, I.N.; Russo, S.; Morpurgo, A.F.; "Bias-dependent contact resistance in rubrene single-crystal field-effect transistors"; *Appl. Phys. Lett.*; 90; **2007**; 212103

[142] Molinari, A.S.; Gutiérrez Lezama, I.; Parisse, P.; Takenobu, T.; Iwasa, Y.; Morpurgo, A.F.; "Quantitative analysis of electronic transport through weakly coupled metal/organic interfaces"; *Appl. Phys. Lett.*; 92; **2008**; 133303

[143] Horowitz, G.; Hajlaoui, M.E.; Hajlaoui, R.; "Temperature and gate voltage dependence of hole mobility in poly-crystalline oligothiophene thin film transistors"; *J. Appl. Phys.*; 87; **2000**; 4456-4463

[144] Vissenberg, M.C.J.M.; Matters, M.; "Theory of the field-effect mobility in amorphous organic transistors"; *Phys. Rev. B*; 57; **1998**; 12964-12967

[145] Silva Filho, D.A. da; Kim, E.G.; Brédas, J.L.; "Transport properties in the rubrene crystal: electronic coupling and vibrational reorganization energy"; *Adv. Mater.*; 17; **2005**; 1072-1076

[146] Tang, Q.; Li, H.; Liu, Y.; Hu, W.; "High-performance air-stable *n*-type transistors with an asymmetrical device configuration based on organic single-crystalline submicrometer/nanometer ribbons"; *J. Am. Chem. Soc.*; 128; **2006**; 14634-14639

[147] Boer, R.W.I. de; Stassen, A.F.; Craciun, M.F.; Mulder, C.L.; Molinari, A.; Rogge, S.; Morpurgo, A.F.; "Ambipolar Cu- and Fe-phthalocyanine single-crystal field-effect transistors"; *Appl. Phys. Lett.*; 86; **2005**; 262109

[148] Takenobu, T.; Watanabe, K.; Yomogida, Y.; Shimotani, H.; Iwasa, Y.; "Effect of postannealing on the performance of pentacene single-crystal ambipolar transistors"; *Appl. Phys. Lett.*; 93; **2008**; 073301

[149] Takenobu, T.; Bisri, S.Z.; Takahashi, T.; Yahiro, M.; Adachi, C.; Iwasa, Y.; "High current density in light-emitting transistors of organic single crystals"; *Phys. Rev. Lett.*; 100; **2008**; 066601

[150] Takahashi, T.; Takenobu, T.; Takeya, J.; Iwasa, Y.; "Ambipolar light-emitting transistors of a tetracene single crystal"; *Adv. Funct. Mater.*; 17; **2007**; 1623-1628

[151] Bisri, S.Z.; Takahashi, T.; Takenobu, T.; Yahiro, M.; Adachi, C.; Iwasa, Y.; "Ambipolar field-effect transistor of high photoluminescent material tetraphenylpyrene (TPP_Y) single crystal"; *Jpn. J. Appl. Phys.*; 46; **2007**; L596-L598

[152] Bisri, S.Z.; Takenobu, T.; Yomogida, Y.; Shimotani, H.; Yamao, T.; Hotta, S.; Iwasa, Y.; "High mobility and luminescent efficiency in organic single-crystal light-emitting transistors"; *Adv. Funct. Mater.*; 19; **2009**; 1728-1735

[153] Nakanotani, H.; Kabe, R.; Yahiro, M.; Takenobu, T.; Iwasa, Y.; Adachi, C.; "Blue-light-emitting ambipolar field-effect transistors using an organic single crystal of 1,4-bis(4-methylstyryl)benzene"; *Appl. Phys. Express*; 1; **2008**; 091801

[154] Brédas, J.L.; Calbert, J.P.; Silva Filho, D.A. da; Cornil, J.; "Organic semiconductors: a theoretical characterization of the basic parameters governing charge transport"; *Proc. Nat. Acad. Sci.*; 99; **2002**; 5804-5809

[155] Cheng, Y.C.; Silbey, R.J.; Silva Filho, D.A. da; Calbert, J.P.; Cornil, J.; Brédas, J.L.; "Three-dimensional band structure and bandlike mobility in oligoacene single crystals: a theoretical investigation"; *J. Chem. Phys.*; 118; **2003**; 3764-3774

[156] Wijs, G.A. de; Mattheus, C.C.; Groot, R.A. de; Palstra, T.T.M.; "Anisotropy of the mobility of pentacene from frustration"; *Synth. Met.*; 139; **2003**; 109-114

[157] Ling, M.M.; Reese, C.; Briseno, A.L.; Bao, Z.; "Non-destructive probing of the anisotropy of field-effect mobility in the rubrene single crystal"; *Synth. Met.*; 157; **2007**; 257-260

[158] Anthony, J.E.; Brooks, J.S.; Eaton, D.L.; Parkin, S.R.; "Functionalized pentacene: improved electronic properties from control of solid-state order"; *J. Am. Chem. Soc.*; 123; **2001**; 9482-9483

[159] Uno, M.; Tominari, Y.; Yamagishi, Doi, I.; Miyazaki, E.; Takimiya, K.; Takeya, J.; "Moderately anisotropic field-effect mobility in dinaphto[2,3-b:2′,3′-f]thiopheno[3,2-b]thiophenes single-crystal transistors"; *Appl. Phys. Lett.*; 94; **2009**; 223308

[160] Hulea, I.N.; Fratini, S.; Xie, H.; Mulder, C.L.; Iossad, N.N.; Rastelli, G.; Ciuchi, S.; Morpurgo, A.F.; "Tunable Fröhlich polarons in organic single-crystal transistors"; *Nat. Mater.*; 5; **2006**; 982-986

[161] Veres, J.; Ogier, S.D.; Leeming, S.W.; Cupertino, D.C.; Khaffaf, S.M.; "Low-*k* insulators as the choice of dielectrics in organic field-effect transistors"; *Adv. Funct. Mater.*; 13; 2003; 199-204

[162] Fratini, S.; Xie, H.; Hulea, I.N.; Ciuchi, S.; Morpurgo, A.F.; "Current saturation and coulomb interactions in organic single-crystal transistors"; *New J. Phys.*; 10; **2008**; 033031

[163] Kirova, N.; Bussac, M.N.; "Self-trapping of electrons at the field-effect junction of a molecular crystal"; *Phys. Rev. B*; 68; **2003**; 235312

[164] Houili, H.; Picon, J.D.; Zuppiroli, L.; Bussac, M.N.; "Polarization effects in the channel of an organic field-effect transistor"; *J. Appl. Phys.*; 100; **2006**; 023702

[165] Rang, Z.; Nathan, M.I.; Ruden, P.P.; Podzorov, V.; Gershenson, M.E.; Newman, C.R.; Frisbie, C.D.; "Hydrostatic pressure dependence of charge carrier transport in single-crystal rubrene devices"; *Appl. Phys. Lett.*; 86; **2005**; 123501

[166] Wang, L.J.; Li, Q.K.; Shuai, Z.; "Effects of pressure and temperature on the carrier transport in organic crystal: a first-principles study"; *J. Chem. Phys.*; 128; **2008**; 194706

[167] Nisikawa, T.; Moriguchi, N.; Anezaki, T.; Unno, A.; Tachibana, M.; Kojima, K.; "Contact pressure dependence of carrier mobility in cleaved tetracene single-crystal field-effect transistors"; *Jpn. J. Appl. Phys.*; 45; **2006**; 5238-5240

[168] Takeya, J.; Tsukagoshi, K.; Aoyagi, Y.; Takenobu, T.; Iwasa, Y.; "Hall effect of quasi-hole gas in organic single-crystal transistors"; *Jpn. J. Appl. Phys.*; 44; **2005**; L1393-L1396

[169] Pope, M.; Swenberg, C.E.; Electronic processes in organic crystals and polymers; **1999**; 2nd ed.; Oxford university press; New York, NY, U.S.A.

[170] Friedman, L.; Pollak, M.; "Hall mobility due to hopping-type conduction in disordered systems"; *Phil. Mag. B*; 38; **1978**; 173-189

[171] Narayan, K.S.; Kumar, N.; "Light responsive polymer field-effect transistor"; *Appl. Phys. Lett.*; 79; **2001**; 1891-1893

[172] Saragi, T.P.I.; Puzich, R.; Fuhrmann, T.; Salbeck, J.; "Organic phototransistor based on intramolecular charge transfer in a bifunctional spiro compound"; *Appl. Phys. Lett.*; 84; **2004**; 2334-2336

[173] Forrest, S.R.; "The path to ubiquitous and low cost organic electronic appliances on plastic"; *Nature*; 428; **2004**; 911-918

[174] Podzorov, V.; Pudalov, V.M.; Gershenson, M.E.; "Light-induced switching in back-gated organic transistors with built-in conduction channel"; *Appl. Phys. Lett.*; 85; **2004**; 6039-6041

[175] Najafov, H.; Biaggio, I.; Podzorov, V.; Calhoun, M.F.; Gershenson, M.E.; "Primary photoexcitations and the origin of the photocurrent in rubrene single crystals"; *Phys. Rev. Lett.*; 96; **2006**; 056604

[176] Najafov, H.; Lyu, B.; Biaggio, I.; Podzorov, V.; "Investigating the origin of the high photoconductivity of rubrene single crystals"; *Phys. Rev. B*; 77; **2008**; 125202

[177] Hepp, A.; Heil, H.; Weise, W.; Ahles, M.; Schmechel, R.; Seggern, H. von; "Light-emitting field-effect transistor based on a tetracene thin film"; *Phys. Rev. Lett.*; 91; **2003**; 157406

[178] Zaumseil, J.; Friend, R.H.; Sirringhaus, H.; "Spatial control of the recombination zone in an ambipolar light-emitting organc transistor"; *Nat. Mater.*; 5; **2006**; 69-74

[179] Cicoira, F.; Santato, C.; "Organic light emitting field effect transistors: advances and perspectives"; *Adv. Funct. Mater.*; 17; **2007**; 3421-3434

[180] Nakamura, K.; Ichikawa, M.; Fushiki, R.; Kamikawa, T.; Inoue, M.; Koyama, T.; Taniguchi, Y.; "Light emission from organic single-crystal field-effect transistors"; *Jpn. J. Appl. Phys.*; 44; **2005**; L1367-L1369

[181] Karl, N.; "Charge carrier transport in organic semiconductors"; *Synth. Met.*; 133-134; **2003**; 649-657

[182] Naber, W.J.M.; Faez, S.; Wiel, W.G. van der; "Organic spintronics"; *J. Phys. D: Appl. Phys.*; 40; **2007**; R205-R228

[183] Szulczewski, G.; Sanvito, S.; Coey, M.; "A spin of their own"; *Nat. Mater.*; 8; **2009**; 693-695

[184] Dediu, V.A.; Hueso, L.E.; Bergenti, I.; Taliani, C.; "Spin routes in organic semiconductors"; *Nat. Mater.*; 8; **2009**; 707-717

[185] Zutic, I.; Fabian, J.; Sarma, S. das; "Spintronics: fundamentals and applications"; *Rev. Mod. Phys.*; 76; **2004**; 323-410

[186] Krinichnyi, V.I.; "2-mm waveband electron paramagnetic resonance spectroscopy of conducing polymers"; *Synth. Met.*; 108; **2000**; 173-222

[187] Jedema, F.J.; Filip, A.T.; Wees, B.J. van; "Electrical spin injection and accumulation at room temperature in an all-metal mesoscopic spin valve"; *Nature*; 410; **2001**; 345-348

[188] Naber, W.J.M.; Craciun, M.F.; Lemmens, J.H.J.; Arkenbout, A.H.; Palstra, T.T.M.; Morpurgo, A.F.; Wiel, W.G. van der; "Controlled tunnel-coupled ferromagnetic electrodes for spin injection in organic single-crystal transistors"; *Org. Electr.*; 11; **2010**; 743-747

[189] Naber, W.J.M.; Electron transport and spin phenomena in hybrid organic/inorganic systems; PhD Thesis; **2010**; University of Twente; Enschede, The Netherlands

Chapter 3

Fabrication and Characterization of Thin Films and Devices

Chapter 3: Fabrication and Characterization of Thin Films and Devices

Abstract

Fabrication of high-quality devices on organic single-crystals demands a high control on the deposition and patterning techniques applied, as well as on the variety of measuring tools used to obtain information on the structural and electrical properties of the substrate and the fabricated thin films, patterns and devices.

3.1 Introduction

The fabrication of high-quality devices requires a high control on deposition, thin film growth, and patterning, as well as on characterization of the structural and electrical properties of the substrate and fabricated devices. All these various aspects will be covered in this chapter.

This chapter is divided in two parts. In the first part, the techniques that have been used to grow thin films, to deposit patterned structures, and to fabricate devices will be described. Here, pulsed laser deposition (PLD) in combination with (quasi-dynamic) patterning through stencils is used in the fabrication process. The basic principles of the PLD process will be described in paragraph 3.2, together with a description of the experimental set-up. Paragraph 3.3 will discuss the basic principles of stencil patterning and its limitations, like clogging and blurring. The experimental details of the stencil design and fabrication, and the *in situ* fabrication of (field-effect) devices are presented as well.

The second part of this chapter focuses on the measuring tools used to obtain information about the structural and electrical properties of the substrate and the fabricated patterns and devices. In paragraph 3.4, the first group of analysis techniques characterizes the structural properties and chemical composition of the samples, and includes optical microscopy (OM), scanning probe microscopy (SPM), scanning electron microscopy (SEM), X-ray diffraction (XRD) and X-ray photoelectron spectroscopy (XPS). The second group describes the electrical transport properties: the generally applied settings and specifications of the used probe stations are detailed in paragraph 3.5. Special focus is on the measuring of organic molecular crystal devices with the nano probing system.

3.2 Thin Film Growth by Pulsed Laser Deposition

Pulsed laser deposition is intrinsically a straightforward technique for depositing thin films, based on the evaporation of material by heating with an intense pulsed laser beam. PLD is a powerful tool for thin film research, as almost all deposition parameters can be controlled independently over a wide range. Most important for this work is that the ablated species can be tuned over a large kinetic energy range, enabling deposition on the fragile organic molecular crystal substrates at room temperature; this will be further treated in Chapter 6.

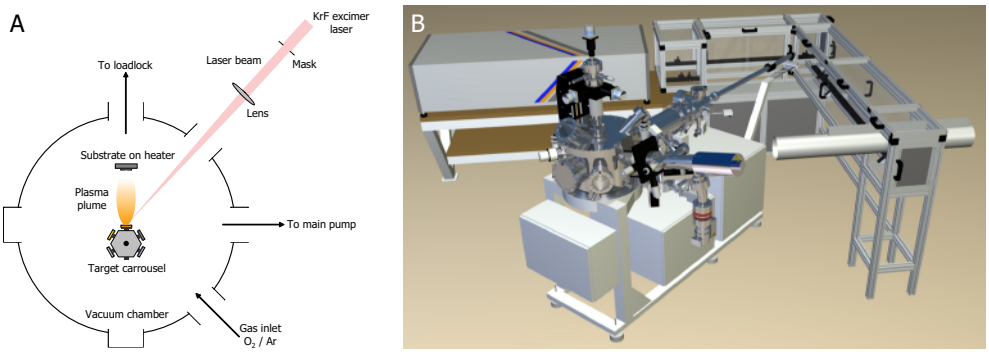

Figure 3.1 *Pulsed-laser deposition. A) Schematic working principle. B) Experimental PLD set-up.*

3.2.1 Historical overview

The development of pulsed laser deposition can be marked by a few events, starting by the high-power ruby laser becoming available in the beginning of the sixties [1]. The first pulsed laser experiments to deposit thin films were carried out in 1965 [2], three years after the initial studies on laser-evaporation and excitation of atoms from solid surfaces [3]. The first major breakthrough came in the mid-1970s, when the electronic Q-switch enabled short pulses with high peak power density, broadening the scope of materials available for deposition and improving the thin film quality [4]. However, PLD remained little known until the second major breakthrough in 1987 [5,6], when the successful growth of high-T_c superconducting films showed PLD is able to grow high-quality thin films of complex oxide materials (like $YBa_2Cu_3O_{7-x}$) superior to other techniques.

The last two decades, PLD has evolved from an academic 'curiosity' into a broadly applicable technique for thin film deposition research, and is used in the deposition of all kinds of materials (*e.g.* insulators, semiconductors, metals, polymers, organic molecules and even biological materials) [7,8]. Also, use of PLD to synthesize nano-structures (*e.g.* carbon nanotubes [9], nanopowders [10] and quantumdots [11]) has been reported.

3.2.2 Basic principles

Pulsed laser deposition is a physical vapor deposition technique based on the evaporation of material from the source material by heating with an intense pulsed laser beam, carried out in a vacuum system, see figure 3.1A [7,8,12]. The lasers most commonly used in thin film fabrication are pulsed gas excimer lasers (ArF (193 nm), KrF (248 nm), XeCl (308 nm)) and solid-state Nd:YAG lasers (266 and 355 nm). In order to get the required energy, the laser pulses are focused by a lens onto the source material (called the target). Irrespective of the laser used, the absorbed beam energy is converted into thermal energy, causing extreme heating of a small target volume. The locally heated source material evaporates within nano-seconds (without forming a melt phase) into a plasma; this process is called ablation. Further laser heating of the evaporated species creates a high-density plasma plume that expands forwards perpendicular to the target surface into the vacuum chamber. These high energetic particles may interact and/or react with the background gas, if present. When a substrate is placed inside or near the plasma plume opposite to the target, a part of the evaporated material will adsorb on this substrate and form a thin film.

3.2.3 Advantages and disadvantages

Important parameters for the PLD process are the laser fluence (energy per pulse per unit area), the laser frequency, the laser spot size, the target-to-substrate distance, the background gas composition and pressure, and the substrate temperature. The direct influence of these parameters on the thin film quality gives PLD the advantages that it has over other physical vapor deposition techniques. Some of the advantages are:

- Compatibility with background gas pressures ranging from ultra-high vacuum (UHV) to 1 mbar. The kinetic energy of the arriving particles can be controlled by the gas pressure and composition, enabling deposition on fragile organic and polymer substrates.

- Compatibility with substrate temperatures ranging from below room temperature to hundreds of degrees Celsius. As the energy source (the laser) is located outside the deposition system, there is no transfer of excessive process heat to the substrate, except the kinetic and thermal energy transferred by the arriving species.
- The parameters can almost all be controlled independently over a wide range. Although there are quite some 'knobs' to turn on, optimization is easy and can be done quickly.
- High instant deposition rates (typical 0.01 nm/pulse [13]; but ranging from 0.0001 to 0.1 nm/pulse [8]). Due to the pulsed nature of the laser, this material is transferred only in the very short duration of a plasma pulse, instead of continuously. The growth takes place in between subsequent pulses at a much longer time scale than the laser frequency.
- Stoichiometric transfer of material from a multi-component target to the substrate [5].

The first of these advantages is the main reason why PLD is applied as deposition technique in this work. To be comprehensive, PLD also has a few disadvantages, some of these are:

- The poor thickness uniformity of PLD grown thin films, due to the relative small volume of the highly forward-directed plasma plume, limits the substrate size. Although this is no problem for a materials scientist in the lab, the last two decades, however, large-area PLD systems have been developed to enable commercial applications [8,14].
- The ejection of micron-size particles in the ablation process ('droplet formation') is another issue often mentioned. Use of highly dense targets, laser wavelengths that are strongly absorbed by the target and a well-defined laser spotsize on the target by imaging a mask placed in the laser beam tend to reduce or eliminate particle formation.

3.2.4 Experimental setup

Almost all thin films, patterns and devices described in this thesis were fabricated by PLD, see figure 3.1B (Thin Film Laboratory; University of Twente, The Netherlands). The energy source used in the experiments is a Lambda Physik LPX 210 KrF excimer laser (Coherent; Santa Clara, CA, USA) with a wavelength of 248 nm and pulse duration of 25 ns. Maximum pulse energy is 1000 mJ and the repetition rate can be varied from <1 to 100 Hz. The ultra-high vacuum chamber is turbo-molecular pumped and has a base pressure below 10^{-8} mbar.

For the ablation, a small homogenous selection of the laser beam passes through a mask, placed in the central part of the beam profile to keep the spatial energy variation low, and is then focused by a lens (focal length 452 mm) through a window onto a target in the chamber at 45° incidence. For metal depositions, a 98 mm^2 mask containing seven 2×7 mm^2 openings in a vertical row was used; for oxide depositions, a 36 mm^2 mask with six 2×3 mm^2 holes. The laser hits the target surface with a spotsize of 1 to 5 mm^2, depending on the mask and lens positions. The amount of material ablated from the target depends on the energy density, which is varied between 1.0 and 5.0 J/cm^2 by varying the spotsize and laser energy.

During deposition, the targets are scanned in the laser beam by a computer-controlled *xyz*-translation-rotation stage, to distribute ablation over the entire target surface. Five different targets can be placed on the multi-target holder. The substrate holder with heater

is placed, opposing the target, on another computer-controlled *xyz*-translation-rotation stage. The heater can heat up to 950 °C (measured by a thermocouple); of course, for the room temperature depositions the heater is not turned on. Both the target carrousel and the sample holder can be inserted via a loadlock into the system without breaking the vacuum. The target to substrate distance can be controlled between 30 and 80 mm.

The pressure inside the vacuum chamber during deposition (10^{-3} to 10^{0} mbar) is controlled by the pump speed and the gas mass flow rate (0 to 40 ml/min). As background gas, inert argon gas was used during metal depositions and molecular oxygen gas during oxide depositions. Note that the formation of droplets in the deposited films has not been observed at all, due to the optimized deposition parameters.

For practical reasons, all *in situ* field-effect transistor device fabrications using quasi-dynamic stencil deposition (see paragraph 3.3.4) have been performed on a different PLD system than the routinely used system described above. As this system is simpler and less computer-controlled, it gives more freedom in hands-on adjustments and experimental flexibility. In principle, both systems function similarly, though the different design results in some practical differences. This set-up uses a Compex 205 excimer laser (Coherent) as energy source, no load-lock system is present, the vacuum chamber is pumped down to a base pressure of only 10^{-6} mbar, and the targets are rotating during deposition.

3.3 Patterning and Device Fabrication

The patterning technique used in this work to fabricate devices is *stencil deposition*. Most important for this work is that this method requires no photoresist or polymer processing, and thereby eliminates the use of chemical, thermal and etch associated steps during fabrication. Therefore, local deposition on non-conventional surfaces that cannot withstand solvents, like the fragile organic single-crystals, are becoming possible. In this thesis, the combination of stencil deposition and PLD is further referred to as *pulsed laser stencil deposition* [15,16].

3.3.1 Basic principles

The main patterning technique used in this work is stencil deposition (also called shadow mask deposition or stencil lithography). In general, it is a resistless lift-off technique, that can be applied to pattern a wide variety of materials by various deposition techniques on a broad range of surfaces [17-20]. Basic principle is blocking the material flux at certain areas of the substrate during deposition. A direct copy of the structures in the stencils is made on the substrate by depositing material through the micro- and nanometer sized apertures realized in a thin membrane stencil (see figure 3.2).

There are three main modes of operation of stencil deposition: static, quasi-dynamic and dynamic. In the *static* mode, the stencil is fixed relative to a substrate during deposition. In the *quasi-dynamic* mode, the stencil moves relative to the substrate in between depositions, without breaking the vacuum. In case the stencil moves relative to the substrate during deposition, the technique is called *dynamic stencil deposition* (DSD) [21-23].

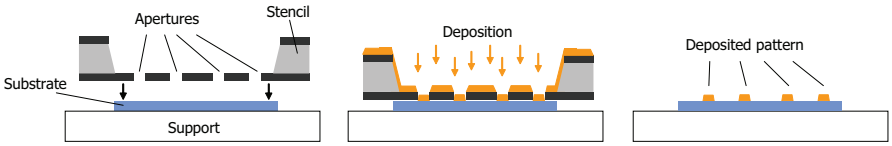

Figure 3.2 *Working principle of stencil deposition. The deposited material is blocked from the substrate on areas shadowed by the stencil mask during deposition.*

3.3.2 Advantages and disadvantages

Stencil deposition as a technique has not been developed with the intention to compete with technologies like photolithography, but is applied in fields where other lithographic techniques are deficient. As an example, photography lift-off techniques cannot be applied at high deposition temperatures (*i.e.* the polymer photoresist cannot withstand the high temperature), whereas the stencil technology is compatible with deposition at these conditions [24]. Advantages of stencil technology include (the first two advantages are the main reason why stencil deposition is used as patterning technique in this work):

- No requirement of polymer resist processing; eliminating the chemical, thermal and etch associated steps enables local deposition on non-conventional surfaces, like polymers [19], organic SAMs [17] or carbon nanotubes [25], without damaging or contaminating them.
- Deposition on non-planar surfaces [17]; stencils can be brought in contact with 3D-objects.
- Minimal number of process steps; this direct deposition technique is less laborious and time-consuming, as one processing step replaces several conventional lithography steps.
- Various sized features can be created in one deposition run; for instance, nanometer-sized device features can be combined with millimeter-sized wiring in one deposition run.
- Stencils can be re-used many times before being clogged and, if needed, some stencil cleaning procedures are present [26,27], making the technique a cost-effective method.

Clogging, blurring and other broadening effects

Like any other patterning technique, the stencil deposition technique has some drawbacks like minimal structure dimensions and loss of resolution [28]. One of the main limitations is aperture clogging (see figure 3.3A). Clogging is the gradual decrease in aperture dimensions due to deposition of material directly inside the apertures, or by surface migration of material deposited on top of the stencil inwards the apertures [29,30]. Clogging has a direct influence on the shape of the resulting patterns and the re-usability of the stencils. The amount of clogging is known to be material dependent (*e.g.* on the diffusive properties of the deposited material), but it is also dependent on the used deposition parameters [16]. To suppress the clogging phenomena, coating stencils with organic SAMs [31,32] or etching procedures [26,27] can be helpful to extend the stencils' lifetime.

Another drawback of stencil deposition is related to the presence of a small gap between the stencil and the substrate, which cannot be controlled and results in loss of resolution due to blurring of the patterns called broadening (see figure 3.3B) [16]. Although the stencil is brought in physical contact with the substrate, a gap between stencil and substrate is

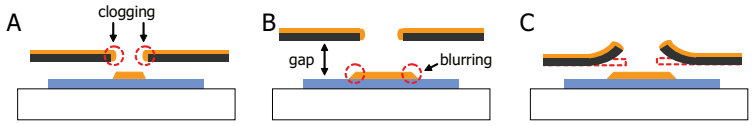

Figure 3.3 *A) Schematic representation of the limitations of stencil deposition: A) clogging of the stencils, B) blurring due to the gap present, and C) stencil deformation due to deposition-induced stress.*

unavoidable. This gap is caused by bending of the membrane, misalignment and curvature of the substrate and stencil, and is assumed to be ~1 µm after proper alignment in the static mode [16]. Two main types of broadening are distinguished. First, the effect of propagation of the material flux into the areas that are shadowed by the stencil, where one can differentiate between geometrical broadening [19,30] and background gas pressure related broadening (*e.g.* shockwave broadening at high gas pressures) [16]. Secondly, broadening is caused by the transport of material into the shadowed areas after adsorption on the surface, the so-called surface diffusion broadening [16].

In an ideal situation (*e.g.* with no gap present), material is only deposited on the areas of the substrate that are not shadowed from the particle flux by the stencil. After removal of the stencil, isolated patterns of the deposited material are revealed with known feature sizes. However, if no gap would be present, which is occasionally observed for the deposition on non-planar substrates or deposition of thick layers of material, the deposited material would attach the stencil to the substrate. During lift-off, the stencil will then either break and remain on the substrate surface, or the deposited material is lift-off together with the stencil.

One more effect stencil deposition can suffer from is deformation of the stencil due to deposition-induced stresses (see figure 3.3C). As material is deposited on top of the stencil, bending of the membrane can be caused by *e.g.* differences in thermal expansion coefficient, lattice mismatches and recrystallization processes. Bending of the membrane will result in an increase of the substrate-to-stencil gap, and therefore in broadening and blurring of the deposited features. The deformation can be reduced by local mechanical reinforcement [28,33].

3.3.3 Stencil design and fabrication

The main used stencils in this work consist of four 1×1 mm^2 500 nm thick silicon nitride membranes embedded in a 10×10 mm^2 silicon chip (see figure 3.4). Every membrane contains four rows of circular and square apertures, with diameters of 5.6, 14.0, 28.2, 56.5 and 112.8 µm and width sizes of 5.0, 12.5, 25.0, 50.0 and 100.0 µm, respectively. Next to

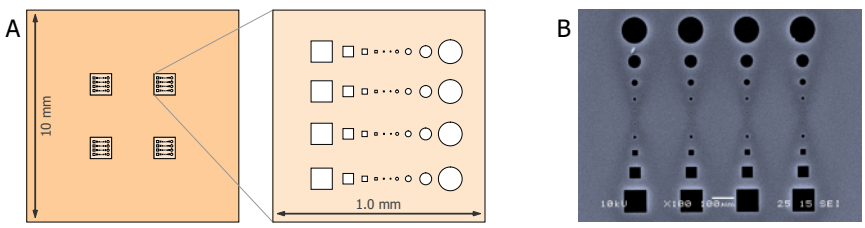

Figure 3.4 *Standard stencil design; A) schematic lay-out, and B) SEM image of one stencil membrane.*

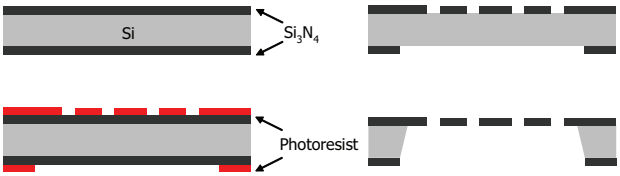

Figure 3.5 *Stencil fabrication procedure (see text for specific details).*

this stencil design, various stencils with another custom design have been used in this work. For the space-charge-limited current experiments, stencil designs with parallel bars have been used (see figure 8.7). Paragraph 3.3.4 describes the stencil design used for the fabrication of complete field-effect transistor structures.

All stencils used in this work have been created by standard UV photolithography and silicon processing, the production procedure described in more detail by van Rijn *et al.* [34]. Figure 3.5 gives a schematic overview of the stencil fabrication procedure. First, a low-stressed Si_3N_4 thin film is deposited on both sides of a [001] oriented silicon wafer by low-pressure chemical vapor deposition. Next, photoresist is structured on the front side to define the stencil membrane apertures, and on the back side to define the silicon support structures. On both sides, the structures in the photoresist are transferred by reactive ion etching into the Si_3N_4 layer. Final step is a KOH wet etch of the back side, along the Si (111) planes, to create a free standing Si_3N_4 membrane.

The fabrication of the stencils used in this work has been carried out by C2V (Enschede, The Netherlands). Also, a few custom-designed stencils have been fabricated at EPFL (Lausanne, Swiss) using the same procedure.

3.3.4 In situ device fabrication

The main method used for stencil deposition is *ex situ* clamping of the stencil on top of the substrate, see figure 3.6A. In this method, the stencil is glued with silver paste onto a stainless steel holder, which is then gently pressed onto the substrate by three screws.

For the fabrication of devices *in situ* with stencil deposition (see ref. [16] for detailed information), the *'quasi-dynamic stencil deposition'* technique is used in this work. In this set-up, the substrate is mounted on a piezo-box inside the apparatus and a stencil is placed in front of the sample (see figure 3.6C). The three-dimensional piezo position system (Piezosystems Jena, Tritor 100; Jena, Germany) can translate the sample over 100 µm in the *x*-, *y*- and *z*-dimensions independently, whereas the stencil position stays fixed. The whole set-up is placed in the PLD vacuum chamber and via electrical connections controlled from outside the system. The system can be used to fabricate quite complex patterns, when combining several deposition steps of various materials and an optimized stencil design. For

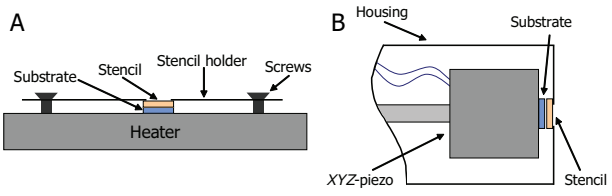

Figure 3.6 *Schematic representation of the two stencil deposition methods used: A) ex situ clamping of a stencil on a substrate, and B) quasi-dynamic stencil deposition set-up.*

example, complete FETs can be fabricated with this technique (see next paragraph). Limitations to this method are broadening effects caused by the small gap between the stencil and sample, and the presence of the stencil in front of the sample during the entire deposition process (*i.e.* a thin film covering the entire substrate cannot be deposited).

In situ field-effect transistor fabrication

Complete field-effect transistors with a top-gate top-contact configuration can be fabricated using the quasi-dynamic stencil deposition set-up. For this, a new stencil lay-out has been designed making use of the acquired freedom in translation during deposition. These stencils were manufactured similar as the stencils described before (paragraph 3.3.3) and the main lay-out is also alike, only the apertures in the four silicon nitride membranes are shaped differently. Lay-out of the stencils designed for preparing complete field-effect transistors is depicted in figure 3.7A. In one deposition series, 16 complete FETs are fabricated through every membrane, leading to a total of 64 devices if all four membranes in a chip are exploited. The aperture dimensions vary between the membranes (see figure 3.7B) and small variations in the orientation of the apertures are incorporated to reduce misalignment issues (*i.e.* the stencil has to be aligned properly by eye to the *xy*-movements of the sample).

The three consecutive deposition steps to fabricate a field-effect transistor are depicted in figure 3.8. In every deposition run, material will be deposited through all four apertures in the membrane; yet in that run only one or two apertures are effectively used for fabricating the device. In the 1st deposition run, the source and drain electrodes are deposited, in the 2nd run the gate dielectric material and in the 3rd run the gate electrode. Between the runs, the sample is transferred over 70 µm in the *x*- or *y*-direction, so that the dielectric gate material will be deposited between the source and drain contacts, and, finally, the gate electrode material on top of the dielectric gate. The result is one top-contact top-gate field-effect transistor, surrounded by eight additional deposited features. Before each deposition, the gap between the substrate and stencil is minimized by transferring the sample in the *z*-direction. After each deposition step, the substrate-stencil gap is maximized first, before transferring the sample in the *x*- or *y*-direction.

3.3.5 Pulsed laser stencil deposition on organic molecular crystals

In paragraph 3.3.2, it was mentioned that the stencils can be brought in contact with *non-planar* substrates. The pentacene single-crystals used in this work are typically not flat and

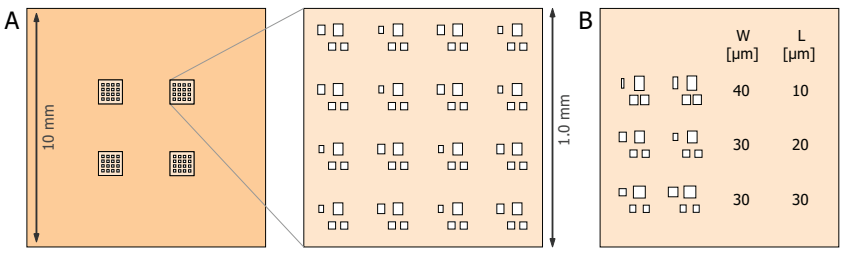

Figure 3.7 *Stencil design for in situ field-effect transistor fabrication.*

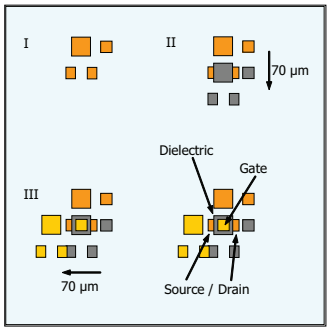

Figure 3.8 *In situ field-effect transistor fabrication via quasi-dynamic stencil deposition.*

Figure 3.9 *Color scale bar applied in all AFM images in this thesis. Height: bottom 0 nm, top Z_{AFM} nm (for Z_{AFM} see image caption).*

have a quite rough surface (on a sub-micrometer scale), which has certain consequences on the success and yield of the transfer of the stencil apertures to the crystal substrate.

Figure 3.10 shows various general experimental aspects of stencil deposition on a pentacene single-crystal substrate. In the areas marked with 'A', a successful direct copy of the structures in the membrane stencil to the substrate has been realized. In the 'B' areas, a continuous film is observed and no individual structures can be identified. When going from 'A' to 'B', an increased loss of resolution due to blurring can be noticed. This geometrical broadening is directly related to an increasing gap between the stencil and substrate (*i.e.* at 'A' the stencil was almost in physical contact with the substrate, whereas at 'B' a quite large gap was present). In the 'D' areas no deposited features are present; the stencil must have been in direct physical contact with the substrate, so that deposited material attached to the stencil and was lifted-off together with the stencil. Finally, in the 'C' area, a thick film is present on the substrate as the stencil membrane broke at this place before the deposition.

Of the other typical stencil deposition drawbacks mentioned in paragraph 3.3.2, aperture clogging or stencil deformation were hardly encountered, as the fragile stencil membranes broke or were replaced before this could become an issue.

The most encountered problem when performing quasi-dynamic stencil depositions on pentacene single-crystals, compared to the static mode, is blurring and broadening of the deposited features, as the gap between the stencil and substrate is less-controlled and exposed to changes between the subsequent depositions. Due to this movement of the stencil relative to the crystal in-between depositions, breakage of the stencil can also occur more easily by coarse features present on the crystal surface.

3.4 Characterization Techniques

Organic crystal substrates, pulsed-laser deposited thin films, patterns and devices created by (quasi-dynamic) stencil deposition have been characterized by a range of techniques, in order to determine the structural properties, chemical composition and functionality of the deposited materials. All analysis measurements were performed in the Thin Film Laboratory (UT, NL) or at the MESA+ Central Materials Analysis Laboratory (UT, NL). This paragraph details the equipments' specifications and generally used settings.

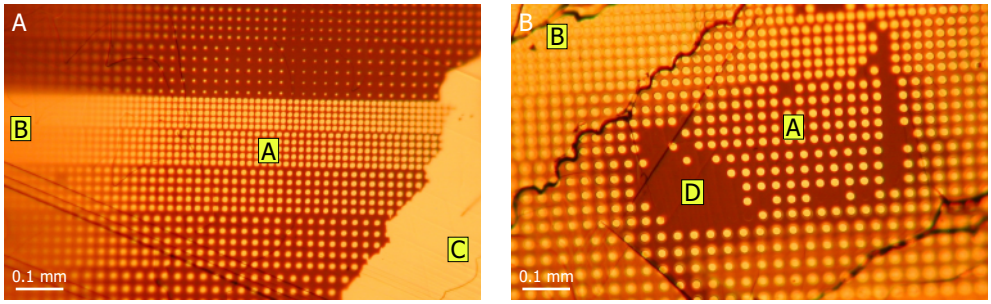

Figure 3.10 *Optical microscopy image of deposited Au-dots, showing various general aspects of stencil deposition on a pentacene single-crystal substrate; A) sharp, well-defined structures, B) thin film, C) thick film and D) no material.*

3.4.1 Optical microscopy

First step in the inspection of organic crystals, deposited patterns and fabricated devices is by means of optical microscopy with polarized light. Optical microscopy (OM) measurements were performed on a Nikon Eclipse ME600L (Nikon; Tokyo, Japan) optical microscope, equipped with a Nikon E990 digital camera.

Anisotropic materials, like the organic conjugated crystals inspected, have optical properties that vary with the orientation of incident light with the crystallographic axes. Visualization of domain structures and presence of stress is possible due to this birefringence of the crystals [35]. Therefore, OM provides a fast and useful first analysis of the crystal quality and simplifies the selection of single-crystals for further processing [36].

3.4.2 Scanning probe microscopy

Atomic force microscopy (AFM) measurements were performed on two AFM systems. Regular measurements were performed on a Multimode SPM (Veeco; Cambridge, UK) equipped with a Nanoscope IV controller (Digital Instruments; Santa Barbara, CA, USA) and a small-scale (16×16 μm^2) *e*-type piezo scanner. Large-area measurements (up to 88×88 μm^2) were performed on a Veeco Dimension Icon AFM system equipped with a Nanoscope V controller and placed on an AVH-100 workstation. Both instruments are capable of imaging in contact mode and tapping mode, revealing surface characteristics such as topography, morphology and surface roughness. If present, friction contrast can be imaged in contact mode by scanning at a 90° angle, whereas phase contrast can be revealed in tapping mode. The resolution is tip shape, sample roughness and instrumental setting (*e.g.* scan speed and feedback control) dependent, but is typically sub-Angstrom in *z*-direction (height).

All AFM measurements were performed *ex situ* at ambient conditions, directly after thin film growth, structure patterning or device fabrication to minimize surface contamination. In general, 10×10 μm^2 areas were scanned at 1024×1024 data points and maximum channels available (*e.g.* to collect both trace and retrace data). For contact mode, Al-coated silicon probes (PPP-CONTR, Nanosensors; Neuchatel, Switzerland) were used, with a typical stiffness of 0.2 N/m, resonance frequency of 13 kHz and tip radius of curvature <7 nm. For

tapping mode imaging, Al-coated silicon probes (PPP-NCHR, Nanosensors) were used, with a typical force constant of 40 N/m, 330 kHz resonance frequency and tip radius <7 nm. All acquired data is processed either by the Nanoscope v6.14r1 or Nanoscope 8.00 software, depending on the system used, with additional use of WSxM 5.0 Develop 1.2 software [37].

In data processing, typically, a 1st order flatten and a 2nd order *XY*-plane fit modification over a selected flat area were applied to level the acquired image before obtaining the height and roughness numbers. The *flatten* procedure centers the data and removes the tilt on each scan line by a first order polynomial. The *plane fit* procedure calculates a second order two-dimensional polynomial and subtracts it from the image. The thickness of the individual Au-features was measured using the *section* procedure with at least six randomly chosen line sections. Roughness data was obtained using the *roughness* procedure.

All AFM images in this thesis are colored according the color scale bar in figure 3.9, with the height ranging from 0 to Z_{AFM} nm (with Z_{AFM} given in the image caption).

3.4.3 Scanning electron microscopy

Scanning electron microscopy (SEM) surface analysis measurements were carried out on a JSM-5610 SEM (Jeol; Tokyo, Japan), operating between 0.5 and 30 kV, and a large-chamber JSM-6490 high-vacuum SEM (Jeol), operating between 0.3 and 30 kV. Both systems are equipped with a secondary electron detector to image the samples' structure and morphology. The large-chamber SEM is part of the nano probing station (see section 3.5.2).

In general, image scans were acquired at 2560×1920 data points. All SEM images in this thesis have been colored bluish by applying a cooling filter on the raw image. Effectively, this photo filter corrects the color balance with -6 (red), 0 (green) and +19 (blue) in RGB mode.

3.4.4 X-ray diffraction

X-ray diffraction (XRD) measurements were performed on a multipurpose, two-circle X'pert APD (Panalytical; Almelo, The Netherlands) diffractometer with a sample changer using Cu Kα radiation. The organic crystals were analyzed using θ-2θ scans to validate their crystal structure. The X'pert system uses an X-ray source operating at 50 kV and 25 mA, and the minimum resolution is as small as 0.001°. A graphite monochromator is used in the diffracted beam path to eliminate high-order spectral reflections. To increase intensity, the samples were spun with 1 Hz during the measurement.

3.4.5 X-ray photoelectron spectroscopy

X-ray photoelectron spectroscopy (XPS) measurements were performed on a PHI Quantera SCM Scanning ESCA Microprobe (Physical Electronics; Chanhassen, MN, USA). Data obtained with XPS gives surface sensitive information on the composition and chemical bonding of the material (*i.e.* typically of the first 10 nm). An Al Kα monochromatic hv = 1486.6 eV X-ray source operating at 25 W is used to investigate the samples at a vacuum base pressure of $<1 \times 10^{-8}$ mbar. Spectra were referenced to the main C1s peak at 284.80 eV. Depth-profiling is possible by using an argon sputter source.

3.5 Electrical Transport Characterization

To characterize the electrical properties of the fabricated devices, a specialized nano probing station has been used. With this system, it is possible to perform electrical measurements on dimensions not reachable by a conventional micro probing station. Important for this work is that the sample probing can be performed without damaging the fragile organic molecular crystals or patterned structures. The specifications and generally used settings of this system, which is located in the Thin Film Laboratory (UT, NL), are detailed in this paragraph.

3.5.1 Nano probing system

The central part of the nano probing system is the Zyvex S100 nanomanipulator (Zyvex Instruments; Richardson, TX, USA). The four probes of the nanomanipulator can be independently moved in *xyz*-directions in a coarse and fine mode, with a top speed of 3 mm/s. Maximum range of coarse motion is 12 mm in *x*- and *z*-direction, and 10 mm in *y*-direction. The maximum fine positioner ranges are ±50 µm in *x*- and *z*-direction, and +10 µm in *y*-direction [38]. Positioner resolution of the coarse axes is 100 nm; of the fine axes is 5 nm. The probes are manually controlled one at a time by a remote joystick via the control cabinet or by the Zyvex software [39].

The Zyvex S100 nanomanipulator is positioned inside a scanning electron microscope (*viz.* the large-chamber JSM-6490 high vacuum Jeol SEM described in paragraph 3.4.3), to view and perform a careful 'landing' of the probes on the sample surface. The SEM is thus a fundamental part of the nano probing system, as the probes cannot be simply placed on the sample by eye anymore, when working at these small dimensions.

Attached to the system is a Keithley 4200-SCS semiconductor characterization system, equipped with four 4200-SMU source-measure units and four 4200-PA remote pre-amplifiers, and a 4200-CVU capacitance voltage unit (Keithley Instruments; Cleveland, OH, USA).

3.5.2 Carbon fiber nano-prober tips

The Zyvex nano probing station is intentionally equipped with tungsten probes with a tip diameter of 100 - 200 nm. This set-up is optimized for probing inorganic nano-electronic devices (see figure 3.11A). Tungsten wire has long been used for making probes for scanning probe microscopy (SPM), because of the ability to sharpen the metal through electrochemical etch techniques to tip diameters as sharp as 50 nm [40].

In general, tungsten probes have two disadvantages. First, a chemical treatment is necessary to remove the native tungsten oxide layer and achieve clean probe tips. Following the *in air* chemical treatment, an *in vacuum* oxide removal treatment must be performed as well in order to acquire high-quality probes. This *in situ* cleaning procedure involves shorting two probe tips, followed by locally heating the tip ends with a current sweep (*e.g.* with the Keithley 4200 SCS) [40]. Second disadvantage; the sharp end of the tungsten probe tips easily bends when landed too fast on the sample or when accidently touched during mounting on the sample stage (see figure 3.11B). Difficulty with bent tips is the uncertainty of where the lowest point of the tip is located. To preserve probe tip sharpness, the fine

motion piezo-positioners have to be used in the final stage of approaching the surface. However, determining when to begin movement in the fine motion mode requires quite some hands-on experience; although the position of the tip in the plane perpendicular to the electron beam can be resolved with an accuracy of a few nanometers, the height can only be estimated by the focusing position of the image and the tip, resulting in an uncertainty in the order of tens of micrometers. In practice, this results in a time-consuming surface approach (*i.e.* tens of minutes per probe) before *'the eagle has landed'*.

When landing tungsten probes on organic molecular crystal devices, two more disadvantages show up. As these crystals are much softer compared to the tungsten probes, damage to the device occurs very quickly when landing too hard on the sample or when the probe is scratching over the surface after landing (*e.g.* from stabilization of the fine motion piezo-positioners). Besides that, when the sample or probe is only slightly charged by the SEM's electron beam, the tungsten probe tip can be pulled towards the sample during the final approach, resulting in a *crash* (see figure 3.11C).

To probe the fragile organic molecular crystal devices without the problems described above, replacement of the rigid tungsten probe tips by homemade flexible carbon fiber tips turned out to be successful. After fabrication, no (chemical cleaning or heating) treatments are needed anymore, as no native oxide layer is present on these probe tips. Due to the flexibility of the carbon fiber probe tips, they can be landed on the surface of the fragile organic molecular crystal devices without damaging them (see figure 3.12A-B). After landing, further movement downwards of the probe positioner leads to a lateral movement of the flexible probe tip on the sample surface. In fact, the entire surface approach can be executed in the course motion mode and thus be performed within a few minutes.

Fabrication carbon fiber nano-prober tips

One end of a copper wire (length 20 mm, diameter 0.25 mm) is fixed with conducting silver paste (LeitSilber 200) to a pin-connection, which fits in the Zyvex nano-prober positioner connectors; the other end of the copper wire is flattened. An individual carbon fiber (length 6 mm, diameter ~7 µm), separated with tweezers from a bundle of pelletized short-chopped carbon fibers (Tenax-A HT C124 6 mm, Toho Tenax America Inc.; Rockwood, TN, USA), is

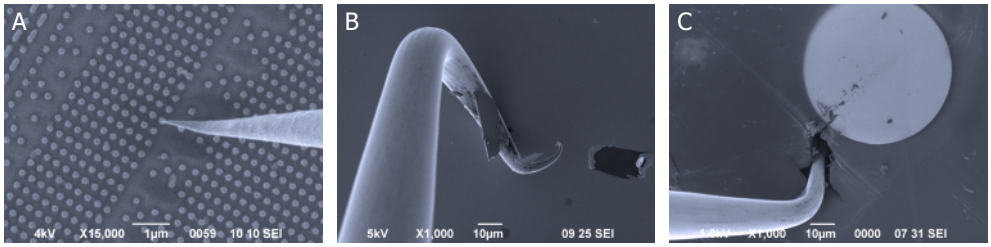

Figure 3.11 *SEM images from tungsten probe tips on various samples in the Zyvex nano manipulator. A) Tungsten probe with ~100 nm tip diameter succesfully landed on an inorganic device with ~200 nm features. B) The sharp end of a tungsten probe easily bends when landed too fast on a sample. C) A tungsten probe crashed into an organic molecular crystal device by slight charging-up of the sample.*

carefully attached to the flattened end of the copper wire by conducting silver paste. To reduce vibrations of the probes during a surface approach, the carbon fibers were shortened a few millimeters. For improved electrical contact characteristics, the probe tips could be coated with a thin gold layer (several tens of nanometer thick) by PLD or sputtering.

Characterization carbon fiber nano-prober tips

Figure 3.12C-D shows two (non-Au-coated) carbon fiber probe tips shorted to each other within the Zyvex nano probing station and an *I-V* sweep through the shorted probes. Total resistance of the complete set-up is about 2 kΩ. Electrical resistivity of the carbon fibers is 1.5×10^{-3} Ω cm [41], which corresponds to the measured resistance. A similar measurement with two shorted tungsten probe tips had a total resistance of 10-15 Ω (resistivity tungsten 5.6×10^{-6} Ω cm). These resistances show the capability of measuring samples in the nano prober system in general, with a low series resistance.

3.5.3 Organic molecular crystal devices in the nano-prober

The main challenge of probe landing is to make a proper electrical contact of the probes to the device electrodes, and at the same time not to modify or induce stresses in the sample. When landing a probe on fragile organic crystals, it is therefore important not to execute a large force with the probe on the sample.

In general, whether or not a tungsten or carbon fiber probe tip has landed on a surface, can be best observed by the appearance of a shadowing effect (a darker region of a few micrometers in size) around the probe tip upon landing (see figure 3.12A). When landing on the fabricated organic molecular crystal devices, the moment of contact can be observed even more noticeably. This is also illustrated in figure 3.12A; the two probed Au contacts appear brighter in the SEM image than the unprobed Au contact at the bottom. After take-off (figure 3.12B), the three Au contacts reveal the same, original contrast again

This type of contrast in the SEM is an example of *passive voltage contrast* (PVC) [42]. PVC is a popular failure analysis technique for locating gate shorts or leakage and open circuit defects in the semiconductor process technology [43]. As a sample is exposed to the electron beam, floating and grounded structures acquire different surface potentials. This will generate different amounts of secondary electron emission, resulting in variations in SEM contrast. Areas with a path to ground appear bright, while charged areas will be darker [44].

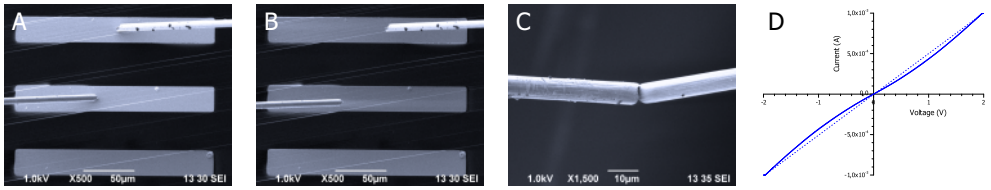

Figure 3.12 *A) Two carbon fiber probe tips landed on gold contacts deposited on a pentacene single-crystal. B) The same two carbon fiber probe tips lifted-up after the landing, revealing no damage to the device. C) Two carbon fiber probe tips shorted to each other. D) Corresponding I-V sweep through the shorted probes (forward and reverse sweeps overlap). The dotted line corresponds to a 2kΩ resistance.*

The probed Au contacts in figure 3.12A have a conductive path to ground through the landed carbon fiber probes. On the other hand, the path to ground for the unprobed Au contacts goes through the insulating pentacene single-crystal. So, some charging of these features can be expected, and thus a difference in surface potential and SEM contrast between the probed and unprobed Au contacts.

Electron beam-induced deposition

It should be noted that the voltage contrast effect drops off if the samples' surface gets covered with an electron beam-induced deposition (EBID) layer, when imaging a certain area for a longer period. The vacuum level in the nano-prober SEM is down to 7×10^{-6} mbar [45], so there are some residual hydrocarbon molecules present. The hydrocarbons decompose under the electron beam radiation, resulting in an amorphous sp^3-hybridized diamond-like carbon layer deposited on the exposed area [46,47]. This contaminating EBID layer is normally observed as a dark rectangle on the surface when going from high to lower magnification in secondary electron imaging. In general, build-up of this layer is of little consequence as it does not interfere with image collection.

However, as this carbonaceous layer is completely insulating (resistivity is in the order of 10^{11} Ω cm [48]), it will form a barrier for good ohmic contact during probing [49]. As a consequence, to achieve reliable measurements with the nano-prober system, imaging of the (organic) devices and exposure of the sample and the prober tips to the electron beam, especially under high magnification, should be restricted as much as possible. For this reason, the fast surface approach that is possible with the flexible carbon fiber probe tips is quite beneficial.

Measurements

Because the scanning electron beam induces charge on the sample surface, it must be switched off during electrical measurements, to avoid additional current from incident primary electrons (*e.g.* Noyong *et al.* [50] observed the appearance of a saw tooth-like overlay with currents up to 10^{-10} A in their nanomanipulation system when not switching off the scanning electron beam).

Normally, the sample and the probe tips are grounded during scanning to eliminate any charging caused by the electron beam. However, when performing electrical measurements, this grounding of the sample to the sample stage is unwanted as it will result in additional current paths through the sample. Therefore, an additional setup was installed on the system to quickly enable or disable grounding of the sample relative to the sample stage.

3.6 Concluding Remarks

In this chapter, a description of the deposition and patterning techniques that are applied in the upcoming chapters to fabricate devices on organic single-crystal substrates has been given. Besides that, the various analysis techniques used to obtain information about the structural and electrical properties of these devices were introduced as well.

3.7 Reference

[1] Maiman, T.H.; "Stimulated optical radiation in ruby"; *Nature*; 187; **1960**; 493-494

[2] Smith, H.M.; Turner, A.F.; "Vacuum deposited thin films using a ruby laser"; *Appl. Optics*; 4; **1965;** 147-148

[3] Breech, F.; Cross, L.; "Optical microemission stimulated by a ruby maser"; *Appl. Spectrosc.*; 16; **1962**; 59

[4] McClung, F.J.; Hellwarth, R.W.; "Giant optical pulsations from ruby"; *J. Appl. Phys.*; 33; **1962**; 828-829

[5] Dijkkamp, D.; Venkatesan, T.; Wu, X.D.; Shaheen, S.A.; Jisrawi, N.; Min-Lee, Y.H.; McLean, L.; Croft, M.; "Preparation of Y-Ba-Cu oxide superconductor thin films using pulsed laser evaporation from high T_c bulk material"; *Appl. Phys. Lett.*; 51; **1987**; 619-621

[6] Moorjani, K.; Bohandy, J.; Adrian, F.J.; Kim, B.F.; "Superconductivity in bulk and thin films of $La_{1.85}Sr_{0.15}CuO_{4-\delta}$ and $Ba_2YCu_3O_{7-\delta}$"; *Phys. Rev. B*; 36; **1987**; 4036-4038

[7] Chrisey, D.B.; Hubler, G.K.; Pulsed laser deposition of thin films; **1994**; Wiley-Interscience; New York, NY, U.S.A.

[8] Eason, R.; Pulsed laser deposition of thin films – Applications-led growth of functional materials; **2007**; Wiley-Interscience; Hoboken, NJ, U.S.A.

[9] Zhang, Y.; Gu, H.; Iijima, S.; "Single-wall carbon nanotubes synthesized by laser ablation in a nitrogen atmosphere"; *Appl. Phys. Lett.*; 73; **1998**; 3827-3829

[10] Geohegan, D.B.; Puretzky, A.A.; Rader, D.J.; "Gas-phase nanoparticle formation and transport during pulsed laser deposition of $Y_1Ba_2Cu_3O_{7-\delta}$"; *Appl. Phys. Lett.*; 74; **1999**; 3788-3790

[11] Goodwin, T.J.; Leppert, V.J.; Risbud, S.H.; Kennedy, I.M.; Lee, H.W.H.; "Synthesis of gallium nitride quantum dots through reactive laser ablation"; *Appl. Phys. Lett.*; 70; **1997**; 3122-3124

[12] Ohring, M.; Materials science of thin films; **2002**; 2nd ed.; Academic Press; San Diego, CA, U.S.A.

[13] Strikovski, M.; Miller, J.H. Jr.; "Pulsed laser deposition of oxides: Why the optimum rate is about 1 Å per pulse"; *Appl. Phys. Lett.*; 73; **1998**; 1733-1735

[14] Greer, J.A.; Tabat, M.D.; "Large-area pulsed laser deposition: techniques and applications"; *J. Vac. Sci. Technol. A*; 13; **1995**; 1175-1181

[15] Riele, P.M. te; Rijnders, G.; Blank, D.H.A.; "Ferroelectric devices created by pressure modulated stencil deposition"; *Appl. Phys. Lett.*; 93; **2008**; 233109

[16] Riele, P.M. te; Direct patterning of oxides by pulsed laser stencil deposition; PhD Thesis; **2008**; University of Twente; Enschede, The Netherlands

[17] Brugger, J.; Berenschot, J.W.; Kuiper, S.; Nijdam, W.; Otter, B.; Elwenspoek, M.; "Resistless patterning of sub-micron structures by evaporation through nanostencils"; *Microelectron. Eng.*; 53; **2000**; 403-405

[18] Speets, E.A.; Ravoo, B.J.; Roesthuis, F.J.G.; Vroegindeweij, F.; Blank, D.H.A.; Reinhoudt, D.N.; "Fabrication of arrays of gold islands on self-assembled monolayers using pulsed laser deposition through nanosieves"; *Nano Lett.*; 4; **2004**; 841-844

[19] Takano, N.; Doeswijk, L.M.; Boogaart, M.A.F. van den; Auerswald, J.; Knapp, H.F.; Dubochet, O.; Hessler, T.; Brugger, J.; "Fabrication of metallic patterns by microstencil lithography on polymer surfaces suitable as microelectrodes in integrated microfluidic systems"; *J. Micromech. Microeng.*; 16; **2006**; 1606-1613

[20] Cojocaru, C.V.; Harnagea, C.; Pignolet, A.; Rosei, F.; "Nanostenciling of functional materials by room temperature pulsed laser deposition"; *IEEE Trans. Nanotechn.*; 5; **2006**; 470-477

[21] Egger, S.; Ilie, A.; Fu, Y.; Chongsathien, J.; Kang, D.J.; Welland, M.E.; "Dynamic shadow mask technique: a universal tool for nanoscience"; *Nano Lett.*; 5; **2005**; 15-20

[22] Wasserman, J.L.; Lucas, K.; Lee, S.H.; Ashton, A.; Crowl, C.T.; Markovic, N.; "Fabrication of one-dimensional programmable-height nanostructures via dynamic stencil deposition"; *Rev. Sci. Instr.*; 79; **2008**; 073909

[23] Savu, V.; Boogaart, M.A.F. van den; Brugger, J.; Arcamone, J.; Sansa, M.; Perez-Murano, F.; "Dynamic stencil lithography on full wafer scale"; *J. Vac. Sci. Technol. B*; 26; **2008**; 2054-2058

[24] Riele, P. te; Janssens, A.; Rijnders, G.; Blank, D.H.A.; "Direct patterning of complex oxides by pulsed laser deposition through stencils"; *J. Phys. Conf. Series*; 59; **2007**; 404-407

[25] Zhou, Y.X.; Johnson, A.T. Jr.; Hone, J.; Smith, W.F.; "Simple fabrication of molecular circuits by shadow mask evaporation"; *Nano Lett.*; 3; **2003**; 1371-1374

[26] Tun, T.N.; Lwin, M.H.T.; Kim, H.H.; Chandrasekhar, N.; Joachim, C.; "Wetting studies on Au nanowires deposited through nanostencil masks"; *Nanotechnology*; 18; **2007**; 335301

[27] Vazques-Mena, O.; Villanueva, G.; Boogaart, M.A.F. van den; Savu, V.; Brugger, J.; "Reusability of nanostencils for the patterning of aluminum nanostructures by selective wet etching"; *Microelectron. Eng.*; 85; **2008**; 1237-1240

[28] Lishchynska, M.; Bourenkov, V.; Boogaart, M.A.F. van den; Doeswijk, L.; Brugger, J.; Greer, J.C.; "Predicting mask distortion, clogging and pattern transfer for stencil lithography"; *Microelectron. Eng.*; 84; **2007**; 42-53

[29] Deshmukh, M.M.; Ralph, D.C.; Thomas, M.; Silcox, J.; "Nanofabrication using a stencil mask"; *Appl. Phys. Lett.*; 75; **1999**; 1631-1633

[30] Racz, Z.; He, J.; Srinivasan, S.; Zhao, W.; Seabaugh, A.; Han, K.; Ruchhoeft, P.; Wolfe, J.; "Nanofabrication using nanotranslated stencil masks and lift off"; *J. Vac. Sci. Technol. B*; 22; **2004**; 74-76

[31] Kölbel, M.; Tjerkstra, R.W.; Brugger, J.; Rijn, C.J.M. van; Nijdam, W.; Huskens, J.; Reinhoudt, D.N.; "Shadow-mask evaporation through monolayer-modified nanostencils"; *Nano. Lett.*; 2; **2002**; 1339-1343

[32] Kölbel, M.; Tjerkstra, R.W.; Kim, G.; Brugger, J.; Rijn, C.J.M. van; Nijdam, W.; Huskens, J.; Reinhoudt D.N.; "Self-assembled monolayer coatings on nanostencils for the reduction of materials adhesion"; *Adv. Funct. Mater.*; 13; **2003**; 219-224

[33] Boogaart, M.A.F. van den; Lishchynska, L.; Doeswijk, L.; Greer, J.; Brugger, J.; "Corrugated membranes for improved pattern definitaion with micro/nanostencil lithography"; *Sens. Act. A*; 130-131; **2006**; 568-574

[34] Rijn, C.J. M. van; Veldhuis, G.J.; Kuiper, S.; "Nanosieves with microsystem technology for microfiltration applications"; *Nanotechnology*; 9; **1998**; 343-345

[35] Vrijmoeth, J.; Stok, R.W.; Veldman, R.; Schoonveld, W.A.; Klapwijk, T.M.; "Single crystallites in 'planar poly-crystalline' oligothiophene films: determination of orientation and thickness by polarization microscopy"; *J. Appl. Phys.*; 83; **1998**; 3816-3824

[36] Boer, R.W.I. de; Gershenson, M.E.; Morpurgo, A.F.; Podzorov, V.; "Organic single-crystal field-effect transistors"; *Phys. Stat. Sol. A*; 201; **2004**; 1302-1331

[37] Horcas, I.; Fernández, R.; Gómez-Rodríquez, J.M.; Colchero, J.; Gómez-Herrero, J.; Baro, A.M.; "WSXM: a software for scanning probe microscopy and a tool for nanotechnology"; *Rev. Sci. Instrum.*; 78; **2007**; 013705

[38] Ross, R.; Technical Support Zyvex Instruments, LLC; Richardson, TX, USA; *private communication*

[39] Zyvex; IC nanoprober user manual; Zyvex nanoworks product line; **2005**; Zyvex Instruments, LLC; Richardson, TX, USA

[40] Zyvex; IC nanoprobing, application manual; Zyvex nanoworks product line; Application notes 9716 and 9717; **2007**; Zyvex Instruments, LLC; Richardson, TX, USA

[41] Toho Tenax; Carbon fibers; Typical properties; www.tohotenaxamerica.com/contfil.php; last visited on 13-09-2010

[42] Seiler, H.; "Secondary electron emission in the scanning electron microscope"; *J. Appl. Phys.*; 54; **1983**; R1-R18

[43] Gemmill, Z.; Durbha, L.; Jacobson, S.; Gao, G.; Weaver, K.; "SEM and FIB passive voltage contrast"; 432-438 in Microelectronic failure analysis desk reference; 5th ed.; **2004**; ASM International; Materials Park, OH, U.S.A.

[44] Mahanpour, M.; "Emission microscopy and passive voltage contrast: solving a problem quickly"; *III-Vs Rev.*; 9; **1996**; 46-50

[45] Borsboom, R.; Chief Engineer JEOL Benelux BV; *private communication*

[46] Stewart, R.L.; "Insulating films formed under electron and ion bombardment"; *Phys. Rev.*; 45; **1934**; 488-490

[47] Lau, D.; Hughes, A.E.; Muster, T.H.; Davis, T.J.; Glenn, A.M.; "Electron-beam-induced carbon contamination on silicon: characterization using Raman spectroscopy and atomic force microscopy"; *Micros. Microanal.*; 16; **2010**; 13-20

[48] Miura, N.; Ishii, H.; Shirakashi, J.; Yamada, A.; Konagia, M.; "Electron-beam-induced deposition of carbonaceous microstructures using scanning electron microscopy"; *Appl. Surf. Sci.*; 113-114; **1997**; 269-273

[49] Chen, Q.; Wang, S.; Peng, L.M.; "Establishing Ohmic contacts for in situ current-voltage characteristics measurements on a carbon nanotube inside the scanning electron microscope"; *Nanotechnology*; 17; **2006**; 1087-1098

[50] Noyong, M.; Bleck, K.; Rosenberger, A.; Klocke, V.; Simon, U.; "In situ nanomanipulation system for electrical measurements in SEM"; *Meas. Sci. Technol.*; 18; **2007**; N84-N89

Chapter 4

Pentacene Single-Crystals: Growth and Morphology

Chapter 4: Pentacene Single-Crystals: Growth and Morphology

Abstract

First, a review on the crystal structure of pentacene and on the growth mechanism models of vapor-grown organic molecular crystals is presented. Next, the crystal structure, geometry and surface morphology of pentacene single-crystals grown by physical vapor transport are investigated by various experimental techniques, as these crystals are applied as substrate in the fabrication of devices in the upcoming chapters. Finally, it will be shown that for pentacene a step flow type of crystal growth is the dominant mechanism, yet several observations show that the pentacene crystal growth behavior is not limited to this type of growth.

4.1 Introduction

Pentacene, the benchmark material studied in this work, is the fifth in the linear aromatic hydrocarbon series composed of laterally fused benzene rings. The molecules in this series are called linear acenes (the name 'acene' was thought up by Clar [1]); yet the terms polyacenes or oligoacenes are used in literature as well. The linear acene family (see figure 4.1) starts with benzene, followed by naphthalene, anthracene, tetracene (also called naphthacene) and pentacene. The next members in the series are hexacene and heptacene; the latter molecule was synthesized only a few years ago [2]. Larger members (*e.g.* octacene and nonacene) of the acene family appear to be so highly reactive, photo-unstable and poorly soluble that they cannot be synthesized, but can only be studied in theory [3]. In the acene series, molecules that contain two or more fused rings are also members of a broad group of well-studied chemicals called polycyclic aromatic hydrocarbons (PAHs) [4].

Acenes are functional materials that possess a set of interesting physical and chemical properties (*e.g.* a wide range of bandgaps, tunable colors) that can be easily manipulated by substitution of functional groups to the aromatic backbone. Anthracene, tetracene and pentacene, and their derivatives, are extensively used in organic field-effect transistors (OFETs) [5,6], organic light-emitting diodes (OLEDs) [7,8] and organic photovoltaics (OPVs) [9]. In fact, pentacene is by far the most popular organic semi-conductor for OFET fabrication [10].

For organic thin films, it has been demonstrated that surface defects and surface morphology both have important effects on the performance of OFETs [11,12]. Accordingly, there have been many reports about the growth and morphology of organic thin films [13-15]. Interestingly, in contrast to its polycrystalline thin film counterpart, the nucleation and growth processes of organic semiconducting single-crystals by physical vapor transport have rarely evoked interest. So far, only a few studies on the surface morphology and structural defects, and especially on the growth mechanism, have been performed on such crystals [16-21]. These parameters are important for the performance of organic single-crystal field-effect transistors, since the conductive channel will be located in the first molecular layers at the crystal surface [22,23]. Furthermore, the surface morphology will influence the interface between the organic semiconducting crystal and the dielectric layer.

The aim of this chapter is therefore to study the growth mechanism of pentacene single-crystals, and to investigate their crystal structure, geometry and surface morphology as well, as these crystals are applied as substrate in the fabrication of devices in the upcoming chapters. As will be discussed in the review on the growth mechanism models for organic molecular crystals, several different models are at present proposed in literature to describe

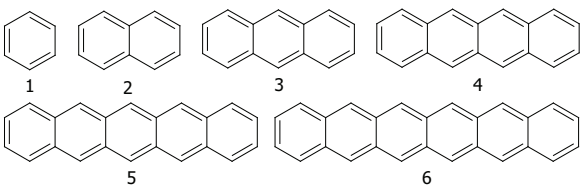

Figure 4.1 *Chemical structures of the linear acenes: 1. benzene, 2. naphthalene, 3. anthracene, 4. tetracene, 5. pentacene, and 6. hexacene*

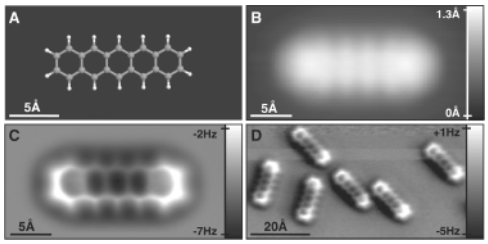

Figure 4.2 *A) Ball-and-stick model of a pentacene molecule, B) constant-current STM, and C) and D) constant-height AFM images of one or more pentacene molecules adsorbed on Cu(111), acquired with a CO-modified tip. Figure with permission from [25].*

the growth behavior of organic single-crystals. In this chapter, it will be shown that for pentacene a step flow type of crystal growth is the dominant mechanism. Nonetheless, several observations show that the crystal growth is not limited to this type of growth.

4.2 Theoretical Background

In this section, various general aspects of pentacene, like its synthesis and solubility in solvents are introduced first, followed by a review on the crystal structure of pentacene and on the growth mechanisms of organic molecular crystals grown by physical vapor transport.

4.2.1 Pentacene

The pentacene molecule ($C_{22}H_{14}$, 278.33 g/mol) is an aromatic, conjugated planar molecule of five linearly fused benzene rings (see figure 4.1) [24]. Recently, Gross and co-workers at IBM revealed the chemical structure of an individual pentacene molecule by imaging with AFM and STM (see figure 4.2) [25]. The molecule itself is poorly soluble in most solvents and can only be obtained by multistep synthesis; a combination responsible for the high material price (*e.g.* several hundred euro per gram [26]). In the solid state, pentacene has a deep blue color and is highly crystalline. Due to the poor solubility, research has mainly focused on pentacene thin films and single-crystals, and not on pentacene in solution or on individual pentacene molecules. A historic overview of the number of 'pentacene' publications is presented in figure 4.3, showing the enormous boost in research the last decade.

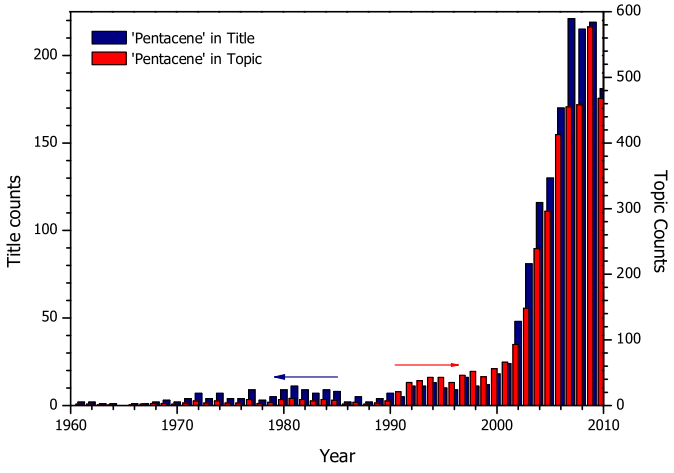

Figure 4.3 *Number of journal publications in which 'pentacene' is mentioned in the title (blue, left) or topic (red, right) in the ISI web of knowledge.*

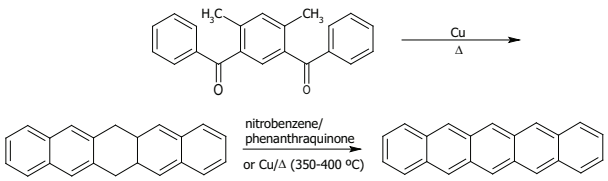

Figure 4.4 *Synthesis of pentacene as described by Clar and John [29]. A Friedel-Crafts reaction of m-xylophenone yielded 4,6-dibenzoyl-1,3-dimethylbenzene, which is converted into dihydropentacene by heating with copper. Dehydrogenation to pentacene was accomplished by boiling the dihydropentacene in nitrobenzene with phenanthraquinone or by passing over copper at 350-400 °C.*

Synthesis of pentacene

Pentacene cannot be directly isolated from coal or petroleum sources. The lower homologues in the acene family, from benzene to anthracene, can be extracted from coal, while the longer members can be obtained only by multistep synthesis [27]. Already back in 1912, Mills and Mills described the first synthesis of pentacene (named *β*,*β*′,*β*′-dinaphtanthracene) and some of its derivatives, from pyromellitic anhydride and benzene as starting materials and in the presence of $AlCl_3$ catalyst [28]. Clar and John described synthesis of pentacene starting from *m*-xylophenone via 4,6-dibenzoyl-1,3-dimethylbenzene and dihydropentacene in 1930 (see figure 4.4) [29]. In 1943, an improved synthesis of pentacene is reported by Allen and Gates, by adding 1,3-diphenylisobenzofuran to benzoquinone [30]. Bailey and Madoff reported in 1953 the synthesis of pentacene from 1,2-dimethylenecyclohexane by a three-step procedure [31].

The most convenient method nowadays to obtain pentacene is to synthesize it from 6,13-pentacenequinone via a reduction reaction by an aluminum-cyclohexanol mixture, as depicted in figure 4.5. 6,13-pentacenequinone itself can be prepared by a fourfold aldol condensation reaction between 1,2-phthalic dicarboxaldehyde and 1,4-cyclohexanedione [32].

Solubility of pentacene

The solubility of pentacene in most common organic solvents at normal conditions is extremely poor; however, there are a few solvents in which it can be dissolved to a certain extent. Pentacene is reported to be very slightly soluble in a cyclohexane : benzene mixture [33], and in benzene [34,35] and dimethyl sulfoxide [36] at elevated temperatures. Pentacene can be dissolved in some halogenated aromatic hydrocarbon solvents (*e.g.* 1,2,4trichloro-

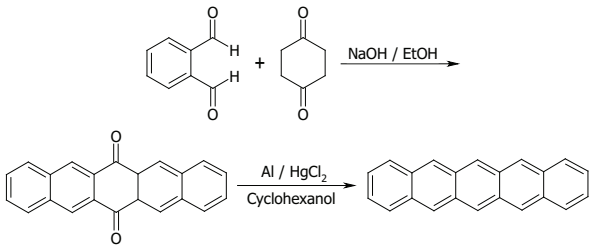

Figure 4.5 *Synthesis of pentacene by reducing 6,13-pentacenequinone by an aluminium-cyclohexanol mixture. The 6,13-pentacenequinone is the product of a fourfold aldol condensation reaction between 1,2-phthalic dicarboxaldehyde and 1,4-cyclohexanedione.*

benzene and 1,2-dichlorobenzene) at elevated temperatures as well [32,37,38]. The solution is quite unstable, as very dilute solutions of pentacene in 1,2-dichlorobenzene bleach within minutes unless isolated from air and light [32]. Finally, pentacene has also been found to be soluble in some heated liquid crystal materials that possess large *π*-electron conjugated groups, like cyanobiphenyl or -terphenyl liquid crystal [35,39].

A simple procedure to deposit pentacene thin films directly from solution using a common organic solvent has not yet been found. One approach to increase the solubility of pentacene is by adding functional side groups to the pentacene molecule that can be removed by heating or irradiating the deposited film after solvent evaporation [40-42]. A soluble precursor currently gaining much interest in the scientific world is 6,13-bis(triisopropyl-silylethynyl) pentacene (TIPS-pentacene) [43].

Influence of solvents on pentacene

The influence of common organic solvents on the crystallographic structure and morphology of pentacene films and single-crystals has not been investigated much. Gundlach *et al.* [44] reported a solvent-induced phase transition in pentacene thin films. Exposure to solvents such as acetone, isopropanol and ethanol resulted in shifting of the *d*(001) interplanar spacing (see paragraph 4.2.2), accompanied by macroscopic buckling of the pentacene film. Mattheus *et al.* [45] verified these findings.

In addition to the morphological and crystallographic transformations, the performance of pentacene thin film transistors also dramatically degraded after exposure to solvents. Kuo and Jackson [46] reported on the exposure of pentacene thin film transistors to water, isopropanol, dimethyl sulfoxide and hexadecane. They connected the dramatic device degradation to cracking and film detachment, most likely caused by swelling of the film, instead of dissolving or a chemical reaction [47]. Remarkably, water was the only solvent that did not cause severe damage to the pentacene thin films and their device performance [47].

These structural crystallographic and morphological changes are the main reason why photolithographic processes cannot be used in the fabrication of pentacene thin film devices. For pentacene single-crystals, the conventional idea is to totally exclude the exposure of solvents and photolithographic resists to the crystals as well [48].

4.2.2 Pentacene crystal structure

Gavezzotti and Desijaru [49,50] analyzed the structure of numerous organic aromatic molecules and found that all examined compounds crystallize in layered structures. They distinguished four possible packing modes, depending on the specific intermolecular interactions: the herringbone structure, the *γ*-structure (flattened-out herringbone), the sandwich herringbone structure and the layered 'graphitic plane' *β*-structure. The 'ideal' complete co-facial *π*-stacking, theoretically leading to a very high charge carrier mobility, is hardly ever found in molecular crystals [51]. As can be seen in figure 4.6, pentacene crystallizes in a layered structure and the molecules pack in a face-to-edge herringbone structure within the layers [49]. In fact, all acenes from benzene to pentacene, as well as several thiophenes and phenylenes crystallize in the herringbone arrangement [27].

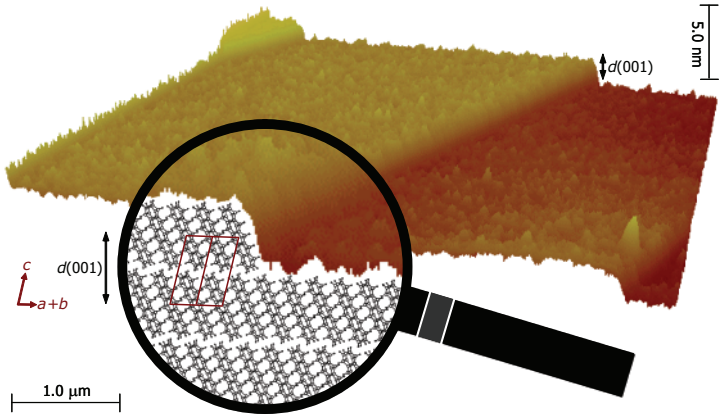

Figure 4.6 *Artist impression of the pentacene single-crystal morphology (based on a 3D-AFM height image), showing the layered structure of the pentacene molecules. Within the layers, the molecules pack in a face-to-edge herringbone structure.*

The existence of more than one crystal structure for a particular material is frequently observed for aromatic hydrocarbons and organic crystals [27]. The intermolecular forces between the pentacene molecules within the two-dimensional layers are rather weak, and result from the cooperation and competition between π–σ and π–π bond interactions [52]. The adjacent layers are bonded by weak van der Waals forces only. Due to the small interaction forces between the molecules, little variations in the crystal packing can be present, leading to polymorphism. Pentacene has several polymorphs, each with a specific *d*(001)-spacing along the *c**-axis (*i.e.* the *c**-axis is defined as the direction perpendicular to the *ab*-plane). The (001) plane spacing is the largest spacing present, and is therefore the characteristic spacing for this material (*i.e.* the 'layer periodicity'). For pentacene thin films, four polymorphs are reported in literature, with *d*(001) values of 1.41, 1.44, 1.50 and 1.54 nm [53]. The obtained polymorph depends amongst others on the substrate type, the substrate temperature during growth, the thickness of the film and the growth rate [53]. For pentacene single-crystals, only one polymorph exists, and it has a unique *d*(001) spacing of 1.41 nm [54].

Although being a relatively small molecule, the crystal structure of pentacene is of low symmetry and rather complicated, due to the asymmetry present in the molecule. The low symmetry is expressed by the triclinic crystallographic structure of pentacene, with two molecules in a unit cell (see figure 5.2), which results in anisotropy of various electrical and optical crystal properties [55].

The first crystal and molecular structure determination of bulk pentacene is reported by Campbell *et al.* [56] in 1961, with slight modifications reported in 1962 [57]. In this work, the single-crystal unit cell parameters determined by Mattheus are followed: $a = 0.6266$ nm, $b = 0.775$ nm, $c = 1.453$ nm, $\alpha = 76.475°$, $\beta = 87.682°$, $\gamma = 84.684°$, and $\rho = 1.349$ g/cm^3 [45,53,54]. The most significant difference between the Campbell and Mattheus parameters is Campbells *d*(001) spacing of 1.44 nm, where Mattheus observed 1.41 nm. The latter value is in good agreement with the results from Holmes *et al.* [24] and Siegrist *et al.* [58],

and since then commonly accepted as the crystal structure adopted by pentacene single-crystals at room temperature. Recently, Siegrist *et al.* [59] reported the presence of a phase transition upon heating around 190 °C, and that the unit cell parameters of the high-temperature pentacene polymorph were similar to those reported by Campbell. Conversely, the low-temperature polymorph is consistent with the Mattheus' unit cell parameters.

Note that in this work, the common crystallographic convention for a triclinic system is adopted: the lattice parameters of the axes are chosen as short as possible, $|a| < |b| < |c|$, and α, β and $\gamma < 90°$ [54]. The last years, in literature, a different unit cell choice is sometimes adopted, with the *a*-axis defined as the longest axis in the *xy*-plane (*i.e.* $|a| > |b|$) [60,61].

4.2.3 Growth mechanism models for organic molecular crystals

As mentioned in the introduction, the growth mechanisms of organic single-crystals by physical vapor transport (PVT) have not evoked much interest [16-21], in contrast to its poly-crystalline thin film counterpart. Thin film formation processes and growth kinetics of organic small molecules by physical vapor deposition (PVD) and molecular beam epitaxy (MBE) have been widely investigated [13-15,62-64]. Many parameters influence the thin film growth, structure and morphology, like the substrate nature and temperature, the deposition rate, the background gas pressure, and the kinetic energy of the molecular beam. In general, the conditions for a certain thin film growth mode depend on the delicate balance of anisotropic interactions between the molecules, and between the molecules and the substrate [65].

There are a few differences between the growth of organic thin films and organic single-crystals. Due to the limited or absent influence of a substrate in the formation process of crystals grown by PVT, the main driving force depends solely on the interactions between the molecules in the crystal itself. Another difference is that the (PVD and MBE) thin films are grown far away from thermodynamic equilibrium, whereas the organic single-crystals are grown at (near-) thermodynamic equilibrium in PVT.

In literature, there is a small discrepancy on the onset of crystallization in PVT crystal growth. On the one hand, it is reported that the crystals grow in the tube furnace without any contacts to the wall, due to spontaneous gas phase nucleation [66,67]. On the other hand, it is reported that the crystals grow in the tube furnace hanging on the tube wall [16,17], as is the case for the pentacene single-crystals grown for this work [68]. In the initial stage of crystal nucleation and growth, several molecules nucleate, either spontaneously or in the form of two-dimensional islands on the inner surface of the glass tube, and then other molecules combine with the previously nucleated molecules by intermolecular interactions. The main point is that only some initial molecules might be influenced by the tube wall substrate. For virtually the entire crystal growth process, the main driving force is the inter-action between the molecules.

The final crystal shape is controlled by the anisotropy of these intermolecular interactions. For many materials, the largest dimensions of the final crystal shape correspond to the direction of the strongest interactions. Most of the PVT-grown organic crystals are shaped as thin platelets or needles. In platelet-like crystals, the largest facet typically corresponds to the *ab*-plane or (001) crystal plane [69], which is also the case for pentacene [45].

According to a note in [69] for tetracene and TCNQ crystals, the slow crystal growth in the direction perpendicular to the *ab*-facet proceeds by the *flow of steps* at a very low growth rate (<10 μm/h). This results in molecularly flat facets with a low density of molecular steps, separated by wide (0.5 - 1.0 μm) terraces.

In the crystal formation model proposed by Wang *et al.* [17] for tetracene and three other slice-like crystals, first several molecules in the form of two-dimensional islands nucleate on the inner surface of the furnace tube and form a small crystal plane vertical to the wall. Then, other molecules grow on the crystal plane forming monolayer thick islands, while the primary crystal plane continues expanding. The two-dimensional islands on the crystal expand and join each other, creating an intact molecular layer (a new crystal plane). The large-scale crystal is formed ultimately by *layer-plus-island* periods growth. Besides the step-like morphology observed in most regions of the crystal surface by AFM, regions characteristic for two-dimensional joint islands have been found verifying the layer-plus-island growth mode.

Zeng *et al.* [16] and Zhang *et al.* [18] proposed a somewhat different crystal formation model, as they observed an array of parallel large straight steps on the surface of pentacene and anthracene single-crystals, besides the elementary molecular steps. Although they mentioned that two-dimensional nucleation processes can also occur on the crystal surface, they observed no two-dimensional joint islands and proposed a *layer-by-layer* growth model. In this case, each large step on the large-scale crystal is formed from the piling of elementary steps. Overall, it is concluded that the growth mechanism is a *two-dimensional nucleation – elementary steps – large straight steps – layer-by-layer* periods growth.

In the papers discussed so far, no (large) spiral steps grown from screw dislocations were found on the surface of the PVT-grown crystals. Jo *et al.* [70] did observe spiral steps originating from screw dislocations present on the (001) plane of anthracene single-crystals grown from the vapor phase (see figure 2.2A). Cuppen *et al.* [21] even concluded that screw dislocations are a requirement for the crystallization of platelet-like acene crystals under normal conditions, as the nucleation barrier for growth on the (001) face is much higher compared to the other crystal faces, which limits two-dimensional nucleation of new islands. They observed that the (001) faces of vapor-grown naphthalene, anthracene and tetracene crystals are indeed fully covered with spiral steps protruding from screw dislocations.

4.3 Experimental Procedure

In this paragraph, the experimental details of the purification and growth of the pentacene single-crystals and the applied analysis techniques are being discussed.

4.3.1 Purification and growth of pentacene single-crystals

The pentacene and rubrene single-crystals used in this study have been grown by the PVT method [66,71,72], after purification of the starting powder by vacuum sublimation under a temperature gradient [52,73,74], by Jurchescu and Arkenbout (Solid State Chemistry group; University of Groningen, The Netherlands); see refs. [52] and [54] for specific details.

First, the as-received pentacene powder (Sigma Aldrich; Germany) is purified by a vacuum sublimation process. After placing several tens of milligram of the starting powder in an alumina boat inside a glass tube and applying the vacuum, the purification process takes places at T = 160 °C for ~70h, in the dark (see figure 2.4). The sublimed impurities (*i.e.* 6,13-pentacenequinone) can be found afterwards as a brown powder on the tube walls, whereas the purified violet pentacene powder is used as starting material for the single-crystal growth.

30 to 40 mg of the pre-purified powder is then placed in an alumina crucible in a horizontal glass tube reactor set in the dark to prevent photo-oxidation (see figure 2.3). The material is placed in the hottest region of the tube where it vaporizes (~270 °C); the crystal growth occurs about 30 cm further along the tube at a lower temperature (~220 °C), the vaporized material carried there by an inert transport gas (*e.g.* ultrapure dry argon). Presence of hydrogen in the transport gas is avoided, to prevent hydrogenation of the acene at the middle ring, forming 6,13-dihydropentacene impurities [45,54].

Typically, the growth process takes around 3 days. After growth, the crystals were harvested and stored in vacuum or dry nitrogen atmosphere and darkness before further use, as exposure to oxygen and light may cause slow oxidation [52]. The grown platelet-like pentacene crystals vary in size, with in-plane dimensions up to several millimeters and thicknesses of several tens of micrometers. Typically, no needle-like crystals were present.

4.3.2 Characterization of pentacene single-crystals

To verify and check the quality of the vapor-grown pentacene single-crystals, room temperature X-ray diffraction (XRD) measurements were performed on a X'pert APD diffractometer. To inspect the crystal shape, structure and geometry, optical microscopy (OM) measurements were performed on a Nikon Eclipse ME600L microscope and scanning electron microscopy (SEM) measurements were carried out on a Jeol JSM-6490 high-vacuum SEM, operating at a low acceleration voltage between 0.3 and 2.0 kV. Finally, to study the surface morphology of the crystals, atomic force microscopy (AFM) measurements were performed on a Veeco Multimode SPM and a Veeco Dimension Icon, on several areas of various crystals. For more details of the used equipment, see paragraph 3.4.

4.4 Results and Discussion

With the aim of acquiring more information on the growth mechanism of organic molecular crystals, the crystal structure, geometry and surface morphology of vapor-grown pentacene single-crystals have been investigated and the results will be discussed in this paragraph.

4.4.1 Shape and crystal plane orientation of pentacene single-crystals

To verify and check the crystal quality, room temperature X-ray diffraction analyses have been performed on the crystals used in this work. A typical θ-2θ diffraction pattern of vapor-grown pentacene single-crystals is shown in figure 4.7. In the experiments, the crystals were mounted parallel on an amorphous polymer substrate, with the largest facets facing upwards. The small curvature in the baseline is due to the polymer substrate, and can be further

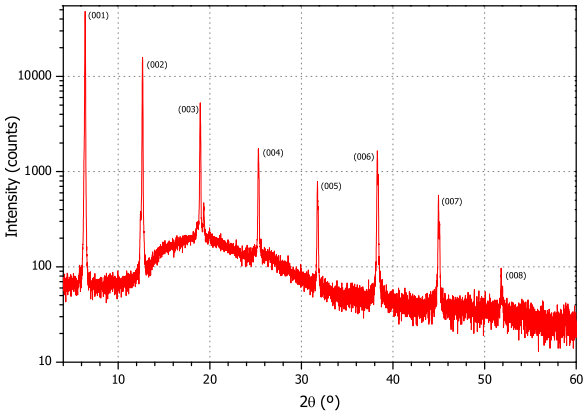

Figure 4.7 *Experimental θ-2θ X-ray diffraction pattern of a pentacene single-crystal.*

ignored. The actual diffraction peaks are sharp, indicating the crystalline quality of the crystals is good. The equidistant diffraction peaks confirm the ordered layer structure of the crystals. The peaks can be indexed as 00*l* reflections. The strong diffraction peak at $2\theta = 6.388°$ corresponds to the (001) crystal plane. Other equivalent periodic peaks can be observed, corresponding to (00*l*) crystal planes, with *l* from 2 to 8, respectively. According to the Bragg equation [75], the thickness of one pentacene monolayer is found to be 1.404 nm. This measured *d*(001) spacing is in accordance with the 1.41 nm *d*-spacing value reported in literature for vapor-grown pentacene single-crystals [52,54].

The theoretical shape of a crystal can be derived from the relative growth rates of various low-index faces, since the growth rate of a crystal face is assumed to be proportional to its surface formation energy [76,77]. The surface energies of several low-index pentacene single-crystal surfaces have been calculated by Northrup *et al.* [78] (*e.g.* the surface energy is the energy required for cleaving a surface from a bulk material). Using density functional calculations, they predicted an equilibrium crystal shape in terms of the surface energy of the crystal structure. The unit cell parameters used by Northrup, however, are defined differently compared to the parameters used in this work. The calculated formation and surface energies for pentacene with the unit cell parameters redefined are presented in table 4.1, and these surfaces are indicated schematically in figure 4.8.

Table 4.1 *Formation energy E_{form} and surface energy γ of pentacene surfaces [78].*

Pentacene surface	E_{form}/cell [eV]	γ [meV/A^2]
(001)	0.15	3.1
(010)	0.45	4.8
(1-10)	0.71	4.7
(110)	0.72	4.8
(100)	0.75	6.4

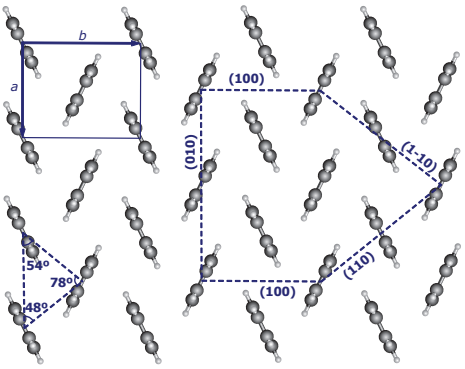

Figure 4.8 *A single ab-layer of pentacene is depicted. The unit cell of pentacene crystal contains two molecules. In the figure, the viewpoint of the (001) surface is along the longitudinal axis of the molecules. The angles between the facets are indicated as well.*

During crystal growth, pentacene molecules are expected to deposit preferentially on the planes that have the largest surface energy, in order to minimize the surface energy. As expected, the (001) surface is found to have the lowest surface energy in the calculation, so it should be the largest natural facet of the platelet-like pentacene crystals, which has been proven by the XRD analysis. The basal (001) plane is surrounded by the lateral (010), (1-10), and (110) planes; however, their areas are much smaller. The (100) facet has the highest surface energy, thus pentacene molecules are likely to cohere to this surface and this facet will mostly be absent in the equilibrium crystal shape. Hence, the crystal growth was theoretically predicted to proceed preferably along the minor axis in the *ab*-plane of the pentacene crystal under equilibrium conditions [78].

For thermodynamically grown crystals, these planes can be often recognized in the overall crystal shape and geometry. Jo and Takenaga [19] showed images of platelet-like pentacene single-crystals with a pair of large parallelogram planes and with a pair of large dendrite-shaped planes. The shape of these crystals is clearly dissimilar, however, there are no large differences; both crystal shapes have the basal (001) plane and the lateral planes in common (*i.e.* the (1-10) and (110) planes). The main branch of the dendritic crystal is parallel to the [010] direction. Natsume *et al.* [79] reported for pentacene crystals grown from solution that a low cooling rate leads to platelet-like crystal growth, whereas a high cooling rate (*i.e.* a high supersaturation) results in dendritic pentacene crystals.Figure 4.9 shows OM images of a platelet-like and a dendrite-like pentacene single-crystal obtained by physical vapor growth. In contrast to [18], here the lateral (010) planes can also be identified in the crystal shape and large terrace steps present on the (001) basal plane, besides the (1-10) and (110) planes. However, identifying the crystal planes in the overall pentacene crystal shape is not so easy in all cases; in these situations a more detailed XRD analysis to obtain the correct crystal orientation has to be performed.

4.4.2 Surface morphology of pentacene single-crystals

In figure 4.10, two optical microscopy images of selected areas of the (001) pentacene crystal plane are presented. On the surface of the crystal in figure 4.10A, an array of straight features can be distinguished. The straight features are parallel with each other, but the width between the features is variable. Besides these horizontal features, the surface appears to be

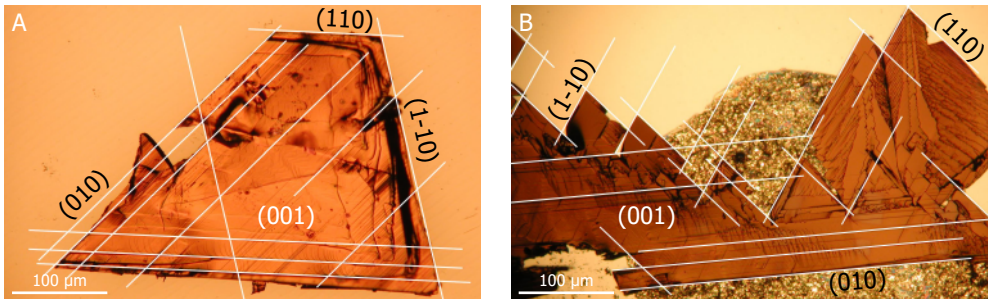

Figure 4.9 *Optical microscopy image of the (001) surface of A) a flaky, platelet-like pentacene single-crystal, and B) a dendrite-like pentacene single-crystal. The white lines indicate the (010), (1-10) and (110) crystal planes.*

rather flat. In figure 4.10B, these straight parallel features are again present on the crystal surface. Yet, also bent features with a random curvature are now clearly visible. These two types of features appear to continue their own path upon intersecting each other. A noticeable characteristic in both figures is that some of the straight parallel features peter out at a certain moment. A similar view is obtained when observing the pentacene crystals with the SEM (see figure 4.11).

Obviously, these features on the pentacene crystal are (quite large) terrace steps on the surface. To get more insight in the height of these terrace steps, AFM measurements were performed on different areas of several crystals.

The AFM images presented in figure 4.12 show the diverse step-like structures observed on the surface of the platelet-like pentacene single-crystals. For every scan, the height data, the deflection data and three cross-section curves are given.

Figure 4.12A shows a 5.0×5.0 µm^2 area of a pentacene crystal with a step-like structure of four terraces. The width of the terraces extends over 2 - 3 micrometers. The terraces were found to be flat at the molecular level and defects like pinholes, cavities or cracks were not observed. It is also noteworthy that individual two-dimensional islands were not found on the terraces. The appearance of wide terraces with no islands suggests that the as-grown single-

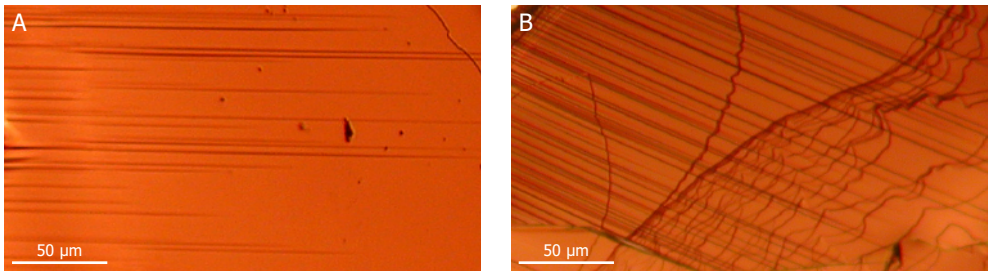

Figure 4.10 *Optical microscope images of selected areas of a pentacene single-crystal under normal illumination, showing A) straight, parallel features, and B) a combination of straight, parallel features and randomly curved features on the surface.*

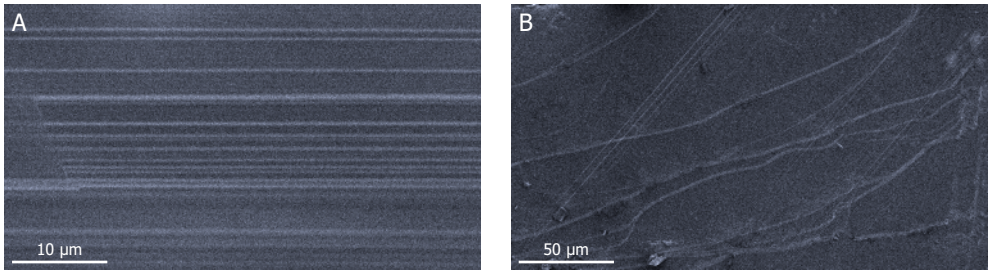

Figure 4.11 *Scanning electron microscopy images of selected pentacene single-crystal areas showing A) straight, parallel features, and B) randomly curved features on the surface.*

crystals are perfect with no defects. On a few very flat crystals, surprisingly wide terrace with widths of several tens of micrometers have been seen, even up to 50 µm width (not shown). Note these crystals with very large terraces and only occasionally a monomolecular terrace step are the best for fabricating field-effect devices with a high charge carrier mobility [48].

All terrace steps observed in figure 4.12A are ca. 1.3 - 1.5 nm high, see the cross section lines. This height matches the interlayer *d*(001) spacing value of 1.41 nm obtained in the XRD measurements on single-crystalline pentacene. Therefore, it can be concluded that the surface of the platelet-like pentacene single-crystals corresponds to the (001) crystal plane. Obviously, these terrace steps are elementary pentacene steps that have a height of one pentacene monolayer. More statistics on these steps will be presented in chapter 5. The pentacene crystal surface structure as shown in figure 4.12A is the morphology presented in most literature [16,80]. Typical for this morphology is that the terrace steps are straight and run parallel, suggesting that the samples are single-crystalline.

On the 5.0×5.0 µm^2 crystal surface area shown in figure 4.12B, again monomolecular terrace steps of about 1.4 nm high are present. In this case, the terrace steps are neither straight nor aligned parallel, but curved. There is no particular preference in the curvature or direction of the steps, yet the steps do not cross each other. The width of the terraces extends over 0.1 - 3.0 micrometer. In Figure 4.12C, an 80×80 µm^2 AFM image of a pentacene single-crystal area is displayed. Large terrace steps up to several tens of nanometers in height are present, besides the curved 1.4 nm high monolayer steps. The terraces are continuous up to reaching a large terrace step, *i.e.* the 1.4 nm high terrace steps do not intersect. The resemblance of this morphology with rice fields on an oriental hill side is striking.

In Figure 4.12D, a 10×10 µm^2 scan of a pentacene crystal, an array of large straight and parallel terrace steps can be observed. On the first hand, the step-like structure looks similar to the one shown in figure 4.12A. However, the height of these multilayer terrace steps ranges between 4 - 6 nanometers and no individual 1.4 nm monomolecular steps are present. The steps consist of three or four pentacene monolayers together, having a height of about 4.2 nm and 5.6 nm, respectively. Other AFM measurements (not presented) showed the presence of very large many-layer terrace steps, with step heights up to tens and even hundreds of nanometers. Clearly, such large terrace steps will demote the in-plane charge carrier mobility, as the mobility μ in the *ab*-plane is larger than μ along the *c** axis [81,82].

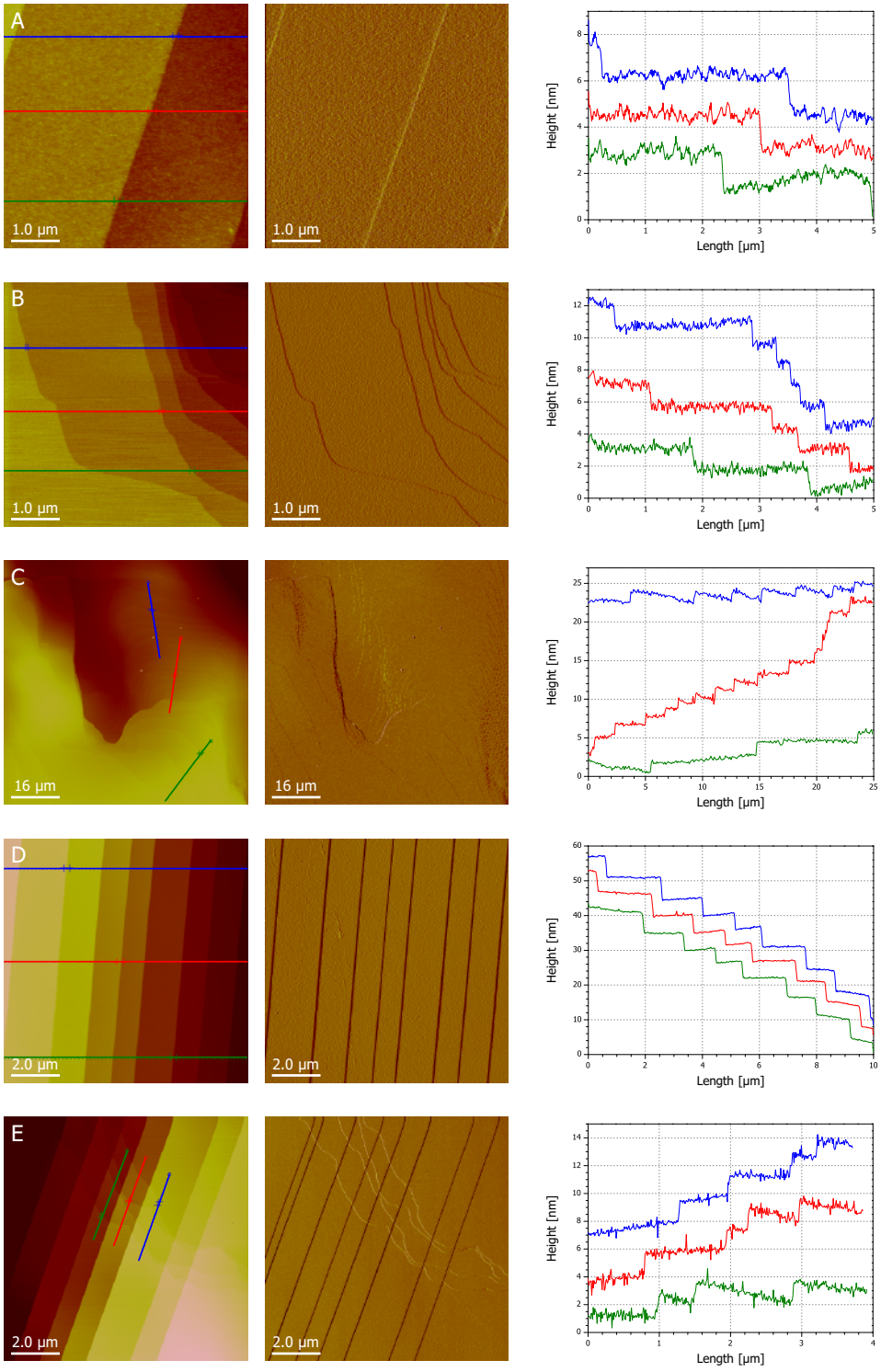
A
1.0 µm
1.0 µm
Height [nm]
Length [µm]
B
1.0 µm
1.0 µm
Height [nm]
Length [µm]
C
16 µm
16 µm
Height [nm]
Length [µm]
D
2.0 µm
2.0 µm
Height [nm]
Length [µm]
E
2.0 µm
2.0 µm
Height [nm]
Length [µm]

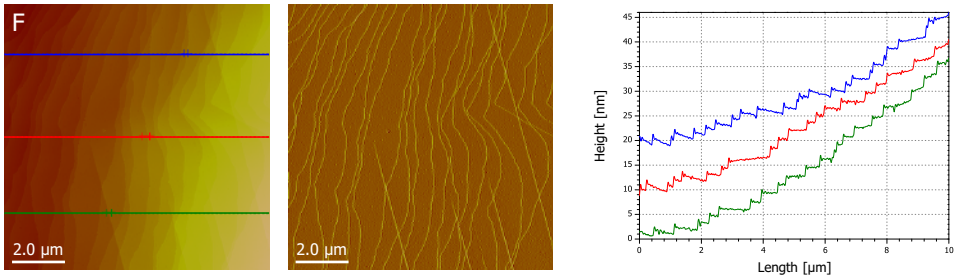

Figure 4.12 *AFM images on different areas of several as-grown pentacene single-crystals showing the diverse step-like structures observed on the surface of the plate-like crystals. For every scan, the height and deflection data and three cross-section curves are given. For more details, see the text. (Z_{AFM} = 10, 20, 150, 50, 50 and 75 nm, respectively).*

A similar multilayer structure can be seen in the 10 × 10 µm^2 map in figure 4.12E. Eight large straight vertical steps, 4 to 9 nm high, are present in the image from right top to left bottom. Superimposed on this structure are four curved monomolecular terrace steps, 1.4 nm high, running from left top to right bottom. Note the prolongation of the monolayer steps over the different terraces, irrespective of the larger terrace steps they go across.

Finally, the morphology shown in figure 4.12F of a 10 × 10 µm^2 pentacene crystal area illustrates the sixth surface morphology observed. Present here are over twenty terraces (width < 1.0 µm, length > 10.0 µm), with curved monolayer terrace steps. Interesting here are the five straight and parallel steps present in the right bottom of the image that seem to *originate* at this place.

Note that in the surface morphology study on pentacene single-crystals by Zeng *et al.* [16], no two-dimensional joint islands or screw dislocations were found, as has been for other organic molecular single-crystals, but only monomolecular and larger terrace steps [17,19]. The AFM and dark-light OM images presented in figures 4.13 show that both two-dimensional joint islands and spiral dislocations in fact can be found on the pentacene (001) crystal plane.

4.4.3 Growth mechanism of pentacene single-crystals

From the surface morphologies observed in figures 4.12 and 4.13, the following conclusions on the growth mechanism of pentacene single-crystals are drawn. First, the terraces are very flat and no small two- or three-dimensional islands are present on the individual terraces.

The morphology in figure 4.12A-C point towards a *step flow* type of crystal growth in the direction perpendicular to the *ab*-plane of the crystal. The molecularly flat terraces have a low density of molecular steps that are separated by wide terraces. At the crystal growth temperature, pentacene molecules deposited on the (001) terraces have enough energy to diffuse towards a step edge, where they will remain as this minimizes the surface energy. The result is that the terrace step edge 'moves forward' over the crystal surface. It can be seen in figure 4.12C that some larger terrace steps are the result of piling of elementary steps (*i.e.* step bunching), as the monomolecular terrace steps coincide together.

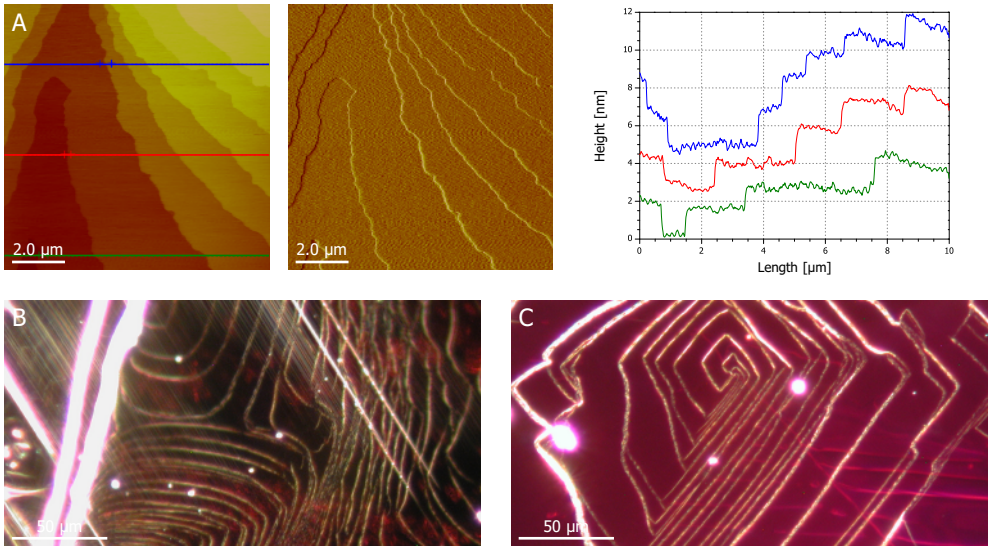

Figure 4.13 *AFM (height, deflection and cross-section curves) and two dark-light optical microscopy images of a pentacene single-crystal surface, showing the presence of A-B) two-dimensional joint islands (Z_{AFM} = 20 nm), and C) spiral screw dislocation surface steps.*

The aspect that in figure 4.12A the terrace steps are straight and aligned parallel, indicates the thermodynamically most stable crystal planes have been formed. The randomly curved terrace steps in figure 4.12B-C show this is not always the case. To acquire more insight on this, it is recommended to correlate the surface morphology with the exact growth temperature (*viz.* the location of crystal growth in the tube furnace).

Nucleation of new 'islands' on the (001) crystal plane is not easy, due to the increase in surface energy [21,78]; thus step flow is the predominant crystal growth mode. Nevertheless, the nucleation of new individual islands on the crystal surface happens occasionally, as can be seen in figures 4.13. Now, obviously from the spiral steps, the three-dimensional island in figure 4.13C is the result of a spiral dislocation. However, different to the acene crystals in [21], this was only observed occasionally and the (001) faces of pentacene single-crystals are typically not covered with spiral steps protruding from screw dislocations. As the two three-dimensional islands in figure 4.13B seem to originate at a huge terrace step, it can be expected that these islands started to nucleate at a defect spot or impurity. Yet, after nucleation, further growth of these islands proceeds via two-dimensional step flow as well.

The array of large straight steps observed in figure 4.12D can be explained by the piling of elementary steps (*i.e.* step bunching), similar to [16] and [18]; yet, it remains remarkable that no monomolecular steps are observed at all on the terraces in-between the large steps.

For the crystal surface morphologies of figure 4.12E-F, an additional model is needed. The concurrent presence of monomolecular (curved) terrace steps and larger (straight and parallel) terrace steps that extend over the crystal surface can be described by the introduction of stress-induced steps after crystal growth, see figure 4.14. The left side of the

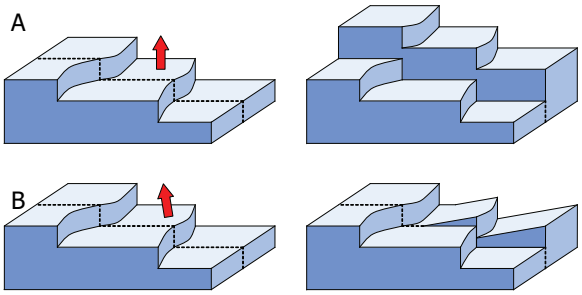

Figure 4.14 *Model for the stress-induced terrace steps observed on the surface of pentacene single-crystals in A) Figure 4.12E and B) Figure 4.12F.*

image shows the as-grown crystal surface, the right side the crystal surface after a stress is applied perpendicular or with an angle on the crystal. The resulting morphologies in figure 4.14A and B correspond to the ones observed experimentally in figure 4.12E and F, respectively. In other words, the original crystal surface only had monomolecular terrace steps, and the array of large steps is the result of stress-induced sliding of crystal planes at a later moment. The origin of this crystal plane sliding can be either temperature-induced stress from cooling the crystals after growth too rapidly, or results from applied forces during harvesting or subsequent handling on the crystals.

4.5 Concluding Remarks

In this chapter, the crystal structure, geometry and surface morphology of pentacene single-crystals grown by physical vapor transport were investigated by XRD, OM, AFM and SEM, as these crystals are applied as substrate in the fabrication of devices in the upcoming chapters. The experimental results show that the basal surface of the platelet-like pentacene single-crystals corresponds to the (001) crystal plane, and often the lateral (1-10), (010) and (110) planes can be identified in the crystal shape as well.

On the crystal surface, pentacene monomolecular terrace steps of 1.4 nm high are present, yet also larger terrace steps up to tens and even hundreds of nanometers can be found. In some cases, the terrace steps are straight and parallel aligned, which indicates the thermodynamically most stable crystal planes have been formed; however, in other cases, the steps are randomly curved.

The observed pentacene single-crystal morphology shows a *step flow* type of crystal growth is the dominant growth mechanism. Nevertheless, the presence of large terrace steps, two-dimensional joint islands and screw dislocations on the pentacene surface shows that the crystal growth is not limited to this type of growth. Finally, the observed prolongation of monolayer steps over different terraces, irrespective the presence of larger terrace steps, can be described by the introduction of stress-induced steps after crystal growth.

4.6 References

[1] Briggs, J.B.; Miller, G.P.; "[60]Fullerene-acene chemistry: a review"; *C.R. Chimie*; 9; **2006**; 916-927

[2] Mondal, R.; Shah, B.K.; Neckers, D.C.; "Photogeneration of heptacene in a polymer matrix"; *J. Am. Chem. Soc.*; 128; **2006**; 9612-9613

[3] Bendikov, M.; Wudl, F.; Perepichka, D.F.; "Tetrathriafulvalenes, oligoacenes, and their buckminster fullerene derivatives: the brick and mortar of organic electronics"; *Chem. Rev.*; 104; **2004**; 4891-4945

[4] Moss, G.P.; "Nomenclature of fused and bridged fused ring systems (IUPAC recommendations 1998)"; *Pure Appl. Chem.*; 70; **1998**; 143-216

[5] Dimitrakopoulos, C.D.; Malenfant, P.R.L.; "Organic thin film transistors for large area electronics"; *Adv. Mater.*; 14; **2002**; 99-117

[6] Ito, K.; Suzuki, T.; Sakamoto, Y.; Kubota, D.; Inoue, Y.; Sato, F.; Tokito, S.; "Oligo(2,6-anthrylene)s: acene-oligomer approach for organic field-effect transistors"; *Angew. Chem. Int. Ed.*; 42; **2003**; 1159-1162

[7] Wolak, M.A.; Jang, B.; Palilis, L.C.; Kafafi, Z.H.; "Functionalized pentacene derivatives for use as red emitters in organic light-emitting diodes"; *J. Phys. Chem. B*; 108; **2004**; 5492-5499

[8] Odom, S.A.; Parkin, S.R.; Anthony, J.E.; "Tetracene derivatives as potential red emitters for organic LEDs"; *Org. Lett.*; 5; **2003**; 4245-4248

[9] Lloyd, M.T.; Mayer, A.C.; Tayi, A.S.; Bowen, A.M.; Kasen, T.G.; Herman, D.J.; Mourey, D.A.; Anthony, J.E.; Malliaras, G.G.; "Photovoltaic cells from a soluble pentacene derivative"; *Org. Elect.*; 7; **2006**; 243-248

[10] Kymissis, I.; Organic field effect transistors - theory, fabrication and characterization; **2009**; Springer; New York, NY, U.S.A.

[11] Yang, H.; Shin, T.J.; Ling, M.M.; Cho, K.; Ryu, C.Y.; Bao, Z.; "Conducting AFM and 2D GIXD studies on pentacene thin films"; *J. Am. Chem. Soc.*; 127; **2005**; 11542-11543

[12] Shtein, M.; Mapel, J.; Benziger, J.B.; Forrest, S.R.; "Effects of film morphology and gate dielectric surface preparation on the electrical characteristics of organic-vapor-phase-deposited pentacene thin-film transistors"; *Appl. Phys. Lett.*; 81; **2002**; 268-270

[13] Heringdorf, F.J.M. zu; Reuter, M.C.; Tromp, R.M.; "Growth dynamics of pentacene thin films"; *Nature*; 412; **2001**; 517

[14] Ruiz, R.; Choudhary, D.; Nickel, B.; Toccoli, T.; Chang, K.C.; Mayer, A.C.; Clancy, P.; Blakely, J.M.; Headrick, R.L.; Iannotta, S.; Malliaras, G.G.; "Pentacene thin film growth"; *Chem. Mater.*; 16; **2004**; 4497-4508

[15] Witte, G.; Wöll, C.; "Growth of aromatic molecules on solid substrates for applications in organic electronics"; *J. Mater. Res.*; 19; **2004**; 1889-1916

[16] Zeng, X.; Qiu, Y.; Qiao, J.; Dong, G.; Wang, L.; "Morphological characterization of pentacene single crystals grown by physical vapor transport"; *Appl. Surf. Sci.*; 253; **2007**; 3581-3585

[17] Wang, H.; Xie, Z.Q.; Yang, B.; Shen, F.Z.; Li, Y.P.; Ma, Y.G.; "Several slice-like organic crystals grown by the physical vapor transport method: combining atomic force microscopy and X-ray diffraction to explore the characteristics of crystal formation"; *Cryst. Eng. Comm.*; 10; **2008**; 1252-1257

[18] Zhang, P.; Deng, J.; Zeng, X.; Zheng, L.; Qiu, Y.; Zhong, H.; Fan, Y.; Huang, J.; Zhang, J.; Xu, K.; "Growth mechanism of large-size anthracene single crystals grown by a solution technique"; *J. Cryst. Growth*; 311; **2009**; 4708-4713

[19] Jo, S.; Takenaga, M.; "Morphologies of pentacene crystals obtained by physical vapor growth technique"; *Jpn. J. Appl. Phys.*; 49; **2010**; 078002

[20] Zhang, P.; Zeng, X.; Deng, J.; Huang, K.; Bao, F.; Qiu, Y.; Xu, K.; Zhang, J.; "Growth mechanism of large-size rubrene single crystals grown by a solution technique"; *Jpn. J. Appl. Phys.*; 49; **2010**; 095501

[21] Cuppen, H.M.; Graswinckel, W.S.; Meekes, H.; "Screw dislocations on polycenes: a requirement for crystallization"; *Cryst. Growth Des.*; 4; **2004**; 1351-1357

[22] Dodabalapur, A.; Torsi, L.; Katz, H.E.; "Organic transistors: two-dimensional transport and improved electrical characteristics"; *Science*; 268; **1995**; 270-271

[23] Dinelli, F.; Murgia, M.; Levy, P.; Cavallini, M.; Biscarini, F.; "Spatially correlated charge transport in organic thin film transistors"; *Phys. Rev. Lett.*; 92; **2004**; 116802

[24] Holmes, D.; Kumaraswamy, S.; Matzger, A.J.; Vollhardt, K.P.C.; "On the nature of nonplanarity in the [N]phenylenes"; *Chem. Eur. J.*; 5; **1999**; 3399-3412

[25] Gross, L.; Mohn, F.; Moll, N.; Liljeroth, P.; Meyer, G.; "The chemical structure of a molecule resolved by atomic force microscopy"; *Science*; 325; **2009**; 1110-1114

[26] Pentacene; Sigma-Aldrich; www.sigmaaldrich.com; last visited on 21-02-2011.

[27] Bendikov, M.; Wudl, F.; Perepichka, D.F.; "Tetrathriafulvalenes, oligoacenes, and their buckminster-fullerene derivatives: the brick and mortar of organic electronics"; *Chem. Rev.*; 104; **2004**; 4891-4945

[28] Mills, W.H.; Mills, M.; "The synthetical production of derivatives of dinaphthanthracene"; *J. Chem. Soc.*; 101; **1912**; 2194-2208

[29] Clar, E.; John, Fr.; "Über eine neue Klasse tiefgefärbter radikalischer Kohlenwasserstoffe und über das vermeintliche Pentacen von E. Philippi; gleichzeitig Erwiderung auf Bemerkungen von Roland Scholl und Oskar Boettger. (Zur Kenntnis mehrkerniger aromatischer Kohlenwasserstoffe und ihrer Abkömmlinge, VII. Mitteil.)"; *Chem. Ber.*; 63; **1930**; 2967-2977

[30] Allen, C.F.H.; Gates, J.W.; "A new synthesis of the pentacene ring system"; *J. Am. Chem. Soc.*; 65; **1943**; 1502-1503

[31] Bailey, W.J.; Madoff, M.; "Cyclic dienes II. A new synthesis of pentacene"; *J. Am. Chem. Soc.*; 75; **1953**; 5603-5604

[32] Anthony, J.E.; "The larger acenes: versatile organic semiconductors"; *Angew. Chem. Int. Ed.*; 47; **2008**; 452-483

[33] Nijegorodov, N.; Ramachandran, V.; Winkoun, D.P.; "The dependence of the absorption and fluorescence parameters, the intersystem crossing and internal conversion rate constants on the number of rings in polyacene molecules"; *Spectrochimica Acta A*; 53; **1997**; 1813-1824

[34] Pentacene; Polysis; www.polysislab.com/html/pro2.html; last visited on 09-03-2010.

[35] Fujikake, H.; Suzuki, T.; Murashige, T..; Sato, F.; "Self-assembled submicron-height terrace structures of pentacene single crystals formed in liquid crystal cells"; *Liq. Cryst.*; 33; **2006**; 1051-1057

[36] Nagano, M.; Hasegawa, T.; Myoujin, N.; Yamaguchi, J.; Itaka, K.; Fukumoto, H.; Yamamoto, T.; Koinuma, H.; "The first observation of 1H-NMR spectrum of pentacene"; *Jpn. J. Appl. Phys.*; 43; **2004**; L315-L316

[37] Tao, C.L.; Zhang, X.H.; Zhang, F.J.; Liu, Y.Y.; Zhang, H.L.; "Solution processed pentacene thin films and their structural properties"; *Mat. Sci. Eng. B*; 140; **2007**; 1-4

[38] Minakata, T.; Natsume, Y.; "Direct formation of pentacene thin films by solution process"; *Synth. Met.*; 153; **2005**; 1-4

[39] Fujikake, H.; Suzuki, T.; Isaka, F.; Sato, F.; "Orientation-controlled growth of pentacene single crystal films on an alignment layer using liquid crystal as solvent"; *Jpn. J. Appl. Phys.*; 43; **2004**; L536-539

[40] Anhony, J.; "Engineered pentacenes"; Ch. 3 in Organic Electronics – Materials, manufacturing and applications; Ed. Klauk, H.; **2006**; Wiley-VCH; Weinhiem, Germany

[41] Herwig, P.T.; Müllen, K.; "A soluble pentacene precursor: synthesis, solid-state conversion into pentacene and application in a field-effect transistor"; *Adv. Mater.*; 11; **1999**; 480-483

[42] Afzali, A.; Dimitrakopoulos, C.D.; Breen, T.L.; "High-performance, solution-processed organic thin film transistors from a novel pentacene precursor"; *J. Am. Chem. Soc.*; 142; **2002**; 8812-8813

[43] Park, S.K.; Jackson, T.N.; Anthony, J.E.; Mourey, D.A.; "High mobility solution processed 6,13-bis(triisopropyl-silylethynyl) pentacene organic thin film transistors"; *Appl. Phys. Lett.*; 91; **2007**; 063514

[44] Gundlach, D.J.; Jackson, T.N.; Schlom, D.G.; Nelson, S.F.; "Solvent-induced phase transition in thermally evaporated pentacene films"; *Appl. Phys. Lett.*; 74; **1999**; 3302-3304

[45] Mattheus, C.C.; Dros, A.B.; Baas, J.; Oostergetel, G.T.; Meetsma, A.; Boer, J.L. de; Palstra, T.T.M.; "Identification of polymorphs of pentacene"; *Synth. Met.*; 138; **2003**; 475-481

[46] Kuo, C.C.; Jackson, T.N.; "Direct lithographic top contacts for pentacene organic thin-film transistors"; *Appl. Phys. Lett.*; 94; **2009**; 053304

[47] Kuo, C.C.; High performance small-molecule organic thin film transistors; PhD Thesis; **2005**; Pennsylvania State University; Pennsylvania, PA, USA

[48] Jurchescu, O.D.; *private communication*

[49] Desijaru, G.R.; Gavezzotti, A.; "Crystal structures of polynuclear aromatic hydrocarbons. Classification, rationalization and prediction from molecular structure"; *Acta Cryst. B*; 45; **1989**; 473-482

[50] Gavezzotti, A.; Desijaru, G.R.; "A systematic analysis of packing energies and other packing parameters for fused-ring aromatic hydrocarbons"; *Acta Cryst. B*; 44; **1988**; 427-434

[51] Cornil, J.; Beljonne, D.; Calbert, J.-P.; Brédas, J.-L.; "Interchain interactions in organic π-conjugated materials: impact on electronic structure, optical response, and charge transport"; *Adv. Mater.*; 13; **2001**; 1053-1119

[52] Jurchescu, O.D.; Molecular organic semiconductors for electronic devices; PhD Thesis; **2006**; University of Groningen; Groningen, The Netherlands

[53] Mattheus, C.C.; Dros, A.B.; Baas, J.; Meetsma, A.; Boer, J.L.; Palstra, T.T.M.; "Polymorphism in pentacene"; *Acta Cryst. C*; 57; **2001**; 939-941

[54] Mattheus, C.C.; Polymorphism and electronic properties of pentacene; PhD Thesis; **2002**; University of Groningen; Groningen, The Netherlands

[55] Cheng, Y.C.; Silbey, R.J.; Silva Filho, D.A. da; Calbert, J.P.; Cornil, J.; Brédas, J.-L.; "Three-dimensional band structure and bandlike mobility in oligoacene single crystals: A theoretical investigation"; *J. Chem. Phys.*; 118; **2003**; 3764-3774

[56] Campbell, R.B.; Robertson, J.M.; Trotter, J.; "The crystal and molecular structure of pentacene"; *Acta Cryst.*; 14; **1961**; 705-711

[57] Campbell, R.B.; Robertson, J.M.; Trotter, J.; "The crystal structure of hexacene, and a revision of the crystallographic data for tetracene"; *Acta Cryst.*; 15; **1962**; 289-290

[58] Siegrist, T.; Kloc, C.; Schön, J.H.; Batlogg, B.; Haddon, R.C.; Berg, S.; Thomas, G.A.; "Enhanced physical properties in a pentacene polymorph"; *Angew. Chem. Int. Ed.*; 40; **2001**; 1732-1736

[59] Siegrist, T.; Besnard, C.; Haas, S.; Schiltz, M.; Pattison, P.; Chernyshov, D.; Batlogg, B.; Kloc, C.; "A polymorph lost and found: the high-temperature crystal structure of pentacene"; *Adv. Mater.*; 19; **2007**; 2079-2082

[60] Northrup, J.E.; Tiago, M.L.; Louie, S.G.; "Surface energetics and growth of pentacene"; *Phys. Rev. B*; 66; **2002**; 121404(R)

[61] Goose, J.E.; First, E.L.; Clancy, P.; "Nature of step-edge barriers for small organic molecules"; *Phys. Rev. B*; 81; **2010**; 205310

[62] Tersigni, A.; Shi, J.; Jiang, D.T.; Qin X.R.; "Structure of tetracene films on hydrogen-passivated Si(001) studied via STM, AFM, and NEXAFS"; *Phys. Rev. B*; 74; **2006**; 205326

[63] Al-Mahboob, A.; Sadowski, J.T.; Nishihara, T.; Fujikawa, Y.; Xue, Q.K.; Nakajima, K.; Sakurai, T.; "Epitaxial structures of self-organized, standing-up pentacene thin films studied by LEEM and STM"; *Surf. Sci.*; 601; **2007**; 1304-1310

[64] Virkar, A.A.; Mannsfeld, S.; Bao, Z.; Stingelin, N.; "Organic semiconductor growth and morphology considerations for organic thin-film transistors"; *Adv. Mater.*; 22; **2010**; 3857-3875

[65] Last, J.A.; Hillier, A.C.; Hooks, D.E.; Maxson, J.B.; Ward, M.D.; "Epitaxially driven assembly of crystalline molecular films on ordered substrates"; *Chem. Mater.*; 10; **1998**; 422-437

[66] Laudise, R.A.; Kloc, Ch.; Simpkins, P.G.; Siegrist, T.; "Physical vapour growth of organic semiconductors"; *J. Cryst. Growth*; 187; **1998**; 449-454

[67] Miyamoto, S.; Shimada, T.; Ohtomo, M.; Chikamatsu, A.; Hasegawa, T.; "Direct observation of gas phase nucleation during physical vapor transport growth of organic single crystals using a transparent furnace"; *Jpn. J. Appl. Phys.*; 48; **2009**; 118003

[68] Arkenbout, A.H.; *private communication*

[69] Podzorov, V.; "Charge carrier transport in single-crystal organic field-effect transistors"; Ch. 2 in Organic field-effect transistors; Ed. Bao, Z.; Locklin, J.; **2007**; CRC Press; Taylor & Francis Group; New York, NY, U.S.A.

[70] Jo, S.; Yoshikawa, H.; Fujii, A.; Takenaga, M.; "Surface morphologies of anthracene single crystals grown from vapor phase"; *Appl. Surf. Sci.*; 252; **2006**; 3514-3519

[71] Kloc, Ch.; Simpkins, P.G.; Siegrist, T.; Laudise, R.A.; "Physical vapor growth of centimeter-sized crystals of *α*-hexathiophene"; *J. Cryst. Growth*; 182; **1997**; 416-427

[72] Kloc, Ch.; "Single crystal growth of organic semiconductors for field effect applications"; *Proc. SPIE*; 6336; **2006**; 633606

[73] McGhie, A.R.; Garito, A.F.; Heeger, A.J.; "A gradient sublime for purification and crystal growth of organic donor and acceptor molecules"; *J. Cryst. Growth*; 22; **1974**; 295-297

[74] Boer, R.W.I. de; Gershenson, M.E.; Morpurgo, A.F.; Podzorov, V.; "Organic single-crystal field-effect transistors"; *Phys. Stat. Sol. A*; 201; **2004**; 1302-1331

[75] Bragg, W.L.; "The diffraction of short electromagnetic waves by a crystal"; *Proc. Cambr. Phil. Soc.*; 17; **1913**; 43-57.

[76] Docherty, R.; Clydesdale, G.; Roberts, K.J.; Bennema, P.; "Application of Bravais-Friedel-Donnay-Harker, attachment energy and Ising models to predicting and understanding the morphology of molecular crystals"; *J. Phys. D: Appl. Phys.*; 24; **1991**; 89-99

[77] Berkovitch-Yellin, Z.; "Toward an ab initio derivation of crystal morphology"; *J. Am. Chem. Soc.*; 107; **1985**; 8239-8253

[78] Northrup, J.E.; Tiago, M.L.; Louie, S.G.; "Surface energetics and growth of pentacene"; *Phys. Rev. B*; 66; **2002**; 121404(R)

[79] Natsume, Y.; Minakata, T.; Aoyagi, T.; "Pentacene thin film transistors fabricated by solution process with directional crystal growth"; *Org. Electr.*; 10; **2009**; 107-114

[80] Jurchescu, O.D.; Popinciuc, M.; Wees, B.J. van; Palstra, T.T.M.; "Interface-controlled, high-mobility organic transistors"; *Adv. Mater.*; 19; **2007**; 688-692

[81] Fraboni, B.; Fraleoni-Morgera, A.; Cavallini, A.; "Three-dimensional anisotropy density of states distribution and intrinsic-like mobility in organic single crystals"; *Org. Electr.*; 11; **2010**; 10-15

[82] Jurchescu, O.D.; Baas, J.; Palstra, T.T.M.; "Effect of impurities on the mobility of single crystal pentacene"; *Appl. Phys. Lett.*; 84; **2004**; 3061-3063

Chapter 5

Pentacene Single-Crystals: Oxidation and Surface Treatment

Chapter 5: Pentacene Single-Crystals: Oxidation and Surface Treatment

Abstract

The arrangement and morphology of 6,13-pentacenequinone impurities on the surface and in the bulk of pentacene single-crystals have been studied. By using the combination of low-kV SEM contrast, AFM step height differences and AFM tapping-mode phase contrast, it is observed that the quinone material is preferentially located as a 0.9 nm thick monolayer (partly) covering the pentacene crystal surface. Cleaving experiments showed no large patches of quinone impurities are present in the crystal bulk.

In order to remove the 6,13-pentacenequinone monolayer selectively from the pentacene single-crystal surface, the partly-oxidized crystals were heated in vacuum at a fixed temperature overnight. Performing the heating treatment at 75-80 °C removes the quinone material completely, yielding an unoxidized pentacene single-crystal with a clean and undamaged surface morphology that is suitable for subsequent device fabrication.

5.1 Introduction

One of the crucial aspects for the realization of long-term reliable organic electronic applications is the aging and air stability of the organic materials applied in the devices. Oxidation degradation is widely encountered in conjugated organic materials and is believed to be one of the major reasons for early device failure. It is well known that organic materials are sensitive to photo-oxidation, when they come into contact with oxygen under light exposure. As it may be needed to process and handle the materials at ambient conditions (to fabricate at a low cost), degradation of organic films at these conditions has to be minimal and prevented as much as possible. Therefore, it is important to investigate the oxidization process.

For pentacene, the most common oxidation product is 6,13-pentacenequinone [1,2]. As pentacene is normally synthesized from this quinone (*i.e.* small traces will still be present after purification), it is also the most common impurity that affects the conductivity of pentacene [3]. The quinone molecules can act as trapping centers for charge carriers [4] or can create scattering centers by distorting the pentacene lattice locally (*i.e.* the quinone molecules are non-planar and larger than pentacene molecules) [2].

If 6,13-pentacenequinone is present on the surface of pentacene thin films or crystals, either originating from impurities or due to photo-oxidation, it will form scattering sites at the conducting interface in the field-effect geometry and alter the level alignment significantly (see paragraph 8.2.2) [4]. The quinone molecules will reduce the mobility and, in a worst case, suppress the field-effect completely. The lower mobility of FET devices built on the surface of pentacene single-crystals, compared to the mobility observed for bulk pentacene (*e.g.* with SCLC spectroscopy), indicates the necessity of a structurally and chemically clean interface as well. From a fundamental point of view, a better understanding of the stability of organic semi-conductors in air is also important in connection with the 'flip crystal' technique, which has been used to study the intrinsic electronic properties of organic molecular crystals.

The aim of this chapter is therefore to study the stability of pentacene single-crystals towards oxidation, to examine the presence and arrangement of quinone impurities on the crystal bulk and surface, and to investigate the possibilities of obtaining a clean pentacene crystal surface that is free from oxidation products, as these crystals are applied as substrate in the fabrication of devices in the upcoming chapters.

5.2 Theoretical Background

In this section, two different aspects of the oxidation degradation of pentacene will be discussed. First, the degradation of pentacene upon exposure to oxygen and ambient conditions is reviewed. Second, the most common oxidation product of pentacene, namely 6,13-pentacenequinone, is looked into with more detail.

Investigating the influence of ambient conditions on organic molecular crystals similar to pentacene is important too (*i.e.* many similarities can be expected in the oxidation mechanisms due to the resemblance of the molecules involved and the intermolecular forces

present in these materials); therefore, a few results from studies on tetracene [5,6], rubrene [7-9] and anthracene [6] crystals will be mentioned as well.

5.2.1 Oxidation of pentacene

Some effects of ambient oxygen on the electrical properties of a pentacene film were already reported by Kuroda and Flood in the year 1961 [10]. Due to the rise of organic electronics, many studies have investigated the oxidation effects of exposing air to pentacene thin films in the last years [1,11-15]. Also, the device characteristics have improved by investigating the effects of environmental factors on pentacene field-effect transistors [1,12-14,16-18]. Both instantaneous and reversible effects, as well as long-term irreversible effects due to the presence of oxygen and water present in air on pentacene have been reported. When pentacene is exposed to oxygen, the oxygen molecules diffuse into the pentacene film and may interact with the pentacene molecules [11]. Several parameters seem to be important for the oxidation process: the presence of oxygen (and ozone), the presence of water (*e.g.* the humidity) and the presence of light to create 'reactive oxygen species'.

Purification of pentacene powder and crystal growth

Purification of pentacene powder to a high purity is quite a difficult task [2]. Normally, pentacene is synthesized from 6,13-pentacenequinone (see paragraph 4.2.1), and small traces of the quinone can still be found in the pentacene powder [15]. In fact, 6,13-pentacenequinone is present as the most dominant impurity in pentacene powder, as is shown by infrared (IR) spectroscopy and mass spectroscopy (MS) measurements by Jurchescu *et al.* [2]. With high-pressure liquid chromatography (HPLC), a 6,13-pentacenequinone impurity concentration of 0.68% is determined in commercial pentacene powder obtained from Aldrich (see Table 1). Without further purifying the pentacene powder, these quinone impurities will for a part be incorporated in the pentacene film or crystal after growth. In a typical pentacene single-crystal, vapor-grown from untreated pentacene powder, 6,13-pentacenequinone was found to be present at a concentration of 0.11% [2].

To improve the purity of pentacene powder, vacuum sublimation under a temperature gradient (see paragraph 2.4.4) is the only suitable technique; pentacene decomposes around its melting point disabling zone refining techniques [19]. The carbonyl groups at each side of the middle ring reduce the sublimation enthalpy of the quinone compared to the host molecule, The sublimation enthalpy of 6,13-pentacenequinone is 116.4 kJ/mol, which is about 24% lower than the 156.9 kJ/mol value for pentacene, both calculated from thermal desorption spectra [20]. Purification of pentacene powder takes place at ~160 °C in vacuum for several days [3]. Under these conditions, pentacene does not sublime yet, however the quinone impurities will sublime and thus be removed.

HPLC measurements revealed a 0.49% 6,13-pentacenequinone concentration in the pentacene powder after one vacuum sublimation purification step, and a 0.17% concentration after two purification steps. Single-crystals, vapor-grown from the double-cleaned powder, show a 0.028% 6,13-pentacenequinone concentration (the quinone concentration in single-crystals grown from once-purified powder is not mentioned) [2].

Table 5.1 *6,13-pentacenequinone impurity concentration in pentacene measured by HPLC in different stages of purification. Data obtained from [2].*

Pentacene	Stage of purification	[6,13-pentacene-quinone] (%)
Powder	As-received	0.68
Crystal	Vapor-grown from as-received powder	0.110 ± 0.006
Powder	After one sublimation step	0.49
Powder	After two sublimation steps	0.17
Crystal	Vapor-grown from double-cleaned powder	0.028 ± 0.004

Location of impurities in pentacene crystals

A common assumption was that the pentacenequinone impurity molecules are evenly distributed throughout the pentacene crystal lattice. Jurchescu *et al.* [15] demonstrated that this is not the case, but that the quinone is located preferentially at the surface of the pentacene crystals instead. From AFM measurements, they concluded that the quinone molecules agglomerate in patches that are distributed over the surface of the pentacene crystals. No detailed quantitative analysis is presented; however, it is remarked that the observed pentacenequinone *d*(001) steps of 1.8 nm high are five times more abundant on the surface than the 1.4 nm high pentacene *d*(001) steps. A consequence of their findings is that, if the pentacenequinone molecules are more located on the surface of the crystal than in the bulk, the measured mobility in field-effect devices will be significant lower than the mobility obtained by space-charge-limited current spectroscopy measurements.

Similar effects have been reported by Pflaum *et al.* [6] for 5,12-tetracenequinone ($C_{18}H_{10}O_2$) impurities in tetracene ($C_{18}H_{12}$) crystals. Gas chromatography (GC) measurements on the surface and the bulk of tetracene crystals show that the density of the quinone impurities is strongly enhanced at the surface of the crystals. The quinone concentration at the crystal surface is about one order of magnitude larger than the bulk impurity concentration (see figure 5.1). Faltermeier *et al.* [21] found no indication for an additional oxidation layer on the pentacene single-crystal surface. In later work, the presence of a 5,13-tetracenequinone surface layer of defined thickness on top of tetracene films exposed to ambient conditions is calculated, however [22,23].

Oxidation conditions

When pentacene crystals are exposed to ambient conditions for up to a few hours, minimal degradation is observed [17]. A possible explanation for this stability could be that the crystal structure of pentacene does not allow diffusion of oxygen molecules into the crystal lattice. However, pentacene packs in a herringbone arrangement with spacing between the planes of around 0.4 nm; large enough for diffusion of oxygen into the crystal [3]. Thus, when pentacene is exposed to ambient conditions, oxygen molecules can diffuse in and out the crystal lattice easily. The time required for oxygen molecules to penetrate the pentacene crystal bulk is on the order of tens of minutes (~100 minutes for a 15 μm thick crystal [16]).

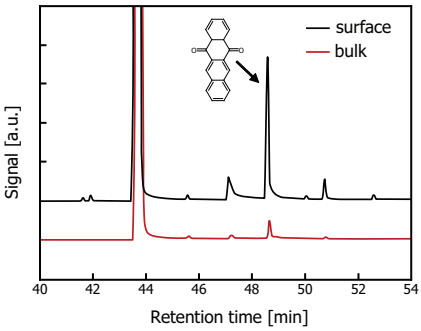

Figure 5.1 *Gas chromatography spectra obtained for the surface (black curve) and the bulk (red curve) of a sublimation-grown tetracene single-crystal. Impurities found at the surface and in the bulk are similar, but the absolute concentrations on the surface are about one order of magnitude larger. As indicated, the 48.8 min retention time peak belongs to 5,12-tetracenequinone. Figure with permission from [6].*

Jurchescu *et al.* [2] investigated the diffusion of oxygen in pentacene crystals and observed that this process is reversible and that no irreversible chemical reactions (*e.g.* oxidation to quinone) are taking place. Vollmer *et al.* [12,14] and Parisse *et al.* [24] confirmed these results, as they observed no irreversible changes in the electronic structure of pentacene films and crystals after exposure to oxygen in their ultraviolet photoelectron spectroscopy (UPS) measurements on the timescale of several hours, as long as the oxygen exposure is performed in the dark or under visible or near-UV light. XPS measurements by Yang *et al.* [13] are consistent with these findings. Kalb *et al.* [11] also showed that several hours of exposure to oxygen, in the presence of light, are necessary to observe significant and irreversible changes in the transfer characteristics of pentacene thin film transistors. Consequently, pentacene films and crystals are not very sensitive towards oxidation, as long as the samples are not exposed to UV-light.

Exposing the pentacene films to UV-light leads to a rapid degradation of the conjugated molecules [12]. A mixture of 'reactive oxygen species' (oxygen atoms, singlet oxygen and ozone) present under UV-irradiation readily oxidizes the pentacene molecule. De Angelis and co-workers [1] confirmed these results, as their mass spectroscopy experiments on pentacene thin films exposed to air indicate that light is essential to activate the reaction mechanism. Thus, it can be concluded that only the simultaneous presence of oxygen and UV-light can produce a significant oxidation of pentacene thin films.

Oxidation mechanism and oxidation products

There is much consensus on the fact that organic thin films and crystals are susceptible to oxidation and degradation, when exposed to ambient conditions. The reported data on the formed products after the exposure are however contradicting. For pentacene, most reports assume the formation of 6,13-pentacenequinone, by oxidation of the molecule at its most reactive positions (*e.g.* the 6 and 13 positions on the middle ring) [15]. Northrup *et al.* [25] reported first principle calculations for several hydrogen- and oxygen-related additions onto a pentacene molecule, showing the 6 and 13 positions are indeed the most reactive positions.

Theoretical studies predict various types of oxidation-related defect mechanisms for pentacene [1,11,17,26]. The formation of an intermediate endoperoxide across the most reactive central ring (an intramolecular bridge of a single oxygen atom) is a possibility. Also, the formation of a transitional intermolecular bridge, where a single oxygen atom is covalently

bound to the carbon atoms on the center rings of two neighboring pentacene molecules, is an option. An alternative is the replacement of a hydrogen atom by an oxygen atom in a pentacene molecule, forming an intermediate $C_{22}H_{13}O$ molecule.

Besides the formation of 6,13-pentacenequinone, various other oxidation products can be formed, especially when pentacene is exposed to reactive oxygen species created by UV-light. Vollmer *et al.* [12] conclude, from a combination of UPS, IR and AFM experiments on the influence of reactive oxygen species on pentacene thin films, that small volatile products are formed. IR spectroscopy on pentacene films upon exposure to UV-light in air indicate the formation of a variety of oxidized intermediate species, but no 6,13-pentacenequinone absorption could be identified. Significant mass losses of the films during UV-exposure observed by Yang *et al.* [13] in XPS measurements are consistent with the pentacene being oxidized by reactive oxygen species to highly volatile reaction products.

Mass spectroscopy measurements by De Angelis *et al.* [1] show a little formation of the oxidation products 6-hydroxypentacene, 6,13-pentacenequinone and 6,13-dihydroxy-pentacene in pentacene films stored for weeks in ambient conditions. Mattheus provided experimental evidence for the existence of $C_{22}H_{16}$ molecules in pentacene, when H_2 is used as carrier gas for growth of pentacene crystals [27].

Niemax *et al.* [5] investigated the content of chemical impurities present in tetracene crystals by gas chromatography. Several contaminants were visible in the spectra, with 5,12-tetracenequinone being the most significant impurity. In a follow up paper, Pflaum *et al.* [6] showed a more complete impurity profile for tetracene crystals grown by sublimation of two-step purified tetracene powder. In the GC spectra, besides 99.8% tetracene, four impurities were identified: 0.08% 5,12-tetracenequinone, 0.02% 5,12-dihydroxytetracene ($C_{18}H_{12}O_2$), 0.04% 5-hydroxytetracene ($C_{18}H_{14}O$) and 0.01% 5,12-dihydrotetracene ($C_{18}H_{14}$).

Rubrene (5,6,11,12-tetraphenylnaphthacene, $C_{42}H_{28}$) is expected to be much less prone to oxidation than tetracene or pentacene. In rubrene, a phenyl side group is located on the four most reactive sites towards oxidation of the tetracene backbone. Nevertheless, rubrene also reacts with oxygen and forms rubrene endoperoxide; however, the oxidation of rubrene is restricted to a thin surface layer [7,8,9]. Analysis on rubrene films after exposure to air by mass spectrometry analysis identified only rubreneperoxide ($C_{42}H_{28}O_2$) as impurity [7].

For anthracene ($C_{14}H_{10}$), the 9,10-anthracenequinone ($C_{14}H_8O_2$) impurity is mentioned as the major impurity present [6].

Morphology after oxidation

The few AFM studies on pentacene thin films after exposure to air give a somewhat dissimilar view on the photo-oxidation process. First of all, in [2] it is reported that exposure of pentacene crystals to air and light will cause slow oxidation, which preferentially takes place at the dislocations present. However, no further proof for this statement is presented.

Vollmer *et al.* [12] showed with AFM measurements that after UV-irradiation in air for one day (*e.g.* thus upon exposure to reactive oxygen species) the terraces of a pentacene film

became corrugated and sieve-like. The reactive species corroded the films both at the step edges as well as on the terraces, indicating no preferential reaction site. Yang *et al.* [13] investigated the aging of pentacene thin films stored in air and in light or dark for months. The films stored in light displayed pronounced surface corrugations, while the films stored in dark revealed fewer morphological changes.

An AFM study by Qiu *et al.* [18] showed the pentacene film morphology had changed after storage in ambient conditions for a week. The surface showed new features: small grain-like matter appeared in the pores between the pentacene grains. Based on IR adsorption spectra and phase contrast in AFM images, they contributed the degradation to adsorption of water molecules on the pentacene film.

5.2.2 6,13-pentacenequinone

Pure 6,13-pentacenequinone ($C_{22}H_{12}O_2$, 308,33 g/mol) has a yellow color. This oxidized form of pentacene belongs to the family of linear *para*-acenequinones, which are organic compounds formed by replacing two hydrogen atoms by two oxygen atoms in polycyclic aromatic hydrocarbons (PAHs). *Para*-quinones and their derivatives play an important role as industrial dyes, pigment materials and photochromic molecules [28,29]. Thin films of 6,13-pentacenequinone are stable in air [30] and have an insulating character [28], with a dielectric constant of 3.5 [15]. Jurchescu *et al.* [15] made use of these properties, by applying a 6,13-pentacenequinone film as gate dielectric in pentacene single-crystal OFETs (see paragraph 2.5.3). In this paragraph, the crystal structure of 6,13-pentacenequinone crystals and thin films is presented.

Crystal structure

The 6,13-pentacenequinone molecule is strictly planar, apart from the two carbonyl (C=O) side groups. The middle *p*-quinone ring adopts a flattened chair-like form, with the planar carbonyl groups at an angle of 3.1° out of the molecular plane [31].

A common packing motif adopted in crystals of planar organic molecules is the layered face-on-edge herringbone structure. 6,13-pentacenequinone in contrast has an almost co-planar stacking: the molecules are packed parallel within the layers and no internal herring-bone structure exists (see figure 5.2). The long molecular axes and planes of molecules in neighboring layers are tilted with respect to each other, which is also dissimilar to pentacene.

The pentacenequinone bulk phase has a monoclinic structure packed along the long axis of the molecule [29]. The first crystal structure and molecular packing analysis on 6,13-pentacenequinone was performed by Dzyabchenko and co-workers in 1979 [31]. In this work, the single-crystal unit cell parameters are as follows: a = 0.495 nm, b = 1.778 nm, c = 0.817 nm, $\alpha = \beta = 90.00°$, $\gamma = 93.26°$, and $\rho = 1.426$ g/cm^3 [20,31]. For the bulk, the d(001) plane spacing is 1.779 nm [15]. Due to tilting of the long molecular axis in neighboring layers, the pentacenequinone single-crystal also exhibits a layered structure along the (002) cleavage plane, with a d-spacing of 0.887 nm [32].

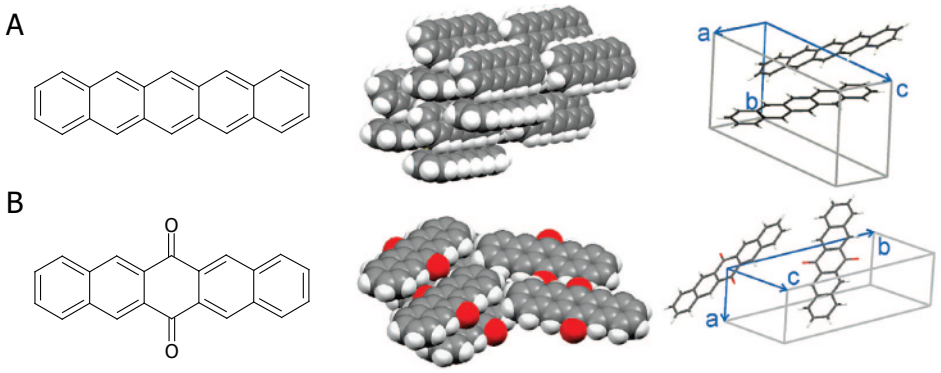

Figure 5.2 *Individual molecule and crystal structure of A) bulk pentacene, where molecules form a face-on-edge herringbone packing motif and a layered structure of upstanding molecules, and B) bulk 6,13-pentacenequinone, where the molecules are coplanarly stacked, forming a zigzag layered structure of upstanding molecules. Figure with permission from [20].*

Various studies on quinone thin films grown on inorganic substrates by thermal evaporation at room temperature show the existence of a thin film phase, besides the crystal bulk phase [28-30,32]. XRD measurements show the presence of a metastable substrate-induced strain phase ($d(001) = 1.27$ nm), besides the diffraction peaks from the bulk crystal planes ($d(002) = 0.87$ nm) [29,30]. AFM height histograms on evaporated 6,13-pentacenequinone films show an interplanar distance of 1.3 ± 0.2 nm [28] or 1.4 ± 0.2 nm [32]; both are comparable with the reported 1.27 nm interplanar distance of the strained film phase. Upon further film growth, the co-appearance of the bulk phase with steps of 1.8 nm was also observed [28].

As a result, two distinct crystallographic phases with two different orientations exist for 6,13-pentacenequinone, namely the bulk crystal phase with an interplanar distance $d(001) = 1.779$ nm and a metastable substrate-induced strain thin film phase with interplanar distance $d(001) = 1.27$ nm. As mentioned above, the bulk phase also exhibits a layered structure with $d(002) = 0.887$ nm; however, this structure is so far only observed in XRD measurements and not in AFM measurements. In other words, no 6,13-pentacenequinone monolayer films with the bulk phase and with vertical $d(002)$ terrace steps of 0.9 nm have been reported so far.

5.3 Experimental Procedure

The pentacene single-crystals used in this study were grown by a physical vapor transport method [33-35], after purification by vacuum sublimation under a temperature gradient [2,36] (see chapter 4 for more details). In order to investigate the presence and arrangement of 6,13-pentacenequinone impurities on the surface and in the bulk of pentacene single-crystals, various crystals were investigated by low-kV SEM and contact- and tapping-mode AFM (see chapter 3 for specific details). These techniques (and OM) were also applied to investigate the crystal surface morphology after the cleaving experiments, the water adsorption tests and the heating treatments.

For the Scotch-tape method cleaving experiments to investigate the crystal bulk, pentacene single-crystals were subtly positioned on a piece of double-sided carbon adhesive tape (SPI Supplies, 8 mm carbon tape) attached on a solid substrate for handling. A second piece of tape, attached on another solid substrate, was gently pressed to the sample and then removed, thereby cleaving the crystal.

For the heating treatment to selectively remove the quinone surface impurities, pentacene single-crystals were fixed with a small droplet of thermally conducting silver paste (Leitsilber 200) on a supporting silicon chip, and placed on a heater block in a vacuum chamber with base pressure $<10^{-7}$ mbar. All heating treatments were performed at a fixed temperature between 70 and 110 °C overnight (~16 h).

5.4 Results and Discussion

In this paragraph, the results from various experiments on the location and arrangement of 6,13-pentacenequinone impurities on the pentacene crystal surface and bulk will be discussed, as well as the results from the surface treatment experiments to obtain a clean pentacene crystal surface that is free from oxidation products.

5.4.1 The surface of partly-oxidized pentacene single-crystals

In order to investigate the presence and arrangement of 6,13-pentacenequinone impurities on the surface of pentacene single-crystals, various crystals were investigated by scanning electron microscopy. As can be seen in figure 5.3, the electron beam acceleration voltage has an enormous impact on the way a pentacene crystal appears in the final image. At a 5.0 kV beam voltage, no much contrast is observed on the pentacene crystal surface in the image; the only visible details (cracks, large surface steps, etc.) originate from topographic image contrast (see figure 5.3A). Charge build-up also occurs easily at this beam voltage, as can be noticed by some bright features at the right bottom side of the image. At a 0.5 kV beam voltage, a substantial contrast is observed on the surface of the pentacene crystal (see figure 5.3B). Interestingly, much detailed information about the surface morphology of the pentacene crystal becomes visible when imaging with this low beam voltage. An additional advantage of the lower acceleration voltage is no charge build-up is observed.

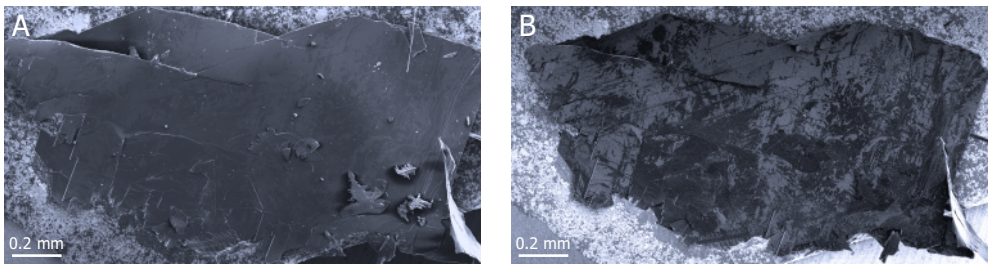

Figure 5.3 *SEM images of a pentacene single-crystal at A) 5.0 kV and B) 0.5 kV electron beam voltage.*

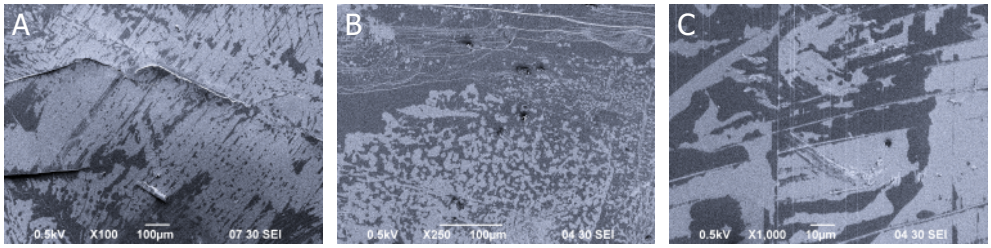

Figure 5.4 *SEM images of selected areas on three different, partly-oxidized pentacene single-crystals, illustrating the contrast difference observed on the crystal surface at a low 0.5 kV acceleration voltage. Please note the different magnifications between the images: x100, x250 and x1000, respectively.*

Figure 5.4 presents low-voltage SEM (LVSEM, *i.e.* imaging in a SEM with a low beam acceleration voltage between 0.1 and 5.0 kV [37,38]) images of selected areas on three different, partly-oxidized pentacene single-crystals at higher magnifications. Again, a clear contrast is visible on the crystal surface; light gray areas and dark gray areas are present next to each other. In figures 5.4A and C, the shape of the light and dark features appears to be related with the terrace steps on the surface. The features in figure 5.4B, on the other hand, seem to be more randomly orientated.

Reducing the energy of the electrons incident on a solid has a profound effect on the interactions that occur within that material [39]. Electrons in the energy range up to a few keV interact much stronger with the material through which they travel than is the case at higher energies. As a consequence, the distance an electron will penetrate a material decreases rapidly with decreasing incident energy. Besides that, the rate at which secondary electrons are produced (the SE yield) also increases rapidly with decreasing incident energy, making the SEM more sensitive to the chemical nature and topography of the surface.

By performing Monte Carlo simulations of the electron trajectories in a specimen, Joy [40] displayed the variation in beam interaction volume with beam energy. Both the electron range (*i.e.* the penetration depth of the primary electrons) and the interaction volume of the incident electrons are significantly reduced at low energies. Based on data for carbon samples in [41], it is calculated that for pentacene the range depth of the primary electrons decreases from ~800 nm at 5 kV to only ~20 nm at 0.3 kV energy.

Due to their low energy (<50 eV, by definition), only secondary electrons (SE) ejected from within a few nanometers from the sample surface can leave the specimen. The escape depth λ of SE is typically 3 - 6 nm (which corresponds to the first two to five top pentacene layers) [39]. Type 1 secondary electrons (SE1) are the electrons ejected from the outer shells of the specimen atoms near the surface by inelastic scattering with the primary electrons (PE). Besides the SE1 generated by incident primary electrons, also secondary electrons (SE2) produced by backscattered electrons (BE) that have enough kinetic energy to leave the sample are detected (see figure 5.5). Detected as well are secondary electrons (SE3) generated by BEs outside the sample (which will be further ignored).

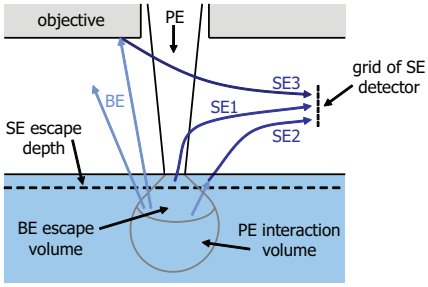

Figure 5.5 *Generation of SE1 and SE2 secondary electrons by primary electrons (PE) and by backscattered electrons (BE), respectively. SE3 electrons are generated outside the specimen when, for example, a BE strikes the bottom of the objective lens.*

It is important to distinguish between the SE1 and SE2 signals, since these two components have very different spatial distributions. At all voltages, the SE1 signal is localized within a few nanometers of the beam impact position and contains information from the specimen surface. The SE2 signal comes from a larger surface region around the beam point, that has a size of about one third of the total penetration depth of the primary electrons in radius. The SE2 signal is thus largely dependent on the beam acceleration voltage [39]. For pentacene, this corresponds to ~250 nm at 5 kV to ~6 nm at 0.3 kV. Typically, the SE2 signal is two to three times the SE1 signal in total intensity [39]. Therefore, the SE1 signal is greatly diluted by the SE2 signal at higher acceleration voltages, reducing the resolution that can be obtained. Only at low beam voltages, the emission volume for the SE2 becomes of the same order as that for the SE1, due to the decreased range depth of the primary electrons. To conclude, the similar emission volumes for the SE1 and SE2 signals, combined with the larger total SE yield, are the main reasons for the increased surface contrast observed in low-voltage SEM [39].

In general, electron-sample interactions are quite complicated, especially when low-energy electrons are used [39]. Depending on the material of interest, many factors can contribute to the observed image contrast: material composition, topography, crystal orientation, voltage contrast, magnetic contrast, charging contrast, etc. [37]. Using LVSEM, also the chemical contrast between materials based on the differences in secondary electron yield can be measured: the 'true' SE1 contrast. This contrast that does not result from a change in SE2 yield (*e.g.* caused by different elements inside the specimen), but results from differences in the position of the energy levels between materials.

Several examples can be found in literature showing true chemical contrast in LVSEM: *p*- and *n*-doped multilayers in a GaAs sample [42], doping contrast in InP/InGaAsP hetero-structures [43] and Al-doped SiC samples [44]. Since these composites were only ppm-doped, the contrast is not due to variations in the mean atomic number *Z*, but is allocated to a change in the work function of the material. Recently, the effect of bandgap variations and ionization energy on the SE emission has been demonstrated in GeSi heterostructures [45] and undoped SiC heterostructures [46].

For a metal, substantial SE emission will occur if the generated electrons have an energy greater than the work function Φ_M, which is defined as the energy required to take an

electron from the Fermi level E_F to a position at a macroscopic distance from the surface (*i.e.* the vacuum level *VL*), due to the high electron population and high density of states at the Fermi level. For semiconductors, however, having a relatively low occupation of the conduction band, the most relevant value for SE emission yield is the difference between the nearly fully occupied states at the valence band edge (*i.e.* the HOMO level for organics) and the vacuum level [43]. This energy is called the ionization energy *IE* (or ionization potential *IP*). Koch *et al.* [4] measured an ionization energy *IE* of about 5.0 and 6.5 eV, for pentacene and 6,13-pentacenequinone thin films, respectively. Consequently, the ~1.5 eV difference in ionization energy *IE* between pentacene and 6,13-pentacenequinone is attributed as the main reason for the observed contrast in SE yield in figures 5.3 and 5.4.

In the end, the contrast in a SEM image is a number contrast: the intensity of the signal depends on the number of SE reaching the detector. Based on its lower ionization energy, pentacene should have a higher SE emission than 6,13-pentacenequinone, and thus appear brighter in a LVSEM image. Figure 5.6A presents a SEM image of another selected area of a partly oxidized pentacene crystal surface. Again, a clear contrast is visible on the crystal surface; light gray pentacene areas are present in an overall dark gray 6,13-pentacene-quinone matrix. To examine the crystal surface in more detail, atomic force microscopy measurements were performed.

The inset in figure 5.6A shows an AFM height and deflection image of the area marked by the white square. The scanned area contains three terraces of several microns wide, separated by two distinct terrace steps running vertically over the image. The terrace planes themselves are partly covered by another layer, which is markedly thinner. The morphology imaged by AFM corresponds clearly with the structure visible in the marked SEM area: the SEM dark gray and light gray areas are visible as the higher-lying yellow and lower-lying red areas in the AFM image, respectively. Thus, the contrast observed in the SEM image between the pentacene and the quinone areas can be imaged as a height difference in AFM scans.

Cross sections of the six horizontal lines in the inset AFM height image are presented in figure 5.6B. Several step heights that have a different value than the 1.4 nm high *d*(001)-spacing of pentacene are observed. From the combined SEM and AFM data, one can distinguish three different step types on the crystal surface, as indicated by the yellow, red en green circles. Figure 5.6C presents a histogram of the three vertical terrace step heights present in the AFM height image. The color of the histogram bars corresponds to the different step types present. For the histogram, every individual AFM scan line has been analyzed separately, to exclude noisy steps in the final results (*e.g.* from scratches, dirt). Average height of the three step types present is 0.89 ± 0.13 nm (green bars), 1.44 ± 0.12 nm (yellow bars) and 2.37 ± 0.15 nm (red bars). Combining all data, it can be concluded that the pentacene crystal terraces are partly covered by a thin oxidized layer.

Let's, for clarity reasons, define the normal, unoxidized 1.41 nm high *d*(001) pentacene crystal terrace step (see chapter 4) as step type 1, with abbreviation P_1-P_2. The most predominant step value encountered in figure 5.6 is the 0.89 nm step (green bars): the

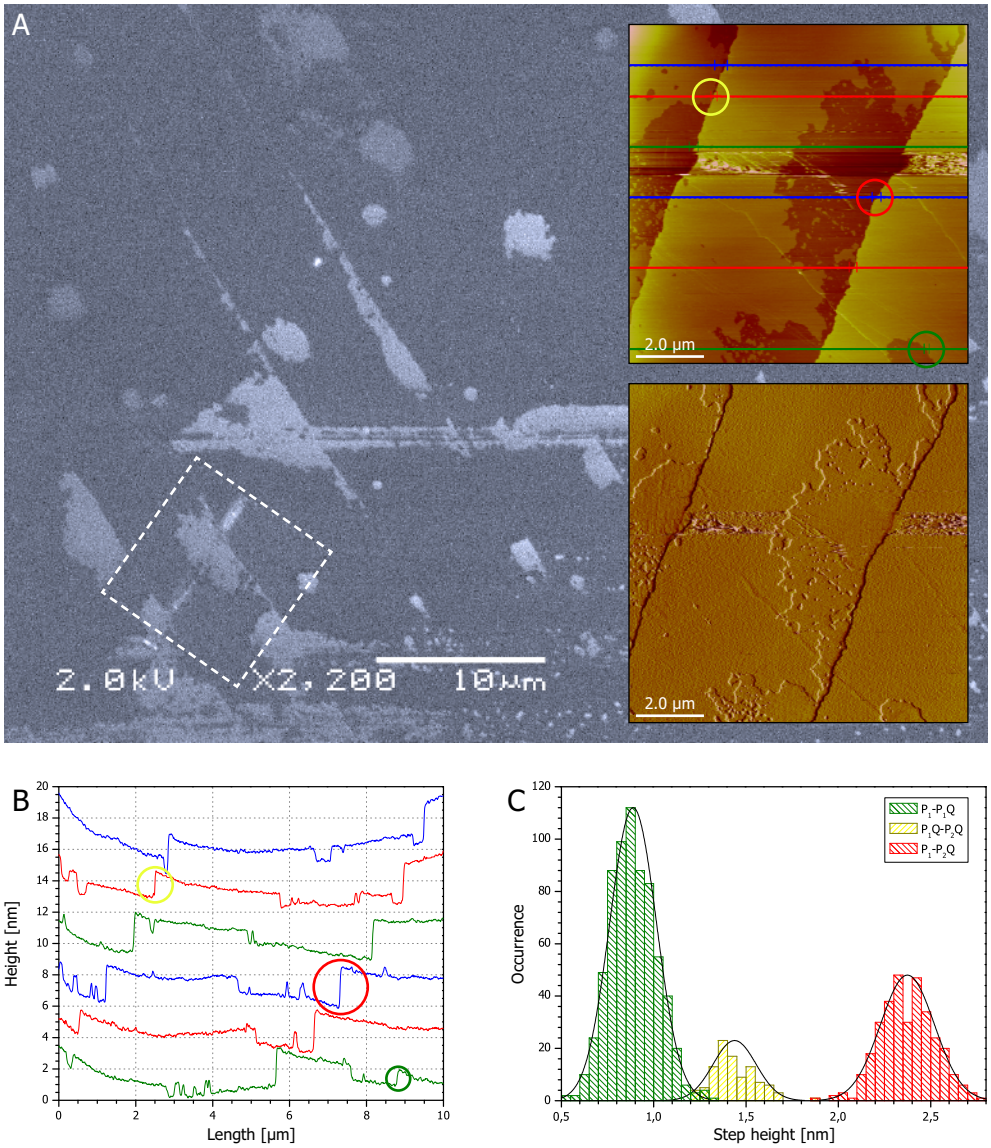

Figure 5.6 *A) Scanning electron microscopy image of a partly-oxidized pentacene single-crystal. The inset is an AFM height image with corresponding deflection image of the area marked by the white square (Z_{AFM} = 10 nm). B) Cross sections of the six horizontal lines in the AFM height image. C) Histogram of the vertical terrace step heights present in the AFM height image. The Gaussian curves in the histogram are a guide for the eye. The yellow, red en green circles indicate the three different vertical steps encountered.*

thickness of the oxidized material on an unoxidized pentacene terrace plane. This step will be defined as step type 2 and abbreviated as P_1-P_1Q. The next step type observed, with a height of 1.44 nm (yellow bars), has the same height as a normal P_1-P_2 step. However, all encountered 1.44 nm steps here are different, in the way that they originate from oxidized material on one terrace to oxidized material on the next terrace. Therefore, these steps will be defined as type 3 and abbreviated P_1Q-P_2Q. A closer look to the last step type observed in the AFM image (*i.e.* the 2.37 nm step, red bars) reveals that this step can be considered a combination of step types 1 and 2. This combination of a P_1-P_2 step and a P_1-P_1Q step will be called step type 4, and abbreviated as P_1-P_2Q.

Scanning another crystal area displayed a similar presence in step types; however the morphology is somewhat different, as can be seen in figure 5.7. In this AFM image all four step types defined so far can be identified; both 1.4 nm high P_1-P_2 and P_1Q-P_2Q step are

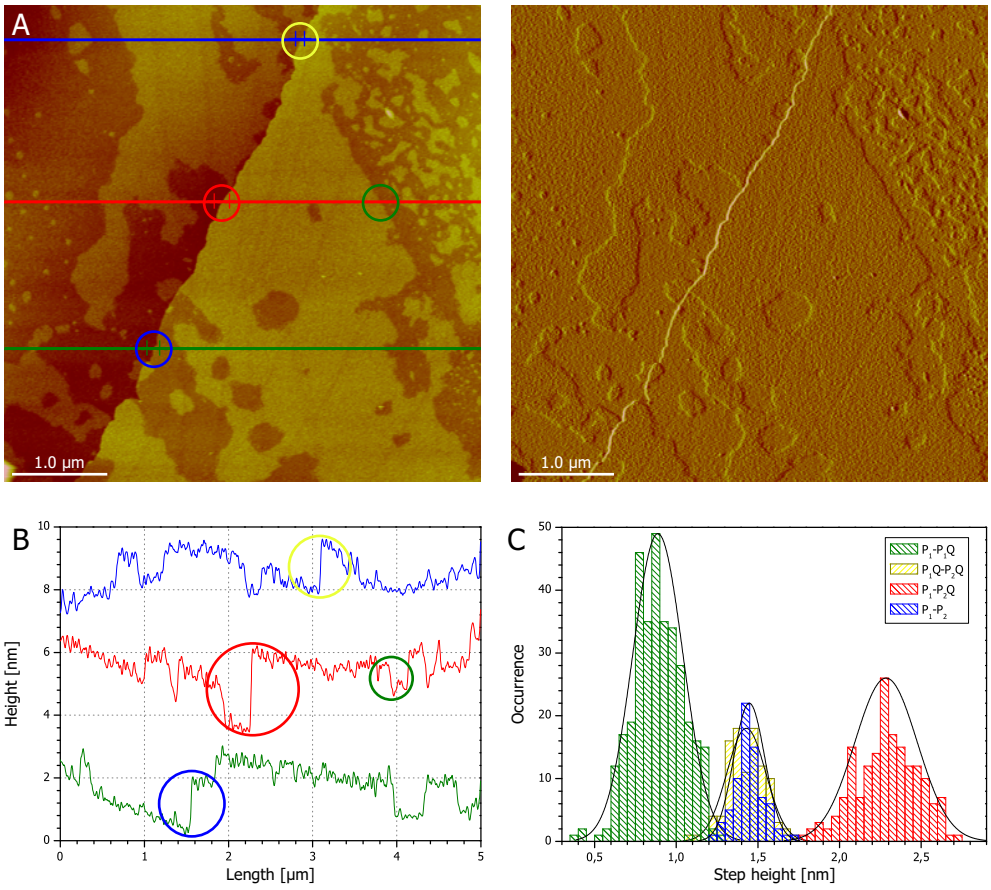

Figure 5.7 *A) AFM height and deflection image of a partly-oxidized pentacene single-crystal surface (Z_{AFM} = 10 nm). B) Cross sections of the horizontal lines in the AFM height image. C) Histogram of the vertical terrace step heights present in the AFM height image. The Gaussian curves in the histogram are a guide for the eye. The circles indicate the different vertical steps encountered.*

present here (the P_1-P_2 blue bars and P_1Q-P_2Q yellow bars overlap in the histogram). Histogram statistics (figure 5.7C) give the following step height information: P_1-P_1Q: 0.89 ± 0.15 nm, P_1Q-P_2Q: 1.43 ± 0.12 nm, P_1-P_2: 1.44 ± 0.10 nm, and P_1-P_2Q: 2.29 ± 0.19 nm. The somewhat different morphology will be further discussed later.

The 0.9 nm high P_1-P_1Q step corresponds to the 0.9 nm *d*(002)-spacing of bulk 6,13-pentacenequinone [32]. This correspondence implies the pentacene single-crystal surface is partly covered by a single *monolayer* of 6,13-pentacenequinone. Additionally, it indicates that only the outmost layer of the pentacene crystal is prone to oxidation.

From AFM measurements on pentacene single-crystals directly after growth, Jurchescu *et al.* [15] concluded that 6,13-pentacenequinone impurities agglomerate in patches that are distributed over the crystal surface. They observed terraces at the surface that exhibited step heights with, predominantly, two values: 1.41 ± 0.05 nm and 1.78 ± 0.08 nm. The former value corresponds to the *d*-spacing of single-crystal pentacene (*i.e.* P_1-P_2 step), and the latter to the *d*(001)-spacing of 6,13-pentacenequinone.

Looking at the molecular packing in the bulk 6,13-pentacenequinone unit cell (see figure 5.2), a 1.78 nm high *d*(001) step implies the presence of a *doublelayer* of quinone molecules on the pentacene crystal surface. This double molecular step will be further abbreviated as P_1-P_1QQ. A *d*(002) spacing step implies the presence of a quinone *monolayer*, conversely.

After the SEM and AFM results described above, a model is proposed, based on the presence of a 6,13-pentacenequinone *monolayer* on the pentacene crystal surface, see figure 5.8. For

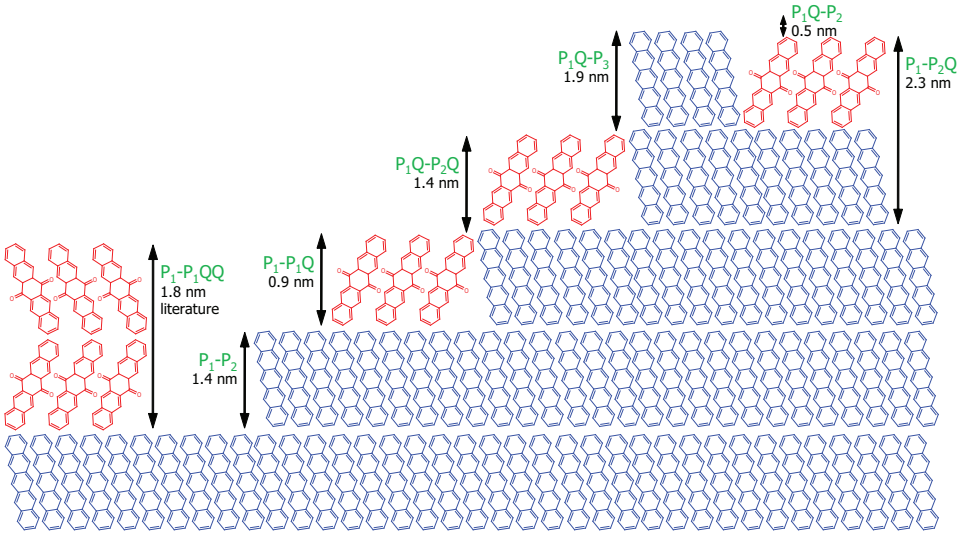

Figure 5.8 *Schematic for the various step heights observed in AFM measurements on the surface of partly-oxidized pentacene single-crystals. For comparison, also the 1.8 nm high P_1-P_1QQ step found in literature is added.*

comparison, also the P_1-P_1QQ doublelayer step found in literature is included. A consequence of this model is that even more step types can exist, depending on the precise location of the quinone impurities relative to the pentacene terraces. Two new step types are defined in this figure: a P_1Q-P_2 step of ~0.5 nm and a P_1Q-P_3 step of ~1.9 nm high. It should be noted that both P_1Q-P_3 and P_1-P_1QQ steps are approximately 1.8 nm high.

In figure 5.9, more AFM data is presented for a 6,13-pentacenquinone monolayer partly covering the surface of a pentacene single-crystal. Here, tapping-mode AFM was applied, and a clear contrast is observed in the phase data signal. The phase contrast is consistent with the different step heights observed before (*i.e.* the yellow and red areas in the phase image correspond to 6,13-pentacenequinone and pentacene, respectively), and with the contrast in the low-kV SEM images (not shown). Thus, using the contrast in the phase image, a clear distinction can be made in the AFM images between the oxidized and unoxidized crystal areas (dark orange regions and light yellow regions, respectively).

A few things should be noted on figure 5.9. First, the morphology of the quinone material is quite different than observed in figures 5.6 and 5.7. This observation will be discussed more a few sections below. Second, experimental proof is presented for the two

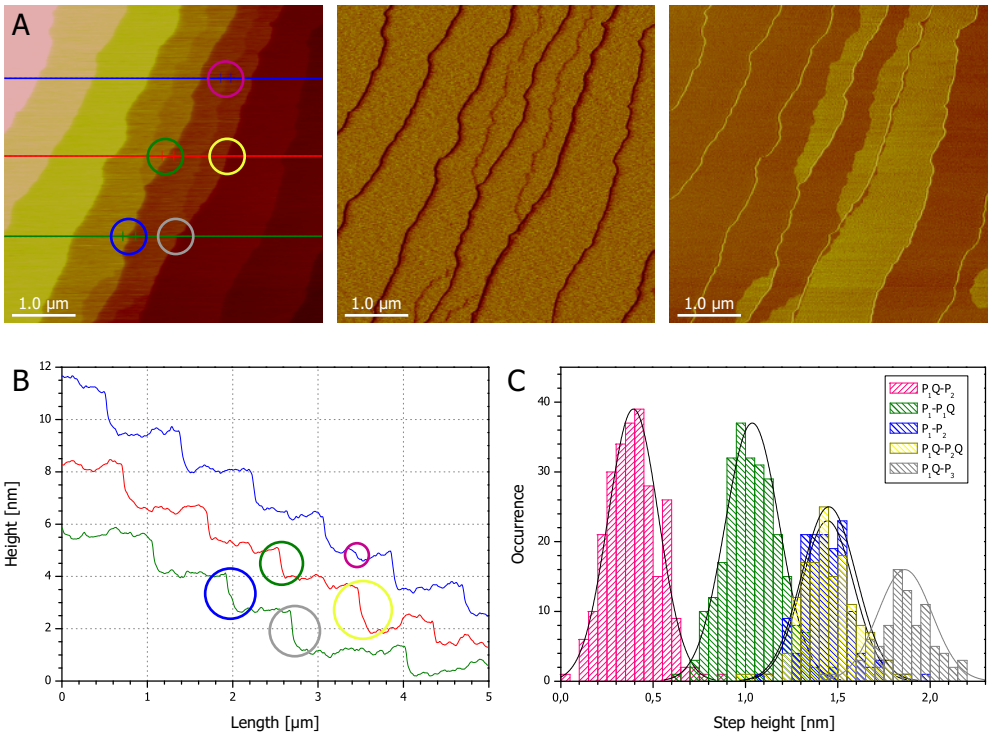

Figure 5.9 *A) AFM height, amplitude error and phase image of a partly-oxidized pentacene single-crystal surface (Z_{AFM} = 10 nm). B) Cross sections of the horizontal lines in the AFM height image. C) Histogram of the vertical terrace step heights present in the AFM height image. The Gaussian curves in the histogram are a guide for the eye. The circles indicate the different vertical steps encountered.*

Table 5.2 *Overview of all encountered terrace step types in AFM imaging of the surface of (partly-oxidized) pentacene single-crystals.*

Step type	Name	Height [nm]
1	P_1 - P_2	1.42 ± 0.08
2	P_1 - P_1Q	0.92 ± 0.15
3	P_1Q - P_2Q	1.44 ± 0.13
4	P_1 - P_2Q	2.34 ± 0.17
5	P_1Q - P_2	0.39 ± 0.14
6	P_1Q - P_3	1.87 ± 0.15
Lit. [3,11]	P_1 - P_1QQ	1.78 ± 0.08
	P_1 - P_3	2.84 ± 0.11
	P_1 - P_4	4.16 ± 0.16
	P_1 - P_7	8.23 ± 0.16

new step types defined in the model in the previous paragraph. Step type 5, the P_1Q-P_2 steps (pink bars/circle), and step type 6, the P_1Q-P_3 steps (gray bars/circle), can be found in the data. Histogram statistics (figure 5.9C) give the following step height information: P_1Q-P_2: 0.39 ± 0.14 nm, P_1-P_1Q: 1.04 ± 0.15 nm, P_1-P_2: 1.45 ± 0.14 nm, P_1Q-P_2Q: 1.45 ± 0.15 nm, and P_1Q-P_3: 1.87 ± 0.15 nm. An overview of all encountered terrace step types on the surface of partly-oxidized pentacene single-crystals is presented in table 5.2.

In all AFM measurements performed on partly-oxidized pentacene crystal surfaces, the double molecular quinone P_1-P_1QQ step described in [3,15] has not been encountered. Most likely, their 1.8 nm steps appointed to P_1-P_1QQ should have been appointed as P_1Q-P_3 steps, which have the same height: the difference between these two steps is clear from the AFM phase contrast images. As the statistic data in [3,15] is limited (it covers only terrace steps between 1.2 nm and 2.0 nm), it remains unclear if there were monomolecular 0.9 nm high P_1-P_1Q quinone steps present on their examined crystals.

All the data together shows the 6,13-pentacenequinone material is present as a molecular monolayer (partly) covering the pentacene crystal surface. The 0.89 nm thickness of this layer corresponds with the *d*(002) spacing of the bulk or crystal phase.

Various AFM and XRD studies on 6,13-pentacenequinone thin films grown on inorganic substrates show the existence of a meta-stable thin film phase (with terrace steps of 1.27 nm), besides the bulk phase [28-30,32]. Also, when pentacenequinone is deposited on a pentacene thin film, the quinone film is induced to grow preferentially in the thin film phase [32]. This 6,13-pentacenequinone thin film phase was not at all observed in the experiments discussed in this work. Using the powerful combination of low-kV SEM contrast, AFM step height differences and tapping-mode phase contrast, only the presence of mono-molecular 6,13-pentacenquinone layers with bulk phase *d*(002) thickness was encountered.

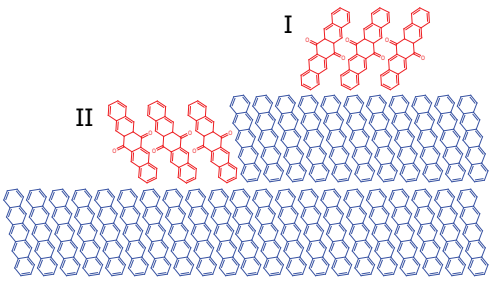

Figure 5.10 *Model showing the possible locations of the 6,13-pentacenequinone patches on a pentacene crystal surface. In case I, the quinone moiety is located on top of the outmost pentacene layer. In case II, the quinone is embedded within the outmost pentacene layer.*

When investigation the position of the quinone material on the pentacene crystal terraces in the AFM images, two possible locations are encountered, as depicted in figure 5.10. In case I, the quinone monolayer is situated as patches on top of the outmost pentacene layer. This is the situation encountered in AFM figures 5.6 and 5.7, where quinone patches can be found all over the pentacene terrace planes. In case II, the quinone moieties are embedded within the outmost pentacene layer; the situation encountered in AFM figure 5.9. In this figure, all quinone areas are located at the edges of the terrace planes. However, other AFM images (not included) do also show the occurrence of quinone 'pit holes' in the middle of a plane (*i.e.* type II quinone patches completely surrounded by the outmost pentacene layer).

The characteristic difference between the two cases, as long as the normal pentacene terrace steps are monomolecular, is the lack of P_1Q-P_3 steps in case I, and the lack of P_1-P_2Q steps in case II.

Classifying the location of the quinone moieties is important for specifying the origin of the oxidized material. As mentioned in paragraph 5.2.1, the 6,13-pentacenequinone patches on the pentacene crystal surface can derive from impurities already present in the pentacene starting powder. On the other hand, the pentacene crystals may also have oxidized after growth or during storage, in the presence of oxygen and light. The morphology observed in case I points towards deriving from crystal growth dynamics (*i.e.* not incorporating the quinone molecules in the pentacene crystal lattice during growth). The case II morphology, conversely, suggests oxidation of the outmost pentacene layer after crystal growth. The structure indicates the oxidation has proceeded from the terrace edge inwards, which is reasonable as the step edge molecules possess more degrees of freedom.

Although the crystals were stored in a dark and dry nitrogen environment, some oxidation after crystal growth cannot be excluded. To investigate the stability of the investigated partly-oxidized pentacene crystals towards further oxidation, a second series of SEM images of the samples was made after storage in a dark and dry nitrogen environment for one and a half year. As can be seen in figure 5.11, the SEM images are almost identical. Thus, further oxidation of the crystals when stored in a dark and dry nitrogen environment is limited.

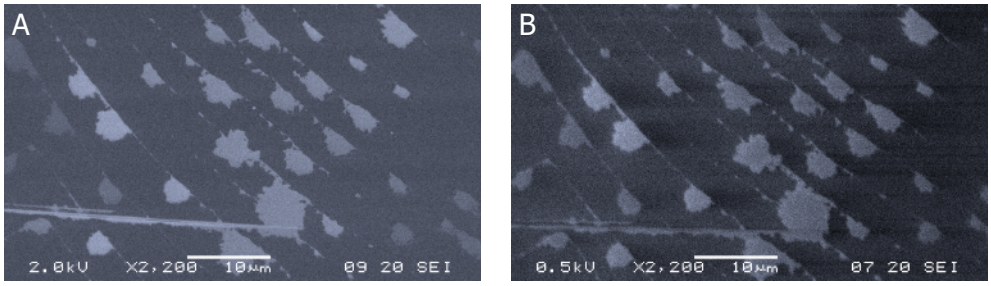

Figure 5.11 *SEM images of a partly-oxidized pentacene single-crystal surface with 1½ year in between, showing no significant further oxidation during storage of the crystal in a dark and dry nitrogen environment. A) Image made on t = 0 , B) made on t = 1.5 years.*

5.4.2 Adsorption of water on the surface of pentacene single-crystals

At this point, a small detour has to be made to exclude the presence of adsorbed water on the pentacene single-crystals. That is to say, Qiu *et al.* [18] presented AFM height and phase images of a pentacene thin film which had been stored in ambient conditions. They distinguished two different phases in their AFM phase image and concluded that, although pentacene is highly hydrophobic, water is adsorbed on the polycrystalline film. As no other images of pentacene films or crystals have been found in literature, it has to be confirmed that the phase contrast observed in figure 5.9 does not originate from adsorbed water.

In order to exclude the presence of adsorbed water on the surface of the partly-oxidized pentacene single-crystals, two experiments were performed. First, a pentacene crystal was dipped in water for 5 s and then blown dry with nitrogen gas. Figure 5.12 presents AFM data of the subsequent surface. As can be seen in the figure, the normal surface morphology was maintained: the typical 1.4 nm high P_1-P_2 surface steps are still present and no abnormal swelling of the crystal could be observed on this scale. Clearly present on top of the pentacene crystal surface are small patches (or droplets) of residual water, that appear in the AFM friction image with a red color. The cross section lines show that the water patches have a smooth rounded shape and a clearly different height of several nanometers. Compared to the previous AFM phase image in this chapter (figure 5.9), it can be concluded that the phase contrast in the AFM images cannot be explained by adsorbed water.

In a second experiment, the surface of a pentacene single-crystal was touched with a wet pair of tweezers, so that it was locally wetted. Figure 5.13 shows a series of consecutive SEM

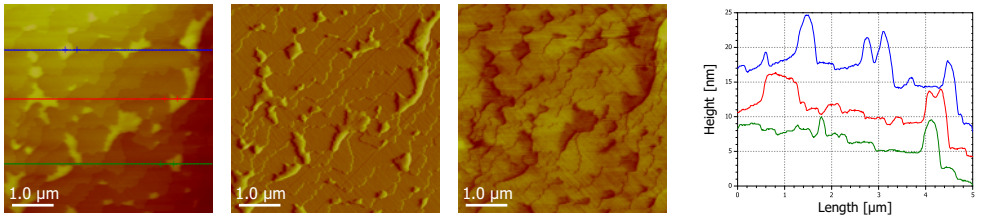

Figure 5.12 *AFM height, deflection and friction image, and three cross-section curves of a pentacene single-crystal with water adsorbed on its surface (Z_{AFM} = 35 nm).*

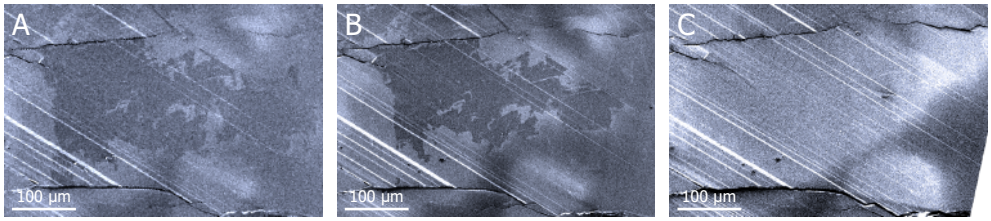

Figure 5.13 *SEM image sequence of a pentacene single-crystal with water adsorbed on its surfaced imaged. Time between image A and B is 5 minutes; between B and C 30 minutes.*

images of the wetted crystal area, which appear with a darker color. The darker area disappears in time, which shows the adsorbed water is desorbing from the crystal surface in the vacuum environment of the electron microscope. This desorption behavior has not been observed during the imaging of the partly-oxidized pentacene single-crystals in the SEM (*i.e.* the 6,13-pentacenequinone moieties did not change shape upon imaging in time).

Based on these two experiments, it can be concluded that the presence of adsorbed water on the surface of the examined (partly-oxidized) pentacene single-crystals can be excluded, and that the AFM phase contrast does not originate from absorbed water.

5.4.3 The bulk of partly-oxidized pentacene single-crystals

In paragraph 5.4.1, it was shown that the 6,13-pentacenequinone impurities are present as a monolayer on parts of the pentacene crystal surface. In order to verify if no quinone is present in the bulk of the pentacene crystals as well, the internal composition of these crystals was investigated by AFM, directly after cleaving by the 'Scotch-tape method'.

The 'Scotch-tape method' is a well-established technique to cleave for instance a graphite sample and prepare a fresh non-contaminated graphite surface. In this dry mechanical exfoliation method (to give the method its formal name), a piece of Scotch-tape is gently pressed to a graphite sample to peel off the uppermost layers from the bulk, leaving a freshly exposed graphite surface, for example for STM experiments [47]. Using this approach, micrometer-wide sheets of graphene were obtained in 2004, by repeatedly peeling flakes off a graphite sample, which is essentially a stack of graphene sheets [48].

An example of a relatively flat area of a freshly-cleaved pentacene single-crystal surface is given by the AFM images in figure 5.14. In the height image, the monomolecular 1.4 nm high *d*(001) P_1-P_2 pentacene terrace step (blue bars/circle) is present most. Two other steps, not defined so far, are encountered as well: a 2.8 nm high step (purple bars/circle) and a 4.2 nm high step (pink bars/circle). From the surface morphology and the step height numbers, one can simply deduce that these steps must originate from a double and a triple mono-molecular pentacene step; they will be defined as P_1-P_3 and P_1-P_4, respectively. Histogram statistics (figure 5.14C) give the following step height information: P_1-P_2: 1.42 ± 0.07 nm, P_1-P_3: 2.84 ± 0.11 nm, P_1-P_4: 4.16 ± 0.16 nm, and P_1-P_7: 8.23 ± 0.16 nm (not shown).

Most importantly, not one of the 6,13-pentacenequinone-related terrace steps defined so far could be found on any of the cleaved pentacene single-crystal surfaces investigated;

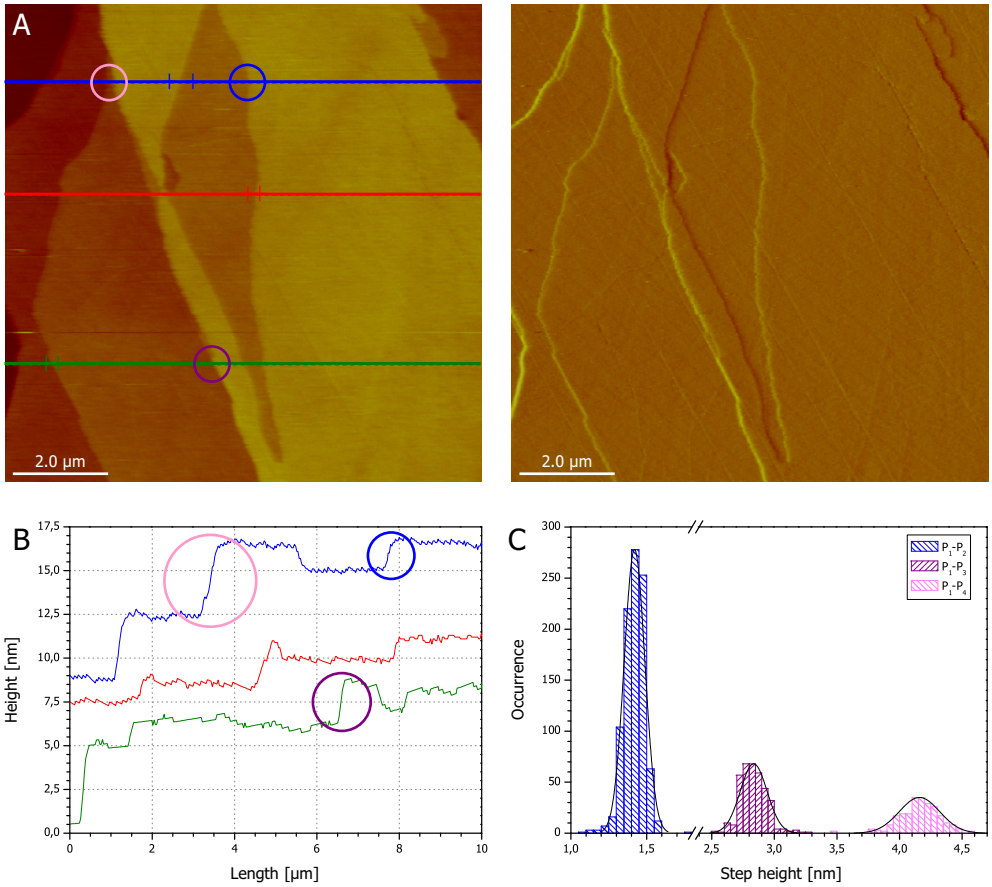

Figure 5.14 *AFM height and deflection image of a freshly cleaved pentacene single-crystal by the Scotch-tape method (Z_{AFM} = 20 nm). B) Cross sections of the horizontal lines in the AFM height image. C) Histogram of the vertical terrace steps present in the AFM height image. The Gaussian curves in the histogram are a guide for the eye. The circles indicate the different vertical steps encountered.*

i.e. no large patches of quinone impurities are present in the crystal bulk, similar to Jurchescu's findings [15]. This again strengthens the conclusion that the 6,13-pentacene-quinone material is preferentially present as a monomolecular layer (partly) covering the pentacene crystal surface, and not present in or evenly distributed through the bulk.

Manual cleaving as surface treatment

As shown in the previous paragraphs, the 6,13-pentacenequinone impurities are present as a monolayer on parts of the crystal surface. These molecules form scattering centers at the conducting interface in a field-effect transistor, thus reduce the charge carrier mobility [3]. Therefore, aim is now to remove the quinone moieties selectively from the crystal surface and obtain a clean, molecular flat and quinone-free surface that is suitable for fabricating devices with a well-controlled interface. As both graphite and crystalline pentacene are layered materials, it is first investigated if the Scotch-tape method can be used to achieve this aim.

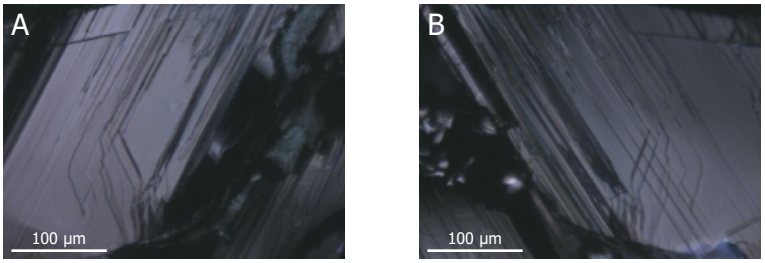

Figure 5.15 *Optical microscopy images of a cleaved pentacene single-crystal by the Scotch-tape method. A) Crystal part remaining from original crystal after cleaving. B) Crystal part peeled off from original crystal.*

Cleaving the fragile pentacene single-crystals was not straightforward; in contrast to graphite, the peeling off is not restricted to only the uppermost layers of the bulk. A large platelet-like pentacene single-crystal, with practical dimensions for OFET studies of a few millimeters, is impossible to cleave in two useful parts. Although large areas of the crystal are cleaved, some parts of the original crystal remained completely on the substrate, whereas other crystal parts transferred completely with the tape.

Figure 5.15 presents two optical microscopy images of both fresh sides of a manually cleaved pentacene single-crystal by the Scotch-tape method. Figure 5.15A shows the crystal part remaining on the substrate after cleaving, whereas the crystal part peeled off is shown in figure 5.15B. Similar (mirrored) features can be distinguished on the surfaces of both crystal parts, though some dissimilarities are present as well. Due to the fact that the OM images show large (terrace) steps on the crystal surface, it can directly be concluded that the cleaved crystal is not molecularly flat on a large millimeter-wide scale. However, both cleaved crystal parts show micrometer-sized areas that may be molecularly flat.

A series of AFM images of both fresh sides of the manually cleaved pentacene single-crystal is presented in figure 5.16. Figure 5.16A presents two AFM images showing the surface of the crystal part remaining on the substrate after cleaving, whereas the two AFM images in figure 5.16B reveal the surface morphology of the peeled-off crystal part. Upon comparing the images, it can be clearly observed that similar features are present on both surfaces: in principle the two parts fit precisely together like two mirrored puzzle pieces. This observation holds for both the monomolecular steps and the larger terrace steps observed (up to several tens of nanometer); the only large difference is the presence of additional large steps in the peeled-off crystal part (from the left top to the right bottom corner). The latter large steps on the peeled-off crystal part probably originate from sliding of crystal parts due to the relative large forces acting on the fragile crystal during the cleaving procedure. Note that this morphology is consistent with the surface morphology observed in figure 4.12E and supports the model for stress-induced surface steps in figure 4.14A.

The fact that graphite, a layered material of essentially a stack of graphene sheets, can be cleaved so easily with the Scotch-tape method, originates directly from the internal arrangement of the carbon atoms. Within the flat sheets, each carbon atom is covalently

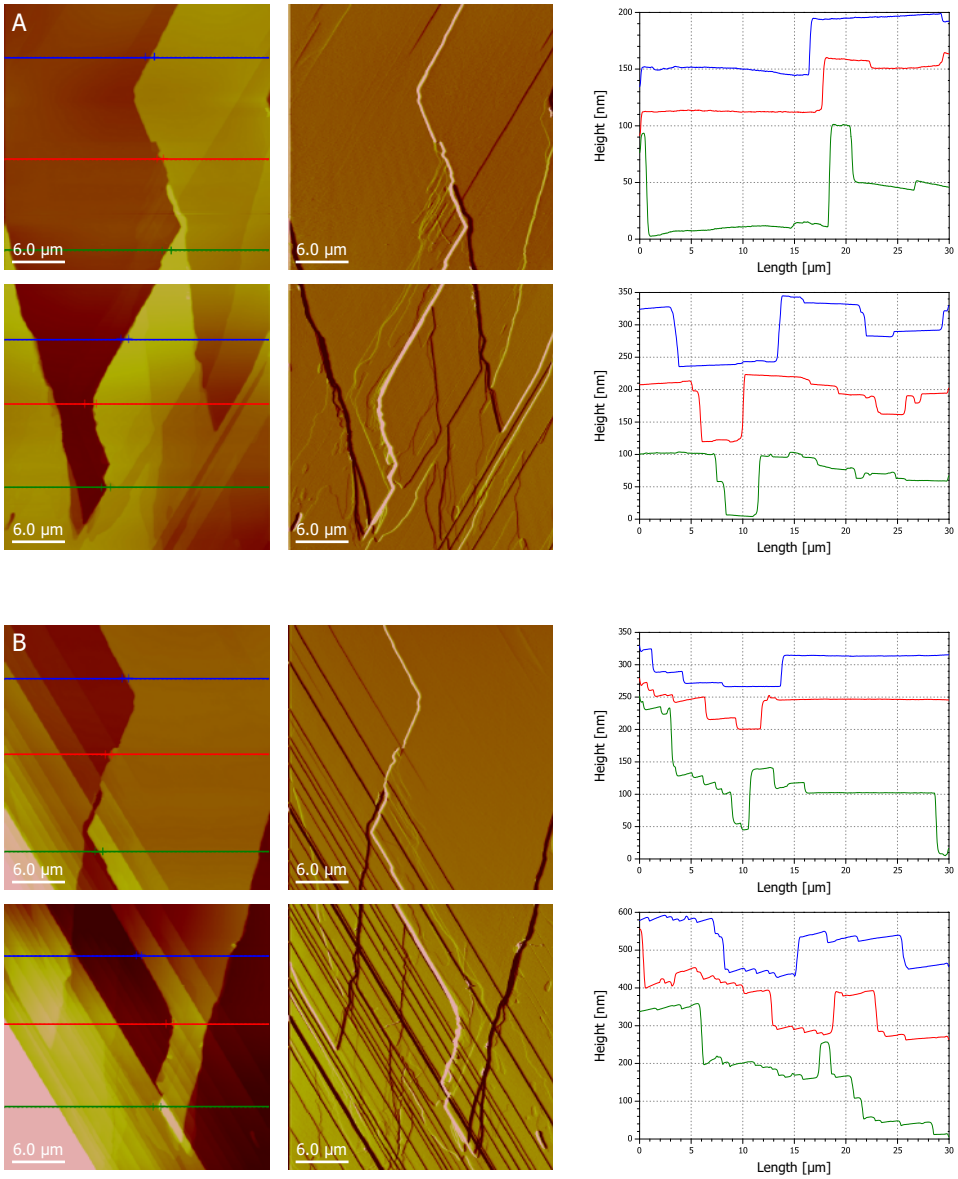

Figure 5.16 *Series of AFM images presenting the surface morphology of a cleaved pentacene single-crystal by the Scotch-tape method. A) Crystal part remaining from original crystal after cleaving. B) Crystal part peeled off from original crystal. For every scan, height data (Z_{AFM} = 300 nm (A) and 250 nm (B)), deflection data, and three cross-section curves are shown.*

bonded to three other carbon atoms. The layers themselves are held together only by weak van der Waals interactions originating from delocalized *π*-orbitals [49]. In other words, the forces between the layers are quite weak compared to the strong covalent bonds within the sheets, which enables the sharp cleaving of graphite along the graphene sheets. The inter-molecular forces between the molecules in single-crystalline pentacene are rather weak, as

discussed in paragraph 4.2.2, and the intralayer interactions are not so much stronger than the forces between the layers. As a consequence, cleaving of pentacene crystals is not restricted to occur along the layers only, and can proceed through the molecular sheets as well. The cleavage plane, as it can be viewed in figure 5.16, shows that cleaving through the molecular layers happened to a great extend.

In conclusion, the Scotch-tape method is suitable for obtaining a pentacene single-crystal surface that is free of 6,13-pentacenequinone impurities and molecular-flat on a micrometer-large scale. However, the method is too destructive to prepare a millimeter-large pentacene crystal substrate for consecutive device fabrication, as the fragile crystals are easily crashed in pieces, and the cleaving is not restricted to occur along the layers, but proceeds through the molecular sheets to a great extend. Furthermore, sliding of crystal parts can take place easily, due to the relative large forces acting on the crystal during the cleaving procedure.

5.4.4 Heating treatment on partly-oxidized pentacene crystals

With the aim of removing the 6,13-pentacenequinone monolayer selectivity from the pentacene surface, the crystals were heated in vacuum at fixed temperatures overnight. The selective separation in the heat treatment is based on a difference in sublimation enthalpy: 116.4 kJ/mol and 156.9 kJ/mol, for bulk 6,13-pentacenequinone and pentacene, respectively. These values are calculated from thermal desorption spectra, measured by subliming polycrystalline powder of both materials under vacuum conditions (see figure 5.17) [20]. The spectra show there is a small temperature window in which 6,13-pentacenequinone begins to sublime, whereas pentacene does not and remains solid. Onset of sublimation is around 44 and 60 °C (begin tail desorption peak), whereas the flank of the exponentially increasing desorption peak (start linear fit) gets stable around 67 and 85 °C, both for 6,13-pentacenequinone and pentacene, respectively.

Figure 5.18 presents low-kV SEM images of a pentacene single-crystal before and after an overnight heating treatment at 70 °C in vacuum. The surface contrast observed in the images before the treatment has disappeared completely after the treatment. The only remaining contrast originates from a few large terrace steps (see figure 5.18D, right side) and dirt particles. The same observation is found after the heating treatments at the other investigated temperatures (figures not shown).

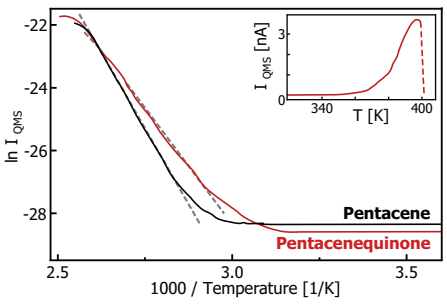

Figure 5.17 *Thermal desorption spectra (TDS) of pentacene and 6,13-pentacenequinone. The inset shows the thermal desorption spectrum for 6,13-pentacenequinone. Figure with permission from [20].*

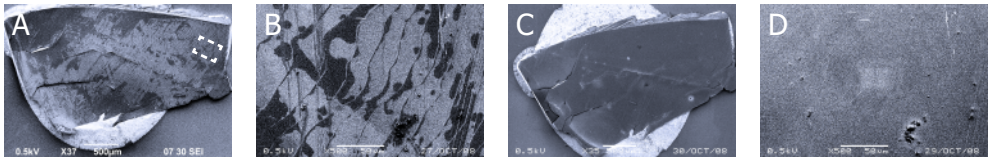

Figure 5.18 *SEM images of a pentacene single-crystal before (A,B) and after (C,D) an overnight heating treatment at 70 °C in vacuum. Images B and D are close-ups (x500 magnification) of the same area, indicated by the white square in image A.*

After heating at 100 and 110 °C, areas with extensive structural damage on the crystal surface could be observed with the OM and SEM. This observation indicates the crystal structure breaks down as pentacene molecules start to sublime (see figure 5.19). The large damage extends in both cases over a crystal area larger than 100 micrometer, clearly showing the heating treatment conditions were too harsh for the fragile crystal.

Figure 5.20 presents in a series of AFM images the influence of the temperature during the overnight heating treatments on the pentacene crystal morphology. The crystals were heated in vacuum at temperatures between 70 and 110 °C (70, 80, 85, 90, 100 or 110 °C).

Based on the AFM *height* data, all quinone material seems to be removed after the overnight heating at 70 °C, as only 1.4 nm terrace steps are found on the smooth terraces (see figure 5.20A). The *phase* image, however, still shows some contrast within the terraces, indicating no complete removal of the oxidized material. This observation may imply that some of the quinone material is embedded deeper in the pentacene crystal, and is not present on the surface alone. However, this consideration is not further included in the model of figure 5.8, as no confirmation is found in the AFM or SEM data so far supporting this.

After heating a crystal overnight at 80 °C or higher (figure 5.20B-F), a clean pentacene surface was obtained with no obvious presence of quinone material. No quinone-related terrace steps (see figure 5.8) are detected and no phase contrast is observed anymore.

The crystals heated at 80 and 90 °C (figures 5.20B and D) show smooth terraces and normal step edges after the treatment. All 6,13-pentacenequinone areas have sublimed from the surface, leaving behind a well-defined and clean pentacene single-crystal morphology.

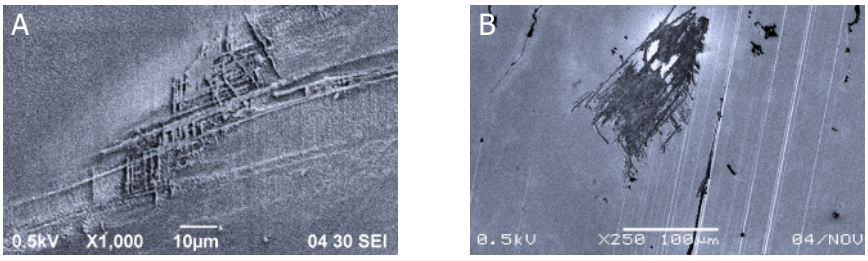

Figure 5.19 *Two SEM images of a pentacene single-crystal after the overnight heating treatment in vacuum at a temperature of A) 100 °C, and B) 110 °C. Markedly visible is the substantial structural damage to the crystal surface after heating at this temperature. SEM images before the treatment show this damage was not already present before applying the heat (not shown).*

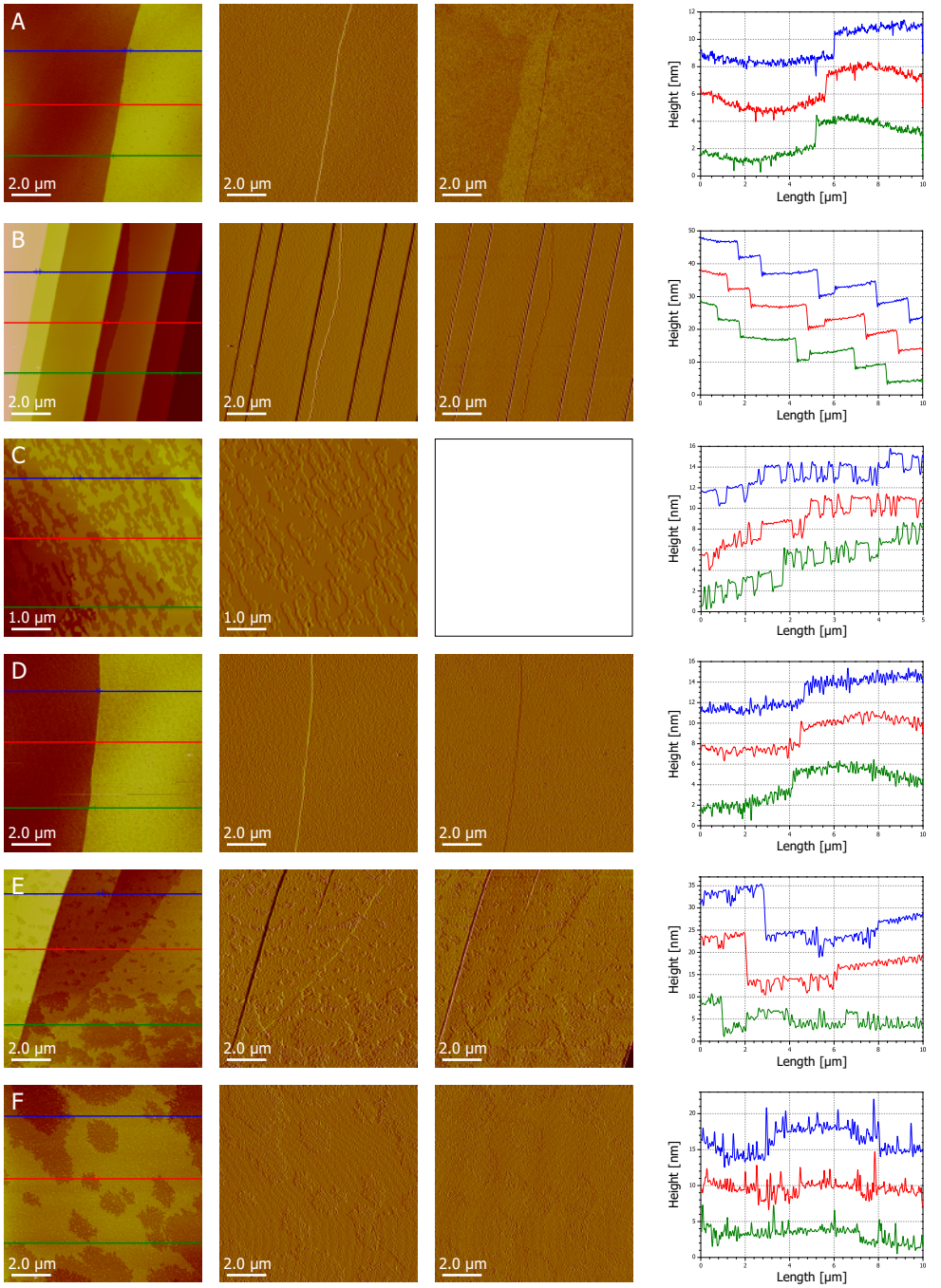

Figure 5.20 *Series of AFM images presenting the influence of the temperature during the overnight heating treatment on the pentacene crystal surface morphology. The crystals were heated in vacuum at a fixed temperature: A) 70 °C, B) 80 °C, C) 85 °C, D) 90 °C, E) 100 °C and F) 110 °C. For every scan, the height, deflection and phase data, and three cross-section curves are shown (Z_{AFM} = 10, 30, 20, 10, 30 and 20 nm, respectively).*

Starting around 85 °C, the pentacene began to sublime as well, as can be observed in figure 5.20C. Although the terraces are still smooth at the molecular level, they contain quite a lot 1.4 nm deep and up to several hundreds of nanometer large voids. At this point, the separation process is not selective anymore; the sublimation is not limited to the quinone material and pentacene molecules will sublime from the outer layers as well.

At the highest temperatures investigated (100 and 110 °C, see figure 5.20E-F), the pentacene crystal structure started to break down. The layered terrace morphology cannot be recognized in the AFM images after the heating treatment anymore. The samples contained numerous cavities and the surface was no longer molecularly smooth, as the spikes in the cross sections in figure 5.20F show. The spikes indicate an uncontrolled sublimation of the pentacene terraces; yet they may also originate from re-deposition of elsewhere-sublimed material.

In literature, various studies on post-deposition annealing of pentacene thin films (*e.g.* to achieve a more uniform film morphology and improve the transistor characteristics) confirm there is a maximum temperature to which a heating treatment can be applied before pentacene molecules start to re-evaporate [50-53]. Wu *et al.* [50] find a maximum temperature of 100 °C for pentacene thin films (which is quite higher than the maximum of 70 °C they find for pentacenequinone films). However, various factors can influence the desorption of organic films, and therefore different desorption temperatures may be observed for the same material. Ye *et al.* [51] found that pentacene re-evaporation started to occur at 95 °C, whereas the as-deposited films were completely evaporated from the substrate after annealing at 105 °C. Guo *et al.* [52] observed similar behavior at temperatures 10-15 °C lower, where a 70 °C annealing temperature caused obvious desorption.

Investigating the effects of annealing on pentacene single-crystals is limited to a few remarks in one study, in which Takenobu *et al.* [54] observed an identical surface morphology before and after annealing the crystal at 100 °C for 1 h in a nitrogen atmosphere in AFM images, indicating no obvious degradation.

Since the sublimation of pentacene and 6,13-pentacenequinone takes place under near identical conditions, a slow surface treatment is preferred. As described in chapter 4, removal of pentacenequinone impurities from pentacene powder by vacuum sublimation under a temperature gradient is a slow process. The purification process typically takes several days (~70 h at 160 °C is mentioned in [2]). Initially, it can therefore be expected that the selective sublimation of 6,13-pentacenequinone monolayers from the surface of pentacene single-crystals would proceed at a similar temperature.

However, there are some intrinsic differences between pentacene powder and pentacene single-crystals, and the location of the impurities in both configurations. Pentacenequinone impurities in pentacene powder are most likely uniformly distributed throughout the bulk. As shown in this work, this assumption is not correct for pentacenequinone impurities in pentacene crystals: the quinone is preferentially located as a monolayer on the crystal surface. Therefore, the surface treatment procedure of partly surface-oxidized pentacene

crystals will completely be dominated by surface kinetics, instead of bulk kinetics that dominate the powder purification. This is the main reason for the much lower sublimation temperature encountered in the heat treatment of the pentacene crystals, than is needed in the purification process of commercial pentacene powder.

Based on combining above OM, SEM and AFM results, heating a partly-oxidized pentacene single-crystal at 75-80 °C overnight in vacuum conditions removes the 6,13-pentacene-quinone material completely from the crystal surface, yielding an unoxidized pentacene single-crystal with a normal, clean and undamaged surface morphology.

5.5 Concluding Remarks

The arrangement and morphology of 6,13-pentacenequinone impurities on the surface and in the bulk of pentacene single-crystals were studied. By using the combination of low-kV SEM contrast, AFM step height differences and AFM tapping-mode phase contrast, it was observed that the quinone material is preferentially located as a thin layer (partly) covering the pentacene crystal surface. Thickness of this layer is about 0.9 nm, which corresponds to the *d*(002)-spacing of bulk 6,13-pentacenequinone. Therefore, a model is proposed that describes the pentacene single-crystal surface is partly covered by a single monolayer of 6,13-pentacenequinone, which contradicts with findings in literature that describe the presence of a 1.8 nm thick quinone doublelayer. Cleaving experiments showed no large patches of quinone impurities are present in the crystal bulk.

In order to remove the 6,13-pentacenequinone monolayer selectively from the pentacene single-crystal surface, the partly-oxidized crystals were heated in vacuum at a fixed temperature fixed overnight. Performing the heating treatment at 75-80 °C removes the quinone material completely, yielding an unoxidized pentacene single-crystal with a clean and undamaged surface morphology that is suitable for subsequent device fabrication.

5.6 References

[1] De Angelis, F.; Gaspari, M.; Procopio, A.; Cuda, G.; Di Fabrizio, E.; "Direct mass spectrometry investigation on pentacene thin film oxidation upon exposure to air"; *Chem. Phys. Lett.*; 468; **2009**; 193-196

[2] Jurchescu, O.D.; Baas, J.; Palstra, T.T.M.; "Effect of impurities on the mobility of single crystal pentacene"; *Appl. Phys. Lett.*; 84; **2004**; 3061-3063

[3] Jurchescu, O.D.; "Molecular organic semiconductors for electronic devices"; PhD Thesis; **2006**; University of Groningen; Groningen, The Netherlands

[4] Koch, N.; Salzmann, I.; Johnson, R.L.; Pflaum, J.; Friedlein, R.; Rabe, J.P.; "Molecular orientation dependent energy levels at interfaces with pentacene and pentacenequinone"; *Org. Electr.*; 7; **2006**; 537-545

[5] Niemax, J.; Tripathi, A.K.; Pflaum, J.; "Comparison of the electronic properties of sublimation- and vapor-Bridgman-grown crystals of tetracene"; *Appl. Phys. Lett.*; 86; **2005**; 122105

[6] Pflaum, J.; Niemax, J.; Tripathi, A.K.; "Chemical and structural effects on the electronic transport in organic single crystals"; *Chem. Phys.*; 325; **2006**; 152-159

[7] Käfer, D.; Witte, G.; "Growth of crystalline rubrene films with enhanced stability"; *Phys. Chem. Chem. Phys.*; 7; **2005**; 2850-2853

[8] Podzorov, V.; Pudalov, V.M.; Gershenson, M.E.; "Light-induced switching in back-gated organic transistors with built-in conduction channel"; *Appl. Phys. Lett.*; 85; **2004**; 6039-6041

[9] Nardello, V.; Marti, M.J.; Pierlot, C.; Aubry, J.M.; "Photochemistry without light: oxidation of rubrene in a microemulsion with a chemical source of singlet molecular oxygen ($^1O_2$, $^1\Delta_g$)"; *J. Chem. Ed.*; 76; **1999**; 1285-1288

[10] Kuroda, H.; Flood, E.A.; "The effect of the ambient oxygen on the electrical properties of an evaporated film of pentacene"; *Can. J. Chem.*; 39; **1961**; 1981-1988

[11] Kalb, W.L.; Mattenberger, K.; Batlogg, B.; "Oxygen-related traps in pentacene thin films: energetic position and implications for transistor performance"; *Phys. Rev. B*; 78; **2008**; 035334

[12] Vollmer, A.; Wiess, H.; Rentenberger, S.; Salzmann, I.; Rabe, J.P.; Koch, N.; "The interaction of oxygen and ozone with pentacene"; *Surf. Sci.*; 600; **2006**; 4004-4007

[13] Yang, H.; Yang, L.; Ling, M.M.; Lastella, S.; Gandhi, D.D.; Ramanath, G.; Bao, Z.; Ryu, C.Y.; "Aging susceptibility of terrace-like pentacene films"; *J. Phys. Chem. C*; 112; **2008**; 16161-16165

[14] Vollmer, A.; Jurchescu, O.D.; Arfaoui, I.; Salzmann, I.; Palstra, T.T.M.; Rudolf, P.; Niemax, J.; Pflaum, J.; Rabe, J.P.; Koch, N.; "The effect of oxygen exposure on pentacene electronic structure"; *Eur. Phys. J. E*; 17; **2005**; 339-343

[15] Jurchescu, O.D.; Popinciuc, M.; Wees, B.J. van; Palstra, T.T.M.; "Interface-controlled, high-mobility organic transistors"; *Adv. Mater.*; 19; **2007**; 688-692

[16] Jurchescu, O.D.; Baas, J.; Palstra, T.T.M.; "Electronic transport properties of pentacene single crystals upon exposure to air"; *Appl. Phys. Lett.*; 87; **2005**; 052102

[17] Maliakal, A.; Raghavachari, K.; Katz, H.; Chandross, E.; Siegrist, T.; "Photochemical stability of pentacene and a substituted pentacene in solution and in thin films"; *Chem. Mater.*; 16; **2004**; 4980-4986

[18] Qiu, Y.; Hu, Y.; Dong, G.; Wang, L.; Xie, J.; Ma, Y.; "H_2O effect on the stability of organic thin-film field-effect transistors"; *Appl. Phys. Lett.*; 83; **2003**; 1644-1646

[19] McGhie, A.R.; Garito, A.F.; Heeger, A.J.; "A gradient sublime for purification and crystal growth of organic donor and acceptor molecules"; *J. Cryst. Growth*; 22; **1974**; 295-297

[20] Käfer, D.; Helou, M. el; Gemel, C.; Witte, G.; "Packing of planar organic molecules: interplay of van der Waals and electrostatic interaction"; *Cryst. Growth and Design*; 8; **2008**; 3053-3057

[21] Faltermeier, D.; Gompf, B.; Dressel, M.; Tripathi, A.K.; Pflaum, J.; "Optical properties of pentacene thin films and single crystals"; *Phys. Rev. B*; 74; **2006**; 125416

[22] Faltermeier, D.; Ellipsometrie an organischen Dünnfilmen und Einkristallen zur Bestimmung der optischen und strukturellen Eigenschaften; **2007**; PhD thesis; University of Stuttgart; Stuttgart, Germany

[23] Gompf, B.; Faltermeier, D.; Redling, C.; Dressel, M.; Pflaum, J.; "Tetracene film morphology: comparative atomic force microscopy, X-ray diffraction and ellipsometry investigations"; *Eur. Phys. J. E*; 27; **2008**; 421-424

[24] Parisse, P.; Passacantando, M.; Picozzi, S.; Ottaviano, L.; "Conductivity of the thin film phase of pentacene"; *Org. Electr.*; 7; **2006**; 403-409

[25] Northrup, J.E.; Chabinyc, M.L.; "Gap states in organic semiconductors: hydrogen- and oxygen-induced states in pentacene"; *Phys. Rev. B*; 68; **2003**; 041202

[26] Reddy, A.R.; Bendikov, M.; "Diels-Alder reaction of acenes with singlet and triplet oxygen – theoretical study of two-state reactivity"; *Chem. Commun.*; 1; **2006**; 1179-1181

[27] Mattheus, C.C.; Polymorphism and electronic properties of pentacene; PhD Thesis; **2002**; University of Groningen; Groningen, The Netherlands

[28] Parisse, P.; Picozzi, S.; Ottaviano, L.; "Electronic, morphological and transport properties of 6,13-pentacenequinone thin films: theory and experiments"; *Org. Electr.*; 8; **2007**; 498-504

[29] Hwang, D.K.; Kim, K.; Kim. J.H.; Im, S.; "Structural and optical properties of 6,13-pentacenequinone thin films"; *Appl. Phys. Lett.*; 85; **2004**; 5568-5570

[30] Hwang, D.K.; Kim, K.; Kim. J.H.; Jung, D.Y.; Kim, E.; Im, S.; "Structural and optical properties of 6,13-pentacenequinone film"; *Appl. Surf. Sci.*; 244; **2005**; 615-618

[31] Dzyabchenko, A.V.; Zavodnik, V.E.; Belsky, V.K.; "6,13-pentacenequinone: molecular packing analysis"; *Acta Cryst.*; B35; **1979**; 2250-2253

[32] Salzmann, I.; Opitz, R.; Rogaschewski, S.; Rabe, J.P.; Koch, N.; "Phase separation in vacuum codeposited pentacene/6,13-pentacenequinone thin films"; *Phys. Rev. B*; 75; **2007**; 174108

[33] Kloc, Ch.; Simpkins, P.G.; Siegrist, T.; Laudise, R.A.; "Physical vapor growth of centimeter-sized crystals of *α*-hexathiophene"; *J. Cryst. Growth*; 182; **1997**; 416-427

[34] Laudise, R.A.; Kloc, Ch.; Simpkins, P.G.; Siegrist, T.; "Physical vapour growth of organic semiconductors"; *J. Cryst. Growth*; 187; **1998**; 449-454

[35] Kloc, Ch.; "Single crystal growth of organic semiconductors for field effect applications"; *Proc. SPIE*; 6336; **2006**; 633606

[36] Boer, R.W.I. de; Gershenson, M.E.; Morpurgo, A.F.; Podzorov, V.; "Organic single-crystal field-effect transistors"; *Phys. Stat. Sol. A*; 201; **2004**; 1302-1331

[37] Yao, N.; Wang, Z.L.; Handbook of microscopy for nanotechnology; **2005**; Kluwer Academic Publishers; New York, NY, U.S.A.

[38] Reimer, L.; Scanning electron microscopy: physics of image formation and microanalysis; **1998**; 2nd ed.; Springer-Verlag; Berlin, Germany

[39] Joy, D.C.; Joy, C.S.; "Low voltage scanning electron microscopy"; *Micron*; 27; **1996**; 247-263

[40] Joy, D.C.; Monte Carlo modeling for electron microscopy and microanalysis; **1995**; Oxford University Press; New York, NY, U.S.A.

[41] Cazaux, J.; "Recent developments and new strategies in scanning electron microscopy"; *J. Microscopy*; 217; **2005**; 16-35

[42] Perovic, D.D.; Castell, M.R.; Howie, A.; Lavoie, C.; Tiedje, T.; Cole, J.S.W.; "Field-emission SEM imaging of compositional and doping layer semiconductor superlattices"; *Ultramicroscopy*; 58; **1995**; 104-113

[43] Sealy, C.P.; Castell, M.R.; Wilshaw, P.R.; "Mechanism for secondary electron dopant contrast in the SEM"; *J. Electron Microsc.*; 49; **2000**; 311-321

[44] Ness, J.N.; Page, T.F.; "Microstructural evolution in reaction-bonded silicon carbide"; *J. Mat. Sci.*; 21; **1986**; 1377-1397

[45] Castell, M.R.; Perovic, D.D.; Lafontaine, H.; "Electronic contribution to secondary electron compositional contrast in the scanning electron microscope"; *Ultramicroscopy*; 69; **1997**; 279-287

[46] Suvorova, A.A.; Samarin, S.; "Secondary electron imaging of SiC-based structures in secondary electron microscope"; *Surf. Sci.*; 601; **2007**; 4428-4432

[47] Park, S.I.; Quate, C.F.; "Tunneling of microscopy of graphite in air"; *Appl. Phys. Lett.*; 48; **1986**; 112-114

[48] Novoselov, K.S.; Geim, A.K.; Morozov, S.V.; Jiang, D.; Zhang, Y.; Dubonos, S.V.; Grigorieva, I.V.; Firsov, A.A.; "Electric field effect in atomically thin carbon films"; *Science*; 306; **2004**; 666-669

[49] Chung, D.D.L.; "Review graphite"; *J. Mat. Sci.*; 37; **2002**; 1475-1489

[50] Wu, J.S.; Spence, J.C.H.; "Electron diffraction of thin-film pentacene"; *J. Appl. Cryst.*; 37; **2004**; 78-81

[51] Ye, R.; Baba1, M.; Suzuki, K.; Ohishi, Y.; Mori, K.; "Effect of thermal annealing on morphology of pentacene thin films" *Jpn. J. Appl. Phys.*; 42; **2003**; 4473-4475

[52] Guo, D.; Ikeda, S.; Saiki, K.; Miyazoe, H.; Terashima, K.; "Effect of annealing on the mobility and morphology of thermally activated pentacene thin film transistors"; *J. Appl. Phys.*; 99; **2006**; 094502

[53] Yaginuma, S.; Itaka, K.; Matsumoto, Y.; Ohnishi, T.; Lippmaa, M.; Nagata, T.; Chikyow, T.; Koinuma, H.; "Composition-spread thin films of pentacene and 6,13-pentacenequinone fabricated by using continuous-wave laser molecular beam epitaxy"; *Appl. Surf. Sci.*; 254; **2008**; 2336-2341

[54] Takenobu, T.; Waranabe, K.; Yomogida, Y.; Shimotani, H.; Iwasa, Y.; "Effect of postannealing on the performance of pentacene single-crystal ambipolar transistors"; *Appl. Phys. Lett.*; 93; **2008**; 073301

Chapter 6

Patterning of Metals and Oxides on Organic Single-Crystals and Self-Assembled Monolayers with Pulsed Laser Deposition

Chapter 6: Patterning of Metals and Oxides on Organic Single-Crystals and Self-Assembled Monolayers with Pulsed Laser Deposition

Abstract

In this chapter, a direct deposition technique for the patterning of various materials with a well-defined geometry on pentacene single-crystals and alkylphosphate self-assembled monolayers is presented, without obvious destruction of the fragile organic molecular substrates, mechanical failure of the deposited film or diffusion of the deposited material into the soft organic substrate.

By taking several precautions in the pulsed laser stencil deposition process, which reduce the kinetic energy of the impinging species or reduce build-up of stress during deposition, low-kinetic energy deposition or *'soft-landing'* of arrays of isolated Pt top contacts on TDP-modified Nb-STO substrates is achieved with a high yield of 99.8%. With the optimized *'soft-landing'* settings, the patterning of smooth, well-defined and isolated metal top contacts (*i.e.* Au, Pt, Pd, Ni and Co) and medium-κ oxide dielectric materials (*i.e.* Al_2O_3, HfO_2 and CeO_2) on the surface of pentacene single-crystals is realized as well.

6.1 Introduction

In order to fabricate complete organic single-crystal field-effect transistors, four different approaches have been employed successfully so far (see paragraph 2.5). One of these approaches –the direct deposition of metal contacts and gate dielectric materials onto a free-standing organic molecular crystal– is not straightforward, but has great potential. In principle, well-controlled interfaces between the organic crystal and the deposited patterns with a well-defined geometry, can be obtained when using the direct deposition approach. Besides that, the manufacturing of hybrid (spintronic) devices and more complex electronic circuitry on one crystal substrate can be accomplished.

The fabrication of organic molecular crystal devices by direct deposition poses various technological challenges (see paragraph 2.5.3), as the surface of the fragile organic crystals can be damaged very easily. The organic single-crystals are incompatible with most conventional (silicon) microelectronic processing techniques, as these techniques damage the molecular order at the surface, creating interfacial trapping sites and barriers to charge injection. Metallic contacts are therefore often applied by manual 'painting' of a conducting silver paste on the crystal surface or by thermal evaporation of metals through a shadow mask, yet defects at the interface are still observed. Successful deposition of inorganic dielectric oxides onto the surface of organic crystals by sputtering or other techniques, without damaging the fragile crystal substrate, has not been reported so far. As a consequence, the amount of materials that can be patterned successfully on organic molecular crystals is quite limited at the moment.

A straightforward method to directly deposit metal top contacts on fragile organic substrates, without the use of lithographic process steps, was demonstrated by Steen [1], Vroegindeweij *et al.* [2] and Speets *et al.* [3-6], who investigated the stencil deposition of metallic nano- and micropatterns on organic self-assembled monolayers (SAMs) with pulsed laser deposition (PLD). In their research, 10-20 nm high hexagonal arrays of metal islands (*viz.* Au, Pt, Pd and Cu) were stencil deposited onto *n*-octadecanethiol (ODT, $C_{18}H_{37}$-SH) and 1,9-nonanedithiol (NDT, SH-C_9H_{18}-SH) self-assembled monolayers on gold [1-5]. Besides that, metal nanoclusters with sizes in the order of 1 to 3 nm were deposited locally on ODT and *n*-decane-thiol (DT, $C_{10}H_{21}$-SH) SAMs [4-6]. The use of SAMs as substrate for landing of (silicon) nanoparticles fabricated by laser ablation is demonstrated by Hata *et al.* [7] as well.

Overall, literature describing pulsed laser depositions of thin films and patterns onto soft organic substrates (*i.e.* molecular thin films, self-assembled monolayers or single-crystals) is quite limited. The heat, plasma and ions generated during the laser ablation process are generally believed to be harmful for soft organic materials and limit their use as substrate [8,9]. However, pulsed laser deposition on organic polymer materials has been explored quite extensive, and the combination of polymers with functional and protective inorganic (oxide) coatings can be found in a broad variety of applications (*e.g.* anti-reflection coatings, transparent conductive coatings and gas-barrier protection coatings) [10-13].

PLD enables the direct deposition of various materials on soft and fragile organic molecular substrates by controlling the kinetic energy of the ablated species in the gas phase by means of a background gas [8,9]. To obtain patterns on organic substrates with a well-defined interface, several precautions were taken in the PLD process that lower the kinetic energy of the impinging species, leading to the deposition of thermalized particles that do not diffuse into or damage the organic substrate.

To investigate quantitatively if the deposited gold patterns damaged the ~2nm thick SAM, electrochemical deposition experiments of copper from solution were carried out by Speets *et al.* [3,4]. Electrochemical copper deposition is a quick method to investigate if a gold island is electrically insulating from the underlying gold substrate by the SAM layer, see figure 6.1. In this wet-chemical technique, Cu^{2+} is reduced from an aqueous $CuSO_4$ solution to Cu (s) on the substrate at an overpotential. Au islands with short circuits to the bottom electrode (*i.e.* the SAM is locally damaged by the Au deposition) behave as small electrodes and hence copper will grow on them. Provided that modest potentials are used, no copper will grow on the electrically insulating Au islands without short circuits, showing the SAM remained intact. The bare SAM acts as a reference to see if the SAM shields the conducting substrate and copper deposition does not take place everywhere.

It was found that only for specific PLD deposition parameters no copper growth is observed on some of the gold islands [3,4]. At deposition pressures of 10^{-3} mbar or lower, no insulating islands were obtained: all Au patterns were shorted to the gold substrate below and showed Cu deposition. This shows the kinetic energy of the ablated Au particles was too high and the impinging Au species were not thermalized. The best results so far were obtained for gold patterns deposited at a 10^{-2} mbar argon background gas pressure on ODT SAMs. Using these settings, 15 % of the gold islands did not show the growth of copper on them, indicating the organic monolayer beneath these islands remained intact during deposition. However, 85 % of the gold islands did still show copper growth on them, indicating the process is far from optimal. When deposition pressures of 10^{-1} mbar or higher were used, the plasma plume entered the shockwave regime [14]: the patterned Au islands were blurry and grew together laterally, and could no longer be distinguished individually.

In order to minimize the possibility of metal diffusion into the organic molecular substrate, the kinetic energy of the arriving particles must be as low as possible. In practice, there are two 'knobs' that can be used to reduce the kinetic energy of the ablated species in PLD. Besides increasing the background gas pressure, increasing the target-to-substrate distance

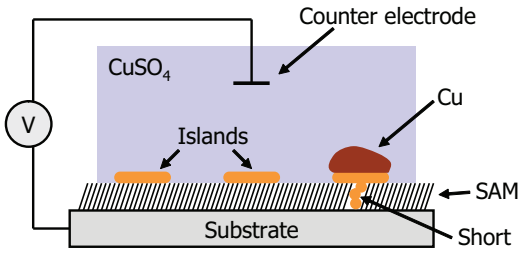

Figure 6.1 *Schematic electrochemical copper deposition on non-insulating metal islands patterned on a self-assembled monolayer.*

lowers the kinetic energy as well [9]. In fact, these two parameters are coupled: the kinetic energy of the ablated species in the plasma is reduced through an increased number of collisions with the background gas molecules in both situations [15].

In stencil deposition, however, the background gas pressure has a direct influence on the blurring and broadening of the patterned features [14]. At vacuum or low pressures, well-defined features can be achieved in stencil deposition, due to the low angular distribution of the material flux. Upon increasing the background pressure, the plasma gets more diffuse and less material will reach the substrate per pulse at a lower speed through multiple collisions with the background gas. As a consequence, larger feature sizes will be obtained when depositing through a stencil. This geometrical broadening is caused mainly by the increased angular distribution of the material flux, and the intrinsic gap that is present between the stencil and the substrate (see paragraph 3.3). At even higher pressures, the plasma plume enters the shockwave regime, resulting in huge undergrowth and blurring of the features when depositing through a stencil [14].

As a consequence, a compromise has to be found in stencil deposition on fragile organics between the patterned feature size and the kinetic energy with which the atoms or atom clusters reach the substrate (*i.e.* the kinetic energy has to be reduced as much as possible by increasing the background gas pressure, but without entering the shockwave regime).

Another important issue when depositing on organic substrates is build-up of stress during deposition, which may lead to cracking and subsequent delamination of the deposited material [13]. Key factor in the coating of organic substrates with inorganic films is the adhesion of the deposited film, as the mechanical properties of the two compound materials are very different. Mechanical failure of thin oxide films due to thermal stress is a well-known problem in the coating of plastics at and above room temperature [10].

In general, tensile stresses greater than the cohesive strength of the coating lead to cracking, whereas excessive compressive stresses result in buckling phenomena. The two main sources for internal stress generation during deposition are temperature gradients and intrinsic disorder during growth [13]. The intrinsic disorder is associated with defects and internal stresses [13]. To reduce possible thermal stress originating from the difference in expansion coefficients between film and substrate, deposition at room temperature is favored (*i.e.* the difference in expansion coefficients is quite large; the thermal expansion coefficient for organic materials is typically one order of magnitude larger than that of inorganic materials [16,17]). However, besides performing the deposition at room temperature, the deposition process itself can also increase the substrate temperature during growth.

At the substrate surface, most of the kinetic energy of the impinging species is available to be converted to thermal energy, increasing the temperature locally. Due to the pulsed character of PLD, heating up of the substrate during the deposition process is supposed to be minimal. Only for the top several micrometers of the substrate for a period of a few micro-seconds after each pulse, a significant variation of the substrate temperature is to be expected [18]. After landing, the thermal energy has to dissipate and the surface temperature declines back in a certain time period. However, if this dissipation process takes

longer than the time given between two pulses, the surface temperature will increase. As an example, a 14 °C rise in substrate temperature was observed after room temperature deposition of ZnO on PET at 10 Hz for 360 seconds, which was proposed as the main cause for the cracking of the deposited ZnO film [10].

The total increase of the temperature at the substrate surface is approximately inversely proportional to the square root of the thermal diffusivity κ of the substrate material, where κ is defined as the ratio between the thermal conductivity (λ_c) and the volumetric heat capacity ($\rho_d C_p$) [10,19]. The thermal diffusivity of solid organics (polymers) is typically $1\text{-}2 \times 10^{-7}$ m^2/s, which is two orders of magnitude lower than κ of most metals and oxides [19].

By decreasing the laser repetition rate, the sample is given more time to relax between pulses and heating up of the sample is averted. To avoid mechanical failure of inorganic films on organic substrates due to the large differences in thermal expansion coefficient and the low thermal diffusivity of the organic substrate, the laser pulse frequency should therefore be as low as possible, without becoming inconvenient (<1 Hz).

In order to fabricate complete field-effect transistors on organic molecular single-crystals, the direct deposition and patterning of metal contacts and inorganic gate dielectrics on the surface of fragile organic substrates (*i.e.* alkylphosphate self-assembled monolayers and pentacene single-crystals) by pulsed laser stencil deposition is examined in this chapter. As described above, the direct deposition of materials on these fragile organic materials is not straightforward, and the amount of different materials that can be patterned successfully at the moment is limited. Aim of this investigation is therefore to pattern a variety of different materials with a well-defined geometry, and without obvious destruction of the fragile organic molecular substrate, mechanical failure of the deposited film or diffusion of the deposited material into the soft organic substrate.

Investigating the penetration and diffusion of pulsed-laser deposited species into a pentacene single-crystal lattice on a nanometer-scale in a direct way is very difficult and expensive to perform. Both the sample preparation required for the analysis, as the characterization technique itself, quickly result in contamination and measurement errors (damage of the organic crystal, penetration of metal atoms into the crystal, etc.). Besides that, the sensitivity of many analysis techniques is too low for this system. The patterning of the alkylphosphate SAM is therefore regarded a *model system* for the patterning on a pentacene single-crystal surface, as for this system the penetration of pulsed-laser deposited metal species into the organic molecular material (*i.e.* the quality of the metal – organic interface) can be easily quantified by performing electrochemical deposition experiments.

As will be demonstrated, successful patterning of various metals and oxides can be achieved on the surface of the organic substrates with the pulsed laser stencil deposition technique, by taking several precautions in the PLD process that reduce the kinetic energy of the impinging species or reduce build-up of stress during deposition. As a result, low-kinetic energy deposition or *'soft-landing'* was realized on the surface of pentacene single-crystals and on alkylphosphate SAMs for the first time, without mechanical failure of the deposited patterns or obvious destruction to the fragile organic substrate.

6.2 Experimental Procedure

In this paragraph, the experimental details of the sample preparation, the used deposition and patterning techniques and of the applied analysis techniques are being discussed.

6.2.1 Deposition of Pt patterns on SAMs and electrochemical Cu deposition

The preparation of SAM-modified Nb-doped $SrTiO_3$ (Nb-STO) substrates was performed according to literature procedures [20-22]. Polished (100) 0.5 wt% Nb-STO ($1 \times 10 \times 10$ mm^3) substrates (SurfaceNet GmbH; Rheine, Germany) were cut into 5×5 mm^2 pieces with a diamond saw and cleaned by ultrasonication in acetone and ethanol for 30 min each. After oxygen plasma-cleaning, the Nb-STO substrates were immersed into a 0.125 mM *n*-tetradecylphosphoric acid (TDP, $C_{14}H_{29}$-OPO_3) solution in 100:1 *v*/*v* hexane:isopropanol for two days at room temperature. After that, the SAM-functionalized samples were rinsed with the solvent mixture, and dried under a flow of N_2 gas.

Water contact angle (CA) measurements on SAM-functionalized samples were done with a goniometer (model G10, Krüss GmbH; Hamburg, Germany) equipped with a CCD camera and Milli-Q water (18.4 MΩ cm) as probe liquid. The CA of oxygen plasma-cleaned Nb-STO was below 10°, which increased to 115° for a TDP-covered surface. This high value points to a hydrophobic surface, which confirms the CH_3-termination and, thus, indicates the successful formation of the TDP SAM on Nb-STO. AFM and STM measurements confirmed the smooth surface without any defects upon SAM formation (data shown in [23]). Earlier work on TDP SAMs on alumina showed a height of the TDP layer of 1.5 nm, which is lower than the extended adsorbate length (2 nm), indicating a tilt in the SAM [20].

Si_3N_4 membranes embedded in a silicon chip with large arrays of 5 and 10 μm^2 square and circular features were used for the patterned deposition of platinum top contacts on the SAM-modified samples by pulsed laser stencil deposition, as described in more detail in chapter 3 (see table 6.1 for experimental settings).

In the electrochemical copper depositions, the Nb-STO / TDP / Pt substrates were used as working electrode and an aqueous solution of $CuSO_4$ (10 mM) and H_2SO_4 (10 mM) as the electrolyte. A Pt mesh functioned as counter electrode, a 3 M KCl Ag / AgCl reference electrode (model REF321, Radiometer Analytical SAS; Lyon, France) was used and the depositions were performed with a precision potentiostat (model POS 73, Bank-IC Elektrotechnik GmbH; Pohlheim, Germany). Cu deposition occurred at 0.05 V vs. reference potential at short-circuited Pt-islands.

6.2.2 Deposition of metal and oxide patterns on organic single-crystals

Micrometer-sized and tens of nanometer thick patterns of various metals (*i.e.* Au, Pt, Pd, Co and Ni) and oxides (*i.e.* Al_2O_3, HfO_2 and CeO_2) were deposited on the surface of pentacene single-crystal substrates by pulsed laser stencil deposition at room temperature, as has been described in more detail in chapter 3. For all materials, the optimized PLD parameters are listed in table 6.1. During the depositions, besides the Si_3N_4 membrane stencils depicted in figure 3.4, stencils with arrays of micrometer-sized circular features were applied for

Table 6.1 *Overview optimized PLD settings.*

Target Material	Au [soft]	Au [hard]	Pt [soft]	Pt [hard]	Pd	Co	Ni	Al_2O_3	HfO_2	CeO_2
Gas type	Ar	Ar	Ar	Ar	Ar	Ar	Ar	O_2	O_2	O_2
Gas pressure [mbar]	0.05	0.003	0.05	0.003	0.05	0.02	0.02	0.025	0.05	0.005
T-S distance [mm]	75	45	75	45	75	75	75	75	75	65
Laser fluence [J/cm^2]	5.0	5.0	5.0	5.0	5.0	5.0	5.0	1.0	3.0	3.0
Laser freq. [Hz]	1	5	1	5	1	1	1	1	1	1
Mask [mm^2]	7×2×7	7×2×7	7×2×7	7×2×7	7×2×7	7×2×7	7×2×7	6×2×3	7×2×7	6×2×3
Spotsize [mm^2]	1.76	1.76	1.76	1.76	1.76	1.76	1.76	0.88	2.35	0.60
Dep. rate [nm/pulse]	0.006	0.017	0.001	0.005	0.014	0.002	0.004	0.012	0.015	0.003

patterning as well. Prior deposition, the stencil membranes were positioned above the crystals and gently pressed onto the substrate by *ex situ* clamping.

Details on the growth of the pentacene single-crystals were described in chapter 4. The organic crystals were glued on a 10x10 mm^2 and 0.5 mm thick silicon (*p*-type doped Si, with a native oxide layer), polyethylene (PET) or polydimethylsiloxane (PDMS) chip for mechanical support during deposition with thermally conducting silver paste (LeitSilber 200) or with a two-component solvent-free conductive silver epoxy (CircuitWorks CW2400; Farnell; Maarssen, The Netherlands). In a few cases, the organic crystals were 'bonded' to the supporting chip by electrostatic forces only. Before introducing the crystals, the supporting chips were first cleaned by rinsing ultrasonically in acetone and ethanol for 1 minute, and subsequently blown dry in a nitrogen gas stream. No cleaning or heating treatment was applied on the pentacene single-crystals.

6.2.3 Analysis of deposited patterns

Optical microscopy (OM) measurements were performed on a Nikon Eclipse ME600L optical microscope and atomic force microscopy (AFM) measurements were performed on a Veeco Multimode SPM and on a Veeco Dimension Icon system to investigate the influence of the deposition parameters on the thickness, structure and morphology of the deposited patterns. All AFM measurements were performed *ex situ* at ambient conditions. Elemental composition was analyzed by performing X-ray photoelectron spectroscopy (XPS) measurements on a PHI Quantera SCM Scanning ESCA Microprobe. For a more detailed description, see chapter 3.

6.3 Results and Discussion

In this paragraph, first the various deposition parameters used in this work will be defined (*i.e.* the *'hard-landing'* and *'soft-landing'* settings). After that, the experimental results from the stencil deposition of metal top contacts on an alkylphosphate self-assembled monolayer model system, and subsequent electrochemical Cu deposition, will be discussed. Finally, the results from various experiments on the patterning of metals and oxides through a stencil on the surface of pentacene single-crystals by PLD will be discussed.

6.3.1 Optimization of deposition parameters

In earlier work on the deposition of gold and platinum patterns on oxide substrates through a stencil by PLD [2,24], the optimal depositions parameters were found to include a laser fluency of 5 J/cm^2 with 5 Hz repetition rate, a target-to-substrate distance of 45 mm and an argon background gas pressure of 3×10^{-3} mbar. These settings were used as starting point in this work, as it was shown for these settings that a direct copy of the stencil' apertures on the substrate can be made without hindrance by broadening effects (see paragraph 3.3.2). However, these parameters were initially optimized for pulsed laser stencil deposition of Au or Pt on robust inorganic substrates, and not for patterning on fragile organic substrates. As mentioned before, the kinetic energy of the impinging species is an important factor when depositing on organic molecular substrates [1-6]. Irissou *et al.* [25,26] investigated the correlation between the background gas pressure and the target-to-substrate distance with the velocity of the ablated gold species impinging the substrate and the final gold thin film structure (see figure 6.2). Based on their findings, the starting deposition parameters described above correspond to a particle velocity of about 9.0 km/s for the gold species when arriving at the substrate, which is equivalent to a kinetic energy of about 80 eV. Obviously, the impinging Au and Pt species are not thermalized with these settings; therefore, these parameters will be further referred to as the *'hard-landing'* settings in his work.

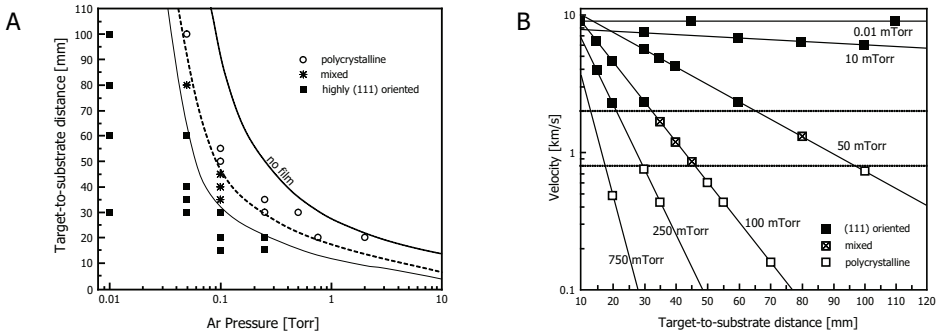

Figure 6.2 *A) Target-to-substrate distance vs. argon background pressure diagram for Au thin films deposited with PLD, showing the deposition conditions with the different types obtained (see legend). B) Velocity of the neutral gold species as a function of the distance along the plasma plume (i.e. target-to-substrate distance). The symbols represent the type of structure of the Au thin films prepared in the same conditions. Figures with permission from [25].*

After investigating the influence of various experimental parameters (which will not be further discussed), the most optimal low-kinetic Au and Pt deposition settings were found to include a laser fluency of 5 J/cm^2 with 1 Hz repetition rate, a target-to-substrate distance of 75 mm and an argon background gas pressure of 5×10^{-2} mbar. Compared to the *'hard-landing'* settings, the particle velocity for the gold species when arriving at the substrate is reduced significantly using these parameters. As a consequence, there is a strong reduction in the kinetic energy of the impinging species as well. Calculated with the results of Irissou *et al.* [25,26], these parameters correspond to a gold particle velocity of about 2.0 km/s, which is equivalent to a kinetic energy of about 4 eV. However, these numbers can only be regarded as an indication for the actual velocity and kinetic energy of the impinging species in this work, due to important differences in the experimental settings (*e.g.* dissimilar laser spotsizes, resulting in a different plasma behavior). In this work, the low-kinetic energy parameters will be further referred to as the *'soft-landing'* settings.

6.3.2 Deposition of Pt patterns on SAMs and electrochemical Cu deposition

The experimental results from the deposition of Pt patterns onto alkylphosphate self-assembled monolayers by pulsed laser stencil deposition are discussed in this paragraph.

Arrays of 10-20 µm-sized and 15-20 nm thick platinum patterns were deposited by PLD on Nb-doped $SrTiO_3$ (Nb-STO) substrates modified with a *n*-tetradecylphosphate (TDP, $C_{14}H_{29}$-OPO_3) SAM, using the *'hard-landing'* and *'soft-landing'* deposition parameters. As a control experiment, Pt patterns were deposited on bare Nb-STO substrates as well, with the *'hard-landing'* settings. After patterning, the diffusion of Pt into the organic monolayer was investigated by performing electrochemical copper deposition experiments. In this case, deposition of Cu could only occur at the places with electrical shorts between the Pt top contact and the conducting substrate, as the TDP monolayer is non-conductive (*i.e.* Cu growth only occurs on short-circuited Pt islands, where the SAM is damaged) [3,4].

Figure 6.3 shows optical microscopy images of Pt top contacts on bare and TDP-covered Nb-STO after pulsed-laser stencil deposition at *'hard-landing'* and *'soft-landing'* settings, and after electrochemical Cu growth. As can be seen, stencil deposition by PLD created many clean, uniform and well-defined Pt features on the bare and SAM-covered substrates in a single deposition step. Corresponding AFM images are presented in figure 6.4.

In the control experiments on bare Nb-STO substrates with the *'hard-landing'* settings, a uniform Cu growth was observed on all of the Pt top contacts after the electrochemical deposition. On these substrates, the Pt patterns were in direct contact with the substrate. No Cu growth was observed on the bare substrate regions, indicating the necessity of Pt to initiate Cu growth. Thus, the control experiment proves that Cu growth occurs if a Pt pattern is in contact with the bottom electrode (*i.e.* the Nb-STO substrate).

In the *'hard-landing'* experiments on the SAM-modified Nb-STO substrates, Cu growth was seen on most of the Pt dots after electrochemical Cu growth, but with lower density when compared to the bare substrate in the control experiment. In this case, the SAM layer acts as a barrier between the conducting substrate and the top contact to a certain degree.

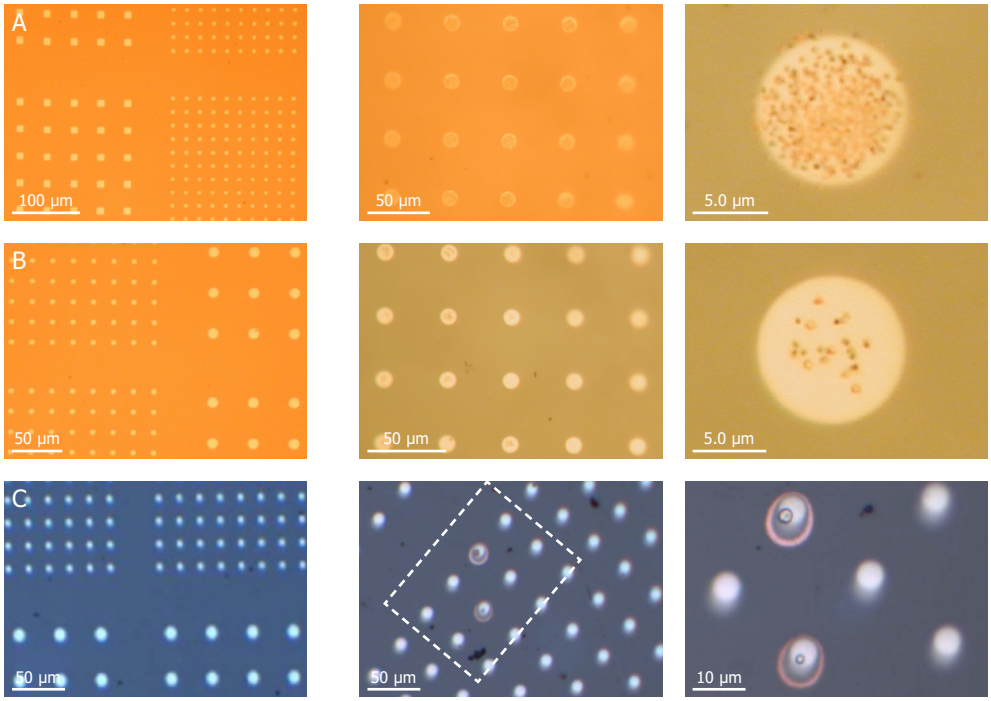

Figure 6.3 *OM images of Pt dots deposited with A) 'hard-landing' settings on bare Nb-STO, B) 'hard-landing' settings on TDP-covered Nb-STO, and C) 'soft-landing' settings on TDP-covered Nb-STO. For all series, the first image is of the deposited Pt dots before, and the second and third images after the electrochemical Cu growth. The white square in C) indicates the XPS mapping area (see figure 6.5)*

It also shows that no copper did grow on the SAM itself, indicating that there are no significant defects in the TDP monolayer [27].

Conversely, after electrochemical Cu deposition in the *'soft-landing'* experiments, almost all of the Pt patterns remained unchanged. The Pt features without shorts are clean and have the same height as before the electrochemical experiments, indicating that no deposition had occurred on these. This shows Pt top contacts without any shorts were successfully prepared on the SAM-modified substrate using the *'soft-landing'* PLD settings, with a yield of 99.8%. Only at two places out of thousand, shorts between the contact and the substrate could be seen, as indicated by the growth of 30-300 nm high non-uniform Cu deposits.

Figure 6.5 shows an XPS mapping of Pt and Cu of a selected area of the *'soft-landing'* sample, where the two shorts between the top contacts and the substrate were observed after the electrochemical Cu growth. The red parts representing Cu match well with the elevated parts seen in the OM and AFM images. Similar to the AFM images, the Pt patterns (green) are much more uniform than the Cu patterns, and do not contain Cu.

6.3.3 Deposition of metal and oxide patterns on organic single-crystals

In this paragraph, the experimental results from the deposition of various metals and oxide patterns on the surface of pentacene single-crystals by pulsed laser stencil deposition are

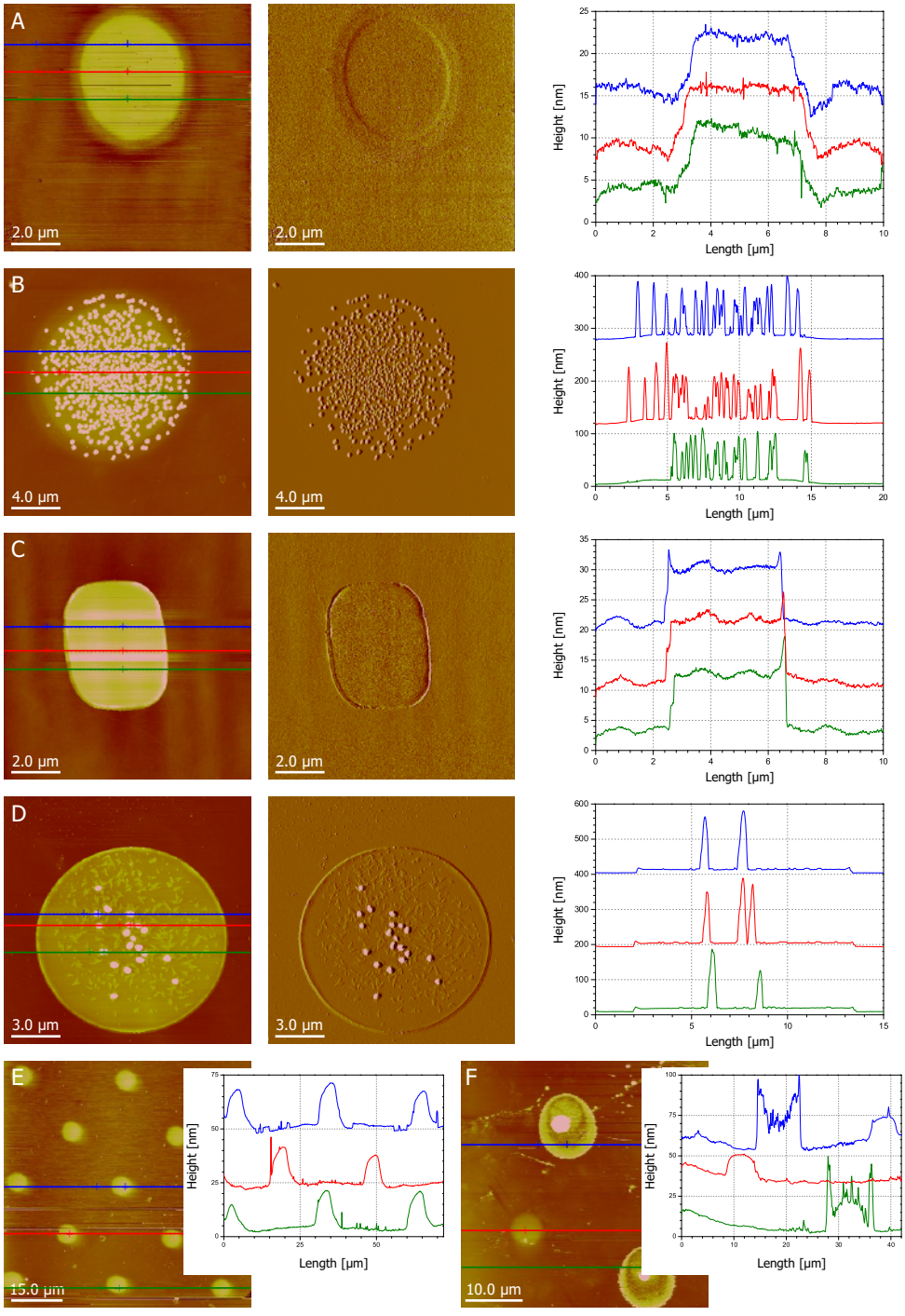

Figure 6.4 *AFM images of Pt dots deposited with 'hard-landing' settings on bare Nb-STO before (A) and after (B), and on TDP-covered Nb-STO before (C) and after (D) electrochemical Cu growth; and Pt dots deposited with 'soft-landing' settings on TDP-covered Nb-STO before (E) and after (F) electrochemical Cu growth (Z_{AFM} = 25, 50, 25, 50, 50 and 100 nm, respectively).*

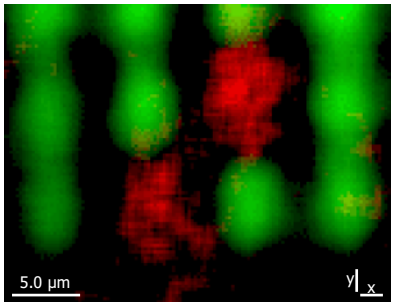

Figure 6.5 *XPS mapping showing the Pt-rich regions (green) and Cu-rich regions (red). Note that the resolution in the y-direction is less good than in the x-direction, due to the dispersive properties of the Quantera XPS analyser.*

discussed. Micrometer-sized and tens of nanometer thick patterns of various metals (*i.e.* Au, Pt, Pd, Co and Ni) and oxides (*i.e.* Al_2O_3, HfO_2 and CeO_2) were deposited through a stencil on the pentacene crystal substrates by PLD. The noble metals Au, Pt and Pd were patterned using both the *'hard-landing'* and *'soft-landing'* deposition parameters, and the influence of the applied settings on the morphology of the deposited patterns was investigated by OM, AFM and XPS measurements. The deposition of the other metals and oxides turned out to be much more sensitive to the applied deposition parameters. The objective for these materials was therefore to fabricate well-defined patterns without mechanical failure or obvious destruction to the organic crystal substrate, but still with the kinetic energy of the impinging species as low as possible.

Au patterns

Figure 6.6 presents optical and atomic force microscopy images of deposited Au features on the surface of pentacene single-crystals using the *'hard-landing'* settings (more AFM images are presented in figure 7.3). These images demonstrate that smooth and crack-free Au patterns can be fabricated with PLD, without obvious destruction of the organic crystal. Due to the roughness of the crystal surface and thus variations in the stencil-to-substrate gap, loss of resolution and deviations in broadening of the features (see paragraph 3.3.5) occurred along the sample, as can be observed in the OM images in figure 6.6A around some deposited patterns on the non-planar crystal surface. Yet, on flat surface areas, the deposited features are well-defined and completely isolated from each other.

Besides the substrate-to-stencil gap, blurring of the deposited features can arise from surface diffusion; highly-mobile materials like gold can diffuse over the hydrophobic crystal surface [14]. However, surface diffusion can be neglected in these experiments, as all depositions were performed at room temperature [14]. The observation that some deposited features are surrounded by a 'corona' of individual small gold particles (see figure 7.3A and C) is therefore attributed to geometrical broadening as well.

Figure 6.7 presents OM and AFM images of deposited Au features on the surface of pentacene single-crystals using the *'soft-landing'* settings (more AFM images are presented in figure 7.4). The deposited dots and squares are sharp and well-defined. Due to a small substrate-to-stencil gap during deposition, there is hardly any geometrical broadening and,

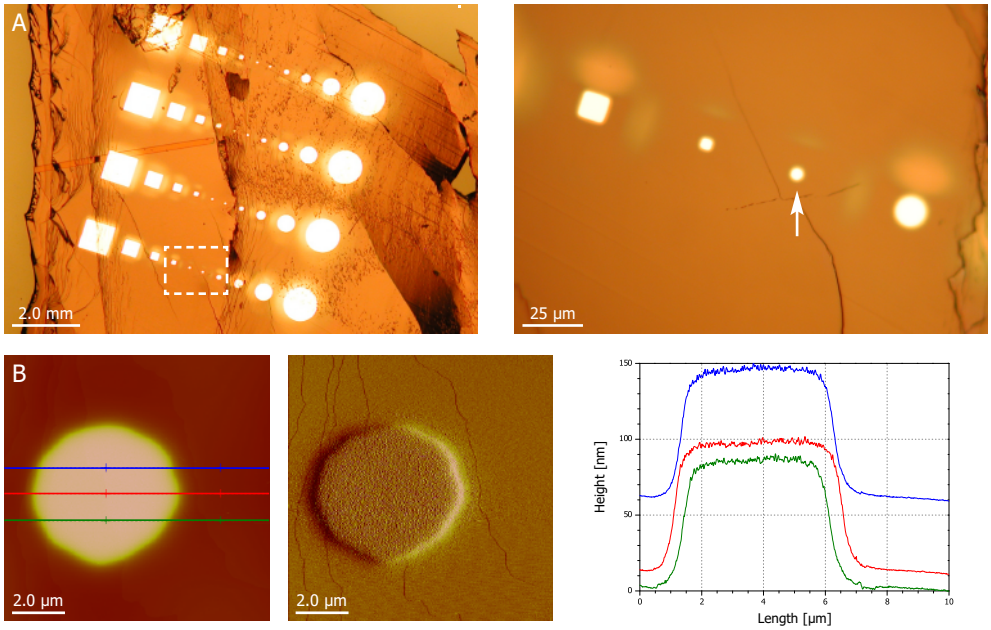

Figure 6.6 *A) Optical microscopy images, and B) AFM height, deflection and cross section images of Au dots stencil deposited on a pentacene single-crystal with PLD at 'hard-landing' settings (Z_{AFM} = 150 nm). AFM images of the Au dot indicated with the white arrow are presented in figure 7.3A-B.*

as a consequence, almost no appearance of small individual gold particles around the deposited features. In the contact-mode AFM friction image (see figure 6.7B), and in the tapping-mode AFM phase image (see figure 6.7C), a clear material contrast can be observed between the deposited Au dots and the underlying pentacene single-crystal substrate. Based on this material contrast, it is concluded that the features in the stencil are well-duplicated on the substrate, and that the deposited dots are indeed sharp and not surrounded by a 'corona' of gold material.

The AFM images in figure 6.6B and figure 7B-C show that the terraced morphology of the underlying pentacene single-crystal substrate (*i.e.* the 1.41 nm high *d*(001) terrace steps) is still noticeable on top of the deposited gold dots (of about 85, 45 and 40 nm high, respectively) for both settings. This observation indicates a high-quality growth, without obvious destruction of the fragile pentacene crystal substrate and most likely with a well-defined interface; *i.e.* the deposition process did at least not destruct the original morphology of the pentacene crystal. A more detailed study on this duplication of the substrate morphology is presented in chapter 7.

It is important to note here that the difference in deposition parameters between the *'hard-landing'* and *'soft-landing'* settings does not seem to influence the structure and morphology of the deposited gold features (*e.g.* smooth films were obtained with both settings), but only influenced the broadening effect and the deposition rate (reduced from ~0.017 to ~0.006 nm/pulse, respectively). However, the surface roughness of the deposited

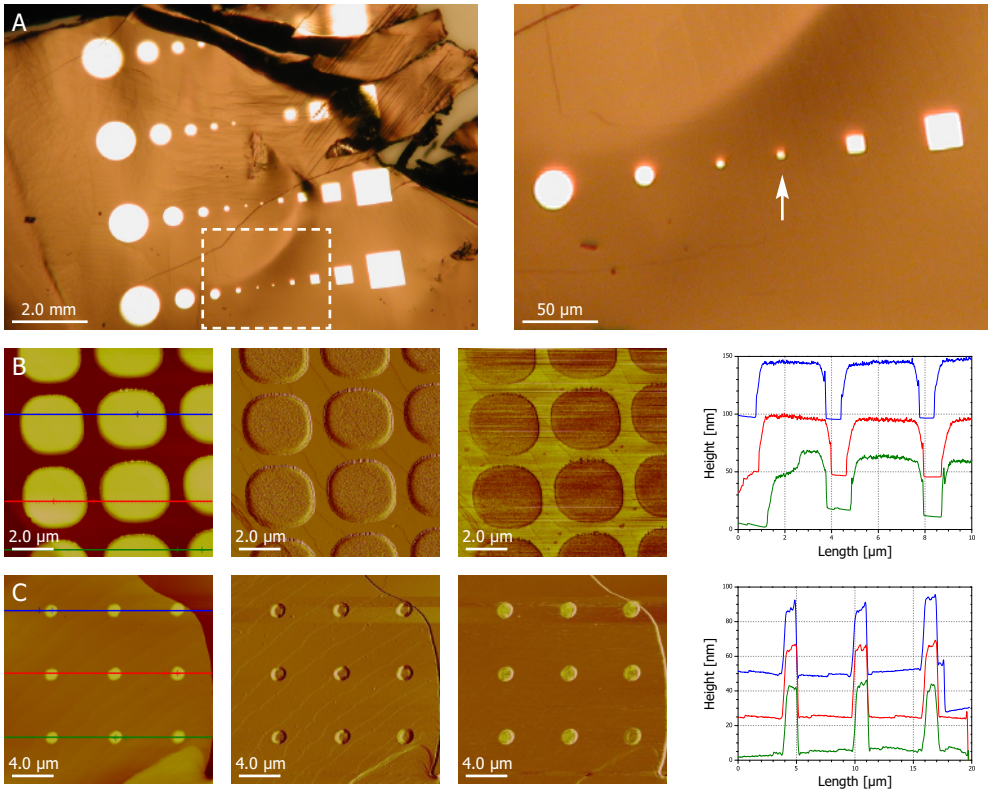

Figure 6.7 *A) Optical microscopy images, B) AFM height, deflection, friction and cross section images, and C) AFM height, deflection, phase and cross section images of Au dots stencil deposited on a pentacene single-crystal substrate with PLD at 'soft-landing' settings (Z_{AFM} = 100 nm and 150 nm, respectively). AFM images of the Au dot indicated with the white arrow are presented in figure 7.4B-C.*

Au features is dependent on the applied settings, as will be shown in chapter 7. Also, the amount of penetration and diffusion of the pulsed-laser deposited gold species into the pentacene single-crystal lattice is dependent on these settings, as can be concluded from the experiments performed on the organic SAM model system described earlier in this chapter. Current-voltage measurements on pentacene single-crystal devices with *'hard-landed'* and *'soft-landed'* gold top contacts will be presented in chapter 8.

Pt and Pd patterns

For the deposition of platinum (Pt) and palladium (Pd) patterns on the surface of organic molecular crystal substrates, it was found that the *'hard-landing'* and *'soft-landing'* settings used for Au could be applied as well: the ablation, deposition and growth conditions of these noble metals were found to be comparable. This is illustrated by the AFM images in figure 6.8, in which a ~15 nm thick Pt and a ~150 nm thick Pd square feature deposited on a pentacene single-crystal with the *'soft-landing'* settings is presented, respectively, showing the same duplication of the substrate morphology on top of the patterned features.

Ni and Co patterns

To broaden the set of metals that can be applied as top contacts on the surface of organic molecular crystals (a very low contact resistance was recently reported for nickel (Ni) and cobalt (Co) contacts on rubrene single-crystals [28,29]), the direct deposition of these two less-noble metals on pentacene single-crystals by pulsed laser stencil deposition was investigated.

In contrast to the noble metals discussed in the previous paragraph, the deposition 'window' leading to successful patterning of these metals was found to be narrower. For the Ni and Co deposition series, the *'soft-landing'* settings optimized for Au deposition on pentacene crystals were chosen as starting point, as the *'hard-landing'* settings resulted in cracked films. To explore these settings further, the argon background gas pressure was varied between 0.005 mbar and 0.05 mbar, whereas all other parameters remained the same.

At argon pressures of 0.005 and 0.01 mbar, no smooth Ni and Co films could be obtained. A few examples of the encountered mechanical failures are presented in figure 6.9. The larger patterns show buckling phenomena, cracking or delamination. Based on the structure of some cracked films, the presence of large terrace steps on the pentacene crystal surface seems to play an important role in the occurrence of mechanical failure. Some of the smaller patterns (5.0 and 12.5 μm^2) did not crack, but the large curvature of these patterns indicates the presence of large internal stresses in the film (see figure 6.9C).

Lowering the kinetic energy of the impinging particles by utilizing a high background pressure of 0.05 mbar resulted in very porous feature structures (see figure 6.10A-B). Collisions with the background gas lowered the kinetic energy so much, that the impinging particles hardly have any energy left for surface diffusion and stick more or less to where they

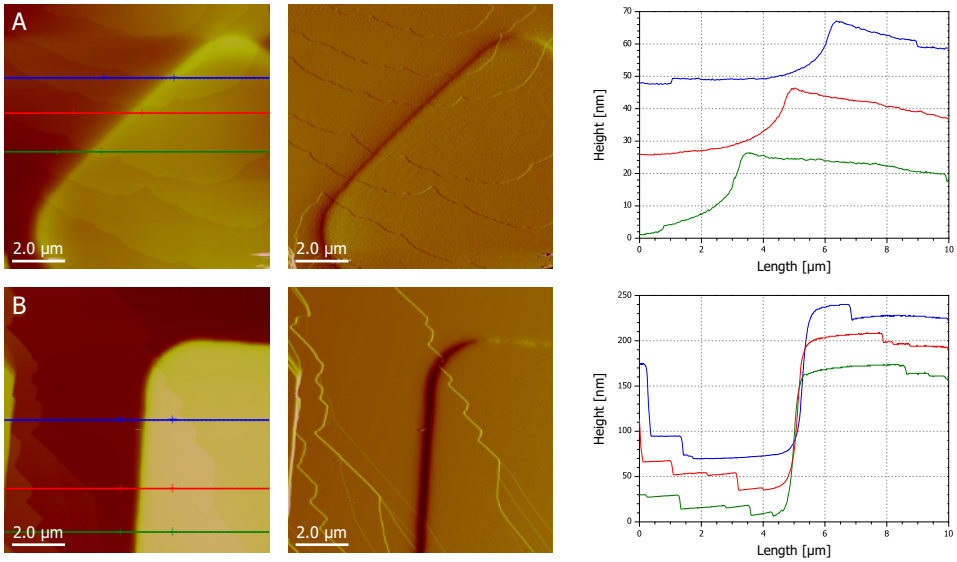

Figure 6.8 *AFM height, deflection and cross section images of a A) Pt dot and a B) Pd dot deposited on a pentacene single-crystal with PLD at 'soft-landing' settings (Z_{AFM} = 75 and 300 nm, respectively).*

hit the substrate, resulting in an island-like growth. Probably, the high background pressure also resulted in the formation of cluster particles in the plasma [9,30], which limits the growth of a smooth film as well. However, the local deposition of large cluster particles is typically not encountered when depositing through a stencil in PLD, as for most materials the shockwave broadening regime is entered first upon increasing the background pressure [14].

Deposition at an intermediate pressure of 0.02 mbar Ar gave the best results. At this pressure, smooth Ni and Co thin films and patterns were obtained (see figure 6.10C-D). The impinging particles have a low kinetic energy for *'soft-landing'*, yet are mobile enough to form smooth pinhole-free films.

The encountered mechanical failure of the Ni and Co patterns (deposited at low background pressures) can also be caused by internal stresses induced by oxidation reactions after deposition. *Ex situ* XPS sputter profiling showed the outmost layer of a ~10 nm thick Ni film deposited on a pentacene single-crystal has oxidized (figures not shown). As the oxygen O1s peak disappeared faster during sputtering than the nickel Ni2p peaks, it is concluded that

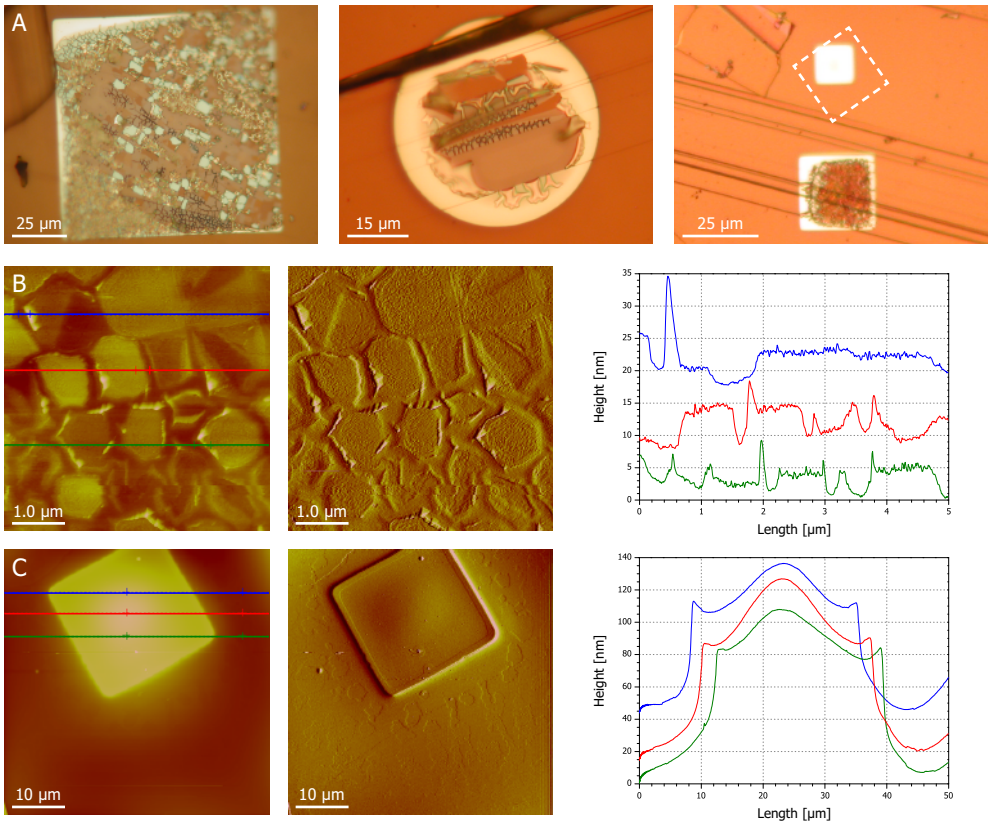

Figure 6.9 *Examples of mechanical failure (buckling, cracking or delamination) in Ni dots deposited on pentacene single-crystals by PLD at an Ar background pressure of 0.005 mbar; A) optical microscopy images, B) and C) AFM height, deflection and cross section images (Z_{AFM} = 25 nm and 200 nm, respectively). The white square in A) indicates the area imaged with AFM in C).*

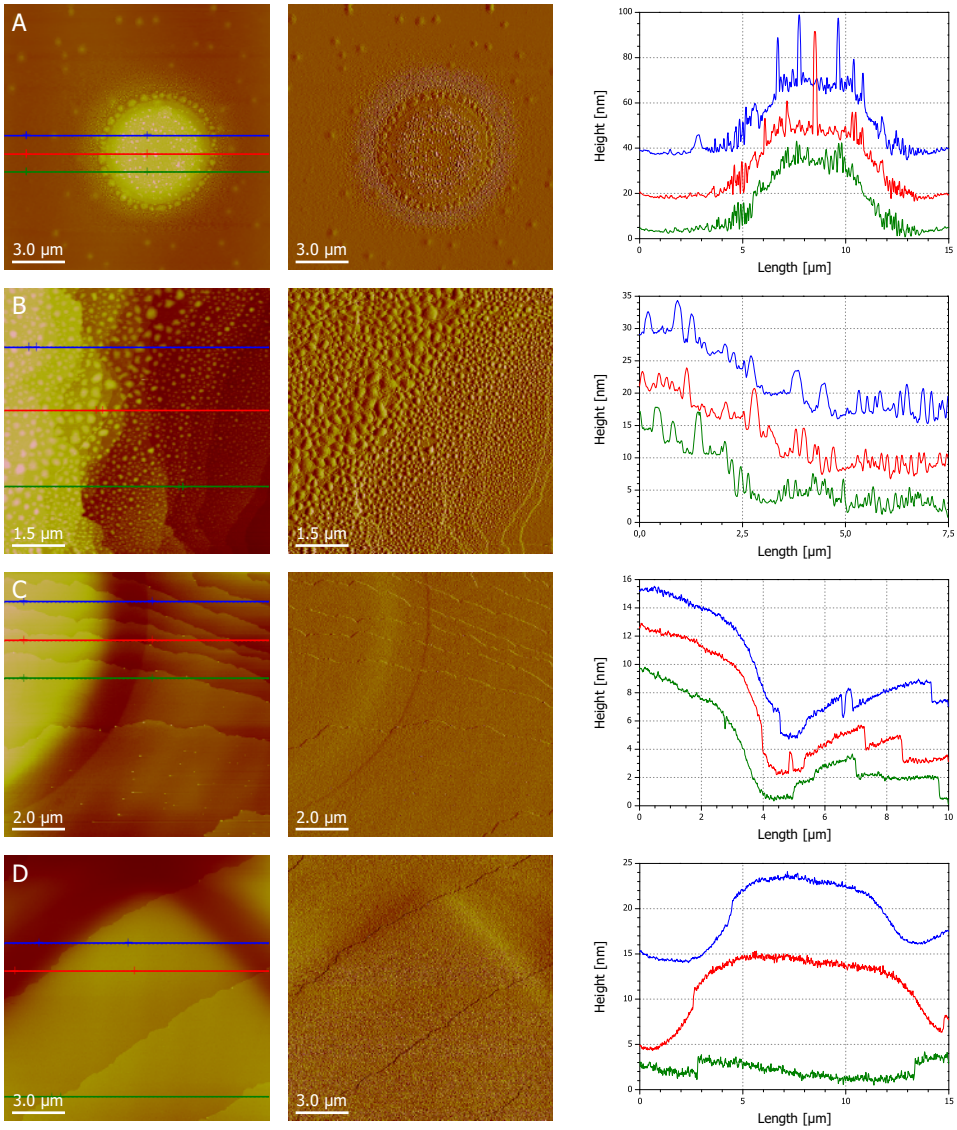

Figure 6.10 *AFM height, deflection and cross section images of A-B) Ni and Co (0.05 mbar), and C-D) Ni and Co (0.02 mbar) features stencil deposited on pentacene single-crystals with PLD at various argon background pressures (Z_{AFM} = 100, 25, 20 and 35 nm, respectively).*

the film was only oxidized on the outer surface and there is still metallic nickel on the Ni – pentacene interface. However, this observation may also derive from a preferential sputtering of oxygen relative to nickel during profiling, implying a complete oxidation of the deposited Ni thin film cannot be excluded. Similar results were observed for Co thin films deposited on a pentacene crystal.

As the (partial) oxidation after deposition is expected to occur for all Ni and Co patterns, irrespective of the deposition gas pressure, it is remarkable that no significant mechanical

failure is encountered for the patterns deposited at 0.02 and 0.05 mbar argon. Therefore, it can be concluded that the oxidation reactions are not the main cause for the mechanical failure of the patterns deposited at 0.005 and 0.01 mbar. More likely, the mechanical failure at these low pressures can be attributed to a higher kinetic energy of the impinging species.

Al_2O_3, HfO_2 and CeO_2 patterns

Besides deposition of metallic features suitable as contacts, deposition of insulating films of dielectric materials are needed in the direct fabrication of (field-effect) devices on organic molecular crystals. Therefore, the patterning of three medium-κ oxides, namely alumina (Al_2O_3, $\varepsilon = 9$), hafnia (HfO_2, $\varepsilon = 25$) and ceria (CeO_2, $\varepsilon = 26$), on pentacene single-crystals by pulsed laser stencil deposition was investigated. Initially, the deposition parameters were chosen similar to those optimized for deposition of oxide dielectric films on silicon at room temperature [31,32]. However, using these settings, mechanical failure and cracks appeared in the film surfaces after stencil deposition of the oxide onto the organic crystal (see figure 6.11). An increased temperature of the film and substrate surface during deposition (*i.e.* the thermal diffusivity κ of the organic substrate is about two orders of magnitude lower than κ of most metals and oxides (see paragraph 6.1)) is suspected to be responsible for the build-up of strain, which is later released by cracking and buckling of the patterned material. Based on the structure of some cracked films, the presence of large terrace steps on the pentacene surface played an important role in the occurrence of mechanical failure as well.

After tuning the deposition parameters (*i.e.* going to milder settings by lowering the laser repetition rate, increasing the target-to-substrate distance and increasing the background gas pressure), which effectively lower the kinetic energy of the impinging particles and reduce

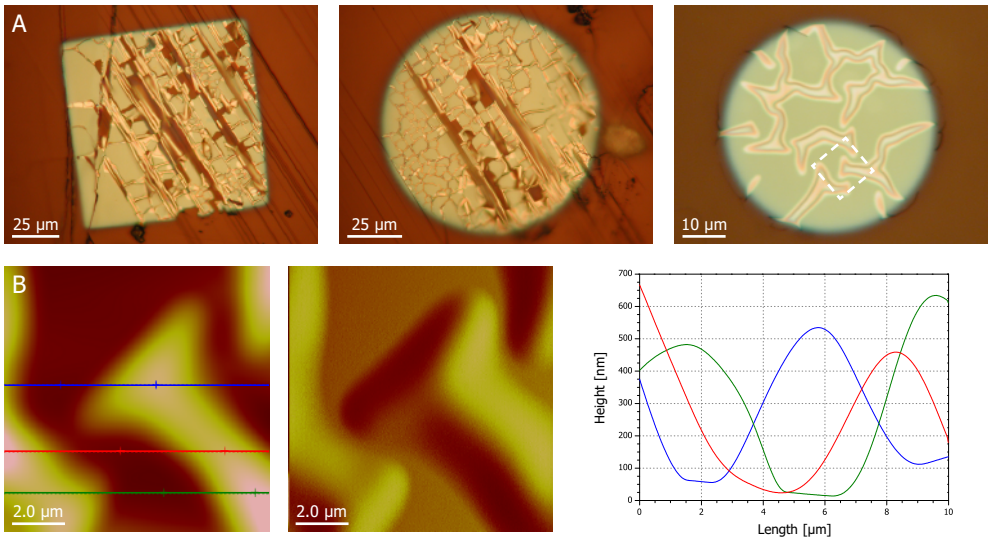

Figure 6.11 *Examples of mechanical failure (buckling, cracking or delamination) in CeO_2 dots deposited on pentacene single-crystals by PLD; A) OM images, B) AFM height, deflection and cross section images ($Z_{AFM} = 750$ nm). The white square in A) indicates the area imaged with AFM in B).*

heating-up of the sample, crack-free, smooth and pinhole-free oxide patterns could be obtained on the pentacene single-crystal surface (see figure 6.12). Besides that, relatively low undergrowth and blurring of the features was observed. As observed in the deposition of metal contacts, again the substrate morphology is duplicated on top of the deposited features. This implies that high-quality growth of oxide dielectric materials on fragile organic crystals with PLD and stencil patterning is achievable.

Using the optimized PLD parameters (see table 6.1), crack-free metal and oxide films completely covering a pentacene single-crystal were obtained as well (not shown), so these settings are not restricted to deposition through a stencil. Besides performing stencil depositions on pentacene crystal substrates, the potential of this technique was demonstrated by depositing Au and CeO_2 patterns on rubrene single-crystals. Similar results were obtained in these experiments (not shown); *i.e.* smooth, crack-free and well-defined features were patterned on the surface of rubrene crystals, with the 1.34 nm high *d*(001) terrace steps [33,34] for example clearly noticeable on top of the ~125 nm high ceria dots.

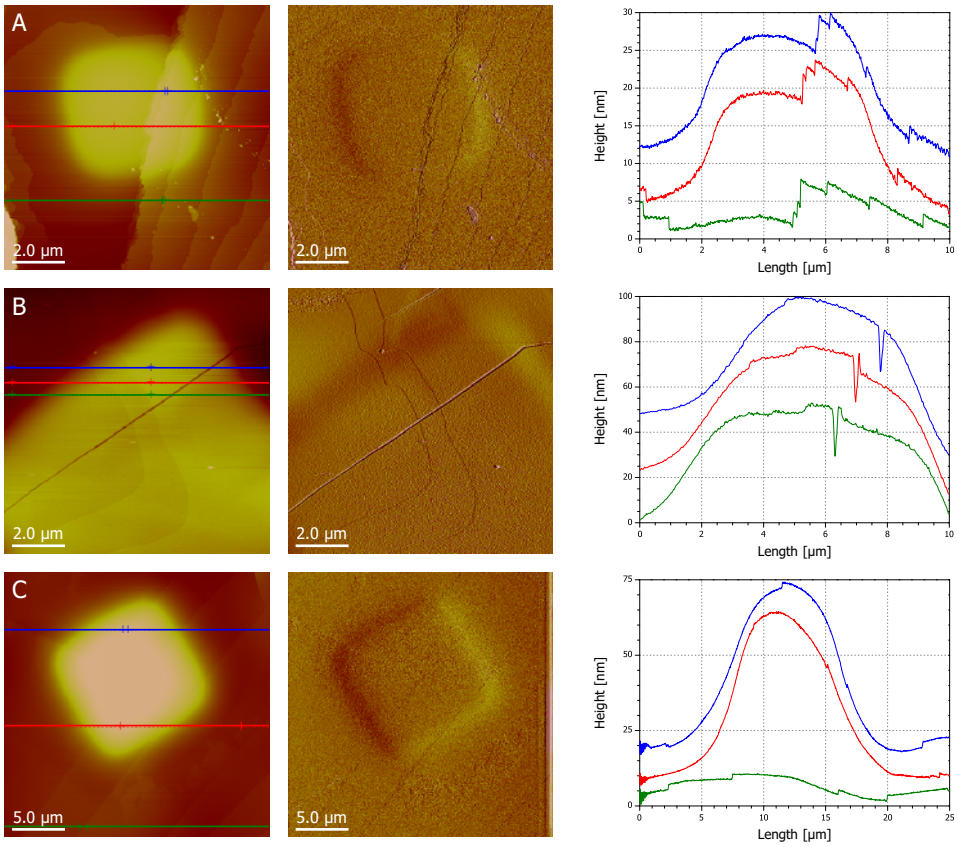

Figure 6.12 *AFM height, deflection and cross section images of A) an Al_2O_3 dot, B) a HfO_2 dot, and C) a CeO_2 feature stencil deposited on pentacene single-crystals with PLD at the optimized settings (Z_{AFM} = 40, 100 and 100 nm, respectively).*

6.4 Concluding Remarks

In order to fabricate complete field-effect transistors on the surface of organic molecular crystals, the direct deposition and patterning of various metals and inorganic dielectric materials on pentacene single-crystal and on alkylphosphate self-assembled monolayer substrates by pulsed laser stencil deposition was investigated in this chapter. Successful deposition of patterns with a well-defined geometry, and without obvious destruction of the fragile organic molecular substrates, mechanical failure of the deposited film or diffusion of the deposited material into the soft organic substrate was achieved, by taking several precautions in the PLD process that reduce the kinetic energy of the impinging species or reduce build-up of stress during deposition.

As a result, low-kinetic energy deposition or *'soft-landing'* of arrays of isolated Pt top contacts on TDP-modified Nb-STO substrates was achieved with a high yield of 99.8% without damaging the SAM layer, as shown by electrochemical deposition experiments of copper from solution. With these optimized *'soft-landing'* settings, the direct deposition and patterning of smooth, well-defined and isolated metal top contacts (*i.e.* Au, Pt, Pd, Ni and Co) and medium-κ oxide dielectric materials (*i.e.* Al_2O_3, HfO_2 and CeO_2) on the surface of pentacene single-crystals was realized as well.

6.5 References

[1] Steen, J.; Sub-micron patterning with shadow-masks using pulsed laser deposition; MSc Thesis; **2002**; University of Twente; Enschede, The Netherlands

[2] Vroegindeweij, F.; Speets, E.A.; Steen, J.A.J.; Brugger, J.; Blank, D.H.A.; "Exploring microstencils for sub-micron patterning using pulsed laser deposition"; *Appl. Phys. A*; 79; **2004**; 743-745

[3] Speets, E.A.; Ravoo, B.J.; Roesthuis, F.J.G.; Vroegindeweij, F.; Blank, D.H.A.; Reinhoudt, D.N.; "Fabrication of arrays of gold islands on self-assembled monolayers using pulsed laser deposition through nanosieves"; *Nano Lett.*; 4; **2004**; 841-844

[4] Speets, E.A.; Riele, P. te; Boogaart, M.A.F. van den; Doeswijk, L.M.; Ravoo, B.J.; Rijnders, G.; Brugger, J.; Reinhoudt, D.N.; Blank, D.H.A.; "Formation of metal nano- and micropatterns on self-assembled monolayers by pulsed laser deposition through nanostencils and electroless deposition"; *Adv. Func. Mater.*; 16; **2006**; 1337-1342

[5] Speets, E.A.; Deposition of metal islands, metal clusters and metal containing single molecules on self-assembled monolayers; PhD Thesis; **2005**; University of Twente; Enschede, The Netherlands

[6] Speets, E. A.; Dordi, B.; Ravoo, B. J.; Oncel, N.; Hallback, A. S.; Zandvliet, H. J. W.; Poelsema, B.; Rijnders, G.; Blank, D. H. A.; Reinhoudt, D. N.; "Noble metal nanoparticles deposited on self-assembled monolayers by pulsed laser deposition show coulomb blockade at room temperature"; *Small*; 1; **2005**; 395-398

[7] Hata, S.; Yoshida, S.; Fujita, M.; Yasuda, S.; Makimura, T.; Murakami, K.; Shigekawa, H.; "Self-assembled mono layer as a template to deposit silicon nanoparticles fabricated by laser ablation"; *J. Phys. Chem. B*; 105; **2001**; 10842-10846

[8] Eason, R.; Pulsed laser deposition of thin films – Applications-led growth of functional materials; **2007**; 1st ed.; Wiley-Interscience; Hoboken, NJ, U.S.A.

[9] Willmott, P.R.; Huber, J.R.; "Pulsed laser vaporization and deposition"; *Rev. Mod. Phys.*; 72; **2000**; 315-328

[10] Dekkers, J.M.; Transparent conducting oxides on polymer substrates by pulsed laser deposition; PhD Thesis; **2007**; University of Twente; Enschede, The Netherlands

[11] Lackner, J.M.; Waldhauser, W.; Schöberl, T.; "Film growth phenomena in high-energetic room temperature pulsed laser deposition on polymer surfaces"; *Surf. Coat. Techn.*; 201; **2006**; 4037-4039

[12] Takano, N.; Doeswijk, L.M.; Boogaart, M.A.F. van den; Auerswald, J.; Knapp, H.F.; Dubochet, O.; Hessler, T.; Brugger, J.; "Fabrication of metallic patterns by microstencil lithography on polymer surfaces suitable as micro electrodes in integrated microfluidic systems"; *J. Micromech. Microeng.*; 16; **2006**; 1606-1613

[13] Leterrier, Y.; "Durability of nanosized oxygen-barrier coatings on polymers"; *Prog. Mater. Sci.*; 48; **2003**; 1-55

[14] Riele, P.M. te; Direct patterning of oxides by pulsed laser stencil deposition; PhD Thesis; **2008**; University of Twente; Enschede, The Netherlands

[15] Haynes, W.M. ed.; Handbook of Chemistry and Physics; **2011**; 91st ed.; CRC Press, Taylor and Francis; Boca Raton, FL, U.S.A.

[16] Kim, H.S.; Kwok, H.S.; "Correlation between target-substrate distance and oxygen pressure in pulsed laser deposition of $YBa_2Cu_3O_7$" *Appl. Phys. Lett.*; 61; **1992**; 2234-2236

[17] Siegrist, T.; Besnard, C.; Haas, S.; Schiltz, M.; Pattison, P.; Chernyshov, D.; Batlogg, B.; Kloc, C.; "A polymorph lost and found: the high-temperature crystal structure of pentacene"; *Adv. Mater.*; 19; **2007**; 2079-2082

[18] Kusumori, T.; Muto, H.; Brito, M.E.; "Control of polytype formation in silicon carbide heteroepitaxial films by pulsed laser deposition"; *Appl. Phys. Lett.*; 84; **2004**; 1272-1274

[19] Lienhard IV, J.H.; Lienhard V, J.H.; A heat transfer textbook; **2011**; 4th ed.; Phlogiston press; Cambridge, MA, U.S.A.

[20] Yildirim, O.; Gang, T.; Kinge, S.; Reinhoudt, D.N.; Blank, D.H.A.; Wiel, W.G. van der; Rijnders, G.; Huskens, J.; "Monolayer-directed assembly and magnetic properties of FePt nanoparticles on patterned aluminum oxide"; *Int. J. Mol. Sci.*; 11; **2010**; 1162-1179

[21] Gawalt, E.S.; Avaltroni, M.J.; Koch, N.; Schwartz, J.; "Self-assembly and bonding of alkanephosphonic acids on the native oxide surface of titanium"; *Langmuir*; 17; **2001**; 5736-5738

[22] Messerschmidt, C.; Schwartz, D.K.; "Growth mechanisms of octadecylphosphonic acid self-assembled monolayers on sapphire (corundim): evidence for a quasi-equilibrium triple point"; *Langmuir*; 17; **2001**; 462-467

[23] Yildirim, O.; Self-assembled monolayers on metal oxides: applications in nanotechnology; PhD Thesis; **2010**; University of Twente; Enschede, The Netherlands

[24] Vroegindeweij, F.; *private communication*

[25] Irissou, E.; Drogoff, B. Le; Chaker, M.; Guay, D.; "Correlation between plasma expansion dynamics and gold-thin film structure during pulsed-laser deposition"; *Appl. Phys. Lett.*; 80; **2002**; 1716-1718

[26] Irissou, E.; Drogoff, B. Le; Chaker, M.; Guay, D.; "Influence of the expansion dynamics of laser-produced gold plasma on thin film structure grown in various atmospheres"; *J. Appl. Phys.*; 94; **2003**; 4796-4802

[27] Sondag-Huethorst, J.A.M.; Fokkink, L.G.J.; "Galvanic copper deposition on thiol-modified gold electrodes"; *Langmuir*; 11; **1995**; 4823-4831

[28] Hulea, I.N.; Russo, S.; Molinari, A.; Morpurgo, A.F.; "Reproducible low contact resistance in rubrene single-crystal field-effect transistors with nickel electrodes"; *Appl. Phys. Lett.*; 88; **2007**; 113512

[29] Molinari, A.; Gutiérrez, I.; Hulea, I.N.; Russo, S.; Morpurgo, A.F.; "Bias-dependent contact resistance in rubrene single-crystal field-effect transistors"; *Appl. Phys. Lett.*; 90; **2007**; 212103

[30] Wood, R.F.; Leboeuf, J.N.; Chen, K.R.; Geohegan, D.B.; Puretzky, A.A.; "Dynamics of plume propagation, splitting, and nanoparticles formation during pulsed-laser ablation"; *Appl. Surf. Sci.*; 127-129; **1998**; 151-158

[31] Karakaya, K.; CeO_2 and HfO_2 high-*k* gate dielectrics by pulsed laser deposition: from binary oxides to nanolaminates"; PhD Thesis; **2006**; University of Twente; Enschede, The Netherlands

[32] Karakaya, K.; *private communication*

[33] Käfer, D.; Witte, G. "Growth of crystalline rubrene films with enhanced stability"; *Phys. Chem. Chem. Phys.*; 7; **2005**; 2850-2853

[34] Zeng, X.; Zhang, D.; Duan, L.; Wang, L.; Dong, G.; Qiu, Y.; "Morphology and fluorescence spectra of rubrene single crystals grown by physical vapor transport"; *Appl. Surf. Sci.*; 253; **2007**; 6047-6051

Chapter 7

Growth Evolution of Gold Patterns deposited on Pentacene Single-Crystals and SiO_x substrates by PLD

Chapter 7: Growth Evolution of Gold Patterns deposited on Pentacene Single-Crystals and SiO_x Substrates by PLD

Abstract

The structure and morphology of gold patterns deposited on pentacene single-crystal and silicon oxide substrates by pulsed laser stencil deposition at room temperature have been studied. From the analysis of atomic force microscopy measurements, it was found that the *rms* surface roughness σ (ranging from 0.4 nm to 2.3 nm) of all deposited patterns generally increases with the layer thickness (ranging from 30 nm to 150 nm). The growth and morphology of gold films deposited on silicon oxide and pentacene single-crystals with *'hard-landing'* settings is found to be similar on both kinds of substrates. For gold features deposited on pentacene single-crystals using *'soft-landing'* parameters, a smoother film morphology is observed than in the *'hard-landed'* films, which is attributed to various differences in the deposition parameters (*viz.* kinetic energy, angular plume distribution and deposition rate).

7.1 Introduction

In the previous chapter, the patterning of metal and oxide features by pulsed-laser stencil deposition on the surface of pentacene single-crystals has been investigated. Interestingly, it was found that the terraced structure of the underlying pentacene substrate is often still noticeable on top of the deposited patterns. For some specific deposition parameters, this duplication of the 1.4 nm high pentacene terraces steps is observed on deposited patterns with a thickness up to several tens of nanometers. As an example, figure 7.1A shows the morphology of 45 nm thick Au dots patterned on a pentacene single-crystal surface. Both the normal monomolecular 1.4 nm high $d(001)$ P_1-P_2 pentacene crystal terrace steps (*i.e.* the parallel thin black features, from top to bottom), as well as larger stress-induced terrace steps (*i.e.* the larger steps going from left to right), are clearly observable on top of the deposited dots. However, as depicted in figure 7.1B, on top of 125 nm high Au stripes patterned on a pentacene crystal surface using other deposition settings, the morphology of the underlying substrate can no longer be recognized.

Earlier work [1] on pulsed laser stencil deposition at room temperature showed that the typical 0.4 nm high TiO_2-terminated $SrTiO_3$ substrate terrace steps [2] were still visible on top of 5 nm high deposited Ni islands. Although not clearly demonstrated, the authors claim that the terrace steps are still present on top of 70 nm high Ni dots, indicating the possibilities of PLD to grow ultra-smooth thin films [1].

These observations raise a couple of questions on the growth behavior of patterned features by PLD on the surface of organic single-crystals. To name a few, how special is this observed duplication of the substrate morphology? To what thickness of the deposited patterns can this duplication be detected? And, what is the influence of the deposition parameters on the progression of roughness and morphology with increasing film thickness?

To answer these questions, the growth dynamics and scaling of the surface roughness for pulsed-laser deposited patterns are further examined in this chapter. Micrometer-sized gold patterns with different thicknesses have been deposited on the surface of pentacene single-crystal and silicon oxide substrates by pulsed laser stencil deposition and the pattern morphology has been investigated by means of atomic force microscopy (AFM).

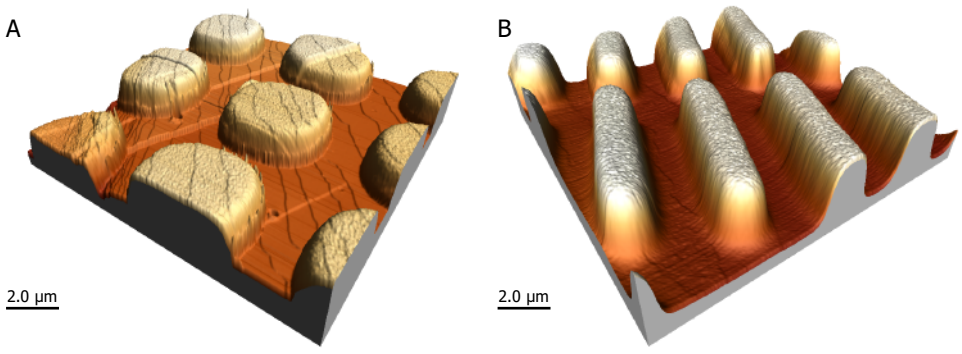

Figure 7.1 *Three-dimensional AFM height images of Au patterns on pentacene single-crystals prepared by pulsed-laser stencil deposition. A) 'soft-landing' settings, thickness Au-dots is ~45 nm, B) 'hard-landing' settings, thickness Au-lines is ~125 nm.*

7.2 Theoretical Background

The observed substrate morphology duplication depends on the evolution of the film roughness and morphology with increasing film thickness. The study of (kinetic) surface roughening under far-from-equilibrium conditions has attracted the interest of researchers in recent years [3-5]. In particular, it has been shown that the surface roughness in many cases exhibits scaling relations as a function of film thickness and lateral length scale. Scaling theories for the surface morphology and dynamics of a growing film have been successfully applied to describe experimental results from growth studies with various deposition techniques [3,6-9]. These findings have practical importance in thin film growth, as kinetic roughening is related to the spatial and temporal correlations of surface roughness as the growth proceeds. This kind of study is especially relevant when different scaling laws, displayed by the kinetic roughening, can be related to specific growth mechanisms [10-12]. From the application point of view, surface morphology is quite relevant in order to optimize the electrical, optical, and heat conductivity properties of materials in the form of thin films.

The growth of a film by particle deposition is typically a far-from-equilibrium process, and different growth models are applied to explain the observed morphology. The growth process is principally determined by the interplay of deposition, desorption, and surface diffusion (relaxation) of the atoms or molecules arriving at the surface [4]. For the global surface morphology, statistical models are often employed. Most common are the surface width, often represented by the root-mean-square (*rms*) roughness value, and the lateral correlation length, which gives the average distance between features in the surface profile within which the surface variations are correlated [5].

The main quantity characterizing the surface is the *rms* roughness σ which is defined as:

$$\sigma(h) = \sqrt{\left\langle h\left(\vec{x}\right)^2 \right\rangle_{\vec{x}}} \tag{7.1}$$

where h is the local relative height (the difference between the local absolute height H and the mean film thickness d) of all data points x. For a constant deposition rate, and in the so-called dynamic scaling regime, the *rms* surface roughness σ scales with both the thickness d (or growth time t) and the image size L following a Family-Vicsek scaling relation [13,14]:

$$\sigma(d,L) \sim L^{\alpha} f\left(\frac{d}{L^{z}}\right) \tag{7.2}$$

with $z = \alpha / \beta$. The scaling exponents α and β are called the roughness exponent and the growth exponent, respectively, and $1 / z$ is called the coarsening exponent. All these exponents are determined by the mechanism of the film growth.

The image size L is chosen large enough, so that the surface roughness σ saturates as a function of image size. This simplifies the equation for the roughness to:

$$\sigma(d) \sim d^{\beta} \qquad \text{for small film thicknesses} \qquad (7.3)$$

$$\sigma(d) = \text{const.} \qquad \text{for large film thicknesses (saturation)} \qquad (7.4)$$

The *rms* surface roughness σ of a film can be calculated directly from AFM measurements. Typical values for the growth exponent β are between 0.2 - 1.0, depending on the deposition method, material and deposition conditions like substrate temperature [15]. Standard diffusion-deposition models give values in the range $\beta = 0$ - 0.5, with a maximum of $\beta = 0.5$ for a pure random deposition model (*i.e.* no surface diffusion takes place) [4]. Characteristic for an unstable growth process is a growth exponent $\beta > 0.5$ [3]. Under these conditions, the growth is favored in the vertical rather than lateral (along the substrate plane) direction [8]. In kinetic Monte Carlo simulations on the amorphous growth of sputtered SiO_2 and Nb_2O_5 films, this rapid kinetic roughening with $\beta > 0.5$ can be explained by including random surface binding energy fluctuations that mimic the amorphous film structure [16-18].

Many of the reported β-values for films grown by sputtering are in the 0.4 - 0.6 range [8,15]. For pulsed laser deposition, most growth studies remain limited to the initial nucleation stage, so typical PLD-values for β are scarcely found. Vasco *et al.* [19] report a $\beta_1 = 1.0 \pm 0.1$ and $\beta_2 = 0.6 \pm 0.01$ for two subsequent regimes in the growth of ZnO films on InP(100) substrates with PLD at elevated temperatures. Álvarez *et al.* [20] report a $\beta = 1.0$ and $\beta = 0.3$ for ZrO_2 thin films pulsed-laser deposited on a silicon wafer at room temperature and at 600 °C, respectively. Using Monte Carlo (MC) simulations, they attributed this change in surface topography with film temperature to the existence of two different growth regimes: a regime dominated by shadowing of incident deposition particles growth, occurring at low temperatures ($\beta_{MC} = 1.00$), and a regime dominated by thermally activated diffusion growth that takes place at high temperatures ($\beta_{MC} = 0.15$).

Besides the growth exponent β, a further characteristic often employed in kinetic growth dynamic studies is the lateral correlation length ξ, which is related to the lateral size of certain features on the surface [9,18]. The correlation length ξ is also proportional to the film thickness d (or growth time t) via a power law, and results in the coarsening exponent $1/z$ [8]. Another characteristic quantity is the so-called roughness exponent α, linked to the self-affine scaling properties of the surface [4]. The coarsening exponent $1/z$ and the growth exponent α are not investigated in this work, due to the small grain sizes in the deposited thin films and the large sample-to-sample variation in the pentacene crystal morphology.

For many systems prepared by different deposition methods, it is rather common that the imperfections of a given layer are transferred partly or fully to the layers subsequently deposited on top [15,21]. The lower the value for β, the longer these imperfections play a role and remain visible. The effect of vertical correlations between interfaces can be taken into

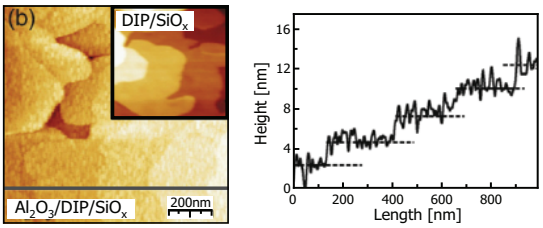

Figure 7.2 *Contact-mode AFM height image with line scan of a 68.1 nm thick Al_2O_3 film sputtered on diindenoperylene (DIP). The inset shows the terraced structure of the native DIP film. Figure with permission from [15].*

account by normalizing the roughness of the deposited film (or pattern) by the roughness of the underlying substrate [15,20], according to:

$$\sigma_{\text{film}}^{\text{norm.}} = \sqrt{\sigma_{\text{film}}^2 - \sigma_{\text{substr.}}^2} \tag{7.5}$$

Sellner *et al.* [15] found a growth exponent $\beta = 0.38$ for sputtered aluminum oxide (Al_2O_3) films on both inorganic and organic substrates (silicon oxide and diindenoperylene, DIP, respectively) after normalization. Native films of the organic semiconductor DIP possess a characteristic topography with large flat terraces of monomolecular (1.65 nm) step height (see inset in figure 7.2), comparable to the pentacene crystal surface investigated in this work. Figure 7.2 shows an AFM image of a 68.1 nm thick Al_2O_3 film sputtered on top of a DIP film. The terraced structure of the underlying DIP film can still be recognized, which implies the Al_2O_3 surface roughness has a certain degree of correlation with the DIP surface roughness. A close-up shows the Al_2O_3 layer on a DIP terrace has a small granular structure itself (not shown). The sputtered aluminum oxide film thus reflects some features of the underlying substrate morphology added to its 'own' grainy morphology. In addition, transmission electron microscopy (TEM) images in an earlier study showed a well-defined Al_2O_3-DIP interface, dominated by the DIP substrate roughness [22].

7.3 Experimental Procedure

In order to investigate the growth dynamics and scaling of the surface roughness for pulsed-laser stencil deposited patterns, the following three experimental series were produced. Various micrometer-sized gold patterns with increasing thickness were deposited on the surface of pentacene single-crystals at *'hard-landing'* and *'soft-landing'* settings, and on *p*-type silicon oxide substrates using the *'hard-landing'* settings, by pulsed laser stencil deposition at room temperature (for more details, see chapter 3).

Before deposition, the SiO_x-substrates were cleaned by rinsing ultrasonically in acetone and ethanol for 1 min, and subsequently blown dry in a nitrogen gas stream. No cleaning treatment was applied on the pentacene single-crystal substrates prior to deposition.

Optimization of the deposition parameters for gold on pentacene single-crystals by PLD has been described in the previous chapter. For the gold depositions, a laser fluence of 5 J/cm^2 is achieved on a 1.76 mm^2 target spot size by focusing the laser beam through a lens and a 98 mm^2 mask. Here, for the *'hard-landing'* depositions, a laser repetition rate of 5 Hz,

a target-to-substrate distance of 45 mm and an argon background gas pressure of 3×10^{-3} mbar were used. For the *'soft-landing'* experiments, a laser frequency of 1 Hz, a target-substrate distance of 75 mm and a background gas pressure of 5×10^{-2} mbar were applied. The thickness of the deposited Au-features was 30 - 150 nm.

After the stencil deposition, the surface morphology of the deposited Au patterns and the surrounding pentacene single-crystal or SiO_x substrate (shadowed by the stencil during deposition) were analyzed *ex situ* by means of contact-mode atomic force microscopy (AFM). All AFM measurements were performed using a Veeco Multimode SPM equipped with a Nanoscope IV controller and v6.14r1 software (see chapter 3). Roughness data was obtained using the software's roughness procedure. To distinguish between the substrate and the deposited feature, five non-overlapping areas of 1.00 μm^2 were selected for both regions and the obtained roughness values were averaged. Although randomly chosen, the selected areas excluded AFM-artifacts and other irregularities. For this reason, and for the samples with smaller-sized Au-patterns, the selected area size was reduced to 0.50 μm^2 or 0.10 μm^2 in a few cases.

An advantage of this stencil patterning approach is the possibility to directly measure the thickness of the deposited film. Another advantage is that the actual local morphology of both film and substrate can be captured within one image, showing the possible prolongation of surface characteristics on the deposited patterns and enabling a more accurate surface roughness normalization. The stenciling procedure is not expected to have a significant influence on the pattern morphology, as the shockwave broadening regime (see paragraph 3.3.2) is not entered in both settings and the aspect ratio of the stencil's apertures is large.

7.4 Results and Discussion

Figure 7.3 shows a selection of AFM images of Au features with increasing thickness, deposited on pentacene single-crystal substrates using the *'hard-landing'* settings. For every image, the height and deflection data is presented, and three line scans to reveal the sample topography. Analogously, figure 7.4 presents an AFM series of deposited Au patterns on pentacene single-crystals using the *'soft-landing'* settings. The AFM images of gold dots deposited on flat SiO_x substrates with the *'hard-landing'* settings will not be presented here.

In figure 7.3A, the terraced structure of the underlying pentacene single-crystal can clearly be recognized on top of the deposited Au dot of 40 nm thick. This implies the Au surface roughness has a certain degree of correlation with the pentacene crystal surface roughness. Figure 7.3B, a close-up of the selected-area in figure 7.3A, shows the deposited Au layer has a granular structure, yet the pentacene terrace steps can also be clearly distinguished. Similar to the Al_2O_3-DIP system described by Sellner *et al.* [15], the deposited Au film thus reflects some features of the underlying pentacene single-crystal substrate morphology added to its 'own' inherent grainy morphology. Figure 7.3C shows a patterned Au square of 75 nm thick. Here, the morphology of the underlying substrate is weakly visible on top of the gold film.

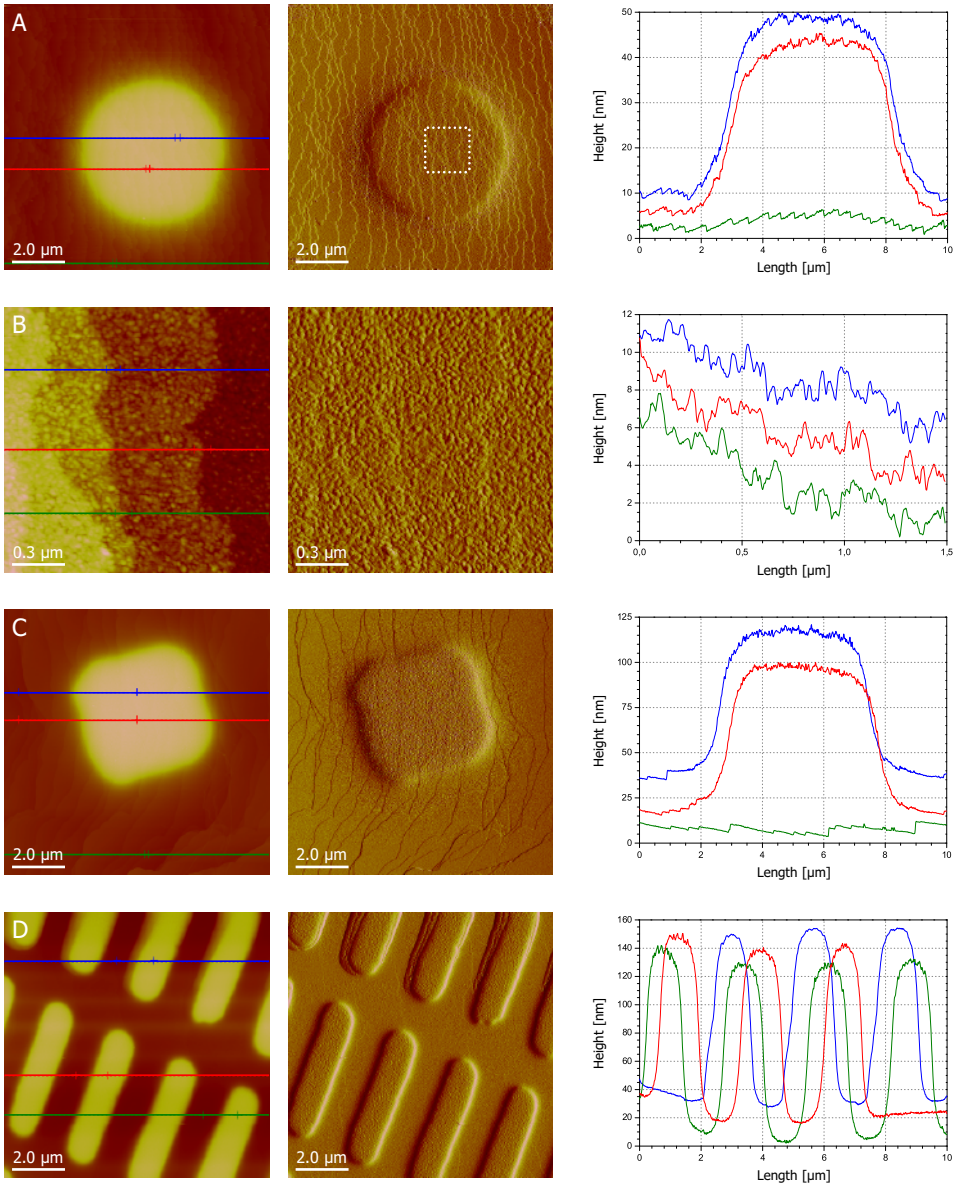

Figure 7.3 *Au dots on pentacene single-crystals, with PLD at 'hard-landing' settings at different thicknesses: A) 40 nm (Z_{AFM} = 75 nm), B) selected area of the dot shown in A, as indicated by the white square (Z_{AFM} = 10 nm), C) 75 nm (Z_{AFM} = 150 nm), and D) 125 nm (Z_{AFM} = 300 nm).*

With increasing the Au film thickness to 100 nm (not shown) and 125 nm (figure 7.3D), the deposited features no longer display the (monomolecular terraced) morphology of the pentacene substrate. Overall, this corresponds to a transition from a morphology whose height correlations are dominated by the underlying substrate to a morphology whose correlations are defined by the deposited film.

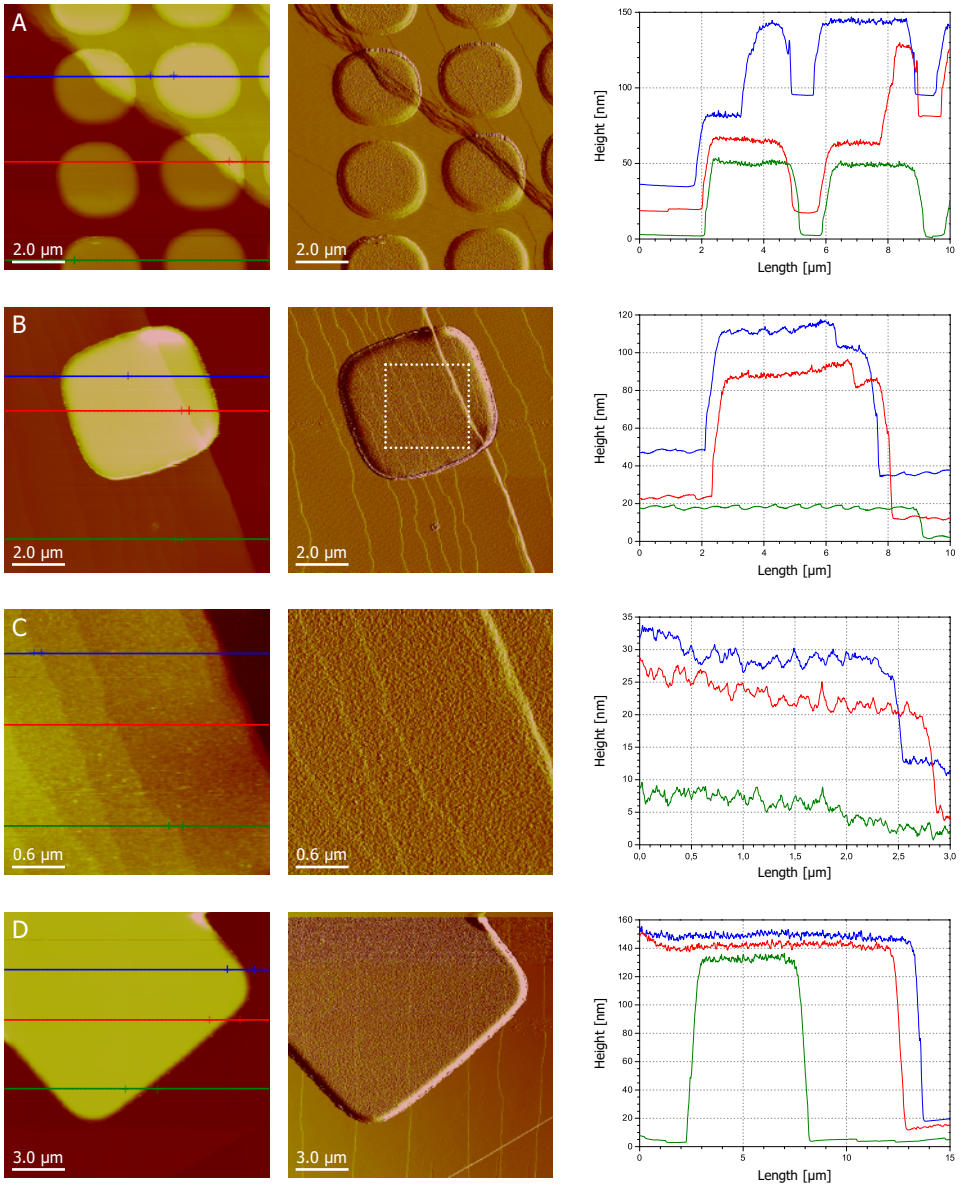

Figure 7.4 *Au dots on pentacene single-crystals, with PLD at 'soft-landing' settings at different thicknesses: A) 50 nm (Z_{AFM} = 200 nm), B) 65 nm (Z_{AFM} = 150 nm), C) selected area of the dot shown in B, as indicated by the white square (Z_{AFM} = 35 nm), and D) 125 nm (Z_{AFM} = 300 nm).*

In figure 7.4, a similar series of deposited micrometer-sized Au patterns on pentacene single-crystal substrates is presented, this time using the *'soft-landing'* deposition settings. In contrast to the preceding *'hard-landing'* series, the morphology of the underlying pentacene single-crystal substrate can still be recognized on top of 125 nm thick deposited gold features (see figure 7.4D).

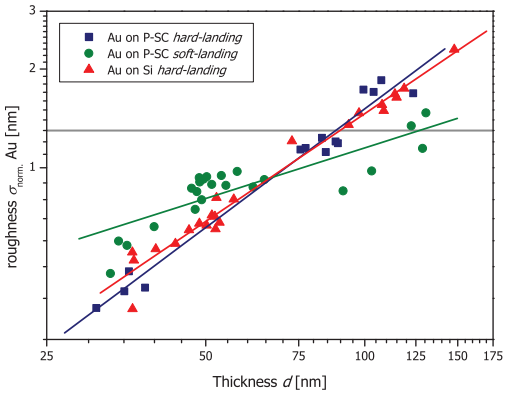

Figure 7.5 *Progression of the film roughness σ of the deposited gold patterns as a function of film thickness d.*
Blue squares: 'hard-landing' of Au patterns on pentacene single-crystals.
Green circles: 'soft-landing' of Au patterns on pentacene single-crystals.
Red triangles: 'hard-landing' of Au patterns on SiO_x substrates.
The lines correspond to a linear fit; the gray line indicates the transition (see text).

In figure 7.5, the progression of the *rms* film roughness σ of the Au features (after measuring and renormalizing according to formula 7.5) as a function of the film thickness d is presented for the three experimental series. The surface roughness, ranging from 0.4 nm to 2.3 nm, of all deposited patterns generally increases with the layer thickness (ranging from 30 nm to 150 nm).

It is concluded that the morphology of the underlying substrate is recognizable when $\sigma < 1.4$ nm (*i.e.* as long as the normalized roughness of the deposited gold patterns remains smaller than the monomolecular P_1-P_2 terrace steps of the pentacene single-crystal). For films with $\sigma > 1.4$ nm, the film roughness is so large that the substrate morphology duplication is no longer present.

This transition from a morphology whose height correlations are dominated by the underlying substrate to a morphology whose correlations are defined by the deposited film (*i.e.* when $\sigma \approx 1.4$ nm, gray line in figure 7.5), occurs around a film thickness of about 90 nm for the *'hard-landing'* series. For the *'soft-landing'* series, this transition is observed around a film thickness of about 140 nm.

For both *'hard-landing'* series (*i.e.* gold patterns on pentacene single-crystal (blue squares) and on silicon oxide (red triangles) substrates in figure 7.5), a clear linear dependence of film roughness σ on the film thickness d can be observed. The slope of the linear fits to the data corresponds to the following growth exponents: $\beta = 1.20$ (blue line, with $R^2 = 0.97$) for *'hard-landing'* on pentacene, and $\beta = 1.09$ (red line, with $R^2 = 0.97$) for *'hard-landing'* on SiO_x (*e.g.* R^2 is the square of the Pearson product-moment correlation coefficient [23]). These β-values are remarkably similar, despite the very different chemical nature of the organic and inorganic substrates. Combined with the similar morphology of gold patterns on flat SiO_x substrates and on the terraced surface of pentacene crystals, it appears that the growth and local structure of the gold films is similar on both kinds of substrates. In other words, although the first arriving gold species encounter a chemically different substrate, this has no influence on the subsequent film growth (*i.e.* the later arriving particles encounter a similar 'gold film' substrate upon landing). Sellner *et al.* [15] came to the same conclusion for their sputtered Al_2O_3 / SiO_x and Al_2O_3 / DIP systems (although they found lower β-values).

The two *'hard-landing'* β-values revealed here are comparable to the experimental and simulated values of $\beta = 1.0$ found by Álvarez *et al.* [19] for ZrO_2 thin films pulsed-laser deposited on a silicon wafer at room temperature (*i.e.* meaning the roughness increases approximately linearly in time). Therefore, it can be concluded that our system is also in a regime where growth is dominated by shadowing of incident deposition particles.

For the *'soft-landing'* series of gold patterns on pentacene single-crystal substrates (green circles), an overall growth exponent value of $\beta = 0.51$ (green line, with $R^2 = 0.70$) is found. Compared to both *'hard-landing'* series, this *'soft-landing'* β-value is considerably lower. The lower R^2-value indicates the fit has a less pronounced linear correlation. The observed β-value corresponds with the growth exponent $\beta = 0.5$ that is found in models for pure randomly deposited amorphous films [4]. In the random deposition model, particles move along straight line trajectories until they reach the top of the column in which they were dropped, at which point they stick to the deposit and become part of the aggregate (*i.e.* there is no surface diffusion) [13]. Introduction of surface diffusion in the model results in the surface becoming smoother ($\beta < 0.5$) [24].

There can be several reasons why the *'soft-landing'* β-value is considerably lower than the *'hard-landing'* β-values. One difference between the two series is the particle velocity or kinetic energy of the ablated gold species when arriving at the substrate [25], as discussed in chapter 6. As stated in ref. [26], deposition of particles with a larger incident kinetic energy results in a greater downhill movement of particles from the top layers, producing a flatter and smoother film surface. This statement contradicts with our findings, as here the films with a high kinetic energy of the arriving species have a higher β-value than the films with low incident particle kinetic energy. However, Elsholz *et al.* [16,17,18] showed that the growth exponent β for amorphous thin film growth depends on the deposition temperature T and an *'energy fluctuation strength'* Δ. By introducing Δ in their Monte Carlo simulations, they mimicked the amorphous structure of a thin film by including a randomly fluctuating surface binding energy for arriving atoms. For depositions at room temperature, a small increase in Δ directly resulted in β-values exceeding the value of 0.5 for random deposition and reaching up to 1.0. Thus, minor differences in the surface binding energy of the impinging species (*i.e.* a minor difference in Δ) between the *'hard-landing'* and *'soft-landing'* series, which can be expected due to the large difference in the kinetic energy of the arriving species between both series, can explain the difference in growth exponents.

The second difference between the *'hard-landing'* and *'soft-landing'* series is the incident angle distribution of the impinging species (*i.e.* the arriving species do not impinge normally on the growing surface). In general, the quite high β-values for pulsed-laser deposited thin films at room temperature (compared to other physical vapor deposition techniques) are the result of a broadening of the plume angular distribution due to scattering of the ablated species with background gas molecules [19]. The incident angular distribution of a material flux is often described by a $\cos^n(\theta)$ distribution, where n depends on the technique, source dimensions and the deposition parameters [27]. Model calculations show that a broader

incident angle distribution function of the deposition species produces wider surface mounds [19]. This effect is expected to gain relevance (*i.e.* higher values of σ) for high background gas pressures and for long distances between the target and the substrate. In the *'hard-landing'* and *'soft-landing'* series, both parameters are dissimilar. However, if we look at the results, this statement contradicts with our findings as well. Here, the films deposited with a high background gas pressure and a large distance between the target and substrate (*'soft-landing'*) are smoother and have a lower β-value than the films deposited with a low background gas pressure and a small target-to-substrate distance (*'hard-landing'*). However, the result matches with Bakalova *et al.* [28], who investigated the surface morphology of AlN films on silicon synthesized by PLD at various deposition pressures. They also observed a decrease in the surface roughness with increasing background gas pressure and attributed this to a change in the surface diffusion length of the adatoms.

The third difference between the *'hard-landing'* and *'soft-landing'* series is the deposition rate of the Au film. Experimentally, a gold deposition rate of about 0.02 and 0.01 nm/pulse was measured, for the *'hard-landing'* and *'soft-landing'* settings, respectively. Although Álvarez and co-workers mentioned in the abstract of ref. [19] that the thermally activated diffusion dominated growth at high temperatures in PLD (resulting in a low β-value of 0.15 - 0.30) also occurs for low deposition rates at room temperature, no further evidence is given to support this statement. In general, because of the instantaneous deposition under typical PLD conditions, the adatoms rearrange on the surface by migration and are subsequently incorporated through nucleation and growth after the deposition pulse [29]. If the deposition rate is lowered, less ablated Au species arrive at the sample per pulse. This will decrease the possibility to encounter other adatoms during surface migration. The chance that an adatom is trapped at a kink or side of an existing cluster has now become larger than that it nucleates with other atoms into a new cluster. Overall, this process will result in a smoother film surface, and thus in a lower β-value when the deposition rate is lowered.

However, the three different parameters discussed above (*viz.* kinetic energy, angular plume distribution and deposition rate) depend to a certain extent on each other, opening space for further research and discussion.

7.5 Concluding Remarks

The morphology of gold patterns deposited on silicon oxide and pentacene single-crystal substrates by PLD has been studied. From the analysis of AFM measurements, a growth exponent of $\beta = 1.09$ and $\beta = 1.20$ is found for gold films deposited with *'hard-landing'* settings on SiO_x and pentacene crystals, respectively. As these β-values are remarkably similar, it appears that the growth and local structure of the gold films at these deposition settings is similar on both kinds of substrates. The lower growth exponent of $\beta = 0.51$ found for gold features deposited on pentacene crystals using *'soft-landing'* parameters is attributed to various differences in the deposition parameters (*viz.* kinetic energy, angular plume distribution and deposition rate), resulting in a smoother film.

7.6 References

[1] Vroegindeweij, F.; Speets, E.A.; Steen, J.A.J.; Brugger, J.; Blank, D.H.A.; "Exploring microstencils for sub-micron patterning using pulsed laser deposition"; *Appl. Phys. A*; 79; **2004**; 743-745

[2] Koster, G.; Kropman, B.L., Rijnders, G.J.H.M.; Blank, D.H.A.; Rogalla, H.; "Quasi-ideal strontium titanate crystal surfaces through formation of strontium hydroxide"; *Appl. Phys. Lett.*; 73; **1998**; 2920-2922

[3] Meakin, P.; Fractals, scaling and growth far from equilibrium; **1998**; Cambridge University Press; Cambridge, United Kingdom

[4] Barabási, A.L.; Stanley, H.E.; Fractal concepts in surface growth; **1995**; Cambridge University Press; Cambridge, United Kingdom

[5] Yang, H.N.; Wang, G.C.; Lu, T.M.; Diffraction from rough surfaces and dynamic growth fronts; **1993**; World Scientific; Singapore

[6] Mayr, S.G.; Moske, M.; Samwer, K.; "Identification of key parameters by comparing experimental and simulated growth of vapor-deposited amorphous $Zr_{65}Al_{7.5}Cu_{27.5}$ films"; *Phys. Rev. B*; 60; **1999**; 16950-16955

[7] Vauth, S.; Streng, C.; Mayr, S.G.; Samwer, K.; "Growth of vapor-deposited amorphous $Zr_{65}Al_{7.5}Cu_{27.5}$ films under oblique particle incidence investigated by experiment and simulation"; *Phys. Rev. B*; 68; **2003**; 205425

[8] Auger, M.A.; Vázquez, L.; Sánchez, O.; Jergel, M.; Cuerno, R.; Castro, M.; "Growth dynamics of reactive-sputtering-deposited AlN films"; *J. Appl. Phys.*; 97; **2005**; 123528

[9] Lindström, T.; Isidorsson, J.; Niklasson, G.A.; "Surface smoothing and roughening in sputtered SnO_2 films"; *Thin Solid Films*; 401; **2001**; 165-170

[10] Ojeda, F.; Cuerno, R.; Salvarezza, R.; Vázquez, L.; "Dynamics of rough interfaces in chemical vapor deposition: experiments and a model for silica films"; *Phys. Rev. Lett.*; 84; **2000**; 3125-3128

[11] Ojeda, F.; Cuerno, R.; Salvarezza, R.; Agulló-Rueda, F.; Vázquez, L.; "Modeling heterogeneity and memory effects on the kinetic roughening of silica films grown by chemical vapor deposition"; *Phys. Rev. B*; 67; **2003**; 245416

[12] Hachenberg, J.; Streng, C.; Süske, E.; Vauth, S.; Mayr, S.G.; Krebs, H.U.; Samwer, K.; "Kinetic roughening of laser deposited polymer films: crossover from single particle character to continuous growth"; *Phys. Rev. Lett.*; 92; **2004**; 246102

[13] Family, F.; Vicsek, T.; "Scaling of the active zone in the Eden process on percolation networks and the ballistic deposition model"; *J. Phys. A: Math. Gen.*; 18; **1985**; L75-L81

[14] Family, F.; "Dynamic scaling and phase transitions in interface growth"; *Physica A*; 168; **1990**; 561-580

[15] Sellner, S.; Gerlach, A.; Kowarik, S.; Schreiber, F.; Dosch, H.; Meyer, S.; Pflaum, J.; Ulbricht, G.; "Comparative study of the growth of sputtered aluminum oxide films on organic and inorganic substrates"; *Thin Solid Films*; 516; **2008**; 6377-6381

[16] Elsholz, F.; Schöll, E.; Rosenfeld, A.; "Control of surface roughness in amorphous thin-film growth"; *Appl. Phys. Lett.*; 84; **2004**; 4167-4169

[17] Elsholz, F.; Schöll, E.; Scharfenorth, C.; Seewald, G.; Eichler, H.J.; Rosenfled, A.; "Roughness evolution in thin film growth of SiO_2 and Nb_2O_5"; *J. Appl. Phys.*; 98; **2005**; 103516

[18] Elsholz, F.; Schöll, E.; Rosenfeld, A.; "Kinetic Monte Carlo simulations of amorphous thin-film growth"; *Phys. Stat. Sol. B*; 244; **2007**; 3639-3646

[19] Vasco, E.; Zaldo, C.; Vázquez, L.; "Growth evolution of ZnO films deposited by pulsed laser ablation"; *J. Phys.: Condens. Matter.*; 13; **2001**; L663-L672

[20] Álvarez, R.; Palmero, A.; Prieto-López, L.O.; Yubero, F.; Cotrino, J.; Cruz, W. de la; Rudolph, H.; Habraken, F.H.P.M.; Gonzalez-Elipe, A.R.; "Morphological evolution of pulsed laser deposited ZrO_2 thin films"; *J. Appl. Phys.*; 107; **2010**; 054311

[21] Schlomka, J.P.; Tolan, M.; Schwalowsky, L.; Seeck, O.H.; Stettner, J.; Press, W.; "X-ray diffraction from Si/Ge layers: diffuse scattering in the region of total external reflection"; *Phys. Rev. B*; 51; **1995**; 2311-2321

[22] Sellner, S.; Gerlach, A.; Schreiber, F.; Kelsch, M.; Kasper, N.; Dosch, H.; Meyer, S.; Pflaum, J.; Fischer, M.; Gompf, B.; Ulbricht, G.; "Mechanisms for the enhancement of the thermal stability of organic thin films by aluminum oxide capping layers"; *J. Mater. Res.*; 21; **2006**; 455-464

[23] Stigler, S.M.; "Francis Galton's account of the invention of correlation"; *Stat. Sci.*; 4; **1989**; 73-86

[24] Family, F.; "Scaling of rough surfaces: effects of surface diffusion"; *J. Phys. A: Math. Gen.*; 19; **1986**; L441-L446

[25] Irissou, E.; Drogoff, B. le; Chaker, M.; Guay, D.; "Correlation between plasma expansion dynamics and gold-thin film structure during pulsed-laser deposition"; *Appl. Phys. Lett.*; 80; **2002**; 1716-1718

[26] Moseler, M.; Gumbsch, P.; Casiraghi, C.; Ferrari, A.C.; Robertson, J.; "The ultrasmoothness of diamond-like carbon surfaces"; *Science*; 309; **2005**; 1545-1548

[27] Riele, P.M. te; Direct patterning of oxides by pulsed laser stencil deposition; PhD Thesis; **2008**; University of Twente; Enschede, The Netherlands

[28] Bakalova, S.; Szekeres, A.; Huhn, G.; Havancsak, K.; Grigorescu, S.; Socol, G.; Ristoscu, C.; Mihailescu, I.N.; "Surface morphology of AlN films synthesized by pulsed laser deposition"; *Vacuum*; 84; **2010**; 155-157

[29] Eason, R.; Pulsed laser deposition of thin films – Applications-led growth of functional materials; **2007**; Wiley-Interscience; Hoboken, NJ, U.S.A.

Chapter 8

Charge Transport Measurements on Pentacene Single-Crystal Devices

Chapter 8: Charge Transport Measurements on Pentacene Single-Crystal Devices

Abstract

The influence of the deposition parameters applied in the device fabrication (*'hard-landing'* vs. *'soft-landing'*) and the influence of the heat treatment to remove the quinone impurities on the electrical properties of pentacene single-crystals is discussed in this chapter.

The highest charge carrier mobility values found in the SCLC measurements were close to values reported in literature, illustrating metal contacts can be reproducibly patterned on organic molecular crystals by *'soft-landing'* in pulsed laser stencil deposition; *'hard-landing'* resulted in a more distorted interface and a lower mobility. Applying the heat treatment resulted in a significant decrease of the mobility as well.

The *in situ* fabrication of complete field-effect transistor devices on the pentacene single-crystal surface is realized by using the *'quasi-dynamic stencil deposition'* technique in PLD; however, the transistor characteristics do not show the presence of a field-effect.

8.1 Introduction

In order to study the intrinsic electronic properties of organic semiconducting materials, the fabrication of devices based on organic molecular single-crystals is the best approach, as discussed in paragraph 2.3. One of the approaches to fabricate these organic molecular crystal (field-effect) devices –the direct deposition of metal contacts and gate dielectric materials onto a free-standing organic crystal– has great potential, but is not straightforward and poses various technological challenges, as the surfaces of the fragile crystals are damaged easily (see paragraph 2.5.3).

In chapter 6, the direct deposition of smooth, well-defined and isolated metal (*i.e.* Au, Pt, Pd, Ni and Co) and medium-κ oxide (*i.e.* Al_2O_3, HfO_2 and CeO_2) patterns on surfaces of pentacene single-crystals and organic self-assembled monolayers by pulsed laser stencil deposition was presented. By taking several precautions during the PLD process, which reduce the kinetic energy of the impinging species, low-kinetic energy deposition or *'soft-landing'* was realized, preventing obvious damage to the fragile organic molecular substrate or mechanical failure of the deposited film.

In chapter 5, it was presented that the pentacene crystal surface is (partly) covered with a thin layer of 6,13-pentacenequinone impurities. In order to remove these quinone molecules selectively from the pentacene crystal surface, it was found that performing a heating treatment procedure at 75 - 80 °C in vacuum removes the quinone material completely, yielding an unoxidized pentacene single-crystal with a clean and undamaged surface morphology that is suitable for subsequent device fabrication.

The influences of the manufacturing process and the heating treatment procedure on the electrical properties of the pentacene single-crystals were not discussed so far. Although the deposition of smooth and well-defined patterns on the fragile organic molecular substrate was achieved, without obvious damage to the pentacene crystal or mechanical failure of the deposited films, it remains unclear whether the pulsed laser stencil deposition technique results in devices with a comparable or better performance than the currently employed processing techniques. Similar questions can be asked for the heating treatment that selectively removes the quinone impurities from the pentacene single-crystal surface.

In this chapter, the influence of the device manufacturing procedure and the heating treatment on the electrical properties of the pentacene single-crystals will be investigated. For this, fabricated space-charge-limited current (SCLC) and field-effect transistor (FET) devices were electrically characterized in a nano probing system (see paragraph 3.5). Focus will be on the influence of the different deposition parameters (*i.e.* the *'hard-landing'* settings versus the *'soft-landing'* settings) on the electrical properties, and on the influence of performing the heating treatment on a pentacene crystal before applying the metal contacts.

Similar to investigating the quality of the metal – pentacene and oxide – pentacene interfaces in a direct way (see chapter 6), this chapter will show that the fabrication and electrical characterization of devices on the surface of pentacene single-crystals is quite a challenge and not straightforward.

8.2 Theoretical Background

In charge transport studies on organic semiconductors, the electrical conductivity of the material is measured under varying circumstances. The conductivity σ in a solid depends on two parameters; the charge carrier density n and charge carrier mobility μ, and is given by:

$$\sigma = ne\mu \tag{8.1}$$

with e the elementary charge. The mobility is an intrinsic material parameter that reflects the drift velocity of the charge carriers in the material, influenced by all the interactions they encounter. The intrinsic drift mobility μ is defined as the magnitude of the drift velocity v_d of a charge carrier per unit electric field E, via:

$$\mu = \frac{v_d}{E} \tag{8.2}$$

Scattering by defects, impurities and phonons (lattice vibrations) decreases the drift velocity of charges, and thus decreases the electronic mobility. In other words, the mobility is a measure of the ease with which the charge carriers migrate through the material. The value of the charge carrier mobility, and its temperature dependence, gives an indication of the type of charge transport in a material: band-like transport or incoherent hopping transport. The value of the mobility also directly affects the performance of the material in devices, as it is related to the maximum switching speed.

Organic semiconductors are typically *wide bandgap* and *small bandwidth* semiconductors. The energy gap between the HOMO and LUMO bands of organic semiconductors is in the range of 1 - 4 eV[1,2]. From the large bandgap, together with the normally fully occupied HOMO levels (resulting in a completely filled valence band and empty conduction band), it might be expected that pure organic semiconductors are actually insulators (*viz.* an electron requires a large thermal energy to excite from the valence band to the conduction band). However, there are some effective methods to generate charge carriers in the organic semiconducting materials (see figure 8.1):

- Optical excitation; creation of electron-hole pairs.
- Injection of charge carriers from metallic electrodes.
- Field-effect doping or chemical doping.

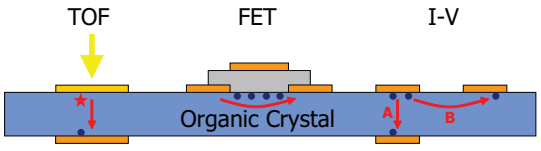

Figure 8.1 *Various opto-electronic methods used for charge transport characterization of organic crystals: time-of-flight photoconductivity, field-effect transistor measurements and (space-charge-limited) current-voltage measurements (A: sandwich-type geometry, B: gap structure).*

In the next paragraphs, the working mechanisms of these three methods will be discussed (the characteristics of these methods on organic single-crystal devices were reviewed in paragraph 2.6).

8.2.1 Time-of-flight measurements

An effective method to create charge carriers in organic semiconductors is optical excitation, in which electron-hole pairs are created by light. This routine is employed in time-of-flight (TOF) experiments. TOF is a direct measurement technique to determine the mobility μ of charge carriers through the bulk of a crystal slice [3-5]. In fact, TOF experiments by Karl *et al.* in 1985 [6,7] with ultrapure acene crystals (see figure 1.7), were benchmark studies that initiated further research on charge transport in organic semiconductors.

In TOF experiments, a platelet-like organic single-crystal is sandwiched between (and capacitively coupled to) two metal electrodes, of which the front one is semi-transparent. A thin 'sheet' of photo-excited charge carrier pairs are generated in the photoconductor near the interface with the semi-transparent electrode, by absorption of a short pulse of light of sufficient photon energy (*i.e.* greater than the materials' bandgap), admitted through the semi-transparent electrode. Depending on the polarity of the field *E,* established by applying a constant voltage bias *V* between the two electrodes, the sheet of electrons or holes is pulled across the crystal (with thickness *L*) at a velocity *v*, with $v = \mu E$. The charge sheet generates a constant displacement current *I*, whose magnitude diminishes rapidly as soon as the moving carriers have been collected by the opposite back electrode. The average travelling time τ (*i.e.* the duration of the displacement current pulse) is a direct measure of the average drift velocity *v* of the carriers, via $v = L/\tau$. In the absence of traps, the intrinsic mobility of the organic material can then be calculated via:

$$\mu = \frac{L}{E\tau} = \frac{L^2}{V\tau} \tag{8.3}$$

Indirectly, the TOF method provides information on the concentration of (shallow) traps in the bulk: the decrease of mobility at low temperatures is caused by multiple-trapping-and-release processes [8,9]. If many shallow traps are present, the measured mobility is just an effective mobility μ_{eff} , and more complex models have to be applied [3].

An important aspect of TOF measurements is that the results are not sensitive to contact effects, as the charge carriers are photogenerated and not injected from a metal electrode. This simplifies the contact preparation and improves the reproducibility. A second advantage is that the transport properties for electron and hole transport can be studied independently, by reversing the polarity of the external field. Disadvantages of the technique are that the organic single-crystal has to be very pure and almost defect-free, as the lifetime of the carriers against charge trapping has to be greater than the time-of-flight between the electrodes. The crystal should also have sufficiently parallel opposite facets and be quite thick (*i.e.* typically a few tenths of a millimeter), to make sure the displacement current pulse is longer than the apparatus time resolution and can be measured. Because of these

limitations, the TOF measurements can be performed only on a small portion of the organic semiconducting crystals available (*e.g.* not on pentacene single-crystals) [10].

8.2.2 Charge injection from metallic contacts

In the devices investigated in this work, the charge carriers are introduced from the electrodes. In general, charge injection into the organic semiconductor is of crucial importance for the device performance. The charge injection is strongly dependent on the quality of the interface between the metallic electrodes and the organic semiconductor, which involves impurities, structural defects or disorder, charging, dangling bonds, dipoles, and other effects, in which also the fabrication method of the device plays a significant role [11].

In an ideal device, the contacts are *Ohmic*; they do not affect the device characteristics, are a non-limiting source of charge carriers and have a linear and symmetrical current-voltage relation. This means the value of the contact resistance R_C is negligibly small in comparison with the channel resistance R_{Ch} of the semiconductor (*i.e.* the device is *'transport-limited'* and not *'injection-limited'*). Creating a low-resistance contact requires alignment of the metal Fermi level (E_F) with the energy levels of the semiconductor. As a starting point, it is assumed that the Mott-Schottky rule (established for the interface of metals with inorganic semiconductors [12]) holds: namely, that the vacuum levels of the metal and organic semiconductor are aligned (see figure 8.2A) [11]. With this assumption, one can estimate the offset of the conduction band (LUMO) and valence band (HOMO) from the metal electrode Fermi level E_F (and thus to the metal work function Φ_M), which is a good estimate of the potential barrier to charge injection from the metal to the semiconductor. The interface barriers heights for hole (Φ_{Bh}) and electron (Φ_{Be}) injection can be expressed as (with *IE* the ionization energy and *EA* the electron affinity of the organic material):

$$\Phi_{Bh} = E_{HOMO} - E_F = IE - \Phi_M \tag{8.4}$$

$$\Phi_{Be} = E_F - E_{LUMO} = \Phi_M - EA \tag{8.5}$$

When a metal and semiconductor are brought in contact, the Mott-Schottky model predicts that their bulk Fermi levels will align, causing band bending in the semiconducting solid [12]. Due to the band bending at the interface, a non-Ohmic Schottky barrier can be formed for electrons or holes, when the Fermi level in the semiconductor is higher or lower than the Fermi level in the metal, respectively. The resulting Schottky barrier, which gives rise to

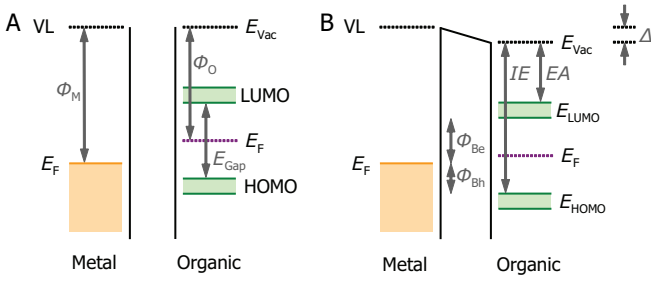

Figure 8.2 *Band model for contact between a metal and an organic semiconductor.*
A) Before contact.
B) After contact with dipole.

non-linear diode-like behavior, usually directly scales with the metal work function (as opposed to the case of inorganic semiconductors, where the barrier only weakly depends on the metal work function [13,14]). The height of the Schottky barrier is given by the difference between the work function Φ_M of the metal and the edge of the semiconductor band into which carriers are injection. Hence, low work function metals such as Ca ($\Phi_M = 2.9$ eV) are used to inject electrons, and high work function metals such as Au ($\Phi_M = 5.1 - 5.4$ eV [15,16]) are typically used to inject holes into the organic semiconductor. Reported *IE* values for pentacene vary between 4.9 and 5.2 eV [15,16], resulting in a theoretical interface barrier for hole injection Φ_{Bh} of a few tens of eV.

In reality, however, many metal – organic semiconductor interfaces do not follow the Mott-Schottky rule and the electronic situation is more complicated [17,18]. Often, an interface dipole (Δ) is present that shifts the vacuum level of the semiconductor with respect to the metal (see figure 8.2B). Interface dipoles have several possible origins, including charge transfer between the semiconductor molecules and the metal, and reduction of the metal work function by adsorption of the organic layer [11]. If an interface dipole Δ is present, it should be incorporated as additional term in the equations 8.4 and 8.5. Another aspect that can have a major influence on the injection of charge carriers is the presence of traps at the metal – organic interface that are induced by the contact fabrication.

In literature, *IE* values between 4.9 - 5.2 eV and 6.5 - 6.6 eV are reported for pentacene and 6,13-pentacenequinone, respectively [16]. For pentacene – gold interfaces, the formation of an interface dipole Δ of 0.9 to 1.1 eV is typically reported, resulting in a hole injection barrier Φ_{Bh} of 0.5 - 1.0 eV [15,16,19,20]. For 6,13-pentacenequinone – gold interfaces, reported dipoles Δ vary between 0.4 and 0.9 eV, resulting in hole injection barriers Φ_{Bh} of 2.0 - 2.6 eV in practice [16]. The drastically increased hole injection barrier Φ_{Bh} measured for 6,13-pentacene-quinone, compared to pentacene, is the main reason for the negative influence incorporated quinone impurities have on the performance of pentacene devices, as this will lower the overall current and achievable charge carrier mobility. To be complete, reported *EA* values vary between 2.7 - 2.8 eV, for both materials [16].

8.2.3 Space-charge-limited current spectroscopy

Since the bandgap of organic single-crystals is about a few electronvolts, high-purity undoped organic single-crystals essentially behave as insulators. Nevertheless, it is possible to pass a current through the crystals by applying a sufficiently large voltage, which acts both to transfer the charge from the electrodes into the crystal and to accelerate that charge. This approach will be further investigated in this chapter.

In general, the maximum current density flowing through a device is limited either by the contacts or the bulk material properties. A device is found to be *'injection-limited'* when the current is determined by the injection process of the charge carriers into the device. In case the injection barriers between the metal contacts and the organic semiconductor are small, and charges can be effectively injected into a device, the device limiting factor is the ability

of the material to transport these charges through the bulk. When the charge injected from the contacts is larger than the charge present in the material in equilibrium, the current-voltage characteristics become non-linear. The excess electric charge present in the bulk of the material, which is treated as a continuum of charge distributed over a region of space rather than distinct point-like charges, is now limiting the maximum current that can flow through the material. Charge transport in such *'space-charge-limited'* or *'bulk-limited'* devices can be described using the theory of space-charge-limited currents (SCLC) [21].

Space-charge-limited current models

The theory of space-charge-limited currents in insulators and semiconductors between plane parallel electrodes was first investigated by Mott and Gurney [22]. In the absence of any trapping effects, the current density is given by the Mott-Gurney Law:

$$J_{SCLC} = \frac{9}{8}\varepsilon_0\varepsilon_r\mu\frac{V^2}{L^3} \tag{8.6}$$

with J_{SCLC} the current density in the SCLC regime, V the applied voltage across a length L between two contacts, ε_0 the permittivity of free space, ε_r the dielectric constant of the semiconductor ($\varepsilon_r = 3$ for pentacene single-crystals [23]), and μ the charge carrier mobility. The current is assumed to be due to carriers of one sign only, the effect of diffusion is neglected, and the mobility is assumed to be independent of the field. Other assumptions are that the contacts are Ohmic and the injecting contact is an infinite source of charge carriers.

In the case of a single set of homogenously distributed traps that have one discrete energy level, a modified form of equation (8.6) can be derived (see [23]), yielding [24]:

$$J_{SCLC} = \frac{9}{8}\varepsilon_0\varepsilon_r\theta\mu\frac{V^2}{L^3} \tag{8.7}$$

This equation has the form of the Mott-Gurney law, except that the current density is reduced by a factor θ. This trap factor θ represents the ratio between the free carriers n_f and the total number of charge carriers n_{tot} introduced in the material:

$$\theta = \frac{n_f}{n_{tot}} = \frac{n_f}{n_f + n_t} \tag{8.8}$$

with n_t the trapped carriers density. In literature data, it is often unclear if the trap-free regime is reached, *i.e.* if the charge carrier mobility μ is extracted with or without taking the trap factor θ into account. The number of traps n_t can be estimated from the value of the trap-filling voltage V_{TFL} (see below), with e the elementary charge:

$$V_{TFL} = \frac{2}{3}\frac{eL^2}{\varepsilon_0\varepsilon_r}n_t \tag{8.9}$$

However, this is valid only under the assumption that the traps are uniformly distributed in space throughout the bulk of the crystal.

From the voltage $V_{\Omega'}$, at which the transition between the Ohmic and space-charge-limited regime with traps occurs (see below), the thermally generated electron density n_0 (or free carrier density n_f) can be estimated [25]:

$$n_0 = \frac{V_{\Omega'}\theta\varepsilon_0\varepsilon_r}{eL^2} \tag{8.10}$$

Device structures

There are two basic architectures to evaluate the space charge transport in organic semiconductors, see figure 8.1. The Mott-Gurney theory describes the current-voltage characteristics for *sandwich-type* contact geometries, in which the electrodes are on the opposite face of the semiconductor. This is a 1-dimensional theory in which the electric field, as well as the space charge, is confined to the channel.

The other geometry is the *gap-structure*, where both electrodes are deposited on the same side of the film or crystal. For this 2-dimensional model, the longitudinal component of the electric field is responsible for the charge transport and the transversal component, perpendicular to the conduction channel, is determined by the magnitude of space charge. Since the excess density of mobile charge in the layer is controlled by the transversal component of the electric field, side effects can play a dominant part in the model.

Two limiting cases can be considered in the *gap structure*, as Grinberg *et al.* [26] pointed out. In the first case, the *'film regime'*, the thickness h of the film or crystal is negligible with respect to the distance L between the contacts ($h \to 0$). This case corresponds to the 2-dimensional geometry first analyzed by Geurst [27] and leads to the following equation for the current density J^* (in A/m):

$$J^* = \frac{2}{\pi}\varepsilon_0\varepsilon_r\mu\frac{V^2}{L^2} \tag{8.11}$$

Zuleeg and Knoll [28] introduced the width W of the electrodes into this expression, improving the approximation of Geurst of infinite long contact length, resulting in a current I (in A):

$$I = \frac{2}{\pi}\varepsilon_0\varepsilon_r\mu W\frac{V^2}{L^2} \tag{8.12}$$

In the second case, the *'bulk regime'*, the thickness h is larger than the distance L between the electrodes. Under these circumstances, the current is thickness h dependent and can be described by an equation similar to that originally developed by Mott and Gurney for the 1-dimensional *sandwich* structure (*i.e.* the current density J is assumed to be uniform over the whole section of the crystal and filled in as $J = I/Wh$ in equation 8.6):

$$I = \frac{9}{8}\varepsilon_0\varepsilon_r\mu hW\frac{V^2}{L^3} \tag{8.13}$$

For single-crystals with *gap structure* electrodes, an intermediate situation between the 1D and 2D cases can be present, depending on the ratio between the parameters h and L [25]. For $h/L \gg 1$, it is expected that the 1D model will dominate, whereas the 2D model is valid when $h/L \ll 1$ [25]. As a consequence, the space-charge-limited current at high voltages varies with L^{-3} to L^{-2} in the cross-over from the Mott-Gurney 1D model to the Geurst 2D model [23,29]. Unfortunately, the transition point between the Ohmic and SCLC regimes increases as L^2 (see equation 8.10), which can have the consequence that the SCLC regime starts outside the explored voltage range if the contacts are separated too far [25].

Measurement characteristics

In the evolution of current density with applied electric field through an insulator or semiconductor, generally, four separate regions can be distinguished (see figure 8.3) [21,23,25]. At low voltages, the current-voltage characteristics demonstrate Ohmic behavior, and the current density depends linearly on the electric field ($J_\Omega \propto V^1$). At higher voltages, the space-charge-limited behavior becomes apparent, and the current-voltage characteristics follow the modified Mott-Gurney equation ($J_{SCLC} \propto V^2$). This transition is marked by a change from slope 1 to slope 2 in the logarithmic current-voltage characteristics, with the transition voltage V_Ω, being proportional to the carrier concentration n_0 (see equation 8.10). Small deviations from the linear and quadratic regimes are often attributed to non-ideal contact behavior (*e.g.* Schottky barriers formed at the metal–organic semiconductor interfaces) [23].

In the first part of the SCLC-regime, the injected carriers are trapped and the current is reduced by the trap factor θ. At the trap-filling voltage V_{TFL}, the amount of charge injected by the contact is sufficient large to fill all traps and the trap-free SCLC-regime is reached ($\theta = 1$). Before reaching the trap-filling voltage V_{TFL}, the current experiences an almost vertical rise and increases many decades for a one-decade increase in voltage, the specific curve shape depending on the energy distribution of the traps in the crystal [30]. The shape of the current-voltage curve is also dependent on the presence of surface traps beneath the contacts caused by damage to the organic crystal during device fabrication [31].

In the trap-free space-charge regime, the mobility is no more affected by impurities or defect states and the current-voltage characteristics follow the trap-free Mott-Gurney law

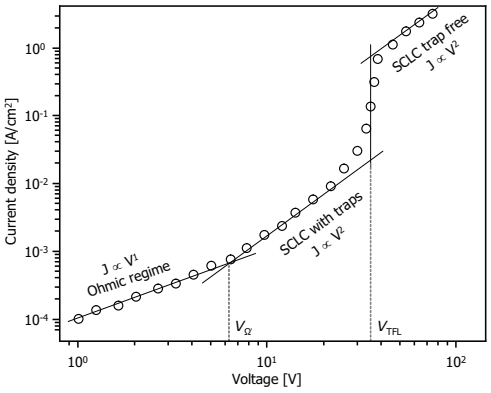

Figure 8.3 *Schematic current density vs. applied voltage graph on a double-logarithmic scale. Four different regimes are clearly visible: a) at low voltage the current rises linearly; the ohmic regime, and b) becomes space-charge-limited at higher field. Up till the c) transition point V_{TFL} the properties are still determined by traps, to the point they become filled and a d) trap free space-charge-limited regime takes place.*

($J_{SCLC} \propto V^2$). Access to the trap-free regime can be obtained only when the trap density is significantly low. In most cases, however, samples fail before that limit is reached, as either too much power has to dissipate through the crystal or because the contacts detach from the crystal at these high voltages.

In literature, in case the trap-free SCLC-regime is not reached experimentally, the value of the current I measured at the maximum applied voltage V_{max} is used to calculate a lower limit μ_{min} for the charge carrier mobility (with $\mu_{min} < \mu$).

8.2.4 Organic field-effect transistors

The second approach investigated in this chapter to generate charge carriers in organic semiconductors is by field-effect doping. The operation principle of a field-effect transistor (FET) was introduced by Lilienfeld, who filed several patents describing the basic idea of the construction and operation of field-effect transistors in the 1930s [32,33]. A similar device was patented by Heil in 1934 [33]. In 1947, Shockley, Bardeen and Brattain discovered the transistor effect and fabricated the first point-contact transistor [35-37], for which they were given the Nobel Prize in Physics in 1956 *"for their researches on semiconductors and their discovery of the transistor effect"* [38]. The first metal–oxide–semiconductor FET (MOSFET) was introduced in 1960 by Khang and Atalla [39]. MOSFETs, based on inorganic semiconductors, have been extensively studied the past 50 years and are the workhorses of many integrated circuits at the moment [12].

The last 25 years, research to organic field-effect transistors (OFETs) has gradually increased and OFETs are now routinely applied in organic electronics (see paragraph 1.4). Owing to similar current-voltage characteristics between organic field-effect transistors (OFETs) and MOSFETs, the theory developed for MOSFETs is often used as a starting point in modeling and understanding the behavior of OFETs. However, as described in paragraph 1.6, the electrical charge transport in organic semiconductors is intrinsically different compared to inorganic semiconductors. Therefore, it is still unknown to what extend the theory developed for MOSFETs can also be applied to organic FETs.

Device structures and working mechanism

The field-effect transistor is a three-terminal device that effectively acts as a switch. The three contacts are referred to as *gate* (G), *drain* (D) and *source* (S). A schematic cross section of the four configurations of lateral OFET structures is drawn in figure 8.4. All of them consist of a gate insulator (or gate dielectric), organic semiconductor, and gate, source and drain electrodes. The different stacking structures may influence the performance of the transistor, but the working mechanism is the same.

A FET can be considered as a parallel plate capacitor: the two capacitor plates are formed by the gate electrode and the semiconductor, separated from each other by an insulating gate dielectric layer. The source and drain electrodes contact the semiconductor and are used to inject charge carriers and probe the conduction in the semiconductor. When an electric field is applied at the gate electrode, charge carriers accumulate capacitively at the semiconductor–insulator interface. This, in turn, creates an active channel in which the

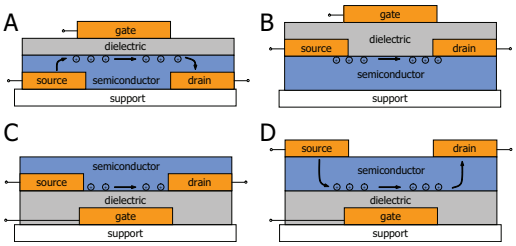

Figure 8.4 *Cross-sections of the four different types of lateral OFET structures: A) top-gate, bottom-contact (staggered) configuration, B) Top-gate, top-contact (coplanar) configuration, C) bottom-gate, bottom-contact (inverse-coplanar) configuration, and D) bottom-gate, top-contact (inverse-staggered) configuration.*

charge carriers can transport between the source and drain electrodes. The charge carrier density accumulated at the interface is determined by the gate voltage; this directly modulates the current between source and drain electrodes and thus controls the switching of the device between its *on* and *off* states.

OFET devices typically operate as accumulation mode devices, whereas MOSFETs are generally depletion or inversion mode devices. For example, during the operation of a *p*-channel OFET, negative gate and drain voltages (V_G, V_D) are applied, compared to the source voltage (V_S). With an increase of the gate voltage V_G towards a threshold voltage V_T, positive carriers are injected from the source electrode into the semiconductor as a result. The injected carriers from the metallic contacts usually dominate the total amount of charge carriers inside the device. The contact-injected carriers are accumulated at the interface and contribute first to filling of trap states in the band gap of the organic semiconductor. These localized in-gap states are associated with impurities and defects in the channel and their energy is separated from the edge of the HOMO band by more than a few k_BT (*i.e.* filling of the deep traps, see figure 1.13). As a result, the Fermi level at the organic surface E_F, initially positioned within the HOMO-LUMO gap, approaches the edge of the HOMO band E_{HOMO} (see figure 8.5). As soon as $E_F - E_{HOMO}$ becomes smaller than a few k_BT (*i.e.* when V_G reaches V_T), the OFETs conductance increases by several orders of magnitude due to the thermal excitation of the carriers from the localized states into the HOMO band. Consequently, a thin active layer is formed at the interface between the organic semiconductor and the gate dielectric, facilitating the carrier transport through the channel.

An important issue in OFETs is that charge transport is practically two-dimensional: the carriers are usually accumulated in the first few monolayers of the organic semiconductor close to the interface with the gate insulator [40,41]. The bulk of the semiconductor is hardly (or not at all) affected by the gate-field, due to screening by the charge in the active layer. The channel thickness of the transistor is thus very small and, therefore, a defect-free interface is desirable in OFET fabrication.

Measurement characteristics

During OFET operation, the carrier concentration of the channel is controlled by the gate voltage V_G. The transistor channel is active only when the gate voltage V_G exceeds the value of the threshold voltage V_T. The threshold voltage V_T is a measure for the amount of electrostatically induced charges needed to switch the electrical conduction in the transistor

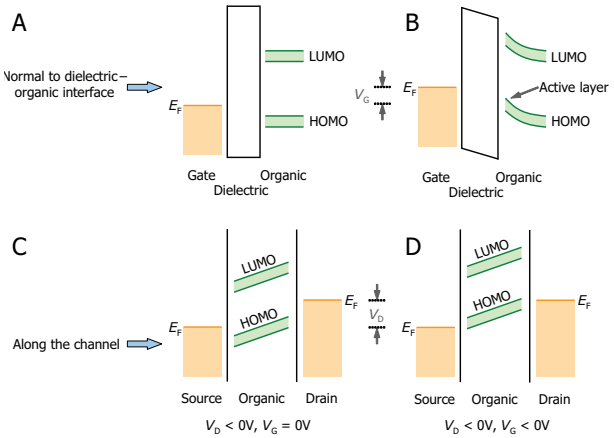

Figure 8.5 *Band diagram scheme of a p-channel OFET under A) zero V_G state; B) negative V_G along the direction normal to the interface; C) and D) Corresponding band diagram along the direction parallel to the interface from source to drain under negative V_D.*

on. The magnitude of V_T depends on several factors, such as the charge trap density at the interface, the presence of impurities and the quality of the contacts. Below this point, the transistor is turned *off*, and there is no conduction between drain and source.

In the operation of a unipolar FET, two distinct regimes can be distinguished: the *linear* regime and the *saturation* regime (see figure 8.6A) [12]. In the *linear* regime (small drain voltage, $|V_G - V_T| \gg |V_D|$), the current between drain and source (I_D) depends linearly on the applied voltage V_D and V_G. The value of the drain current I_D is given by:

$$I_D = \frac{W}{L} \mu C_i (V_G - V_T) V_D \tag{8.14}$$

where L and W are the channel length and width, μ the mobility and C_i is the capacitance per unit area of the gate dielectric, which depends on the permittivity ε and the thickness t of the dielectric layer. This model assumes constant charge carrier velocity, electric field and charge carrier density in the channel. A more realistic model accounts also for the variation of the charge carrier density between source and drain, and yields the following expression for the drain current I_D:

$$I_D = \frac{W}{L} \mu C_i \left[(V_G - V_T) V_D - \frac{V_D^2}{2} \right] \tag{8.15}$$

In the second operation regime, referred to as *saturation* regime (high drain voltage, $|V_G - V_T| \ll |V_D|$), the current I_D is quadratically dependent on the gate voltage V_G and relatively independent on the drain voltage V_D. At these higher V_D voltages, the channel is not continuous, but a depletion area forms at the drain contact; the onset of this region is called *pinch-off*. The value of the drain current I_D is now given by:

$$I_D = \frac{W}{2L} \mu C_i (V_G - V_T)^2 \tag{8.16}$$

The two primary characterization curves that investigate the variance of channel current I_D during device operation are shown in figure 8.6 and are defined as the *output characteristics* (I_D vs. V_D) and the *transfer characteristics* (I_D vs. V_G), respectively.

Output characteristics reveal the current change by sweeping the drain voltage. For a *p*-channel device, V_D is always swept from positive to negative, while in *n*-channel devices the sweeping is along the opposite direction. For *p*-type devices, the current experiences a transition from linear increase to level off (saturation) with increasing drain voltage.

Transfer characteristics reveal the current change by sweeping the gate voltage. For a *p*-channel OFET, the current is kept at a low level before a certain turn-on voltage V_{ON}. Below this point, the transistor is off with an current I_{OFF}. When the gate voltage passes V_{ON}, the injected carriers start to flow and lead to a sudden jump in current. The threshold voltage V_T is obtained by extrapolating the quasi-linear part of the I_D vs. V_G curve to zero current. The region between V_{ON} and V_T is called the *subthreshold region*. The charge induced in the subthreshold regime fills the traps that immobilize the charge carriers.

The equations so far represent expressions that yield values for the mobility of the semiconductor. The mobility can also be obtained from the slope, also known as transconductance g_m, in the linear region of the transfer characteristics, at low drain voltages V_D. The expression for the transconductance is:

$$g_m = \left.\frac{\delta I_D}{\delta V_G}\right|_{V_D} = \frac{W}{L} C_i \mu V_D \tag{8.17}$$

All these expressions assume an electric field independent mobility and that all the charges induced by the gate voltage are mobile. Other important parameters include the on-off current ratio I_{ON}/I_{OFF}, which denotes the quality of switching the current, and the sub-threshold swing S that represents the sharpness of turning the transistor on:

$$S = \frac{\delta V_G}{\delta(\log I_D)} \tag{8.18}$$

As the subthreshold swing S depends on the capacitance of the insulating layer C_i, it is convenient to introduce a normalized subthreshold swing $S_i = S C_i$.

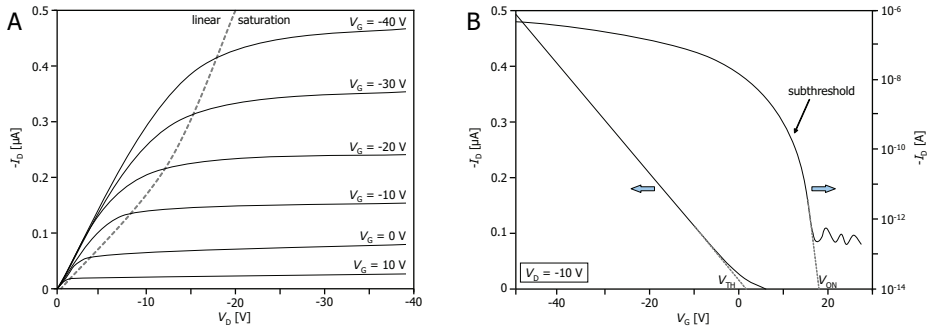

Figure 8.6 *Typical A) output and B) transfer characteristics for single-crystal OFETs.*

In practice, the transistor performance can be strongly affected by carrier traps, which may arise from a variety of sources; like impurities and structural imperfections, the selection of dielectric and electrode materials, the fabrication techniques, as well as the environment. See reference [42] for a detailed discussion of these non-idealities that hinder the performance of organic single-crystal transistors.

8.3 Experimental Procedure

In this paragraph, the experimental details of the SCLC and FET device fabrication techniques and of the applied electrical characterization techniques are discussed.

8.3.1 Fabrication of space- devices

Micrometer-sized and tens of nanometer (~50 nm) thick patterns of Au were deposited on the surface of pentacene single-crystal substrates by pulsed laser stencil deposition at room temperature, as has been described in chapter 3. For details on the vapor-transport growth of the pentacene single-crystals used in this study, see chapter 4. The lay-out of the stencils used for the deposition of various line patterns on the pentacene single-crystals, to perform the SCLC-measurements, is presented in figure 8.7.

Optimization of the deposition parameters for the growth of gold on pentacene crystals by PLD has been described in chapter 6. For the Au depositions, a laser fluence of 5 J/cm^2 was achieved on a 1.76 mm^2 target spot size by focusing the laser beam through a lens and a 98 mm^2 mask. For the *'hard-landing'* depositions, a laser repetition rate of 5 Hz, a target-to-substrate distance of 45 mm and an argon background gas pressure of 3×10^{-3} mbar were used. For the *'soft-landing'* experiments, a laser frequency of 1 Hz, a target-substrate distance of 75 mm and a background gas pressure of 5×10^{-2} mbar were applied.

Prior deposition of the Au contacts, a heating treatment was performed in vacuum at 80 °C overnight (~16 h) on some samples, to selectively remove the 6,13-pentacenequinone monolayer from the surface of the pentacene single-crystal (see chapter 5).

8.3.2 Fabrication of FET devices

To fabricate complete FET devices *in situ* on the surface of pentacene single-crystals, the *'quasi-dynamic stencil deposition'* technique has been used (see chapter 3 for all details).

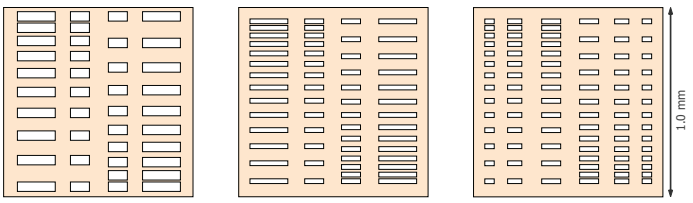

Figure 8.7 *Schematic stencil lay-out for the deposition of various line patterns on a substrate; viz. stencil design for the fabrication of space-charge-limited current devices. The bars are sized: 100-200 × 50 µm, 100-200 × 25 µm, and 50-75-100 × 25 µm, respectively. The vertical spacing between the lines increases with steps of 10, 5 and 5 µm per spacing, respectively.*

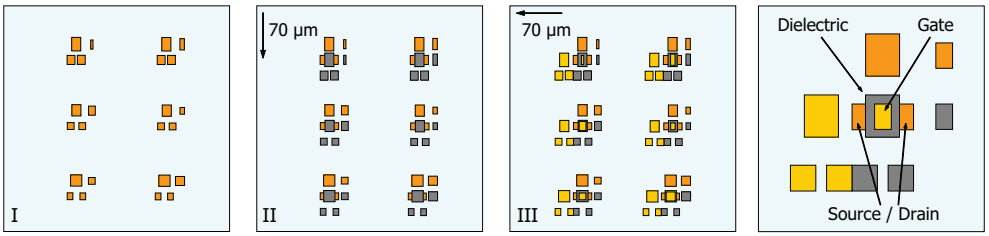

Figure 8.8 *In situ fabrication of various field-effect transistor structures by quasi-dynamic stencil deposition. In step I, the source and drain electrodes are deposited on the semiconducting substrate. After translating the stencil vertically over 70 µm, the gate dielectric material is deposited between the patterned source and drain electrodes in step II. Finally, in step III, after translating the stencil over 70 µm horizontally, the gate electrode is deposited on top of the patterned dielectric material.*

The three consecutive deposition steps to fabricate the top-gate top-contact field-effect transistors, without breaking the vacuum in-between, are depicted in figure 8.8 (see figure 3.7 for the stencil lay-out). In the 1st and 3rd deposition run, Au contacts (~50 nm thick) were deposited with the *'soft-landing'* settings described above. In the 2nd run, cerium oxide was deposited as gate dielectric material (50-500 nm thick). Optimization of the deposition parameters for various gate dielectric materials on pentacene single-crystals by PLD has been described in chapter 6. For the CeO_2 depositions, a laser fluence of 1 J/cm^2 was achieved on a 0.88 mm^2 target spot size by focusing the laser beam through a lens and a 36 mm^2 mask. Further, a laser repetition rate of 1 Hz, a target-to-substrate distance of 75 mm and an oxygen background gas pressure of 2.5×10^{-2} mbar were used.

8.3.3 Electrical characterization

To characterize the electrical properties of the fabricated SCLC and FET devices, the samples were analyzed in a nano probing station. This analytical probing station consists of a Zyvex S100 nanomanipulator, a large-chamber JSM-6490 high vacuum Jeol SEM and a Keithley 4200-SCS/F system. Therefore, all current-voltage measurements were performed in vacuum ($P < 7 \times 10^{-6}$ mbar), at room temperature and in the dark. For a more detailed description of the nano prober, see chapter 3. To characterize the fragile organic molecular crystal devices without problems, the Au contacts were probed by the flexible carbon fiber tips.

To prevent build-up of an insulating electron beam-induced deposition (EBID) layer on the sample surface, imaging of the sample with the SEM's electron beam was restricted to fast scanning at low magnification for a minimal time, only to be able to land the probes on the device contacts. Initial investigations showed that the performance of the SCLC devices deteriorated tremendously if a thin EBID-layer is present on the sample surface (*e.g.* $V_{\Omega'}$ increased to voltages in the range of 50 - 100 V, and μ_{min} dropped to below 10^{-6} cm^2/Vs). Besides that, the *passive voltage contrast* (see paragraph 3.5.3) between probed and unprobed Au contacts (patterned on a pentacene crystal) in the nano prober disappeared.

To ensure a high reproducibility (*i.e.* a measurement not influenced by charge carriers in filled trap states from earlier measurements), a waiting period of at least 12 hours was applied after every measurement. For a proper detection of the Ohmic and SCLC regimes at

low voltage, the SCLC measurements were performed rather slowly, by applying a large measuring time, a high filtering factor to reduce noise and small voltage steps (0.05 V).

To evaluate the space charge transport in the pentacene single-crystals, the Geurst 2D-model with the Zuleeg-Knoll modification (see equation 8.12) was applied on all measurements, as the local thickness h of the pentacene single-crystals could only approximately be obtained. In case the trap-free SCLC-regime was not reached experimentally, a lower limit μ_{min} for the charge carrier mobility was calculated by using the value of the current I measured at the maximum applied voltage V_{max} of ±200 V.

8.4 Results and Discussion

In this paragraph, the electrical characterization of the fabricated SCLC and FET devices on pentacene single-crystals is discussed. Focus will be on the influence of the different deposition parameters applied in the manufacturing of the devices (*'hard-landing'* vs. *'soft-landing'*) and on the influence of performing a heating treatment on the pentacene crystal (before applying the contacts) on the final electrical properties.

8.4.1 Space-charge-limited current measurements

Prior to the SCLC analysis of the fabricted pentacene single-crystal devices, probing the gold contacts by the flexible carbon fiber tips in the nano probing system was investigated first.

Probing of the Au contacts

Figure 8.9A presents a SEM image of a circular gold contact deposited on a pentacene single-crystal, with two carbon fiber probe tips landed on the Au dot. The accompanying graph shows the forward (dark grey) and reverse (light grey) voltage sweeps, starting at 0 V to ±1 V, from one probe through the sample to the other probe. The forward and reverse sweeps overlap, and the curves are symmetrical and linear from zero to 0.5 V. At ±1 V, a current of about $\pm 1.8 \times 10^{-4}$ A is measured, resulting in a resistance of 5.6×10^{3} Ω.

The 'sheet resistance' values of various Au contacts on different pentacene crystals vary between 6.2×10^{2} and 9.8×10^{3} Ω/□, with an average of 3.8×10^{3} Ω/□. Although the series resistances of the cabling and probes are still included in these numbers, the measured values are several orders of magnitude lower than the resistances measured in the SCLC measurements (see next paragraph). In other words, the SCLC-measurements are

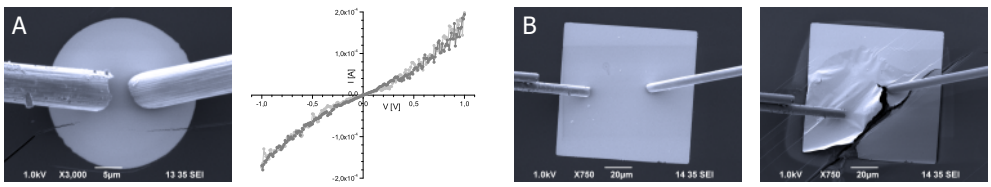

Figure 8.9 *SEM images of gold dots deposited on a pentacene single-crystal, which are contacted by two carbon fiber tips in the nano prober system. A) Typical electrical results used to calculate the sheet resistance of the deposited Au pattern, and B) example of mechanical failure, before and after applying a too high current (>10^{-3} A) through the tens of nanometer thick gold contact.*

completely dominated by the bulk resistance of the pentacene single-crystal, and not by the contact or cabling-probe resistances.

Figure 8.9B presents an example of mechanical failure, before and after applying a too high current (>10^{-3} A) through the tens of nanometer thick gold contact deposited on a pentacene single-crystal. The cracking and delamination of the thin Au film occurred already at quite low voltages (2 - 5 V), and is ascribed to overheating of the sample, combined with the low thermal diffusivity of the pentacene single-crystal substrate (see paragraph 6.1).

Space-charge-limited current measurements

In figure 8.10, three representative current I versus applied voltage V characteristics are presented, measured on pentacene single-crystal devices that were all fabricated in a different manner. The Au contacts on the pentacene single-crystal measured in figure 8.10A were pulsed-laser stencil deposited using the *'hard-landing'* settings, whereas the *'soft-landing'* settings were applied in the fabrication of the devices characterized in figure 8.10B-C. Prior deposition of the Au contacts, a heating treatment was performed in vacuum at 80 °C overnight on the pentacene single-crystal characterized in figure 8.10C, to selectively remove the oxidation products from the crystal surface (*i.e.* the 6,13-pentacene-quinone monolayer, see chapter 5). No heating treatment was performed on the crystal devices shown in figure 8.10A-B. The presence of a 6,13-pentacenequinone monolayer partly covering these pentacene single-crystals can be seen by the color contrast in the inset SEM images in figure 8.10A-B, which is absent in figure 8.10C.

For all current-voltage characteristics, the behavior at low bias is associated with Ohmic behavior ($I \propto V^x$, with $x = 1$). The observed value for x over all measurements ($n = 103$) is found to be 0.97 ± 0.15, for which the error can be related to the quality of the contacts [10,31].

Upon increasing the applied voltage, a transition from the linear Ohmic regime to a non-linear regime occurs. Starting from the voltage $V_{\Omega'}$, marking the onset of this transition (see figure 8.3), the quadratic increase ($I \propto V^2$) of the space-charge-limited regime with traps can be detected in the curves. In some cases (see figure 8.10C), the square law of the SCLC regime with traps is not so clearly observable, and filling of the traps can be observed almost right away by a steeper increase of the curve.

At higher voltages, the current increases by many decades for a one-decade increase in voltage (typically between four to eight, depending on the sample). Failure of the samples at these high voltages, due to too much power dissipating through the crystals or detaching of the gold contacts from the crystal, typically did not occur. In most cases, the maximum applied voltage was not sufficient to fill all traps in the device (*i.e.* V_{TFL} and the SCLC trap-free regime were not reached). Occasionally, the rapid current increase did terminate by crossing over into a lower dependence on voltage (see figure 8.10B), which was at times approximately quadratic. A second vertical rise, a characteristic that could represent either the filling of another discrete trap level, or the breakdown of the system at high injected current density [25], was also observed in a few cases (not shown). In general, the value of the

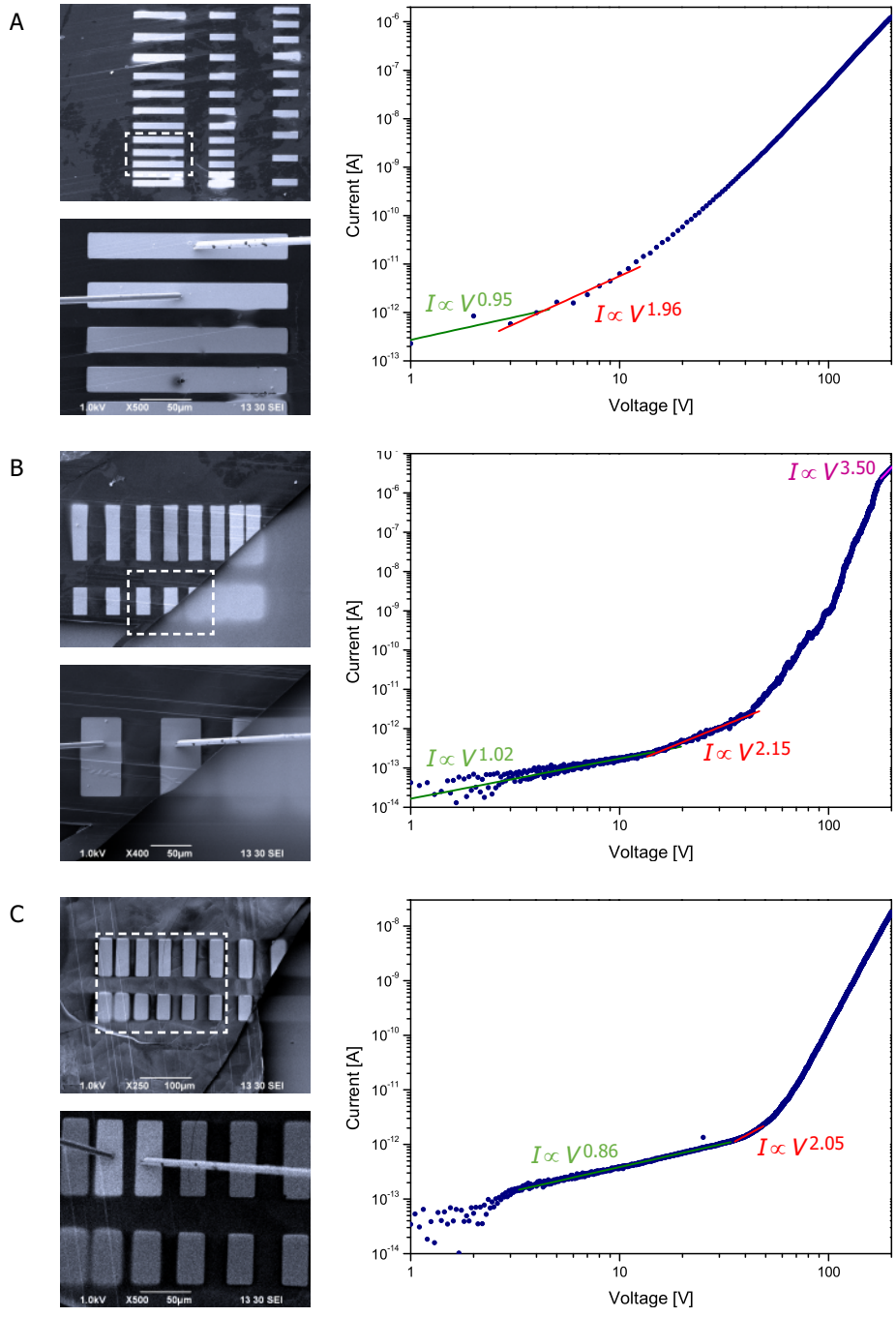

Figure 8.10 *Space-charge-limited current measurements in the nano prober on pentacene single-crystals with the pulsed-laser stencil deposited Au contacts probed by the flexible carbon fiber tips. A) 'Hard-landing' settings, L = 15 µm, W = 200 µm, $\mu_{min} = 5.7 \times 10^{-2}$ cm²/Vs, B) 'soft-landing' settings, L = 50 µm, W = 100 µm, $\mu_{min} = 1.6 \times 10^{0}$ cm²/Vs, and C) 'soft-landing' settings with overnight heat treatment at 80 °C, L = 15 µm, W = 75 µm, $\mu_{min} = 7.8 \times 10^{-4}$ cm²/Vs.*

current measured at the maximum applied voltage (V_{max} = ±200 V) was used to calculate μ_{min} using equation 8.12.

The precise shape of the current-voltage characteristics measured on different crystals exhibited large deviations, but substantial differences could also be observed between different pairs of Au contacts on one crystal. For example, the trap filling limit is reached in the *I - V* characteristics of figure 8.10B, whereas between other pairs of contacts (a few tens or hundreds of micrometers further on the same crystal) the trap filling limit was not reached. This indicates a large spread in the quality of the pentacene single-crystals, but it may also indicate the quality of an individual crystal is not consistent on this length scale (*i.e.* the traps are not homogeneously distributed throughout the crystal bulk or on the crystal surface).

An overview of all calculated space-charge-current mobility μ_{min} values is presented in figure 8.11. In total, 103 current-voltage measurements were performed: 25 on *'hard-landing'* and 59 on *'soft-landing'* samples without a heat treatment; and 2 on *'hard-landing'* and 17 on *'soft-landing'* samples with heat treatment applied. The *I - V* characteristics yielded a broad distribution of different apparent mobilities, similar as the observations of De Boer *et al.* [10,31,43] on tetracene single-crystal samples (see paragraph 2.6.2).

The largest μ_{min} mobility value found for a *'soft-landing'* sample is 8.4×10^0 cm^2/Vs, which is close to the highest mobility values reported for pentacene single-crystals (15 - 40 cm^2/Vs) [23,43,44]. About one third of the measured *'soft-landing'* mobility numbers fall in the category 10^0 - 10^1 cm^2/Vs. This illustrates metal contacts can be reproducibly patterned on organic molecular crystals by *'soft-landing'* in pulsed laser stencil deposition, without damaging the fragile organic substrate.

The largest μ_{min} value found on a *'hard-landing'* sample is 9.2×10^{-1} cm^2/Vs. As can be seen in figure 8.11, the highest μ_{min}values of the *'hard-landing'* samples (green bars) are about one order of magnitude lower than found for the *'soft-landing'* samples (red bars). The major difference between the two series is the kinetic energy of the gold species, when they arrive at the pentacene single-crystal surface (see chapter 6). The larger kinetic energy of the impinging Au species will result in more and deeper diffusion of Au particles into the pentacene crystal matrix, with a more distorted interface as a consequence. Therefore, it is very likely that more deep traps were formed under the gold contacts at the crystal surface when using the *'hard-landing'* settings, with the lower μ_{min} values as a result.

If the samples with applied heat treatment are compared to the samples that did not undergo a heat treatment, it can be concluded the heat treatment resulted in a significant decrease of the charge carrier mobility.

The highest μ_{min} mobility values of the *'soft-landing'* samples with heat treatment (blue bars) are about three orders of magnitude lower than found for the *'soft-landing'* samples without heat treatment (red bars). The largest μ_{min} value found for the *'soft-landing'* samples with heat treatment is only 2.3×10^{-3} cm^2/Vs. Not present in figure 8.11 are the two *'hard-landing'* samples with heat treatment; they both have a μ_{min} value of $<10^{-3}$ cm^2/Vs.

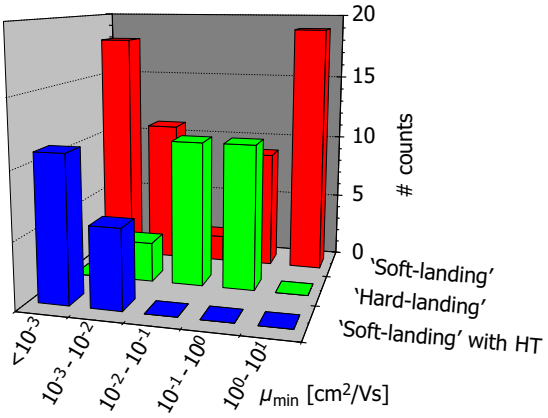

Figure 8.11 *Histogram showing the experimentally observed space-charge-limited current mobility μ_{min} for the 'soft-landing' (red bars) and 'hard-landing' (green) samples without heat treatment, and 'soft-landing' samples with heat treatment (blue).*

The large spread in the calculated values of μ_{min} can be observed best in the series most investigated; *i.e.*, the *'soft-landing'* samples without heat treatment (red bars). The calculated mobility ranges from values below 10^{-3} up to 10^{1} cm^2/Vs. De Boer *et al.* [10,31,43] concluded that the large sample-to-sample variations they observed in their μ_{min} values mainly originated from the quality of the metal contacts (*i.e.* manually painted solvent-free silver epoxy contacts).

In this work, the gold contacts were stencil deposited on the pentacene single-crystals by PLD. Variations between the individual gold contacts (*e.g.* morphology, structure, thickness) are small on this length scale and can be neglected. Variations between the various gold–pentacene interfaces (*e.g.* amount of Au diffusion into the crystal lattice) deriving from the PLD stencil patterning process are also expected to be small. However, as the SEM insets in figure 8.10A-B show, a 6,13-pentacenequinone monolayer is present on some parts of the pentacene single-crystal surface. This implicates that the pentacene–gold interface, and thus the charge injection into the crystal, is influenced by the presence of quinone molecules at the interface. As the 6,13-pentacenequinone monolayer is not homogeneously covering the entire crystal surface, but only partly, the amount of quinone traps at the interface will vary between contacts. A small amount of traps located at the metal – organic interface can already have a large effect in suppressing the current flow (see paragraph 8.2.2) [10,31,43], which makes these traps a logical explanation for the large sample-to-sample variations.

Nevertheless, the spread in mobility values μ_{min} observed between various contacts on one specific pentacene single-crystal is typically only about one order of magnitude large. The main contribution to the large spread in μ_{min} values can therefore not be attributed to the quality of the metal contacts or the metal–organic interface. Instead, the main contribution to the large spread in μ_{min} values is attributed to large quality differences between the various crystals. In other words, the main contributor to the observed mobility μ_{min} values is the bulk resistance R_{Ch}, and not the contact resistance R_c. Nevertheless, for high-quality pentacene single-crystals, the quality of the contacts (*viz.* the different amounts of 6,13-pentacenequinone present at the pentacene–gold interface) has a large influence on the charge carrier mobility.

Optimization of the heat treatment to the current parameters has been discussed in chapter 5. A possible reason for the large decrease in mobility is that the 6,13-pentacenequinone molecules were not selectively removed, but that pentacene molecules sublimated from the crystal surface as well. If this is the case, the sample may have degraded to a large extend, resulting in a largely increased resistance of the pentacene crystal bulk.

The fact that the patterning stencil had to be positioned on the heat-treated crystal before deposition of the Au contacts may also be of influence (*e.g.* the entire procedure was not performed *in vacuo*): parts of the pentacene crystal surface may re-oxidize in this short period. Actually, it can also be argued that the quinone monolayer prevented the adsorption of water or other molecules directly on the pentacene crystal and that, by selectively removing the 'protective' quinone molecules by the heat treatment, an interface with much more traps is created compared to not removing the quinones, resulting in the decreased mobility values. Note that the option that the pentacene single-crystals investigated in these heat treatments were not of the highest quality possible can also not be excluded, as no pre-treatment measurements were performed on these samples as reference.

Based on these results, it is concluded that more research is needed to optimize the heating treatment of the pentacene single-crystals, as carrying out the treatment with the current conditions resulted in a too large decline of the device performance. Nevertheless, as results by Jurchescu *et al.* [23,44,45] and the sample-to-sample variations in mobility show for the *'soft-landing'* series without heat treatment, removing the 6,13-pentacenequinone molecules selectively from the crystal surface (before applying the metal contacts or gate dielectric) to obtain well-defined interfaces ought to improve the device performance.

8.4.2 Field-effect transistor measurements

The SEM images in figure 8.12A demonstrate the proof of principle of the *in situ* fabrication of complete field-effect transistor devices with the *'quasi-dynamic stencil deposition'* technique in PLD (see paragraph 3.3.4). Using the principle shown in figure 8.8, sixteen top-gate top-contact FET structures were manufactured in three consecutive deposition steps on the surface of a pentacene single-crystal, without breaking the vacuum in-between. As can be seen in the SEM images, smooth, crack-free and distinct patterns can be deposited during all three stages, resulting in well-defined FET structures. However, some blurring and broadening was encountered around the patterns of several transistors, due to local variations in the stencil-to-substrate gap. Consequently, the geometry of the final FET structures is less well-defined. Occasionally, the FET structures were not suitable for electrical characterization, as excessive blurring and broadening of the Au patterns resulted in shortage paths between the contacts, which ended up in mechanical failure of the device when applying a few volts between the contacts (not shown).

Figure 8.12B-C shows SEM images of the probing of two FET structures with the flexible carbon fiber probes in the nano probing system, each with two graphs of the final output characteristics and the accompanying gate leakage current data. The output characteristics reveal the drain current I_D change by sweeping the drain voltage V_D, for a constant gate

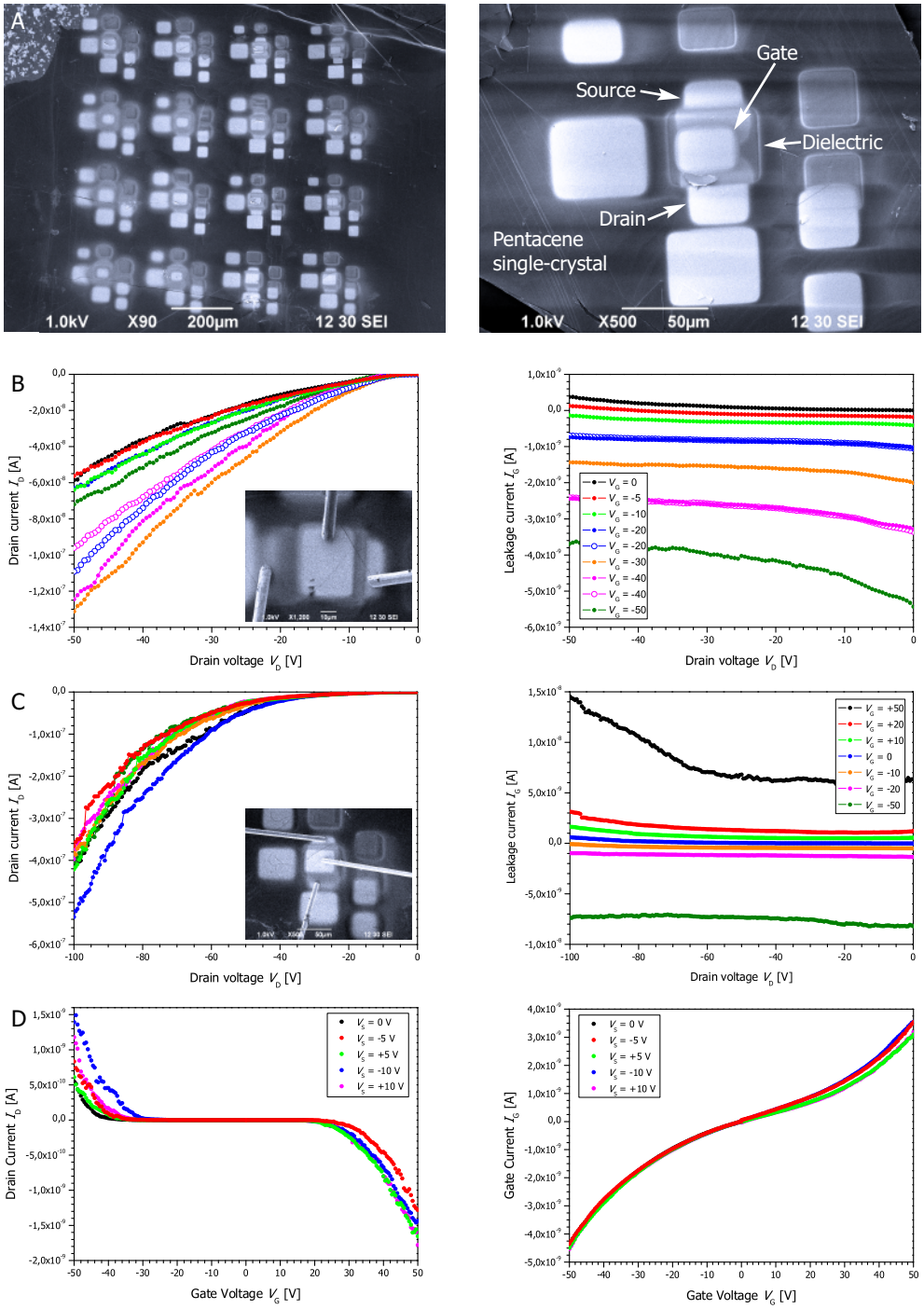

Figure 8.12 *A) SEM images of (top-contact, top-gate) field-effect transistor devices fabricated in situ on a pentacene single-crystal substrate by quasi-dynamic pulsed-laser stencil deposition, B-C) Output characteristics with accompanying gate leakage current data of two FET devices, and D) Transfer characteristics with accompanying gate leakage current data of the FET device shown in figure 8.12B.*

voltage V_G. In figure 8.12B, V_D is swept from 0 to -50 V, while a V_G between 0 and -50 V is applied. In figure 8.12C, V_D is swept from 0 to -100 V, with a V_G between +50 and -50 V. The transfer characteristics in figure 8.12D reveal the drain current I_D change by sweeping the gate voltage V_G from 0 to ±50 V, for a constant drain voltage V_D between +10 and -10 V, with accompanying gate leakage data, of the FET device shown in figure 8.12B.

The leakage current graphs in figure 8.12B-C show a reproducible increase in leakage current I_G when a higher gate voltage V_G is applied. The leakage currents I_G measured instantaneously during the I_D-V_D sweeps are about one to two orders of magnitude lower than the measured drain currents I_D. In the transfer characteristics of figure 8.12D, all sweeps roughly overlap and again do not show a typical field-effect behavior. In this case, however, the gate leakage currents I_G are about two times larger than the measured drain currents I_D for all sweeps.

The output and transfer characteristics presented in figure 8.12B-C do not show the presence of a field-effect in a semiconductor. In figure 8.12B, the drain current I_D sweeps do increase when a higher gate voltage V_G is applied, but these observations are not reproducible (*e.g.* see V_G = -20 V and -40 V) and the arrangement of the curves is random. In the output characteristics of figure 8.12C, all drain current sweeps roughly overlap, regardless of the applied gate voltage. The fact that voltages this high can be applied on the device contacts demonstrates that no shorts were present between the individual gold contacts and that the gate dielectric layer withstands these high voltages as well.

As mentioned, these characteristics do not show the presence of a field-effect, but give the impression of space-charge-limited conduction between the source and drain contacts through an insulator, regardless the presence of the deposited dielectric material and the applied gate voltage. In fact, when calculating the space-charge-limited current mobility with equation 8.12 for, amongst others, the drain current sweeps in figure 8.12C, μ_{min} values between 2.9×10^{-1} and 7.2×10^{-1} cm^2/Vs are obtained, with no correlation to the applied gate voltage V_G (with a constant value between -50 and +50 V). Note that these mobility values are not included in figure 8.11.

From these observations, it is concluded the largest problems arise in the dielectric layer. At low gate voltages, no channel is induced in the semiconductor between the source and drain contacts, due to too much screening by the relatively thick dielectric layer (~500 nm). When higher gate voltages are applied, the gate leakage currents start to dominate the measurements and no field-effect is induced as well. The SCLC measurements discussed in paragraph 8.4.1 show that at these high voltages, large currents can be injected into the pentacene single-crystals by the 'soft-landed' Au contacts without problems. However, in the FET design, the amorphous CeO_2 thin film (patterned at room temperature) is too leaky at these high voltages to function as insulating layer in the 'capacitor' between the gate electrode and the conductive channel. As a consequence, no field-effect is induced in the organic semiconductor. Reducing the thickness of the dielectric layer (down to ~50 nm) was not an option, as it resulted in increased gate leakage currents.

Another possible reason why no field-effect is present is that the pentacene single-crystals were still damaged too much by the deposition of the cerium oxide layer, even though the deposition parameters were optimized for patterning onto soft fragile organic substrates. However, as the SCLC-mobility μ_{min} values for the drain current sweeps of the FET devices are quite reasonable (*i.e.* between 10^{-1} - 10^{0} cm^2/Vs), the molecular order of the crystal at the interface is largely maintained during deposition. In fact, these values indicate a successful *'soft-landing'* of the oxide material on the pentacene crystal.

Finally, note that there is quite some geometrical overlap between the gate contact and the source and drain contacts in the manufactured top-gate, top-contact transistors (see figure 8.12A) in most cases, resulting in large parasitic overlap capacitances.

8.5 Concluding Remarks

In this chapter, the influence of the deposition parameters applied in the device fabrication procedure (*'hard-landing'* vs. *'soft-landing'*) and the influence of performing a heat treatment (before applying the metal contacts) on the electrical properties of pentacene single-crystals was investigated. For this investigation, SCLC and FET devices fabricated on the surface of pentacene single-crystals were electrically characterized in a nano probing system.

The precise shape of the SCLC characteristics measured on different crystals exhibited large deviations, indicating a large spread in the quality of the pentacene single-crystals. This large quality difference is attributed as the main contributor to the large spread observed in the apparent mobility μ_{min}, with values from below 10^{-3} up to 10^{1} cm^2/Vs. However, as substantial differences were also observed between different pairs of Au contacts on individual pentacene single-crystals, the quality of the contacts (*viz.* the different amounts of 6,13-pentacenequinone present at the pentacene – gold interface and gold particles diffused into the crystal lattice) has a substantial influence on the mobility as well.

The largest μ_{min} apparent mobility values were found for the *'soft-landing'* samples (*i.e.* 10^{0} - 10^{1} cm^2/Vs), which are close to the highest mobility values for pentacene single-crystals reported in literature. This illustrates metal contacts can be reproducibly patterned on organic molecular crystals by *'soft-landing'* in pulsed laser stencil deposition, without damaging the fragile organic substrate. The largest μ_{min} mobility values measured for the *'hard-landing'* samples were typically one order of magnitude lower, indicating a more distorted interface at these settings.

By comparing the samples with applied heat treatment to the samples that did not undergo a heat treatment, it is concluded the heat treatment procedure is not completely optimized yet, as it resulted in a significant decrease of the charge carrier mobility.

The *in situ* fabrication of complete top-gate, top-contact field-effect transistor devices on the surface of pentacene single-crystals is realized by using the *'quasi-dynamic stencil deposition'* technique in pulsed laser deposition. However, the characteristics do not show the presence of a field-effect in the organic crystal.

8.6 References

[1] Pope, M.; Swenberg, C.E.; Electronic processes in organic crystals and polymers; **1999**; 2nd ed.; Oxford university press; New York, NY, U.S.A.

[2] Brütting, W.; Physics of organic semiconductors; **2005**; Wiley-VCH; Weinheim, Germany

[3] Karl, N.; "Charge-carrier mobility in organic crystals"; Ch. 8 in Organic Electronic Materials; Ed. Farchioni, R.; Grosso, G.; **2001**; 283-326; Springer-Verlag; Berlin, Germany

[4] Karl, N.; Kraft, K.H.; Marktanner, J.; Münch, M.; Schatz, F.; Stehle, R.; Uhde, H.M.; "Fast electronic transport in organic molecular solids?"; *J. Vac. Sci. Technol. A*; 17; **1999**; 2318-2328

[5] Karl, N.; Marktanner, J.; "Electron and hole mobilities in high purity anthracene single crystals"; *Mol. Cryst. Liq. Cryst.*; 355; **2001**; 149-173

[6] Warta, W.; Stehle, R.; Karl, N.; "Ultrapure, high mobility organic photoconductors"; *Appl. Phys. A*; 36; **1985**; 163-171

[7] Warta, W.; Karl, N.; "Hot holes in naphthalene: high, electric-field-dependent mobilities"; *Phys. Rev. B*; 32; **1985**; 1172-1182

[8] Hoesterey, D.C.; Letson, G.M.; "The trapping of photocarriers in anthracene by anthracenequinone, anthrone and naphthacene"; *J. Phys. Chem. Solids*; 24; **1963**; 1609-1615

[9] Pflaum, J.; Niemax, J.; Tripathi, A.K.; "Chemical and structural effects on the electronic transport in organic single crystals"; *Chem. Phys.*; 325; **2006**; 152-159

[10] Boer, R.W.I. de; Organic single-crystal field-effect transistors; PhD Thesis; **2005**; University of Delft; Delft, The Netherlands

[11] Panzer, M.J.; Frisbie, C.D.; "Contact effects in organic field-effect transistors"; Ch. 2.4 in Organic Field-Effect Transistors; Ed. Bao, Z.; Locklin, J.; **2007**; CRC Press; Taylor & Francis Group; New York, NY, U.S.A.

[12] Sze, S.M.; Physics of semiconductor devices; **1981**; Wiley-Interscience; New York, NY, U.S.A.

[13] Ruden, P.P.; Smith, D.L.; "Theory of spin injection into conjugated organic semiconductors"; *J. Appl. Phys.*; 95; **2004**; 4898-4904

[14] Campbell, I.H.; Smith, D.L.; "Physics of Organic Electronic Devices"; Ch. 1 in Solid State Physics 55; Ed. Ehrenreich, H.; Spaepen, F.; **2001**; Academic Press; New York, NY, U.S.A.

[15] Koch, N.; Kahn, A.; Ghijsen, J.; Pireaux, J.J.; Schwartz, R.L.; Elschner, A.; "Conjugated organic molecules on metal versus polymer electrodes: demonstration of a key energy level alignment mechanism"; *Appl. Phys. Lett.*; 82; **2003**; 70-72

[16] Käfer, D.; Characterization and optimization of growth and electronic structure of organic thin films for applications in organic electronics; PhD Thesis; **2008**; Ruhr University; Bochum, Germany

[17] Kahn, A.; Koch, N.; Gao, W.; "Electronic structure and electrical properties of interfaces between metals and *p*-conjugated molecular films"; *J. Pol. Sci. B: Pol. Phys.*; 41; **2003**; 2529-2548

[18] Hwang, J.; Wan, A.; Kahn, A.; "Energetics of metal-organic interfaces: new experiments and assessment of the field"; *Mat. Sci. Eng. Rep.*; 64; **2009**; 1-31

[19] Vollmer, A.; Jurchescu, O.D.; Arfaoui, I.; Salzmann, I.; Palstra, T.T.M.; Rudolf, P.; Niemax, J.; Pflaum, J.; Rabe, J.P.; Koch, N.; "The effect of oxygen exposure on pentacene electronic structure"; *Eur. Phys. J. E*; 17; **2005**; 339-343

[20] Watkins, N.J.; Yan, L.; Gao, Y.; "Electronic structure symmetry of interfaces between pentacene and metals"; *Appl. Phys. Lett.*; 80; **2002**; 4384-4386

[21] Lampert, M.A.; Mark, P.; Current injection in solids; **1970**; Academic Press; New York, NY, U.S.A.

[22] Mott, N.F.; Gurney, R.W.; Electronic processes in ionic crystals; **1940**; Oxford University Press; London, United Kingdom

[23] Jurchescu, O.D.; Molecular organic semiconductors for electronic devices; PhD Thesis; **2006**; University of Groningen; Groningen, The Netherlands

[24] Murgatroyd, P.N.; "Theory of space-charge-limited current enhanced by Frenkel effect"; *J. Phys. D: Appl. Phys.*; 3; **1970**; 151-156

[25] Braga, D.; Battaglini, N.; Yassar, A.; Horowitz, G.; Campione, M.; Sassella, A.; Borghesi, A.; "Bulk electrical properties of rubrene single-crystals: measurements and analysis"; *Phys. Rev. B*; 77; **2008**; 115205

[26] Grinberg, A.A.; Luryi, S.; Pinto, M.R.; Schryer, N.L.; "Space-charge-limited current in a film"; *IEEE Trans. Electron Dev.*; 36; **1989**; 1162-1170

[27] Geurst, J.A.; "Theory of space-charge-limited currents in thin semiconductor layers": *Phys. Stat. Sol. B*; 15; **1966**; 107-118

[28] Zuleeg, R.; Knoll, P.; "Space-charge-limited currents in heteroepitaxial films of silicon grown on sapphire"; *Appl. Phys. Lett.*; 11; **1967**; 183-185

[29] Jurchescu, O.D.; Palstra, T.T.M.; "Crossover from one- to two-dimensional space-charge-limited conductions in pentacene single crystals"; *Appl. Phys. Lett.*; 88; **2006**; 122101

[30] Sworakowski, J.; Nešpůrek, S.; "The spectroscopy of traps in single crystals, polymers and deposited thin films by space-charge-limited currents"; *Vacuum*; 39; **1989**; 7-10

[31] Boer, R.W.I. de; Morpurgo, A.F.; "Influence of surface traps on space-charge limited current"; *Phys. Rev. B*; 72; **2005**; 073207

[32] Lilienfeld, J.E.; "Method and apparatus for controlling electric current"; U.S. Patent 1,745,175; **1930**

[33] Lilienfeld, J.E.; "Device for controlling electric current"; U.S. Patent 1,900,018; **1933**

[34] Heil, O.; "Improvements in or relating to electrical amplifiers and other control arrangements and devices"; G.B. Patent 439,457; **1935**

[35] Bardeen, J.; Brattain, W.H.; "The transistor, a semi-conducting triode"; *Phys. Rev.*; 74; **1948**; 230-231

[36] Shockley, W.; Pearson, G.L.; "Modulation of conductance of thin films of semi-conductors by surface charges"; *Phys. Rev.*; 74; **1948**; 232-233

[37] Shockley, W.; "Circuit element utilizing semiconductive material"; U.S. Patent 2,569,347; **1951**

[38] Official website of the Nobel Foundation; The Nobel Prize in Physics 1956; http://nobelprize.org/nobel_prizes/physics/laureates/1956/; last visited on 11-10-2009

[39] Kahng, D.; Atalla, M.M.; "Silicon-silicon dioxide field induced surface devices"; *IRE Solid-State Devices Research Conference*; **1960**; Carnegie Institute of Technology; Pittsburgh, PA, U.S.A.

[40] Sinova, J.; Schliemann, J.; Núñez, A.S.; MacDonald, A.H.; "2D bands and electron-phonon interactions in polyacene plastic transistors"; *Phys. Rev. Lett.*; 87; **2001**; 226802

[41] Wehrli, S.; Poilblanc, D.; Rice, T.M.; "Charge profile of surface doped C_{60}"; *Eur. Phys. J. B*; 23; **2001**; 345-350

[42] Xia, Y.; Fabrication and characterization of organic single crystal and printed polymer transistors; PhD Thesis; **2009**; University of Minnesota; Minnesota, MN, U.S.A.

[43] Boer, R.W.I. de; Jochemsen, M.; Klapwijk, T.M.; Morpurgo, A.F.; Niemax, J.; Tripathi, A.K.; Pflaum, J.; "Space charge limited transport and time of flight measurements in tetracene single crystals: a comparative study"; *J. Appl. Phys.*; 95; **2004**; 1196-1202

[44] Jurchescu, O.D.; Baas, J.; Palstra, T.T.M.; "Effect of impurities on the mobility of single crystal pentacene"; *Appl. Phys. Lett.*; 84; **2004**; 3061-3063

[45] Jurchescu, O.D.; Popinciuc, M.; Wees, B.J. van; Palstra, T.T.M.; "Interface-controlled, high-mobility organic transistors"; *Adv. Mater.*; 19; **2007**; 688-692

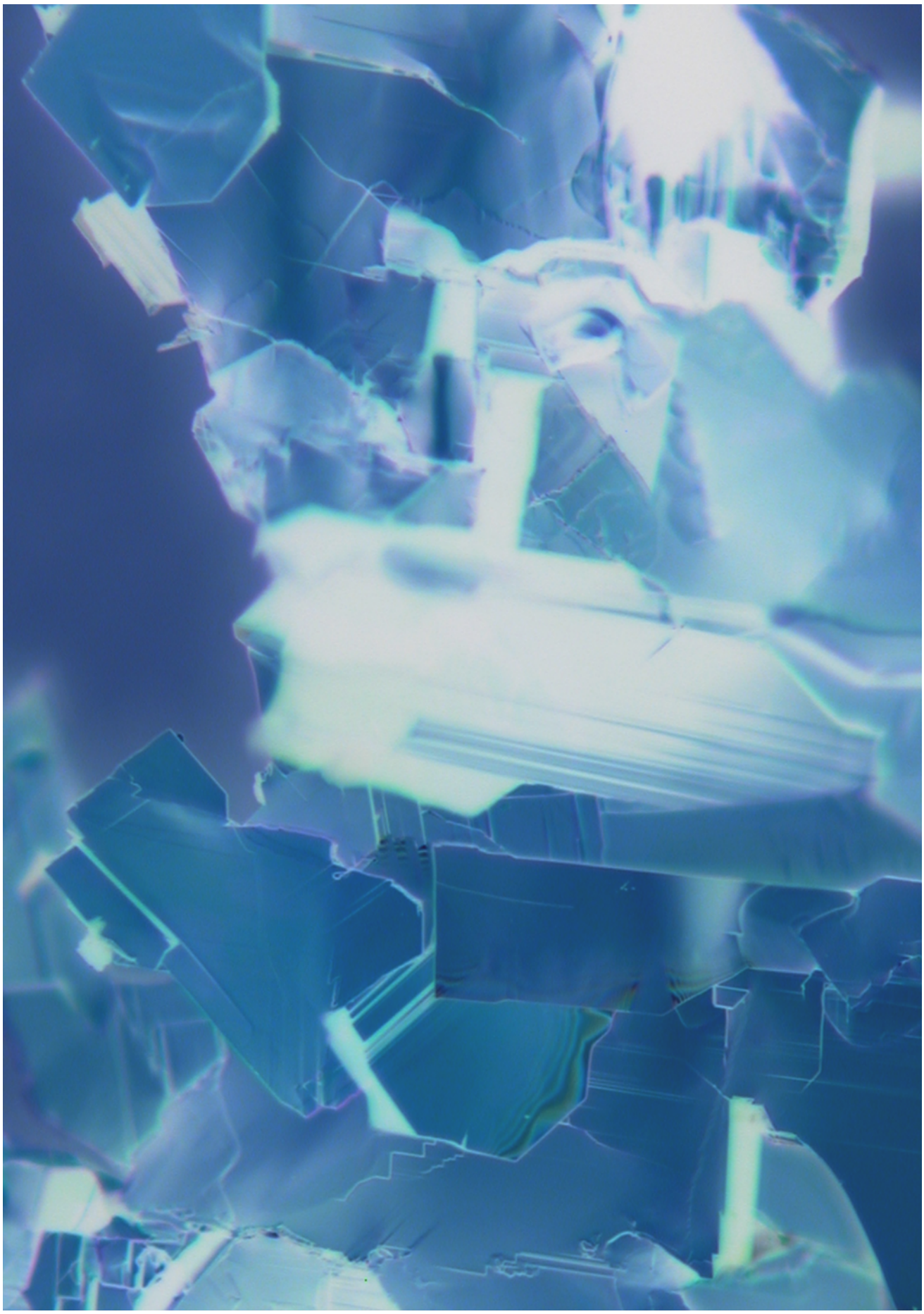

Summary

Organic semiconductors –an extremely interesting class of materials– are at the basis of the new and broad field of *Organic Electronics*. This field of research has grown rapidly in the recent years, mainly due to the perspective of fabricating electronic devices on large, flexible substrates at a low cost. For the manufacturing of organic electronic devices (*e.g.* RFID tags, displays, solar cells), working with thin films is most attractive; however, structural imperfections and polycrystalline orientations limit the study of the intrinsic properties of these materials. The best approach to explore the intrinsic properties of organic semiconductors is therefore the study of single-crystalline systems, as this provides an upper limit of the performance physically attainable by thin films of the same material.

The objective of the work described in this thesis is *"to fabricate high-quality organic molecular single-crystal devices"*. The fabrication of high-quality organic crystal devices is not straightforward and poses various technological challenges: the fragile single-crystals are incompatible with most conventional thin film deposition and patterning techniques, and the molecular order at the surface can be damaged very easily. To achieve the objective, the fabrication of complete field-effect transistor devices by direct deposition of metal contacts and oxide gate dielectrics on the surface of free-standing organic single-crystals at room temperature, with well-defined interfaces, is selected as main approach.

Pentacene, the benchmark material studied in this work, is by far the most popular organic semiconductor used in the fabrication of organic field-effect transistors (OFETs) for organic electronic applications. The crystal structure, geometry and morphology of vapor-grown pentacene single-crystals are investigated by various analytical techniques, as they are applied as substrate in the device fabrication. On the pentacene crystal surface, monomolecular terrace steps of 1.4 nm high are present, yet also larger terrace steps up to tens and even hundreds of nanometers are found. In some cases, the terrace steps are straight and parallel aligned, which indicates the thermodynamically most stable crystal planes are formed; however, in other cases, the steps are randomly curved. The observed pentacene single-crystal morphology shows a *step flow* type of crystal growth is the dominant growth mechanism, yet several observations show that the crystal growth behavior is not limited to this type of growth.

It is well known that organic materials are sensitive to photo-oxidation when they come into contact with oxygen under light exposure. For pentacene, the most common oxidation product is 6,13-pentacenequinone. This quinone is normally also the largest impurity present, as pentacene is synthesized from this material. The presence and arrangement of 6,13-pentacenequinone impurities on the surface and in the bulk of pentacene single-crystals is studied, as these molecules reduce the charge carrier mobility and conductivity. By using the combination of low-voltage scanning electron microscopy (LV-SEM) contrast, atomic force microscopy (AFM) step height differences and AFM tapping-mode phase contrast, it is observed that the quinone is preferentially located as a thin layer (partly) covering the pentacene crystal surface. Thickness of this quinone layer is about 0.9 nm, corresponding to

the *d*(002)-spacing of bulk 6,13-pentacenequinone, which contradicts with findings in literature that describe the presence of a 1.8 nm thick *d*(001) quinone doublelayer. Cleaving experiments showed no large patches of quinone impurities are present in the crystal. In order to remove the 6,13-pentacene-quinone molecules selectively from the pentacene single-crystal surface, the partly-oxidized crystals are heated in vacuum at a fixed temperature overnight. Performing the heating treatment at 75 - 80 °C removed the quinone material completely, yielding an unoxidized pentacene single-crystal with a clean and undamaged surface morphology that is suitable for subsequent device fabrication.

In order to fabricate complete organic molecular single-crystal field-effect transistors, the direct deposition and patterning of various metals (*i.e.* Au, Pt, Pd, Ni and Co) and medium-κ oxide dielectric materials (*i.e.* Al_2O_3, HfO_2 and CeO_2) through a stencil on the surface of pentacene single-crystals by pulsed laser deposition (PLD) is investigated. By taking several precautions in the PLD process that reduce the kinetic energy of the impinging species or reduce build-up of stress during deposition, low-kinetic energy deposition or *'soft-landing'* is achieved. Smooth and isolated patterns with a well-defined geometry are successfully deposited, without obvious destruction of the fragile organic substrate or mechanical failure of the deposited film. A well-controlled interface between the organic crystal and the deposited patterns is obtained with this approach and diffusion of the deposited material into the soft organic substrate is limited, as is demonstrated by a *model system* of Pt top contacts *'soft-landed'* on an alkylphosphate self-assembled monolayer.

After the depositions on pentacene single-crystals, it is observed that the terraced structure of the underlying pentacene substrate (*i.e.* the 1.4 nm high *d*(001) terrace steps) is often still noticeable on top of the patterned metal and oxide features (with a thickness up to several tens of nanometer). A series of gold patterns with increasing thickness is *'soft'* deposited on silicon oxide and pentacene single-crystals with PLD; the results show that the morphology and growth evolution of the surface roughness is similar on both kinds of substrates. Gold features deposited using the *'soft-landing'* parameters have a lower roughness compared to the *'hard-landed'* films.

Finally, the influence of the deposition parameters applied in the device fabrication procedure (*'hard-landing'* vs. *'soft-landing'*) and the influence of performing a heat treatment (before applying the metal contacts) on the electrical properties of pentacene single-crystals is investigated, by characterizing space-charge-limited current (SCLC) and field-effect transistor (FET) devices fabricated on the surface of pentacene single-crystals in a nano probing system. The highest charge carrier mobility values found in the SCLC measurements are close to values reported in literature, illustrating metal contacts can be reproducibly patterned on organic molecular crystals by *'soft-landing'* in pulsed laser stencil deposition; *'hard-landing'* resulted in a more distorted interface and a lower mobility. Applying the heat treatment resulted in a significant decrease of the mobility, indicating the procedure is not completely optimized yet. The *in situ* fabrication of complete FET devices on the pentacene single-crystal surface is realized by using the *'quasi-dynamic stencil deposition'* technique in PLD; however, the transistor characteristics did not show the presence of a field-effect.

Samenvatting

(Summary in Dutch)

Organische halfgeleiders –een zeer interessante groep materialen– vormen de basis van de *Organische Elektronica*. Dit nieuwe en brede onderzoeksgebied is de laatste jaren erg in opmars, voornamelijk door het vooruitzicht om zeer goedkoop elektrische schakelingen te kunnen vervaardigen op grote, flexibele oppervlakken. Voor de fabricatie van commerciële producten (bv. anti-diefstal labels, beeldschermen, zonnecellen) is het werken met dunne lagen het meest aantrekkelijk. Voor het onderzoeken van de intrinsieke eigenschappen van de organische halfgeleiders zijn dunne films door de poly-kristallijne oriëntatie en structurele wanorde echter minder geschikt. Daarom is het bestuderen van halfgeleidende één-kristallen een beter idee.

Doel van het werk dat beschreven staat in deze thesis is *"het fabriceren van organisch moleculaire één-kristal werktuigen van hoge kwaliteit"*. De fabricage van elektrische schakelingen op organisch één-kristallen is niet eenvoudig en vergt ettelijke technische uitdagingen; de meeste conventionele depositie- en structureringstechnieken beschadigen namelijk de moleculaire structuur aan het oppervlak van de fragiele kristallen. Daarom is ervoor gekozen om veldeffect transistor structuren te construeren op het oppervlak van de halfgeleidende één-kristallen door de metallische contacten en oxidische dielektrische materialen buitengewoon voorzichtig aan te brengen.

Pentaceen, het materiaal dat bestudeerd wordt in deze dissertatie, is veruit de meest populaire organische halfgeleider die gebruikt wordt in de fabricatie van veldeffect transistors voor toepassingen in de organische elektronica. Als eerste zijn de kristalstructuur, geometrie en morfologie van pentaceen één-kristallen onderzocht met behulp van verscheidene analysetechnieken. Het pentaceen kristaloppervlak wordt gekarakteriseerd door de aanwezigheid van 1.4 nm hoge mono-moleculaire terrasstappen, als wel door terrasstappen van tientallen tot wel honderden nanometers hoog. In een aantal gevallen zijn de terras-stappen recht en parallel georiënteerd. Dit geeft aan dat de thermodynamisch meest stabiele kristalvlakken zijn gevormd. In andere gevallen hebben de terrasstappen een willekeurig gekromde vorm. De morfologie van de pentaceen één-kristallen laat zien dat *stap-toeloop* groei het dominante mechanisme is tijdens de kristalgroei; echter de kristalgroei is niet gelimiteerd tot dit mechanisme.

Organische materialen zijn over het algemeen gevoelig voor oxidatie wanneer ze onder belichting in contact komen met zuurstof. Het meest voorkomende oxidatieproduct van pentaceen is 6,13-pentaceenchinon. Dit chinon is tevens de grootste vervuiling aanwezig in pentaceen, aangezien het normaliter hieruit gesynthetiseerd wordt. De aanwezigheid en positionering van 6,13-pentaceenchinon vervuilingen aan het oppervlak en in de bulk van pentaceen één-kristallen is onderzocht door (al dan niet gekliefde) kristallen te bestuderen met behulp van raster elektronen microscopie (SEM) en atomaire kracht microscopie (AFM). Uit deze experimenten blijkt dat het chinon preferentieel als een moleculaire *monolaag* het pentaceen kristal oppervlak (gedeeltelijk) bedekt; in de bulk van het kristal zijn

geen grote hoeveelheden chinon aanwezig. De dikte van deze dunne laag is ongeveer 0.9 nm. Dit komt overeen met de *d*(002)-afstand van bulk 6,13-pentaceneenchinon en spreekt bevindingen in de literatuur van de aanwezigheid een 1.8 nm dikke *d*(001) chinon *dubbellaag* tegen. Om de 6,13-pentaceenchinon moleculen selectief te verwijderen van het pentaceen één-kristal oppervlak, zijn de (gedeeltelijk) geoxideerde kristallen gedurende een nacht op een constante temperatuur verwarmd in vacuüm. Door deze warmtebehandeling uit te voeren rond 75–80 °C, sublimeert het chinon materiaal volledig, resulterend in een schoon, ongeoxideerd en onbeschadigd pentaceen één-kristal oppervlak.

Met het oog op de fabricage van veldeffect transistors op het oppervlak van de pentaceen één-kristallen, is het groeien en structureren van verscheidene metalen (Au, Pt, Pd, Ni en Co) en oxiden (Al_2O_3, HfO_2 en CeO_2) door een stencilmasker met behulp van gepulste laser depositie (PLD) verder onderzocht. Door diverse maatregelen te nemen in het PLD proces die de kinetische energie van de landende deeltjes reduceren of de opbouw van stress in de film tijdens de groei verminderen, zijn de *'hard-landende'* parameters geoptimaliseerd tot een *'zacht-landende'* depositie. Met deze aanpak zijn gladde structuren met een goed gedefinieerde geometrie succesvol gegroeid, zonder zichtbare beschadigingen aan het fragiele organische substraat of de film. Er wordt tevens een goed gecontroleerd grensvlak tussen het organische kristal en de gedeponeerde patronen verkregen; een *model systeem* van *'zachte-landing'* Pt elektrodes op een zelf-geassembleerde alkylfosfaat monolaag toont aan dat diffusie in het organische substraat zeer beperkt is.

Op het oppervlak van op pentaceen één-kristallen gegroeide metaal en oxide structuren (met een dikte van tientallen nanometers) is vaak de terrasvormige structuur van het onderliggende substraat nog steeds duidelijk zichtbaar (d.w.z. de 1.4 nm hoge *d*(001) pentaceen terras-stappen). Deze observatie is verder onderzocht, door goud te structureren op siliciumoxide en pentaceen één-kristal substraten met PLD. De resultaten tonen aan dat de evolutie van de morfologie en oppervlakteruwheid vergelijkbaar is op beide substraatsoorten. Ook resulteren de *'zacht-landende'* parameters in een minder ruwe film dan de *'hard-landende'* parameters, waardoor de substraat morfologie langer zichtbaar blijft.

Tenslotte is de invloed van de depositie parameters (*'harde-landing'* t.o.v. *'zachte-landing'*) en de invloed van de warmtebehandeling op de elektrische eigenschappen van de pentaceen één-kristallen onderzocht door deze te karakteriseren in het ruimtelading-gelimiteerde-stroom regime (SCLC) en door veldeffect transistors (FET) die op het oppervlak zijn aangebracht. De hoogs gevonden waarden voor de mobiliteit in de SCLC metingen liggen dicht bij waarden gemeld in de literatuur, wat illustreert dat metaal contacten reproduceerbaar gestructureerd kunnen worden op de organisch moleculaire kristallen door *'zachte-landing'* in PLD; *'harde-landing'* resulteerde in een meer verstoord grensvlak en een lagere mobiliteit. Het toepassen van de warmtebehandeling resulteerde in een significante afname van de mobiliteit; echter de warmtebehandeling is nog niet volledig geoptimaliseerd. De *in situ* fabricage van complete FET structuren op het pentaceen één-kristal oppervlak is gerealiseerd door gebruik te maken van de *'quasi-dynamische stencil depositie'* techniek in PLD; de transistor karakteristieken tonen echter niet de aanwezigheid van een veldeffect.

Dankwoord

(Acknowledgments in Dutch)

Goed, na ruim 4 jaren van onderzoek, na het maken van 13 posters en het geven van 23 presentaties, na het schrijven en bijschaven van 198 pagina's tekst, na het 251 keer groeien van een dunne film met PLD, na het bestuderen van 432 artikelen, en na het maken van 714 scans met de AFM, 1038 foto's met de SEM en 1290 foto's met de optische microscoop… Oftewel, na een *aanzienlijke* inspanning is de voltooiing van mijn proefschrift een feit en kan het promotieonderzoek afgerond worden. Nu is het moment dan ook daar om terug te blikken en alle mensen te bedanken die dit mogelijk hebben gemaakt en mij in deze jaren verder op weg hebben geholpen.

Allereerst zijn daar Dave en Guus, beide wil ik hartelijk bedanken voor de mogelijkheid die ze mij hebben gegeven om onderzoek te doen op een zeer interessant gebied, in een uitermate relaxte omgeving en met een keur aan mogelijkheden. Jullie aanstekelijke enthousiasme en vertrouwen in de goede afloop hebben mij menigmaal verder op weg geholpen. Daarbij is het als promovendus toch wel vrij uniek dat je begeleiding krijgt van twee professoren met wie je net zo makkelijk je laatste wetenschappelijke resultaten bespreekt, als de laatste resultaten van de plaatselijke FC.

Naast de financiële support vanuit NanoNed, wil ik graag de goede sfeer binnen ons NEM-cluster benoemen (Evert, hulde!). In het bijzonder gaat mijn dank uit naar 'Groningen', naar Anne, Oana en Thom, voor hun expertise in en het groeien van de pentaceen en rubreen één-kristallen voor mijn onderzoek. Evenzo wil ik graag Gertjan (ook voor het corrigeren van dit proefschrift en de goede slechte woordgrappen), Wilfred (voor de nuttige discussies) en Jeroen bedanken voor het zitting nemen in mijn promotiecommissie.

Natuurlijk zijn er nog meer mensen die mijn onderzoek mede mogelijk hebben gemaakt; de mensen die altijd tijd voor je vrij maken. Allereerst Henk, Frank en Dick, uiteraard voor de technische ondersteuning in het lab, maar ook voor de ontspannen werksfeer waardoor het fijn samenwerken is geweest met jullie. Marion en José, uiteraard voor de ondersteunende werkzaamheden, maar ook voor de gezellige momenten tussen de arbeid door.

Gerard, je enthousiasme en vindingrijkheid in het lab heeft mijn onderzoek zeker verder geholpen. Ook onze wekelijkse artikelbespreking heb ik erg gewaardeerd; eindelijk een partner die net zo veel plezier beleefde in het verkennen van de organische elektronica als ik had. Adit, jouw experimenten in het lab hebben evenzo een belangrijke bijdrage geleverd aan dit proefschrift. Oktay en Michiel, het combineren van onze expertises in het lab is mij goed bevallen, met als resultaat een mooi artikel.

De afgelopen jaren heb ik met verschillende kantoorgenoten mijn werkplek gedeeld. Eerst waren daar Matthijn, Paul en Frank, daarna Hans (grote dank voor je positieve commentaar op het conceptproefschrift) en Xin, en Josée. Ik heb me prima met jullie vermaakt, wat wel blijkt uit het feit dat ons kantoor menigmaal als laatste het licht uit mocht doen! Gaandeweg veroverde ik alle vrijheid om de muziek te verzorgen op ons kantoor; enfin, bij deze nogmaals excuses voor mijn soms enigszins discutabele muzieksmaak.

Conferenties, symposia, workshops, studiereizen, colloquia, skiën, karten, duiken, zeilen, feesten, barbecues, etentjes, borrels en koffiepauzes waren allen lang niet zo leuk geweest zonder de staf en de vele promovendi, postdocs en afstudeerders die in de loop der jaren een periode bij IMS hebben vertoefd. Uiteraard wil ik alle collega's bedanken met wie ik een fijne tijd heb gehad, maar in het bijzonder noem ik Jeroen, Ruud, Rik, Brian, Nicolas, Michelle, Willem, Minh, Eddy, Herman, Andreas, André en Bernard. Ook Koray, Vittorio, Ole, Gerrit, Wouter, Sjoerd, Werner, Kai, Bouwe, Hajo, Nirupam, Rogier, Peter, Gerard, Antony, Suresh, Ronald, Maarten, Tomasz, Arjen en Joska worden bedankt voor een plezierige periode.

Als captain van het IMS zaalvoetbalteam wil ik mijn hele selectie bedanken, en onze vedette Mark in het bijzonder, die wekelijks dit uurtje ontspanning mogelijk maakten. Ik ben verheugd dat ik, door het winnen van het UT-zaalvoetbaltoernooi 2011, mijn futsal carrière op het hoogtepunt heb kunnen afsluiten.

Vanuit de zaal is het maar een kleine stap naar het echte werk op het veld. Want niets zo mooi als op zaterdagmiddag, na anderhalf uur ploeteren in de stromende regen op een baggerveld ergens diep in de regio, in de kantine aan een lange houten tafel vol met groene flesjes de verhalen te horen over hoe goed men eigenlijk wel niet was die wedstrijd. Conform het 3e team van E.F.C. Prinses Wilhelmina 1885, heeft ook die andere trots uit Enschede het een en ander laten zien de afgelopen jaren, met als absolute hoogtepunt het bereiken van het landskampioenschap op 2 mei 2010. Gerjan en Michiel, ik hoop dat we samen nog vele historische wedstrijden van F.C. Twente '65 mogen meemaken! Daarnaast is het mij een genoegen om, met u als paranimphen, de verdediging van dit proefschrift in onze 'stadionopstelling' te mogen voeren. En Erwin, met jou van gedachten wisselen op vrijdagavond is altijd een mooi begin van het weekend! Maar vooral ben ik jullie alle drie erkentelijk voor jullie bijzonder goede vriendschap!

Uiteraard gaat hier ook een woord van dank uit naar de studenten van B.S.V. Moedt ende Kraght, ofwel de MEK. Ik, trotse erevledbewoner zijnde, verwacht dan ook om –net als de afgelopen jaren– nog lang gastvrij ontvangen te worden aan de Campuslaan 23.

Lindsey, Kirsten, ik wil jullie bedanken voor de mooie momenten die we samen beleefd hebben. Wat ik van jullie heb mogen leren staat niet in dit boekje beschreven, maar jullie hebben mij –beide op je eigen manier– veel waardevols meegegeven voor m'n toekomst!

Tot slot wil ik mijn familie, en vooral mijn ouders, Bram en Coby, en mijn broer Robert, graag bedanken voor hun interesse in de nanotechnologie in het algemeen en mijn werkzaamheden daarin in het bijzonder. Maar bovenal ben ik jullie ontzettend dankbaar voor alles wat jullie mij vroeger geleerd hebben, voor jullie onvoorwaardelijke steun en vertrouwen in mij, en voor alle keren dat jullie voor mij klaar stonden!

Goed, de toekomst ligt nu open voor mij… Tijd voor een nieuwe uitdaging!!

Peter

About the Author

Peter J. de Veen was born on April 7, 1980 in Hardenberg, The Netherlands. After graduating from secondary education (VWO, Vechtdal College, Hardenberg) in 1998, he started his study Chemical Engineering at the University of Twente in Enschede, The Netherlands. In 2004, he performed an internship at BASF AG Polymer Research in Ludwigshafen am Rhein, Germany, on "*Research on the synthesis of oligomeric tanning agents*". Thereafter, he joined the Inorganic Materials Science (IMS) group of prof. Dave Blank at the University of Twente and the MESA+ Institute for Nanotechnology. In 2005, under supervision of dr. Louis Winnubst, he obtained his masters degree with a thesis entitled "*Synthesis and characterization of dense CuO + 3Y-TZP nano-nano composites*".

Starting from January 2006, he performed his doctoral research in the IMS group. Under supervision of prof. Guus Rijnders, he carried out research on the NanoNed-project "*Fabrication of high-quality organic molecular single-crystal devices*". The main results are described in this thesis.

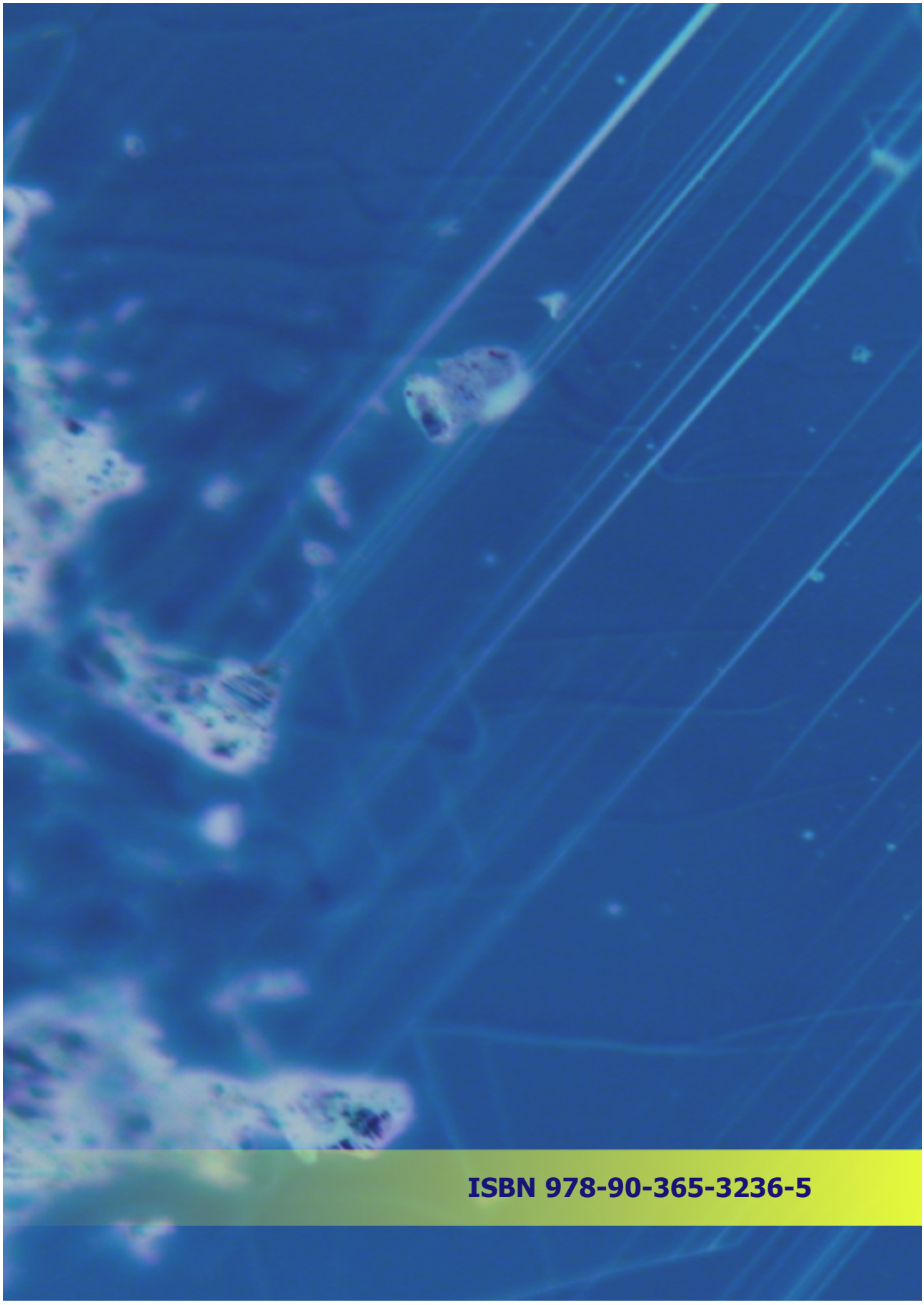

ISBN 978-90-365-3236-5

Stellingen

behorende bij het proefschrift

INTERFACE ENGINEERING FOR ORGANIC ELECTRONICS

MANUFACTURING OF HYBRID INORGANIC–ORGANIC MOLECULAR CRYSTAL DEVICES

Peter de Veen

1. Het is vanuit een chemisch oogpunt fundamenteel onjuist om kleine, organische moleculen met een laag moleculair gewicht, zoals pentaceen en rubreen, te labelen als 'oligomeer', 'oligoaceen' of 'polyaceen'. *Hoofdstuk 1 van deze thesis.*

2. Het is subliem om selectief de geoxideerde oppervlaktelaag van een organisch één-kristal te sublimeren. *Hoofdstuk 5 van deze thesis.*

3. Juist slechte films zijn het bekijken waard. *Hoofdstuk 6 van deze thesis.*

4. De invoering van studieprogramma's voor promovendi, de zogeheten 'graduate schools', belemmert de academische vrijheid van de jonge onderzoeker.

5. Zelfs het maar met mate *opSchönen* van je meetdata is niet toegestaan.

6. Wetenschappers moeten oppassen om zich niet te gaan gedragen als sportcommentatoren, door het stellen van teveel clichématige vragen.

7. Promoveren zonder kampioenschap is als bier zonder schuim.

8. In tegenstelling tot het nasynchroniseren van een Engelstalige film in het Nederlands, verhoogt een Duitse nasynchronisatie juist vaak het kijkplezier.

9. Herhaling is de kracht van de humor.

10. Iej könt better plat proat'n as vals kuiern. *(Twents)*

Propositions

accompanying the thesis

INTERFACE ENGINEERING FOR ORGANIC ELECTRONICS

MANUFACTURING OF HYBRID INORGANIC–ORGANIC MOLECULAR CRYSTAL DEVICES

Peter de Veen

1. It is, from a chemical point of view, fundamentally wrong to label small, organic molecules with a low-molecular weight, like pentacene and rubrene, as 'oligomer', 'oligoacene' or 'polyacene'. *Chapter 1 of this thesis.*

2. It's sublime to selectively sublimate the oxidized surface layer from an organic single-crystal. *Chapter 5 of this thesis.*

3. Especially bad films are worth viewing. *Chapter 6 of this thesis.*

4. The introduction of study programs for doctoral candidates, the so-called 'graduate schools', hampers the academic freedom of the young researcher.

5. It is not allowed *to Schön* your experimental data even only moderately.

6. Scientists must be careful not to behave like sport commentators, by asking too many clichéd questions.

7. A promotion without championship is like beer without a head.

8. As opposed to dubbing an English spoken movie into Dutch, German dubbing often does enhance the viewing pleasure.

9. Repetition is the strength of humor.

10. Iej könt better plat proat'n as vals kuiern. *(Twentish)*